A vibrating carbon nanotube probe to study superfluid ^{4}He

Lancaster University

Saba Mehsar Khan

October, 6 2024

Declaration

I hereby confirm that, unless explicitly acknowledged, the material presented in this thesis is original and has not been presented, either wholly or partially, for evaluation towards any other academic degree or qualification in this or any other educational institution. The research and writings herein are a result of my individual efforts and those of my co-contributors, as detailed within the text. I confirm that this thesis comprises 35,580 words and does not surpass the 80,000-word limit.

Saba Mehsar Khan (MSc)
May 2024

Acknowledgments

I would like to sincerely thank everyone who helped me complete this thesis. First and foremost, I am grateful to Edward for giving me the opportunity to work on this exciting project and for supporting me throughout. I really appreciate his encouragement to try new experiments and different approaches in our well-organized and well-equipped lab.

I've been lucky to receive help from many people during this journey. I would like to thank Malcolm and Roch for their assistance in integrating the capillary lines and gas handling system into our Triton 2 fridge. A big thanks to Fredrik for teaching me electron beam lithography at Manchester, which was important for making devices. Garry and Kunal were also a great help with cleanroom equipment and training in Lancaster. I am grateful to Dr. Natalia Ares and her group for helping us grow nanotubes in Oxford before we had our own furnace.

A special thanks to Sergey for always encouraging me and giving me great advice, both technical and academic. I'd like to thank Alex for his help when I moved to Lancaster, teaching me about the lab and even assisting with administrative tasks. Theo was always helpful in the lab, especially when explaining tricky concepts like Andreev reflection. Thanks to Joshua for being a good friend when I was new in Lancaster, and to Viktor for our interesting conversations about helium physics, which helped me later on. Patrick is one of the hardest-working colleagues I know, always willing to help. I'd also like to thank Slava for quickly machining the first version of our helium cell. Even though the workshop was fast, no one could match your same-day turnaround! I'm also thankful to all the workshop staff for their quick help—our experiments wouldn't have been possible without them.

The first year of my PhD was difficult, mostly because of Covid and moving to England, but things got better when the restrictions lifted and we could return to the lab. I met many wonderful people in Lancaster, more than I ever imagined. Life as a PhD student can be hard, and it's good to have friends around. I'm thankful for all the nice people I've met and the friendships I've made. Matthew, thank you for your patience and for listening when things didn't go well in the lab. Thanks to Shearbhan for teaching me how to carve pumpkins at Halloween and for our late-night tea and chats. Ruben, your pancakes are still the best I've ever had (even though I haven't tried others yet!). Playing pool with George, Deepanjan, Sam, Matthew, Scott, and Shearbhan was always fun, even if I had to wait a while for my turn! Special thanks to Scott for taking over the experiment—I wish you all the best in your future work!

Lastly, I'm incredibly grateful to my family, especially my father, for always being there to listen, offer advice, and give me the best support I could ask for.

Contents

List of Figures

Chapter 1: Introduction

1.1 Research motive

Superfluidity in helium isotopes, ^{4}He [1, 2, 3] and ^{3}He [4, 5, 6], offers a remarkable opportunity to study quantum mechanics on a macroscopic scale. These superfluids exhibit unique properties, primarily due to fundamental excitations or quasiparticles such as phonons and quantized vortices, which offer a comprehensive view of quantum statistics and particle interactions in macroscopic quantum phenomena. ^{4}He, existing as a Bose-Einstein condensate of bosons, and ^{3}He, characterized by its two distinct superfluid phases (A and B) composed of Cooper pairs of fermions, exhibit diverse topological and quantum properties. The purity and controllability of these systems in laboratory environments make them ideal for investigating complex quantum fluid dynamics and for testing theoretical predictions in quantum mechanics and superfluidity.
Research in this domain has driven many technological advancements in low-temperature physics, including the development of novel cryogenic techniques and a deeper understanding of phase transitions at low temperatures [7]. The study of quasi-particle dynamics in superfluid helium can also provide insights into other fields, such as astrophysics, particularly in understanding neutron stars that are believed to contain superfluid components [8]. Additionally, examining vortex formation during phase transitions offers analogues to symmetry breaking events in the early universe [9].
A primary method for studying excitations in superfluids involves immersing a moving object, such as a vibrating-wire viscometer, in the superfluid. Observing the damping of these devices provides insights into the transport of energy by quasiparticles under various conditions. In previous studies, experimental approaches such as using tuning forks [10, 11], vibrating wires [12], and beams [13, 14] have been employed to investigate thermal excitations in superfluid helium. These methods focus on understanding how energy is dissipated in a superfluid, despite its lack of viscosity, and the role of quantum turbulence as a mechanism for energy dissipation at low temperatures. Additionally, the attenuation of second sound has also been employed as a technique to probe vortex density [15]. These experiments aim to elucidate the creation, stability, interaction, and decay of vortices within superfluids, though conclusive experimental evidence remains elusive.

Recently, nano-electromechanical systems (NEMS) sensors have emerged as promising tools for analyzing the rapid dynamics of these excitations in superfluid ^{4}He. The submersion of NEMS devices in superfluids introduces complexities such as acoustic wave emission, nonlinear behavior, and interactions with nearby structures [13, 14, 16]. It is crucial to understand the interactions between the devices and the fluid at the mesoscopic scale for deeper insight into these dynamics. Despite recent advancements in NEMS technology, a technique for probing superfluids at a mesoscopic length scale is yet to be developed. However, carbon nanotube nanomechanical resonators (CNT) present a novel

route for examining mesoscopic systems, such as superfluid ^{4}He and ^{3}He. Their high-quality factor, versatility across various temperature ranges, and heightened sensitivity position them as ideal tools for investigating superfluids at the sub-atomic scale.

The resonance frequency of these resonators can be fine-tuned by adsorbed masses, charges, and impurities up to the energy required for quasiparticle formation, around 70 MHz. This is a crucial attribute since mechanical resonators are most sensitive to external forces when these forces align with the device's mechanical resonance frequency. This characteristic emphasizes the importance of frequency tuning in exploring phenomena that manifest at specific frequencies, including resonant Kelvin waves in quantized vortices within superfluids [17, 18], acoustic modes within cavities [19], and states bound to vortex cores in superfluid helium [20]. We aim to explore these superfluid excitations, employing a carbon nanotube viscometer to probe at unprecedented frequency and length scales.

Research questions

This thesis addresses two primary research questions:

1. **How do CNT resonators interact with superfluid excitations at high frequencies and small diameters?** The resonators operate within the frequency range of 10 MHz to 100 MHz, with diameters between 1 nm to 3 nm and lengths of 1 µm to 2 µm, dimensions smaller than those used in conventional nanomechanical resonators. The CNTs' radii (0.5 nm to 1.5 nm) closely match the coherence length of superfluid ^{4}He (0.34 nm [21]), making them highly sensitive to nanoscale interactions with quantum fluids. This dimensional match allows CNTs to strongly couple with quantum excitations, including phonons, rotons, and individual vortices, whose cores are on the same order as the coherence length. This enables studies of vortex pinning, local perturbations, and dissipation mechanisms in superfluid helium.

2. **How does tuning the resonance frequency enhance the detection sensitivity of CNT resonators?** One key advantage of CNT resonators is their ability to tune resonance frequencies via the DC gate voltage [22], which increases tension in the nanotube. This tunability allows the resonance frequencies to match those of specific superfluid excitations, enhancing the interaction between the CNT and phenomena such as Kelvin waves generated by vortex motion and acoustic emissions. Additionally, tuning the device near a Coulomb peak enhances the coupling between the nanotube's mechanical motion and quantum dot effects via single-electron tunneling [23, 24]. This strong coupling boosts sensitivity, enabling the CNT to detect subtle superfluid interactions, such as quasiparticle excitations. The combined ability to fine-tune resonance frequencies and enhance sensitivity through Coulomb blockade effects makes CNT resonators highly effective tools for studying quantum fluids.

We have developed CNT resonators to study superfluid ^{4}He. Initially, the devices are measured in a vacuum, allowing for a comprehensive understanding of their intrinsic properties. Subsequently, when operated in superfluid ^{4}He, the devices exhibit inherent nonlinear behavior along with a considerable reduction in their Q factor and resonance frequency due to helium adsorption and vortex interactions. This work presents preliminary experiments on bulk superfluid ^{4}He using the CNT resonator. These experiments require

further experimental and theoretical investigation to fully understand their dynamics. However, initial observations suggest that the CNT resonator has greater sensitivity to superfluid excitations, making it a potentially excellent tool for probing even more exotic quantum fluids like ^{3}He in future studies.

1.2 Thesis overview

This thesis presents a detailed investigation into the behavior of CNTs as mechanical resonators, focusing on their interactions with superfluid ^{4}He. The research combines theoretical modeling with experimental measurements to elucidate the dynamics of CNT resonators immersed in superfluid helium. The structure of the thesis is as follows:
Chapter 2: Introduces superfluid ^{4}He and carbon nanotubes, covering the superfluid ^{4}He phase diagram, two-fluid model, and key phenomena such as quantum vortices followed by an introduction to the electronic traits and mechanics of carbon nanotubes. The chapter concludes with a review of how mechanical oscillators have been used to study helium fluids.
Chapter 3: Simulates CNTs' dynamics in ^{4}He, highlighting their potential as tools for studying quantum and hydrodynamic phenomena in low-temperature physics.
Chapters 4 and 5: Offers a detailed overview of the fabrication and characterization of advanced CNT devices, emphasizing controlled growth processes and their preliminary evaluations. Chapter 5 details the design of a specialized ^{4}He cell, along with a gas handling system and associated filling lines. Furthermore, it elaborates on their integration into a Triton dilution refrigerator and provides insights into the experimental setup and measurement methodologies.
Chapter 6: Focuses on the interaction between single-electron tunneling and nonlinear behavior in CNT resonators. It elucidates the factors influencing mechanical motion such as how the mechanical motion of the CNT approaches the quantum ground state through coupling to higher vibrational modes.
Chapter 7: Investigates a CNT resonator in superfluid helium-4, revealing significant damping due to remnant vorticies and resonance frequency shifts due to helium adhesion, alongside detailed observations of fluid-resonator interactions that lead us to observed Kelvin-wave resonances and temperature-dependent behaviors.
Chapter 8: Summarizes the research's key findings and implications, discussing its contributions and limitations, and suggesting potential directions for future study.

Note: Carbon nanotube is referred to as either "CNT" or "nanotube" throughout this thesis.

Chapter 2: Basics of superfluid ^{4}He and carbon nanotube resonators

In this chapter, we discuss the foundational theories that underlie the study of superfluid ^{4}He and carbon nanotube resonators. We begin with superfluid ^{4}He, elucidating its phase diagram, the two-fluid model, and the fascinating phenomena of excitations, like quantum vortices and turbulence. The discussion then transitions into an in-depth look at carbon nanotubes, discussing their electronic properties, quantum dot confinements, and the mechanics that determine their physical behaviors. The CNT resonators are advanced nanotechnological structures that utilize the unique properties of CNTs to produce compact and sensitive devices. These resonators, vibrating at specific frequencies, are crucial in electronics, sensors, and communication systems. With two main types - mechanical and electromechanical - the former relies on physical dimensions like length and tension to vibrate, while the latter uses the piezoelectric properties of CNTs to convert mechanical vibrations into electrical signals. The chapter concludes by reviewing research that employs mechanical oscillators as probes for studying helium fluids, including superfluid ^{3}He.

2.1 Superfluid ^{4}He

^{4}He, one of the two stable isotopes of helium, became a subject of scientific fascination in the early 20th century. It was first liquefied in 1908 by Heike Kamerlingh Onnes as he managed to cool it down to 1.5 K [25]. However, at that time, the phase transition within ^{4}He went unnoticed. It was not until 1932 when Keesom and Clusius examined its specific heat capacity that the pivotal discovery was made. They identified a distinct transition point at 2.17 K, now famously known as the λ-point [1], marking the division between He-I and He-II phases. Additionally, Keesom delved into viscosity within He-II and stumbled upon superfluidity – a state where ^{4}He flowed without any measurable viscosity, as independently confirmed by Kapitza [2] and Allen and Meisner [3] in 1938.

This complex behavior of ^{4}He prompted theoretical exploration. Fritz London [26] in 1939 proposed a connection to Bose-Einstein Condensates (BECs), where a multitude of bosons occupies the lowest energy state of the system. Although ^{4}He is indeed composed of bosons, a liquid with strong intermolecular forces, somewhat challenging BEC assumptions. Nonetheless, BEC theory provides a fundamental framework for understanding what happens below the λ-point. A more comprehensive model emerged when Tisza suggested that He-II consists of two coexisting fluids [27]: a normal fluid with temperature, viscosity, and entropy, as observed by Keesom, and a superfluid with zero temperature, viscosity, and entropy, as noted by Kapitsa. These two fluids interpenetrate each other, remaining non-interacting when no excitations are present. Both the normal and super-

fluid components have their own temperatures, viscosity, densities, and velocities, denoted as ρ_n, v_n, ρ_s, and v_s, respectively. The total density of He-II, ρ, is the sum of these components, expressed as $\rho = \rho_n + \rho_s$. Above the λ-point, the normal fluid dominates, gradually diminishing with decreasing temperature, until it becomes negligible around 1 K. This intricate interplay of components defines the captivating behavior of ^{4}He below its λ-point, offering a window into the intriguing world of superfluidity.

2.1.1 Phase diagram

The phase diagram of ^{4}He, shown in Fig. 2.1(top panel), illustrates its intriguing behavior in the vicinity of the superfluid transition. At atmospheric pressure, this transition occurs at $T = 2.17$ K. Additionally, ^{4}He lacks a liquid-solid transition at low pressures, in contrast to most materials.

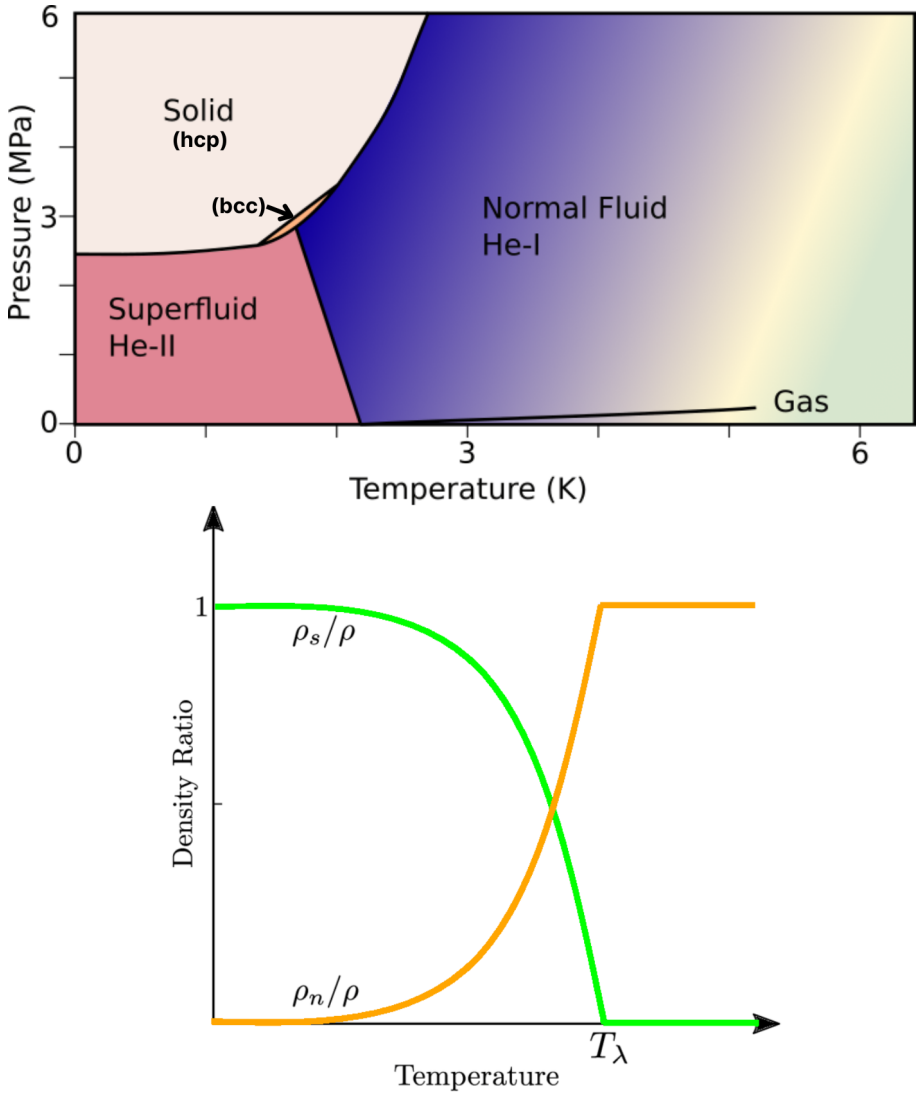

Figure 2.1: Top panel: Phase diagram of ^{4}He, illustrating the regions of distinct phases: gas, liquid, and superfluid. The diagram shows critical point and the lambda transition, which marks the onset of superfluidity in ^{4}He at low temperatures. Bottom panel: The fractional relative density as a function of temperature of the normal (orange) and superfluid (green) components of ^{4}He.

Further insights into the behavior of ^{4}He below the λ-point are provided by Fig. 2.1(bottom panel), which depicts the temperature dependence of the normal and superfluid densities, ρ_n and ρ_s, respectively. Above the λ-point, the normal fluid dominates, but as the temperature decreases, the normal fluid fraction diminishes rapidly, becoming practically insignificant around 1 K [28]. Andronikashvili first experimentally measured the temperature variation of the normal-fluid fraction using a set of rotational discs.

2.1.2 Landau's two-fluid model

Landau [29] and Tisza [27] independently developed the two-fluid model to elucidate the behavior of superfluid helium. However, Landau's model provided a more detailed and successful explanation. Central to Landau's insights was the recognition of an energy gap within the superfluid, which separates the ground state from excitations. This gap is crucial because it prevents energy dissipation in excitations, enabling the superfluid to flow with zero viscosity.

To delve into Landau's key ideas, let's consider an object of mass M moving at a constant velocity $\mathbf{u}$ through a stationary superfluid, generating an excitation. If this excitation has energy E and momentum $\mathbf{p}$, the mass's velocity must change to $\mathbf{v}$ to conserve both momentum and energy. Mathematically, this is expressed as:

$$\mathbf{p} + M\mathbf{v} = M\mathbf{u} \tag{2.1}$$

and

$$\frac{1}{2}M|\mathbf{v}|^2 + E = \frac{1}{2}M|\mathbf{u}|^2 \tag{2.2}$$

Rearranging these equations, we find

$$E = \frac{1}{2}M(|\mathbf{u}|^2 - |\mathbf{v}|^2) \tag{2.3}$$

In the limit where the excitation's mass is much smaller than the massive object's mass, we can approximate $|\mathbf{u} - \mathbf{v}|$ as approximately zero, leading to

$$E \approx \mathbf{p} \cdot \mathbf{u} \tag{2.4}$$

Furthermore, we define Landau's velocity v_L as the minimum velocity required to create an excitation, which is given by

$$v_L = \frac{E}{p} \tag{2.5}$$

In normal fluids, there is no energy gap, and therefore v_L equals zero. However, in superfluid helium (He-II), there exists an energy gap, and Landau's velocity is non-zero. Experimental measurements show that Landau's velocity in He-II is approximately 50 m/s [30].

This model considers the superfluid's total density, ρ, as the sum of the normal fluid density, ρ_n, and the superfluid density, ρ_s. At absolute zero, the normal fluid vanishes, and at the λ-point temperature, the superfluid fraction disappears. Only the normal fluid has non-zero entropy and viscosity.

The momentum density of mass flow, $\mathbf{j}$, combines both fluid components:

$$\frac{\partial \rho}{\partial t} = -\nabla \cdot \mathbf{j} \tag{2.6}$$

Well below the lambda point, the viscosity of the normal fluid is negligible and it behaves like an ideal fluid [31]:

$$\frac{\partial \mathbf{j}}{\partial t} + \rho_{\mathrm{n}} \mathbf{v}_{\mathrm{n}} \cdot \nabla \mathbf{v}_{\mathrm{n}} = -\nabla p \tag{2.7}$$

where p is the fluid pressure. In low velocity superfluid flows, entropy remains conserved. While superfluid helium exhibits zero-viscosity flow, macroscopic objects in it face some resistance. Resonators, for instance, lose energy through acoustic emission. At velocities well below v_{L}, they face higher drag from vortex ring formations, leading to superfluid turbulence.
In superfluid helium, macroscopic objects such as mechanical resonators do encounter damping. Resonators, for instance, emit phonons [32] which deplete their energy. Especially at higher velocities, significantly below Landau's velocity, these objects experience increased drag from vortex rings, inducing superfluid turbulence. This will be further discussed in relation to quantum vortices. In essence, Landau's two-fluid model elucidates superfluid helium's behavior, emphasizing the energy gap's role in zero-viscosity flow. Even with this model, macroscopic interactions with the superfluid reveal damping and fascinating turbulence phenomena.

2.1.3 Drag coefficient

The drag coefficient quantifies the resistance encountered by a resonator moving through superfluid ^{4}He [33], primarily due to interactions with the normal fluid component. In the two-fluid model of superfluid ^{4}He, the fluid consists of a normal component, which exhibits viscosity, and a superfluid component, which flows without viscosity. Only the normal fluid exerts drag on the resonator, while the superfluid does not contribute to viscous drag.

The drag coefficient is a dimensionless parameter used to describe the drag force acting on the resonator, defined as:

$$C_{\mathrm{d}} = \frac{F_{\mathrm{d}}}{\frac{1}{2}\rho_{\mathrm{n}} v^2 A}$$

where:

- C_{d} is the drag coefficient,
- F_{d} is the drag force,
- ρ_{n} is the density of the normal fluid component of superfluid ^{4}He,
- v is the velocity of the resonator,
- A is the cross-sectional area of the resonator.

As the resonator moves through superfluid helium, the drag force increases with the square of the velocity. Below the λ-point, the normal fluid density ρ_{n} decreases, reducing the drag force.

2.1.4 Excitations and quantum vortices

In the two-fluid model, while superfluid ^{4}He behavior is well-described, the microscopic foundations of its phenomena are less explored. Landau pioneered the microscopic perspective by identifying that a finite energy gap, Δ [34], is necessary for the emergence of collective excitations, ensuring dissipationless flow. This gap hinders momentum transfer at low velocities, resulting in a critical velocity, v_{L}, beyond which the superfluid's flow disturbs the condensate.

Landau introduced two primary excitations in superfluid ^{4}He:

1. **Phonons:** These are longitudinal excitations with linear dispersion, playing a pivotal role in sound emission. Their velocity, u_1, determines the first sound's velocity. The dispersion relation is:
$$E = pc_{\mathrm{ph}} \tag{2.8}$$

2. **Rotons:** These excitations are characterized by a specific energy gap. Near the roton momentum p_0, the dispersion relation is:
$$E \approx \Delta + \frac{(p - p_0)^2}{2m^*} \tag{2.9}$$

The critical velocity, v_{L}, corresponding to superfluid ^{4}He, is roughly 50 m/s. Landau posited that these excitations contribute to the normal fluid, as:

$$\rho_{\mathrm{n}} = \rho_{\mathrm{ph}} + \rho_{\mathrm{ro}} \tag{2.10}$$

On the other hand, superfluid ^{4}He also features quantum vortices, rooted in the coherent wave function Ψ [35] shared by the condensate of atoms. This function can be expressed as:

$$\Psi(\mathbf{r}) = \psi_0 e^{i\theta(\mathbf{r})} \tag{2.11}$$

From this, the momentum and superfluid velocity equations are derived as [31]:

$$\mathbf{p} = \hbar \nabla \theta \tag{2.12}$$

$$\mathbf{v}_{\mathrm{s}} = \frac{\hbar \nabla \theta}{m} \tag{2.13}$$

where $\mathbf{v}_{\mathrm{s}}$ represents the superfluid velocity, and m is the mass of a ^{4}He particle. Given the vorticity definition $\boldsymbol{\omega} = \nabla \times \mathbf{v}$, in a superfluid we have $\boldsymbol{\omega} = \frac{\hbar}{m} \nabla \times (\nabla \theta) = 0$.

Although superfluids are irrotational ($\nabla \times \mathbf{v}_{\mathrm{s}} = 0$), they can exhibit rotational motion, as evident in experiments [36]. Landau's proposition of quantized circulation was experimentally validated [37], leading to the concept of a quantum vortex, where vortices in superfluids have their vorticity contained within the core's normal fluid. The energy of these vortices correlates with the surrounding fluid's kinetic energy. Higher-order vortices tend to decay into single quantum vortices due to their energy being proportional to n^2, where n is an integer representing the number of circulation quanta. This quantization arises from the fact that circulation in a superfluid is quantized in multiples of $\kappa = \frac{nh}{m_4}$, with $n = 1$ representing the fundamental vortex state. Therefore, higher values of n correspond to vortices with multiple units of circulation, which are energetically less favorable compared to multiple single-quantum vortices. This understanding estimates the vortex core size in superfluid ^{4}He to be approximately 0.3 nm [38].

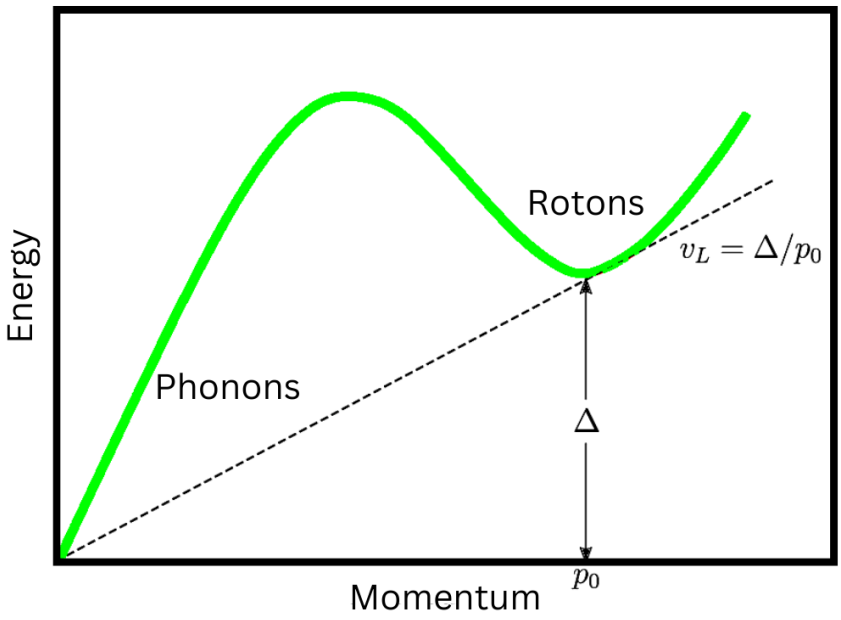

Figure 2.2: The phonons and rotons quasiparticles in superfluid ^{4}He.

2.1.5 Quantum turbulence

Turbulence, commonly observed in all fluids, arises when fast-moving objects generate vortices as they pass through a fluid. These vortices interact, breaking down into smaller ones until they fade due to viscous damping at the Kolmogorov [39] length scale. This transfers energy from the object to the fluid, slowing the object down. The unpredictable nature of vortex development poses challenges for engineers trying to reduce drag on vehicles like airplanes and ships. Thus, turbulence remains one of classical physics' unsolved problems.

Introduction to quantum turbulence

Quantum turbulence in superfluid ^{4}He is a unique form of turbulence that shares some similarities with classical turbulence, which occurs when fluids exhibit chaotic motion at high flow rates. Nevertheless, it's essential to recognize that at the scale of an individual vortex, quantum and classical turbulence are driven by distinct physical principles due to the quantized nature of vortices in quantum fluids [40]. This fundamental difference, evident at the microscopic scale, highlights the unique interplay between quantum and classical principles in fluid dynamics. In this discussion, we will explore the physics of single vortices and delve into systems comprising multiple vortices.

Nature of vortices: Feynman's insights

Historically, it was believed that superfluids, due to their lack of viscosity, could not support any intrinsic circulation. This belief was expressed by the mathematical relationship:

$$\nabla \times \mathbf{v}_\mathrm{s} = \nabla \times \nabla \phi_L = 0 \tag{2.14}$$

However, Richard Feynman challenged this view by proposing that circulation in superfluids is quantized due to the principles of quantum mechanics, specifically suggesting that

the circulation in a superfluid could only take discrete values because of the quantization of angular momentum [41, 42]. Furthermore, Feynman argued that the core of a vortex in a superfluid represents a topological defect [43]. His insights were experimentally confirmed by Vinen [44], who used a vibrating wire in rotating ^{4}He to capture vortices, leading to the splitting of previously degenerate oscillation modes. While Feynman laid the foundation for understanding quantized vortices, the term *quantum turbulence* was introduced later by Carlo Barenghi to describe the turbulent state of quantized vortices in superfluids [43].

Quantization of superfluid circulation

Stokes' theorem provides a method to quantify circulation in superfluids [45]. The circulation in a superfluid region enclosed by a length L and an area A is given by:

$$\kappa = \iint_A (\nabla \times \mathbf{v}_s) \cdot d\mathbf{A} = \oint_L \mathbf{v}_s \cdot d\mathbf{l} = \frac{\hbar \Delta \phi_L}{m_4} \tag{2.15}$$

where $\mathbf{v}_\mathrm{s} = \frac{\hbar \nabla \phi(r)}{m_4}$, and m_4 is the mass of a ^{4}He atom. This equation demonstrates that the circulation, κ, is quantized, taking the form

$$\kappa = \frac{nh}{m_4} \tag{2.16}$$

with n being an integer. This quantization leads to vortices in superfluid ^{4}He having specific quantized values of circulation. The superfluid velocity increases as one approaches the core of the vortex, described by

$$v_\mathrm{s} = \frac{\kappa}{2\pi r_\mathrm{v}} \tag{2.17}$$

However, it does not surpass the Landau critical velocity, ensuring the formation of a core that behaves similarly to normal fluids. The diameter of this core is approximately [46]

$$d = \frac{\kappa}{2\pi v_\mathrm{c}} \approx \frac{9.97 \times 10^{-8}}{2\pi \times 10} \approx 1.59 \times 10^{-9}\,\mathrm{m} \tag{2.18}$$

Here, κ is the quantum of circulation, given by $\kappa \approx 9.97 \times 10^{-8}\,\mathrm{m}^2/\mathrm{s}$, and the critical velocity is $v_\mathrm{c} \approx 10\,\mathrm{m/s}$. This results in a vortex core diameter d of approximately 1.59 nm, representing the distance over which the superfluid fraction decreases to zero from its bulk value.

However, variations in the observed vortex core diameter can arise due to temperature-dependent changes in the coherence length, which also affect the critical velocity. Boundary-induced distortions, as well as excitations that impact the local superfluid density, can further modify the core structure. Additionally, in quantum turbulent states, interactions between vortices, or small deviations from ideal purity in experimental setups, may lead to measurable deviations from the theoretical core size. These factors contribute to the variability in the observed core diameter, although it remains within the nanometer range.

Dynamics of quantum vortices

In systems with multiple quantized vortices, the energy per unit length of a vortex, denoted as E_L, is pivotal. It's calculated by integrating the kinetic energy per unit volume

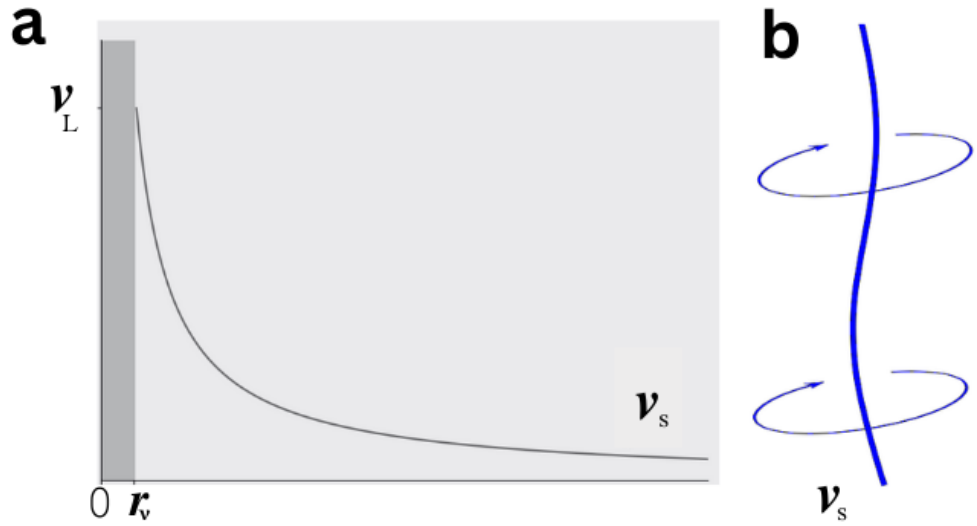

Figure 2.3: (a) The graph showcases the superfluid velocity around the quantum vortex along with its radius. When the superflow reaches Landau's velocity v_L, the superfluid starts to transform into normal fluid, determining the vortex core's radius, r_v as per Equation 2.17. (b) An illustration of quantum vortex core (Adapted from [38]).

from the core of vortex (distance d) to its nearest neighbor (distance b). Mathematically, this relationship is represented as [31]:

$$E_L = \frac{\rho_s \kappa^2}{4\pi} \ln\left(\frac{2b}{d}\right) \tag{2.19}$$

Since $E_L \propto n^2$, where n is the integer number of circulation quanta, the energy increases quadratically with n. This energy consideration implies that it's more efficient to have two vortices with $n = 1$ rather than a single vortex where $n = 2$. A notable characteristic of these vortices is their common, quantized circulation, h/m_4, which imparts simplicity to the study of quantum turbulence.

In addition to linear formations, vortices in ^{4}He can fold onto themselves to form "vortex rings". These closed-loop structures have a length of $2\pi r_v$, where r_v is the ring's radius. Their energy, E_r, is expressed as:

$$E_r = 2\pi r_v E_L \tag{2.20}$$

The propagation velocity of the vortex is defined by equations:

$$v_r = \frac{\kappa}{4\pi r_r}\left[\ln\left(\frac{2r_v}{d}\right) - \frac{1}{4}\right] \tag{2.21}$$

The dynamics of these rings and their propagation velocity offer intriguing insights into the nature of quantum turbulence [31].

Origins and decay of quantum turbulence

There are two primary methods to initiate quantum turbulence in ^{4}He: intrinsic and extrinsic nucleation. The former requires a high critical velocity ($v_c \sim 10\,\mathrm{m/s}$), while the latter, which involves manipulating existing vortex lines under superflow, can occur

at much lower velocities [47, 43] ($v_c \sim 10^{-3}$ m/s). Often, the Kibble-Zurek mechanism [48], a process during rapid cooling through the superfluid phase transition, is responsible for creating initial vortex lines in the system. This leads to the formation of topological defects as quantum vortices.

The dissipation of quantum turbulence is also governed by two mechanisms. At temperatures above 1 K, mutual friction between the normal and superfluid components results in dissipation. However, at lower temperatures, Kelvin waves—helical displacements of vortex cores—dominate the dissipation process. These waves transfer energy across various scales, leading to the generation of high-frequency Kelvin waves that decay into phonons [49, 50].

Classical vs. Quantum turbulence

Classical turbulence's behavior is often described using the Reynolds number (Re), defined as [51]:

$$Re = \frac{\rho v L}{\eta} \tag{2.22}$$

where ρ is the fluid density, v is the velocity, L is the characteristic size, and η is the dynamic viscosity. For low Reynolds numbers ($Re \ll 1$), the flow is laminar and smooth, lacking vorticity. On the contrary, high Reynolds numbers ($Re \gg 1$) result in chaotic and turbulent flow.

In the case of superfluids, quantum vortices give rise to quantum turbulence. Each vortex maintains a fixed size, leading to a tangle of vortex lines that continually reconnect. Despite their differences, the larger-scale motion in superfluids resembles that of classical turbulence.

2.2 Carbon nanotubes

CNTs are renowned for their distinctive structural configuration and associated electronic properties, which closely relate them to graphene [52, 53]. These nanostructures, through their electronic band structure, mechanical resilience, and unique chirality-driven electrical characteristics, serve as a foundation for advanced quantum devices, particularly when configured as quantum dots [54]. In the upcoming sections, we will explore the transport phenomena in CNTs, their electronic and mechanical attributes, and the implications of quantum dot confinement within these nanotubes.

2.2.1 Charge carrier transport in carbon nanotubes

CNTs possess transport characteristics that are intricately shaped by their unique structural and electronic properties. This section provides an insight into the roles of quantum dots and transport spectroscopy in CNTs; see [55, 56, 57] for extensive review.

2.2.1.1 Electronic band structure

Carbon nanotubes, like graphene, possess a hexagonal lattice structure with a lattice constant of approximately 0.25 nm [58, 59]. This hexagonal arrangement can be viewed as a triangular network of two distinct atom types (A and B), defined by lattice vectors $\vec{a_1}$

and $\vec{a_2}$, as shown in Fig. 2.4 (a) [60]. Any point on the graphene lattice can be described using a combination of these vectors, starting from either atom A or B.

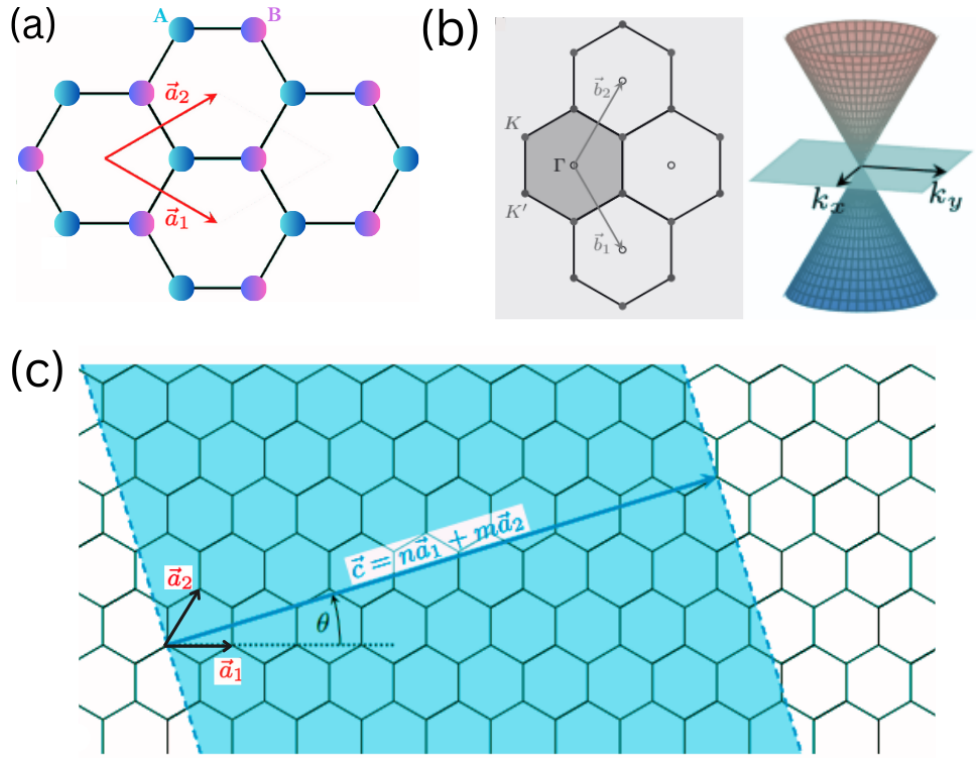

Figure 2.4: Transformation of graphene into CNTs: (a) Highlighting the hexagonal lattice structure with atoms A and B, defined by the lattice vectors $\vec{a_1}$ and $\vec{a_2}$ (reproduced from [60]). (b) The reciprocal lattice of graphene forms a triangular pattern, characterized by the reciprocal lattice vectors $\mathbf{b_1}$ and $\mathbf{b_2}$. Within this lattice, there are two distinct sets of high-symmetry points, denoted as K and K'. The shaded region illustrates the first Brillouin zone. The conduction and valence bands of graphene touch at the Fermi level (blue plane) at the first Brillouin zone (redrawn from [61]). (c) A strip of width $|\vec{c}|$ cut from a graphene sheet, where $\vec{c}$ is a linear combination of the graphene lattice vectors, can be rolled into a seamless cylinder, forming what is known as a single-wall carbon nanotube. n and m represent the chiral vectors that define the CNT's chirality (redrawn from [61]).

Graphene's electronic band structure is well-known [62] (detailed descriptions can be found in [54, 59]). In reciprocal space, the Fermi surface of graphene includes the "K points" located at the corners of the first Brillouin zone, where the energy dispersion is conical. This creates the famous "Dirac points," where the conduction and valence bands meet, resulting in its unique semimetallic behavior (Fig. 2.4 (b)). These points are critical for graphene's ability to conduct electrons with no energy gap, meaning electrons can move freely.

However, when graphene is rolled into a CNT (Fig. 2.4 (c)), its electronic properties change due to the cylindrical structure. This rolling introduces **quantization of momentum** along the nanotube's circumference, resulting in discrete subbands, unlike the continuous band structure of graphene. In simpler terms, wrapping the graphene sheet alters how electrons behave, creating discrete energy levels instead of a continuous range. The electronic nature of the CNT, whether it behaves like a metal or a semiconductor, is

determined by its **chirality**, defined by the chiral vector (n, m), which tells us how the graphene is rolled.

Chirality and electronic nature

The chirality of a CNT, determined by the integers n and m, dictates its electronic properties. If $n-m$ is a multiple of 3, the subbands cross at the Dirac points (Fig. 2.5 (a)), allowing for metallic behavior, where electrons can conduct without an energy gap. On the other hand, if $n-m$ is not a multiple of 3, a bandgap forms between the conduction and valence bands (Fig. 2.5 (b)), and the CNT exhibits semiconducting properties. In simple terms, whether the CNT conducts electricity or not depends on the way the graphene is rolled.

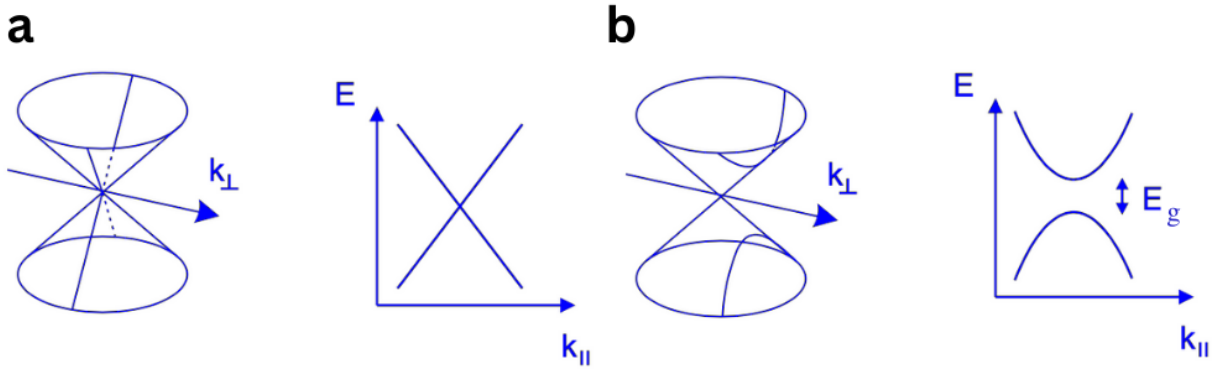

Figure 2.5: (a) Metallic CNT: Defined by a subband crossing either K or K' points, especially when $n-m$ is a multiple of 3. (b) Semiconducting CNT with a bandgap E_g: Characterized by the absence of subband intersections at K or K', typically when $n-m$ is not a multiple of 3.

Bandgap and curvature effects

The bandgap in semiconducting CNTs is inversely related to the tube's diameter, meaning smaller diameter CNTs exhibit larger bandgaps. Mathematically, this relationship can be expressed as $E_g \propto \frac{1}{D}$, where D is the diameter of the CNT. Simply put, as the nanotube becomes narrower, the energy gap widens, making it harder for electrons to jump between energy levels. Additionally, the curvature of the nanotube affects its electronic structure, particularly in smaller CNTs. The curvature induces a rehybridization of the carbon atoms from an sp^2 to a partial sp^3 configuration, which introduces strain and slightly alters the bandgap, depending on the tube's chirality and diameter.

Quantization of $\vec{k}$ and 1D subbands

When transitioning from graphene to a CNT, the component of the wavevector $\vec{k}$ along the tube's circumference (denoted as $\vec{k}_\perp$) becomes quantized, leading to the formation of one-dimensional (1D) subbands (Fig. 2.5). In metallic CNTs, these subbands meet at the K and K' points, resulting in no bandgap. In semiconducting CNTs, however, the subbands are separated by a bandgap. This 1D structure of CNTs, along with their ability to exhibit spin and valley degeneracies, can be further manipulated by external

factors like magnetic fields, enabling the tuning of their electronic properties for specific applications.

Therefore, CNTs can exhibit either metallic or semiconducting behavior depending on their chirality and structural properties, in contrast to the semimetallic nature of graphene.

Electrical properties

- CNTs can be metallic, semiconducting, or small-band gap semiconductors depending on their chirality.
- Semiconducting CNTs have a band gap ($E_g = 0.7\ \text{eV}/D$) that decreases with increasing diameter (D). The diameter of a single walled nanotube is around 1 nm to 3 nm.
- They act as 1D conductors due to their cylindrical structure, following the Landauer-Buttiker model.
- CNTs exhibit quantized conductance in ballistic transport, reaching the quantum limit $G = 4e^2/h$ for ideal transmission [63, 64]. This conductance, predicted by the Landauer-Büttiker formalism, accounts for two spin channels and two subbands (valleys) in CNTs. When the transmission coefficient $T = 1$, electrons travel without scattering, leaving only quantum contact resistance.
- Electrical properties can be modified using an electrostatic field, enabling field-effect transistor (FET) behavior for applications in circuits and sensors.

Mechanical properties

- CNTs possess exceptional mechanical strength due to the strong sp^2 hybridized C-C bonds.
- The elastic modulus (E) ranges from 0.5 TPa to 5 TPa, with tensile strengths (σ_s) between 10 GPa and 40 GPa.
- Experimental measurements, challenging due to CNT size, align with theoretical predictions.
- Mechanical strain can alter the band gap of semiconducting CNTs, offering the potential to induce a band gap in metallic tubes, depending on atomic configuration.

2.2.1.2 Quantum dot confinement in the carbon nanotube

In Figure 2.9, we present a field effect transistor (FET) device utilizing a carbon nanotube to measure the current I through a single nanotube. The device incorporates a CNT between metallic source and drain electrodes [65, 63]. Additionally, gate electrodes are used to modulate the electrostatic potential of the nanotube.

Electrons are confined in the region between the tunnel barriers created by the source, drain, and gate potentials, forming a quantum dot [66, 67]. By measuring the current through this quantum dot under different parameters such as bias voltage V_{sd}, gate voltage V_g, and magnetic field, we can deduce the electron energy levels within the CNT. This

quantum dot transport spectroscopy typically operates at temperatures $\leq$1 K to minimize thermal fluctuations that can obscure the transport properties.

The Constant Interaction Model

This model simplifies the analysis of electron interactions within CNT quantum dots, focusing on electrostatic interactions and stability of energy levels. As outlined by Hanson et al. [55], this model includes:

- **Electrostatic interactions:** These are determined by the total capacitance C_Σ, which is the sum of all capacitances between the quantum dot and its surroundings. Specifically, C_Σ includes contributions from the source C_s, drain C_d, and gate C_g capacitances, as well as any additional stray capacitances C_rest.
- **Energy level stability:** Despite electron-electron interactions, the available energy levels remain unaffected, preserving a constant single-particle energy spectrum.

The total energy of a quantum dot occupied by N electrons in the ground state is given by:

$$U(N) = \frac{(-eN + C_\mathrm{s}V_\mathrm{sd} + C_\mathrm{g}V_\mathrm{g})^2}{2C_\Sigma} + \sum_{n=1}^{N} E_n \tag{2.23}$$

$$= \frac{(Ne)^2}{2C_\Sigma} - Ne(\alpha_\mathrm{s}V_\mathrm{sd} + \alpha_\mathrm{g}V_\mathrm{g}) + \frac{C_\Sigma}{2}(\alpha_\mathrm{s}V_\mathrm{sd} + \alpha_\mathrm{g}V_\mathrm{g})^2 + \sum_{n=1}^{N} E_n \tag{2.24}$$

Here:

- The last term is the sum over all occupied single-particle energy levels E_n, which depend on the spatial confinement of the quantum dot.
- The first term $\frac{(Ne)^2}{2C_\Sigma}$ represents the charge occupation energy of the quantum dot, quantized with respect to the elementary charge.
- $C_\mathrm{s}V_\mathrm{sd}$ and $C_\mathrm{g}V_\mathrm{g}$ represent the effective induced charge, modifying the dot's electrostatic potential continuously.
- The lever arms α_s and α_g are introduced and given by:

$$\alpha_\mathrm{s} = \frac{C_\mathrm{s}}{C_\Sigma}, \quad \alpha_\mathrm{g} = \frac{C_\mathrm{g}}{C_\Sigma} \tag{2.25}$$

  illustrate how the quantum dot's energy levels respond to variations in the source-drain and gate voltages.

2.2.1.3 CNT resonator based single electron transistor

A carbon nanotube, when structured in a transistor geometry, can function as a single electron transistor (SET), especially when the charging energy of the electrons surpasses their thermal energy significantly. Figure 2.6 illustrates a CNT electromechanical sensor, where the nanotube is anchored between the source and drain electrodes. The central

segment of the nanotube remains suspended and initiates vibration when a direct current (dc) voltage is applied across the contact electrodes. Below the nanotube, five local finger gates are placed to adjust the tension in the resonator, aiming to modify the resonance frequencies.

Generally, a nanotube exhibits semiconductor properties as any defects or strain induce a bandgap in it, creating regions of conductivity and non-conductivity. Through a combination of Schottky barriers at the interface and varying gate voltages, the electrical potential of the nanotube can be fine-tuned.

To elucidate further, consider the chemical potentials of the source and drain leads plotted on the left and right respectively, and that of the nanotube in the center as shown in Fig 2.6. Within the leads, the density of states (DOS) is continuous up to the Fermi level as all states are filled. However, within the nanotube, DOS is discrete due to its quantum dot nature, leading to Coulomb blockades. This implies a charge energy penalty must be paid to add an electron to the nanotube. The chemical potential on the nanotube island ascends stepwise, depicted as a ladder in Fig 2.6, indicating that altering the gate voltage can shift this ladder vertically within the nanotube. This mechanism enables the switching between two configurations; in one, available states in the nanotube allow electron tunneling through the island, while in the other, the absence of available states between the source and drain potentials prevents electron addition to the island. As the gate voltage varies, the current through the nanotube oscillates regularly. Peaks occur when the nanotube level is within the permissible window, while dips signify no level within the permissible window. Hence, as depicted in Fig. 2.6, each peak represents an electron addition to the nanotube, illustrating the device's transistor nature since its conductance alters with gate voltage. Moreover, it qualifies as an SET as the entire current cycle toggles on and off corresponding to the addition of a single electron to the nanotube.

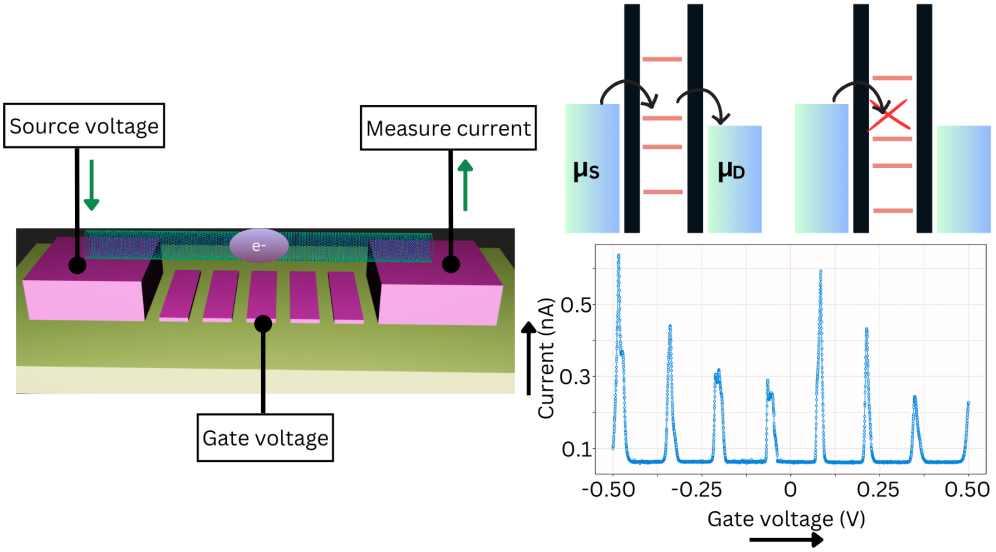

Figure 2.6: A carbon nanotube resonator in a single electron transistor geometry, depicted across three panels. The left panel shows the device model with the nanotube suspended between source and drain electrodes. The top right panel illustrates the band diagram model, demonstrating conditions under which electron tunneling onto the nanotube from the source and drain is allowed or blocked. The bottom right panel displays the current versus gate voltage curve of the nanotube, indicating peaks and dips corresponding to the alignments of the nanotube potential with the source or drain electrodes (data from the same ultra-clean CNT device as presented in Fig. 2.7). These visualizations capture the dynamics of charge transfer and the device's conductance modulation in response to gate voltage changes.

2.2.1.4 Coulomb blockade and transport spectroscopy

At low temperatures, CNT quantum dots exhibit Coulomb blockade, especially when the thermal energy $k_B T$ is much smaller than the quantum dot's charging energy, $E_C = \frac{e^2}{C_\Sigma}$ [68]. In this regime, electron transport only occurs when the quantum dot's energy levels align with the chemical potentials of the source and drain electrodes, μ_S and μ_D. The limited thermal energy prevents electrons from moving between the source, drain, and quantum dot unless this alignment occurs. With $V_{sd} = 0$ and $\mu_S = \mu_D$, the quantum dot remains in a current-blocked state, known as Coulomb blockade, unless its energy levels, $\mu(N)$, align with μ_S and μ_D [69]. Applying a gate voltage V_g shifts the energy levels of the quantum dot, lifting the blockade and allowing electron transport [70].

The chemical potential $\mu(N)$ of a quantum dot is defined as:

$$\mu(N) = U(N) - U(N-1) = \frac{e^2}{2C_\Sigma}(2N-1) - e(\alpha_s V_{sd} + \alpha_g V_g) + E_N \tag{2.26}$$

The chemical potential forms a ladder of discrete steps, with each step corresponding to a change in electron occupation number N. This ladder can be shifted up or down by adjusting the gate voltage. The spacing between adjacent energy levels represents the energy required to add an additional electron to the quantum dot.

The addition energy E_{add} is defined as the difference in chemical potential between

consecutive electron numbers:

$$E_{\text{add}}(N) = \mu(N+1) - \mu(N) = \frac{e^2}{C_\Sigma} + E_{N+1} - E_N = E_{\text{C}} + \Delta E_N \tag{2.27}$$

Here, E_{C} is the constant electrostatic charging energy, and ΔE_N represents the difference between single-particle energy levels due to quantum confinement.
Electron states in CNT quantum dots exhibit a fourfold degeneracy, arising from spin and valley degrees of freedom. This results in larger steps in the chemical potential for every four added electrons. The degeneracy, along with the spacing between single-particle energy levels (ΔE_{conf}), dictates the addition energy. The interplay between electrostatics and quantum confinement, influenced by the CNT's band structure and the quantum dot's environment, is key to understanding and optimizing CNT quantum dots [57].

Applying a bias voltage V_{sd} enables current flow if a quantum dot energy level lies within the bias window defined by $\mu_{\text{S}} - \mu_{\text{D}} = -eV_{\text{sd}}$. By keeping V_{sd} constant and adjusting V_{g}, one observes alternating current peaks and Coulomb blockade regions. As V_{sd} approaches zero, these peaks become sharper, while they blur as V_{sd} increases. Plotting current I or differential conductance $\frac{dI}{dV_{\text{sd}}}$ against gate and bias voltages results in a "stability diagram." This diagram displays diamond-shaped non-conductive regions (Coulomb blockade) surrounded by conductive areas. Analyzing this data provides insights into the quantum dot's fundamental parameters, such as capacitance and addition energy.

By examining Fig. 2.7, it is clear that the quantum dot transitions between conductive and non-conductive states when an energy level aligns with either μ_{D} or μ_{S} [71]. This alignment is governed by the equations:

$$\mu(N) = \frac{e^2}{2C_\Sigma}(2N-1) - e(\alpha_{\text{s}}V_{\text{sd}} + \alpha_{\text{g}}V_{\text{g}}) + E_{\text{N}} = \mu_{\text{D}} \tag{2.28}$$

$$\mu(N) = \frac{e^2}{2C_\Sigma}(2N-1) - e(\alpha_{\text{s}}V_{\text{sd}} + \alpha_{\text{g}}V_{\text{g}}) + E_{\text{N}} = \mu_{\text{S}} \tag{2.29}$$

Where $\mu(N)$ characterizes the energy level of the quantum dot for a specific occupation number (N), and α_{s} and α_{g} describe the variations in energy levels with respect to voltage. Using these equations, we can determine the slopes (λ_1 and λ_2) of the diamonds present in the stability diagram (refer to Fig. 2.7):

$$\frac{\mathrm{d}V_{\text{sd}}}{\mathrm{d}V_{\text{g}}} = -\frac{C_{\text{g}}}{C_{\text{s}}} = \lambda_1 < 0 \tag{2.30}$$

$$\frac{\mathrm{d}V_{\text{sd}}}{\mathrm{d}V_{\text{g}}} = \frac{C_{\text{g}}}{C_\Sigma - C_{\text{s}}} = \lambda_2 > 0 \tag{2.31}$$

The slopes λ_1 and λ_2 also allow us to calculate the lever arms α_{s} and α_{g}, which describe how the energy levels respond to voltage variations:

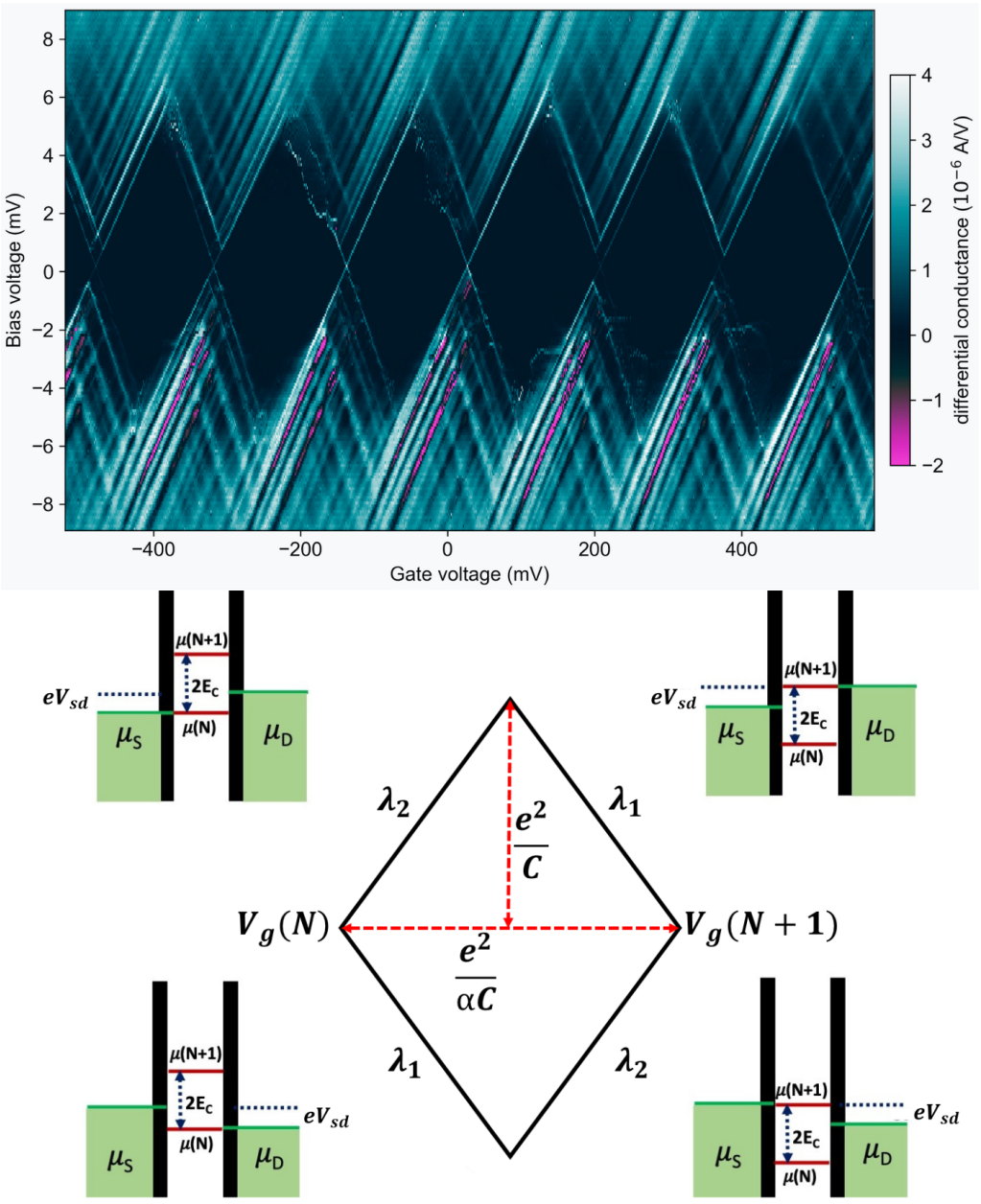

Figure 2.7: Top Panel: Coulomb diamonds measured in our ultra-clean nanotube resonator, allowing us to calculate the energy levels of electronic ground and excited states. Bottom Panel: Energy band diagram explaining the underlying mechanism behind a Coulomb diamond.

$$\alpha_g = \frac{|\lambda_1||\lambda_2|}{|\lambda_1| + |\lambda_2|} \tag{2.32}$$

$$\alpha_s = \frac{\alpha_g}{|\lambda_1|} \tag{2.33}$$

The gate voltage $V_{g,0}(N)$ required to align a quantum dot energy level with $\mu_{S,D}$ when the bias voltage $V_{sd} = 0$ is:

$$V_{g,0}(N) = \frac{e}{2C_g}(2N-1) + \frac{C_\Sigma}{eC_g}(E_N - \mu_D) \tag{2.34}$$

Therefore, when analyzing the stability diagram at $V_{sd} = 0$, the spacing between consecutive conductance peaks $\Delta V_g(N)$ can be calculated as:

$$\Delta V_g(N) = V_{g,0}(N+1) - V_{g,0}(N) \tag{2.35}$$

$$\Delta V_g(N) = \frac{e}{C_g} + \frac{C_\Sigma}{eC_g}(E_{N+1} - E_N) = \frac{E_{add}}{e\alpha_g} \tag{2.36}$$

With the fourfold degeneracy of energy levels in a CNT quantum dot, this leads to a characteristic fourfold symmetry in CNT quantum dot stability diagrams:

$$\Delta V_g(N) = \begin{cases} \frac{1}{e\alpha_g}(E_C + \Delta E_{conf}) & \text{for } N = 4n, n \in \mathbb{N} \\ \frac{1}{e\alpha_g} E_C & \text{otherwise} \end{cases} \tag{2.37}$$

In stability diagrams of CNT quantum dots, a fourfold symmetry pattern is often observed [72]. Coulomb diamonds corresponding to occupation numbers $N = 4n$ are notably larger compared to those corresponding to other N values. This symmetry helps determine the quantum dot's capacitance:

$$C_g = \frac{e}{\Delta V_g} \text{ for } N \neq 4n, n \in \mathbb{N} \tag{2.38}$$

Finally, using Equations 2.30 and 2.31, we can determine the remaining capacitance parameters of the quantum dot:

$$C_s = \frac{C_g}{|\lambda_1|} \tag{2.39}$$

$$C_\Sigma = \frac{C_g}{\alpha_g} \tag{2.40}$$

We have determined the addition energy E_{add}, lever-arm, and capacitances of the nanotube quantum dot shown in Fig. 2.7, and these are plotted in Fig. 2.8. These parameters offer detailed insights into the electrostatic properties and behavior of the quantum dot.

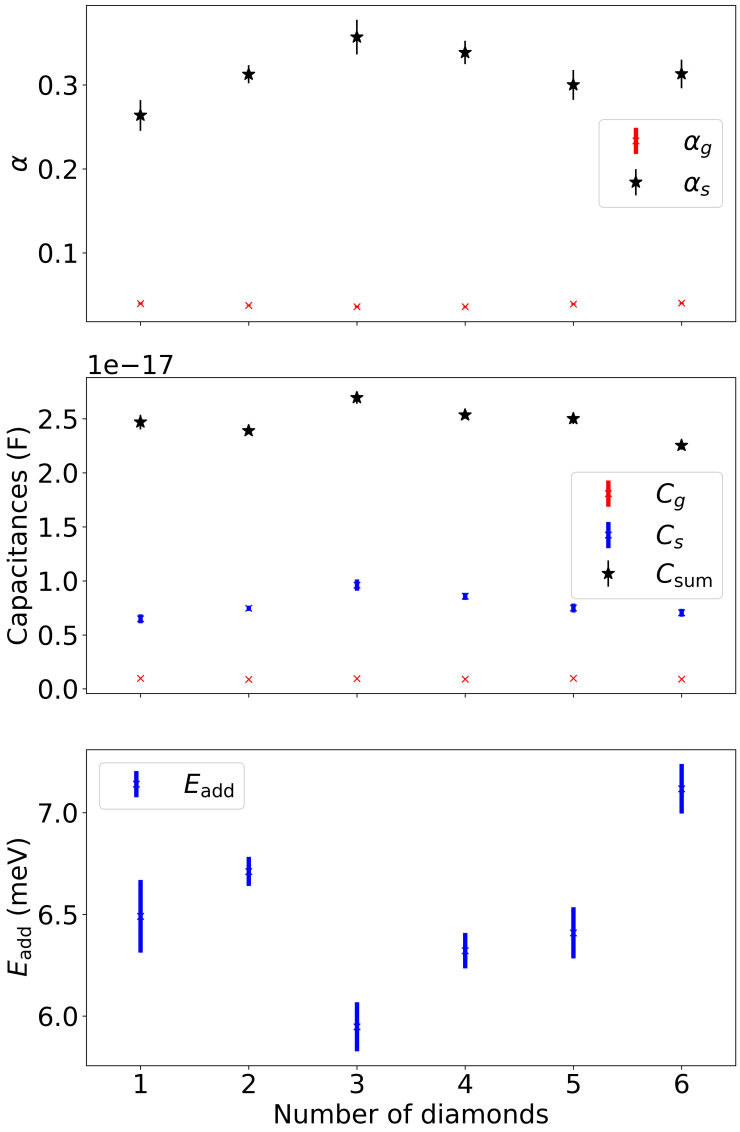

Figure 2.8: Geometrical parameters of a CNT quantum dot derived from the stability diagram shown in Fig. 2.7 using the Eq. 2.25 and Eq. 2.27.

2.2.2 Carbon nanotube mechanics

2.2.2.1 Bending and flexing: Euler-Bernoulli theory

The Euler-Bernoulli beam theory offers insights into material responses under external forces [73]. Even for nanotubes with few atoms in their outer layer, continuum mechanics principles effectively analyze the mechanical attributes of CNT resonators [74].
In Fig 2.9, a CNT of suspended length L along the x-axis is supported over a trench via source and drain electrodes, while five finger-gate electrodes are underneath the nanotube. The displacement $u(x,t)$ is in the z-direction. According to the Euler-Bernoulli theory, the system's motion is described by:

$$\rho A\frac{\partial^2 u}{\partial t^2}+\eta\frac{\partial u}{\partial t}+EI\frac{\partial^4 u}{\partial x^4}-T\frac{\partial^2 u}{\partial x^2}=F \tag{2.41}$$

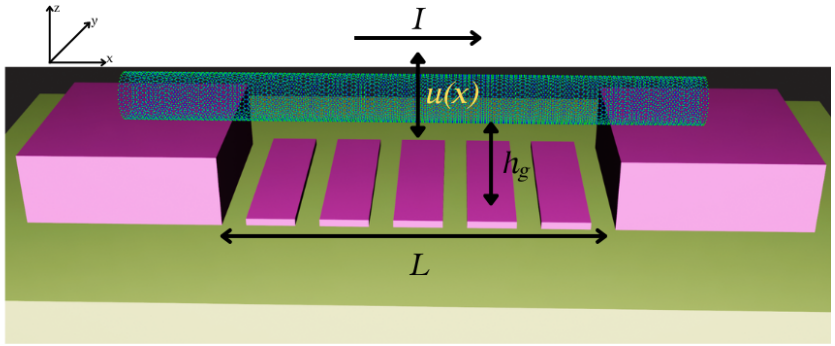

Figure 2.9: A CNT mechanical resonator displays a nanotube segment of length L suspended between source and drain electrodes over a trench. Below the trench, gate electrodes regulate tension and initiate motion, with the displacement direction denoted as $u(x)$.

Here:

- First term: inertia (ρA: mass density times cross-sectional area).
- Second term: damping.
- Third term: restoring force due to bending rigidity (with Young's modulus E and second moment of inertia I).
- Fourth term: restoring force due to tension T.
- F: external force per unit length.

We focus on two scenarios: bending rigidity or tension dominates the behavior. For comprehensive studies on CNT resonators refer to [75, 76].
When bending rigidity dominates ($EI\frac{\partial^4 u}{\partial x^4} \gg T\frac{\partial^2 u}{\partial x^2}$), the corresponding eigenfrequency is:

$$f_0, \text{beam} = \frac{22.37}{2\pi L^2}\sqrt{\frac{EI}{\rho A}} \tag{2.42}$$

Similarly, in tension dominance ($T\frac{\partial^2 u}{\partial x^2} \gg EI\frac{\partial^4 u}{\partial x^4}$), the system acts like a tensioned string. The eigenfrequencies are:

$$f_n, \text{string} = \frac{n}{2L}\sqrt{\frac{T}{\rho A}} \tag{2.43}$$

2.2.2.2 Mechanical resonator-quantum dot interaction

We investigated the interplay between a mechanical resonator and a quantum dot. For simplicity, we neglect the screening effects from source and drain electrodes, allowing us to model the nanotube as an infinite solid cylinder with radius r.

Potential profile of the CNT

This nanotube is positioned at height h_g above a conductive plate with an electrostatic potential V_g at $z = 0$ [77]. The potential profile at $u = 0$ is the following:

$$\phi(y,z) = V_g - \operatorname{arccosh}\left(\frac{h_g}{r}\right) \ln\left[y^2 + \left(z - h_g^2 - r^2\right)^2\right] / \left(2L\rho A \cdot h_g\right) \tag{2.44}$$

This equation describes the electrostatic potential around the CNT due to the gate electrode. The logarithmic term represents the potential due to the cylindrical geometry of the CNT. The arccosh function arises from the geometry of the nanotube and its proximity to the gate. Figure 2.10 depicts the field lines of this potential.

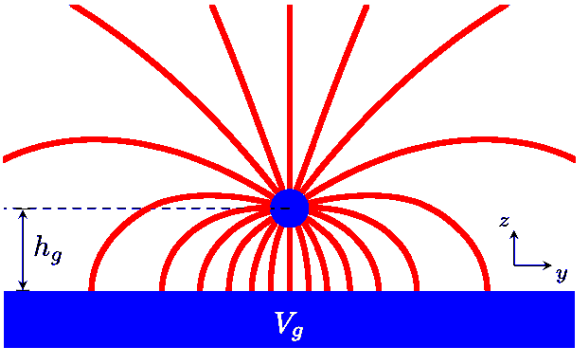

Figure 2.10: Electrostatic potential field lines from the gate electrode in a suspended CNT FET. Adapted from [73]

Capacitance of the CNT

When the nanotube deflects, its height above the conductive plate is $h_g - u$. The capacitance per unit length, $c_g(x)$, is given by [73]:

$$c_g(x) = \frac{2\pi\epsilon_0}{\operatorname{arccosh}\left(\frac{h_g - u(x)}{r}\right)} \tag{2.45}$$

This equation describes how the capacitance between the nanotube and the gate electrode changes with the nanotube's position. As the nanotube gets closer to the electrode, its capacitance increases. The inverse relationship with the arccosh function ensures that the capacitance is always positive and increases as the tube gets closer to the gate.

Electrostatic potential energy

The electrostatic potential energy for a segment of the nanotube, U_F, is given by:

$$U_F = -\int_0^L \frac{c_g(x) V_g^2}{2}\, dx \tag{2.46}$$

The negative sign indicates that the electrostatic force is attractive, pulling the nanotube closer to the gate electrode.

This energy can also be expressed as:

$$U_F = \int_0^L F_u\, dx \tag{2.47}$$

Force on the CNT due to electrostatic interaction

The force $F_{\mathrm{ES}}(t)$ exerted on the nanotube by the gate electrode's electric field is given by:

$$F_{\mathrm{ES}}(t) = \frac{1}{2}\frac{\partial C_{\mathrm{g}}}{\partial u} \cdot V_{\mathrm{g}}^2 \tag{2.48}$$

The force, influenced by gate capacitance C_{g}, draws the CNT resonator towards the gate electrode. This action adjusting the tension and resonance frequency of the nanotube, much like tuning a guitar string.

2.2.3 Tension in nanotube resonator

The tension in the nanotube can be modulated by applying a gate voltage V_{g}. The electrostatic force between the gate and the nanotube results in a bending of the CNT, which, in turn, increases the tension within the device.

The total tension T in the CNT can be expressed as the sum of the initial residual tension T_0 and the additional tension induced by the gate voltage. The total tension can be modeled as:

$$T = T_0 + \frac{ES}{2L}\int_0^L \left(\frac{\mathrm{d}u}{\mathrm{d}z}\right)^2 \mathrm{d}z \tag{2.49}$$

where E is the Young's modulus of the CNT, $S = \pi r^2$ is the cross-sectional area of the CNT, L is the length of the CNT, and $u(z)$ represents the displacement of the CNT due to the electrostatic force. The electrostatic force per unit length F_{ES}, which scales with V_{g}^2, leads to a displacement of the CNT and alters the tension. We can divide the tension behavior into two regimes based on the gate voltage.

2.2.3.1 Weak bending regime

For low gate voltages, the bending of the CNT is weak, and the increase in tension is small. In this regime, the increase in tension is dominated by the initial residual stress, and the tension increases quadratically with the gate voltage:

$$T \approx T_0 + \frac{\epsilon_0 V_{\mathrm{g}}^2}{d^2} \tag{2.50}$$

where ϵ_0 is the permittivity of free space, and d is the distance between the CNT and the gate. The tension in this regime is proportional to the square of the applied gate voltage.

2.2.3.2 Strong bending regime

In the case of higher gate voltages, the bending becomes significant, and the system enters the strong bending regime. Here, the tension scales with $V_{\mathrm{g}}^{2/3}$, as derived from Sapmaz et al. [78]:

$$T \approx \left(\frac{ESV_{\mathrm{g}}^2}{L^2}\right)^{1/3} \tag{2.51}$$

This relationship highlights that in the strong bending regime, the tension increases more slowly with the gate voltage compared to the weak bending regime. In Appendix Sec. A.4, we calculate the tension for the four different modes of the nanotube, using the experimentally observed frequencies in vacuum for both the weak bending and strong bending regimes.

2.2.3.3 Displacement sensitivity

The displacement sensitivity of the device can be directly related to the tension. As the gate voltage increases, the tension in the CNT rises, which leads to a corresponding increase in the resonance frequency of the device. The resonance frequency f_0 is given by:

$$f_0 \propto \sqrt{\frac{T}{m}} \tag{2.52}$$

where m is the effective mass of the resonator. Thus, operating the device in the high-tension regime, where the tension scales with $V_g^{2/3}$, allows for precise control of the resonance frequency, which in turn improves displacement sensitivity.

This analysis provides a useful model for understanding the mechanical response of carbon nanotube-based NEMS devices to applied gate voltages, contributing to improved performance in sensing and quantum dot applications.

2.2.3.4 Measuring the nanotube vibrations via embedded SET

In the section 2.2.1.3, it was mentioned that the electron flow through the nanotube is governed by single-electron charging, leading to a pronounced slope in the current peak. This implies that minor alterations in the potential can trigger significant changes in the current. The characteristic behavior of the nanotube SET is harnessed to transduce its mechanical movements into electrical signals.

The detection mechanism can be elucidated by redrawing the data similar to the current versus gate voltage graph (Fig 2.6), but instead plotting current versus displacement (Fig.2.11). This comparison is reasonable because the potential varies in a way that is directly related to the displacement. Consequently, the movement of the nanotube induces variations in the potential, navigating the current along the slope of the Coulomb peak (Fig.2.11). If the nanotube is oscillating, this would manifest as fluctuations in the current, since the instantaneous nanotube current corresponds to the immediate displacement. Given that the current is tied to the electrical potential, this relationship can be used to discern the displacement direction. Specifically, an upward displacement would result in a notable current, whereas a downward displacement would induce a modest change in current.

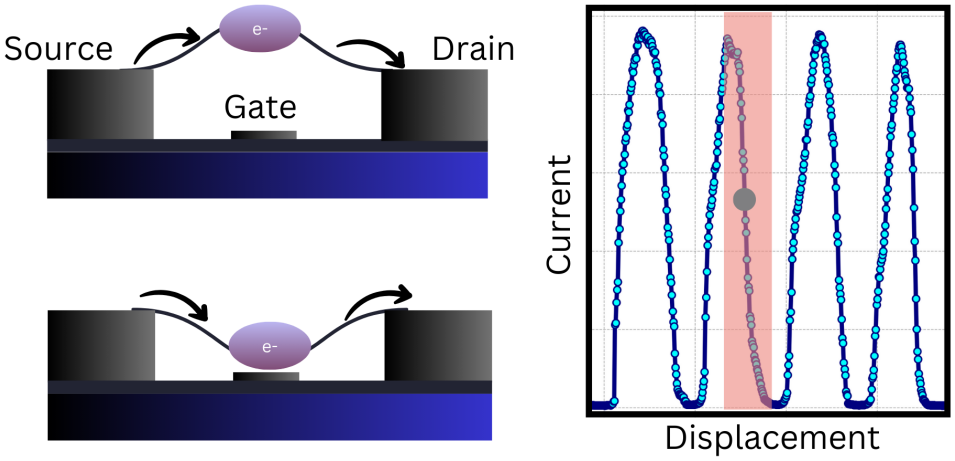

Figure 2.11: Utilizing the embedded SET to gauge carbon nanotube oscillations. The right panel depicts the relationship between current and nanotube displacement, analogous to the current versus gate voltage presented in Fig 2.6. This is just for illustration and not actual data, as we do not experimentally measure the nanotube displacement. The movement of the nanotube modulates the electrical potential, shifting the current along the slope of the Coulomb peak, thereby transducing mechanical movements into measurable electrical signals. Changes in current reflect the nanotube's displacement, enabling precise monitoring of its oscillatory behavior.

In summary, CNTs possess a spectrum of attributes favorable to a range of applications. In electron transport, they enable precise control through Coulomb blockade, essential for quantum computing. At low temperatures, Coulomb diamonds form as energy levels within quantum dots align with source and drain potentials, allowing for controlled electron flow. In mechanics, CNT resonators follow Euler-Bernoulli beam theory or string theory, providing high-quality factor sensing and tunable resonance frequencies. Furthermore, CNT resonators, when coupled with quantum dots, offer intriguing possibilities for tuning and sensing through electrostatic interactions. Since CNTs can function as SETs, sensitive to gate voltage changes, making them powerful detectors of mechanical motion.

We will now discuss the mechanics of various mechanical oscillators to explore their applications in investigating various superfluid phenomena.

2.3 Oscillating structures as probes for helium fluids

2.3.1 Abstract

Understanding the behavior of superfluid helium is crucial in low-temperature research, particularly for its potential in cooling electronic devices to millikelvin temperatures. However, knowledge of possible losses in such a 'mechanical vacuum' is essential to distinguish their contribution from actual measurements. Conventionally, mechanical oscillators have been employed to identify damping sources in cryogenic liquids. This review examines previous research on nano-electromechanical systems (NEMS) and micro-electromechanical systems (MEMS) in helium, where several damping mechanisms are detected, including viscous drag, ballistic scattering in quasiparticles, emission of sound, and generation and detection of turbulent flow. Moreover, recent work involving carbon nanotube resonators has demonstrated impressive sensitivity to helium interactions, particularly in detecting helium adsorption and layering transitions in a quasi-2D system. These findings not only provide insights into confined helium geometries but also offer a framework for exploring bulk superfluid helium, a key focus of this review.

2.3.2 Introduction

The use of liquid helium as a cooling agent has been crucial in low-temperature research for several decades, allowing the investigation of a wide range of quantum phenomena and exotic states of matter. However, this cooling agent can also introduce potential sources of damping that can interfere with measurements and impede progress. To better understand the behavior of liquid helium at ultra-low temperatures, researchers have traditionally used mechanical oscillators to probe damping sources present in cryogenic liquids. Previous work has been done on MEMS and NEMS devices inside the helium chamber, where several theoretically-predicted damping mechanisms have been detected, including viscous drag, ballistic scattering in quasiparticles, emission of sound, and even the generation and detection of turbulent flow. The detection and characterization of these damping sources are essential for accurate measurements and for improving the performance of devices operating at ultra-low temperatures.

The superfluid behavior of ^{3}He and ^{4}He is an example of collective quantum behavior that arises due to the bosonic nature of ^{4}He and the fermionic nature of ^{3}He [79]. Especially as systems approach absolute zero, the manifestation of intriguing quantum phenomena becomes more pronounced, leading researchers into hitherto unexplored realms of the physical world. While superfluid ^{4}He flows without viscosity, its normal fluid component retains a finite viscosity, which plays a key role in turbulence formation even at very low temperatures. The Reynolds number in superfluid ^{4}He can remain high, typically ranging from 10^4 to 10^8, due to the contribution of the normal fluid, the flow velocity, and the system's characteristic length [80, 47]. As a result, interactions involving the normal fluid at high velocities lead to turbulence, despite the inviscid nature of the superfluid component. In contrast, the fermionic quantum fluid, ^{3}He, offers insights into several other complex systems. This includes unconventional superconductors, neutron stars, and potentially even scenarios reminiscent of the early universe [8]. Such insights have far-reaching applications in the realms of high-T_c superconductivity, topological defect dynamics, and cosmology.

Investigations into these superfluids are significantly enriched by employing mechani-

cal resonators whose vibrations are highly sensitive to helium interaction. The resonance frequencies of these oscillators can be influenced by adsorbed masses, charges, and impurities, making them ideal for studying helium fluid's properties [81, 82]. Over the years, numerous phenomena related to helium fluids, such as quantum turbulence [83, 12], Landau critical velocity in ^{3}He [84], and even the quantization of topological defects [44, 85] have been explored using mechanical oscillators.

In light of this, the current literature review discusses the experiments that have employed MEMS and NEMS submerged in liquid helium at ultra-low temperatures. The purpose is to provide a comprehensive understanding of various phenomena observed in this 'quantum vacuum' and the mechanisms, such as viscous drag, ballistic scattering, and sound emission, detected through these oscillating structures.

Comparing damping mechanisms in ^{4}He with nanobeams and other oscillators

Bradley et al.[13] investigated the thermal properties of superfluid ^{4}He using a NEMS resonator. Nanomechanical oscillators, with dimensions comparable to the superfluid coherence length, exhibit exceptionally high sensitivity to changes in resonance frequency. This sensitivity allows for precise probing of quantum phenomena, making it possible to access and explore different quantum regimes at mesoscopic scales [86, 73].
The power dependence of the resonance frequency was initially measured to determine the maximum velocity up to which the nanobeam demonstrates a linear force-velocity relationship. Using the quality factor definition:

$$Q = \frac{f_0}{\Delta f} = \frac{\pi f_0 m_{\text{beam}} v^2}{P_{\text{max}}},$$

velocity and force can be expressed as:

$$v = \sqrt{\frac{P_{\text{max}}}{\pi m_{\text{beam}} \Delta f}}; F = \sqrt{\pi m_{\text{beam}} \Delta f P_{\text{max}}}. \tag{2.53}$$

where, f_0 is the frequency in vacuum and m_{beam} is the mass of the beam resonator. It was found that the nanobeam exhibits a 0.1 m/s maximum linear velocity. Consequently, any non-linear characteristics observed for the beam submerged in helium at velocities below 0.1 m/s are attributed to the beam's interaction with the helium fluid.
Upon immersing Al-beams in ^{4}He fluid near the transition temperature, a notable change in resonance frequency as a function of temperature was observed. Specifically, a significant damping width, approximately 10^5Hz, much greater than intrinsic losses, was noted for the temperature range of 1.3-4.2 K as shown in Fig.2.12(c). Moreover, a reduction of approximately 10% in the resonance frequency from its vacuum value suggests an increased effective mass of the beam, likely due to viscously clamped fluid on the beam surface and fluid back-flow around the oscillator.
The two-fluid model was employed to explain the observed results, treating the 'beam + liquid' as a damped harmonic oscillator with a changeable effective mass and a consistent effective spring constant [87]. The resonant frequency f_{H} of the beam in the viscous fluid is reduced from its vacuum value f_0, and this change is given by:

$$\left(\frac{f_0}{f_\mathrm{H}}\right)^2 = 1 + \beta\frac{\rho_\mathrm{H} V}{m_\mathrm{e}} + B\frac{S}{m_\mathrm{e}}\sqrt{\frac{\eta\rho_\mathrm{n}}{\pi f_0}}. \tag{2.54}$$

In this expression, ρ_n and η represent the normal fluid density and viscosity, respectively, while ρ_H denotes the liquid helium density [87]. S and V are the area and volume of the oscillating body, respectively. The term m_e denotes the effective mass of the system, accounting for both the beam and the surrounding fluid.

For high-frequency scenarios where the penetration depth of the rotational fluid δ is smaller than the dimensions of the beam, the resonance width due to hydrodynamic drag is:

$$\Delta f^\mathrm{hyd} = C\frac{S}{2m_0}\sqrt{\frac{\rho_\mathrm{n}\eta f_0}{\pi}}\left(\frac{f_\mathrm{H}}{f_0}\right)^2. \tag{2.55}$$

The experimental data, as displayed in Fig.2.12, aligns well with the theoretical predictions for the majority of the temperature spectrum. However, for temperatures below 1.7 K, deviations from the theoretical model are evident, the cause of which remains unidentified.

Comparing Al-beams with other resonators like vibrating wires and quartz tuning forks, the relationship in Eq. (2.54) can be reformulated as:

$$\left(\frac{f_0}{f_\mathrm{H}}\right)^2 - 1 = \frac{1}{\rho_\mathrm{beam}}\left(\beta\rho_\mathrm{H} + \frac{4B}{d}\sqrt{\frac{\eta\rho_\mathrm{n}}{\pi f_0}}\right). \tag{2.56}$$

From this, oscillators with a lower density and smaller dimensions display enhanced frequency sensitivity, marking them as preferable for probing the properties of liquid helium. For various oscillators, the fractional change in frequency is illustrated in Fig. 2.14(a).

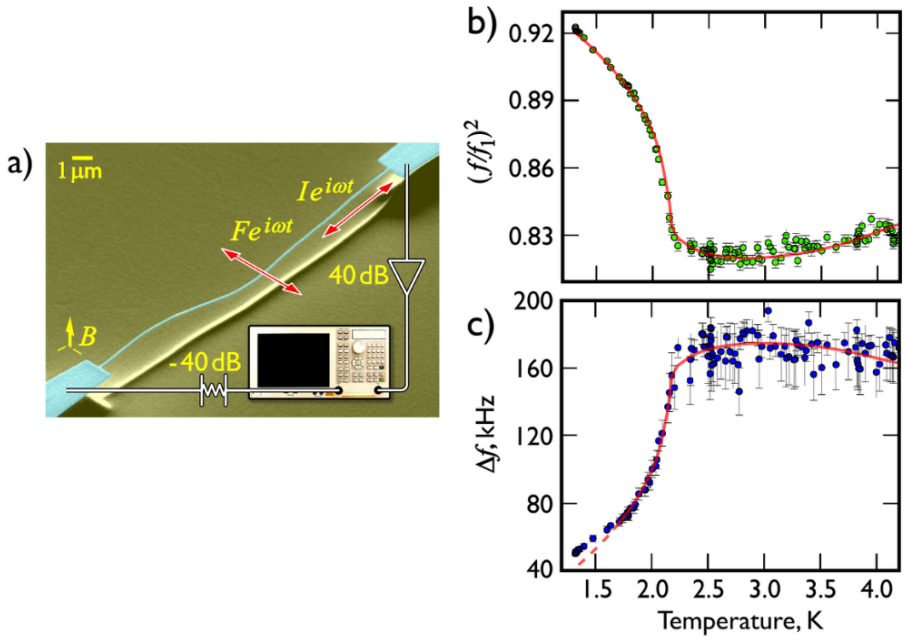

Figure 2.12: (a) SEM image presenting a 15 µm-long, doubly clamped aluminium beam on a silicon substrate, having a cross-sectional area of 0.1 µm × 0.1 µm. This beam is integrated with a microwave circuit under a transverse magnetic field. (b) A depiction of the squared frequency ratio for a nanobeam against liquid helium temperatures. Note the swift change in resonance frequency below the transition point, attributed to the release of normal fluid from the resonator's surface. (c) Illustration of the resonance width's temperature dependence, highlighting a nanobeam's sensitivity in gauging viscous fluid dynamics between 1.7 K and 4.2 K. Adapted from [13].

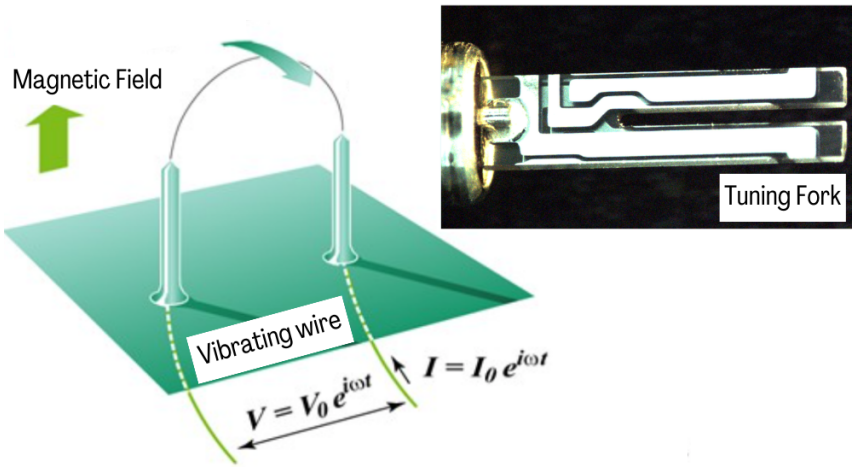

Figure 2.13: Tuning Fork and Vibrating wire resonators.

The Q-factor, deduced from Eq. (2.55), represents another crucial characteristic for determining the optimal device:

$$Q = 2C\sqrt{\frac{\pi}{\rho_{\mathrm{n}}\eta}}\left(\frac{f_0}{f_{\mathrm{H}}}\right)^2\sqrt{f_{\mathrm{H}}}d\rho_{\mathrm{beam}}. \tag{2.57}$$

The relationship between frequency sensitivity and quality factor reveals a trade-off, as illustrated in Fig. 2.14(b).

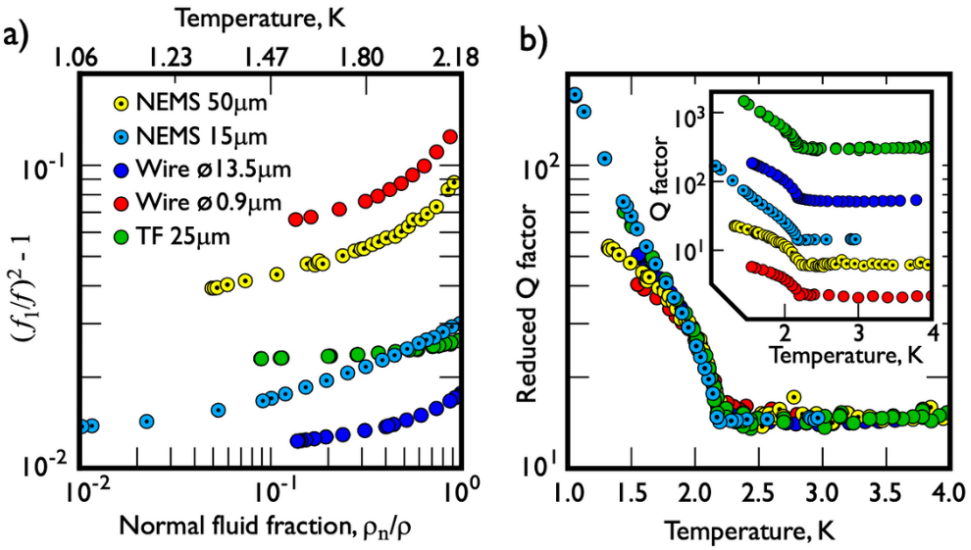

Figure 2.14: (a) Depiction of how the resonant frequency's fractional change depends on the normal helium fraction for various oscillators between 1.06 K and 2.18 K. This highlights the superior sensitivity of smaller, lighter probes in assessing helium fluid's viscous properties. (b) Charting the reduced Q-factor against temperature. Notably, massive resonators with high frequencies have the highest Q-factor (as seen in the **Inset**). For 15μm NEMS, a significant rise in the reduced Q-factor below the superfluid transition suggests potential minimal acoustic losses at these temperatures. Adapted from [13].

In light of the above, NEMS resonators exhibit potential for operations in liquid ^{3}He, an optimal environment for cooling electrons to their ground states [88], thus paving the way for probing uncharted quantum domains.

Transition of damping mechanisms in ^{4}He from ballistic to acoustic regimes with NEMS

Guénault et al.[14] delved into dissipation mechanisms within superfluid ^{4}He by utilizing nanomechanical beams in a helium bath at a base temperature of 7 mK. When these Al-beams were measured in a vacuum, both in their normal and superconducting states, they demonstrated a notably high quality factor ($Q = 5 \times 10^6$), indicating minimal intrinsic losses.

A subsequent evaluation involved measuring damping across varied external magnetic fields B up to 5 Tesla, as depicted in Fig. 2.15(a). Damping remained consistent up to 150 mT, after which magnetomotive forces began to dominate in a B^2 relation. When these nanobeams were then introduced to a ^{4}He chamber, spanning temperatures from 7 mK to 3 K, unexpected damping was observed, even at minimal magnetomotive losses. Given that the normal fraction of superfluid ^{4}He should be inconsequential at 7 mK, this

elevated loss cannot be attributed to the viscous forces from the normal component, given the sparse density of thermal excitations[89].

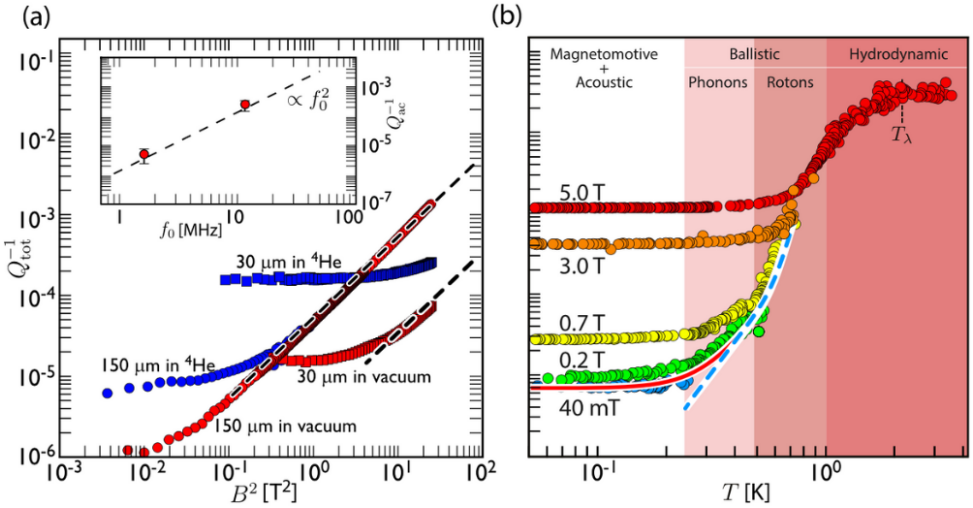

Figure 2.15: (a) Damping in a nanobeam measured against external magnetic field in both vacuum and superfluid ^{4}He at 10 mK. Inset: Variation of acoustic damping with resonator frequency in ^{4}He. (b) Temperature's effect on loss mechanisms, highlighting distinct sources of damping across three temperature zones. Adapted from [14].

To understand the microscopic origins of this damping within superfluid ^{4}He, the nanobeam's quality factor was plotted against temperature, as seen in Fig. 2.15(b). Throughout the temperature regime, dissipation was evident. However, three specific temperature zones revealed additional, distinct loss mechanisms, beyond just intrinsic and magnetomotive dissipation. Above 1 K, hydrodynamic losses become dominant as per Eq. (2.57). Below 1 K, the influence of damping, due to collisions with thermal excitations like phonons and rotons, becomes pronounced[89]. At the lowest temperature bracket, significant, temperature-independent losses were observed, which surpassed internal losses. These can be ascribed to the dipole acoustic emission from the cylindrical beam[90]. The experimentally documented damping regimes align closely with the subsequent theoretical models for phonons, rotons[89], and acoustic emissions[91], respectively:

$$Q_{\rm ph}^{-1} = \mathcal{A}\frac{k_{\rm B}^4}{45\hbar^3 df_0(\rho_{\rm beam}+\rho_s)c_{\rm ph}^4}T^4, \tag{2.58}$$

$$Q_{\rm rot}^{-1} = \frac{\mathcal{A}p_0}{\pi^2 df_0\rho_{\rm beam}}\left(\frac{m^* k_{\rm B}T}{2\pi\hbar^2}\right)^{3/2}\exp\left(-\frac{\Delta}{k_{\rm B}T}\right), \tag{2.59}$$

$$Q_{\rm ac}^{-1} = \frac{\pi^3}{2}\frac{\rho_s}{\rho_{\rm beam}}\left(\frac{df_0}{c_{\rm ph}}\right)^2, \tag{2.60}$$

Here, $c_{\rm ph}$ represents sound velocity, while p_0, m^*, and Δ are the associated Landau parameters for roton[89].
Given that acoustic losses rely quadratically on the resonant frequency [as per Eq. (2.60)], it's inferred that resonators with lower frequencies can significantly curtail sound's dipole emission. Additionally, resonators with a reduced diameter, such as carbon nanotube mechanical resonators, might effectively minimize acoustic emissions. Recent studies,

such as those conducted on low-frequency, high-sensitivity π-shaped NEMS, reported in [16], highlight their suitability for detecting low-frequency excitations in superfluids, including Kelvin waves in both ^{4}He and ^{3}He.

Dissipation Dynamics in ^{4}He Using Tuning Forks

Bradley et al.[10] studied quartz tuning forks' behavior in both normal and superfluid ^{4}He, specifically for temperatures above 1.5 K. They ensured that the oscillation amplitude remained minimal to uphold linear force-velocity dynamics.
The resonance width of the tuning forks, when submerged in liquid helium, was recorded as a function of their resonant frequency. This was done under both normal (4.2 K) and superfluid (1.5 K) conditions. The resultant measurements are depicted in Fig. 2.16, having accounted for intrinsic losses. At sub-100 kHz frequencies, damping showcased a mild dependency on the resonance frequency. However, as the frequency increased, the resonance width experienced substantial changes, escalating by nearly two orders of magnitude in the normal phase and three in the superfluid phase. Initial low-frequency losses align with the hydrodynamic drag exerted by the viscous fluid. In contrast, at elevated frequencies, the dissipation is best explained by the 3D model of quadrupole sound emission[32]. Both theoretical models aptly fit the experimental observations.

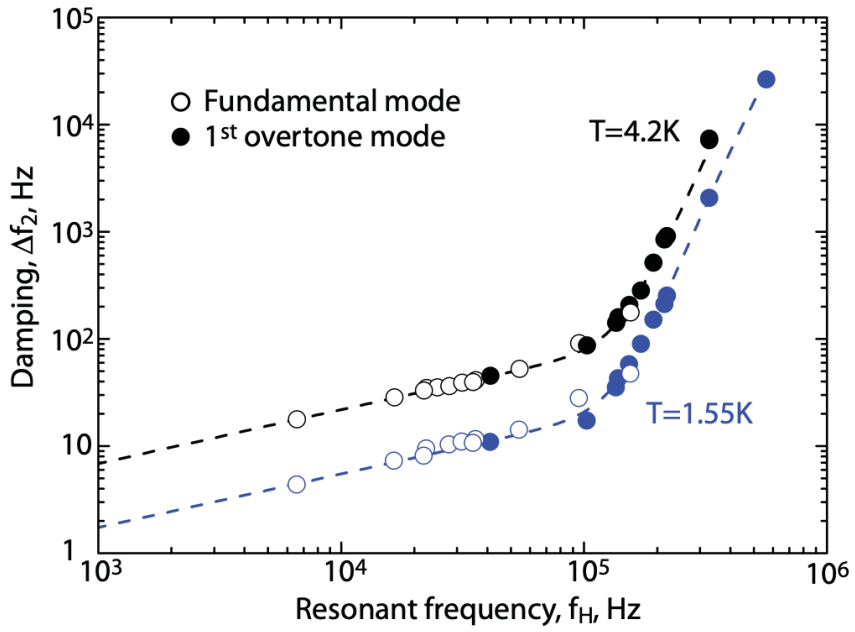

Figure 2.16: Damping width variation of the tuning fork with respect to its resonant frequency. Measurements taken in normal ^{4}He at 4.2 K (black points) and in superfluid ^{4}He at 1.55 K (blue points). The dashed lines represent the cumulative effects of hydrodynamic and the 3-D longitudinal quadrupole acoustic emission models. Adapted from [10].

Dissipation dynamics in ^{3}He using tuning forks

Guenault et al.[11] investigated the behavior of tuning forks in both the normal and superfluid phases of ^{3}He, initially comparing their responses in ^{4}He. As depicted in Figure 2.17(a), damping characteristics in ^{4}He correlate with frequency: lower frequencies

fit the hydrodynamic model, while at higher frequencies, 3D quadrupole acoustic emission dominates the dissipation. This pattern is consistent in both the normal and superfluid states at respective temperatures of 4.2 K and 1.5 K. At 450 mK, where the normal-fluid fraction is negligible, dissipation is predominantly due to quasiparticle scattering in the ballistic regime, as described in Eq. (2.58). The observed ballistic drag coefficient of 18 suggests a geometric influence from the tuning forks and the ambient pressure.

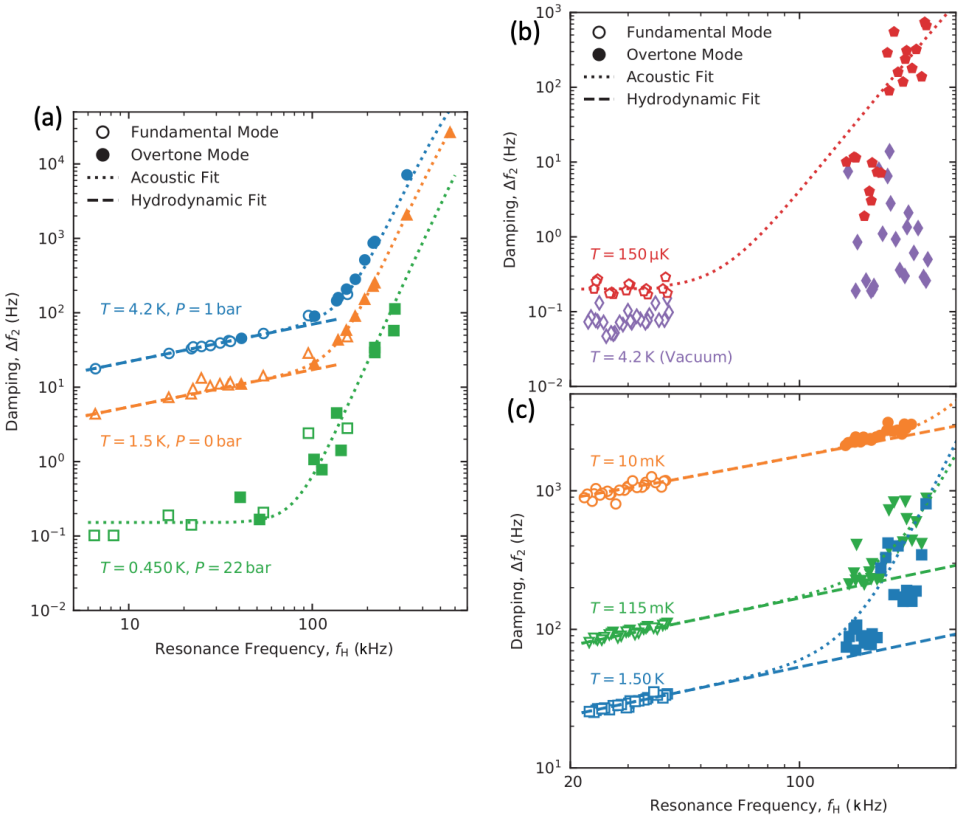

Figure 2.17: Resonance frequency width and damping of tuning forks in ^{4}He and ^{3}He: (a) Normal ^{4}He at 4.2 K and superfluid ^{4}He at 1.5 K and 450 mK with hydrodynamic (dashed lines) and combined 3D sound emission models (dotted lines); (b) Damping in superfluid ^{3}He-B and vacuum; (c) Enhanced damping in normal ^{3}He highlighting the viscous fermionic behavior. Adapted from [11].

Moving to liquid ^{3}He, resonance measurements mirrored those in ^{4}He (Figure 2.17(b)). At frequencies below 100 kHz, damping levels in vacuum and superfluid ^{3}He-B are comparable; beyond this threshold, damping in superfluid ^{3}He-B markedly increases, likely due to additional damping mechanisms inherent to this state. Contrastingly, damping in normal ^{3}He significantly surpasses that in both the superfluid and vacuum conditions (Figure 2.17(c)). Low-frequency damping aligns with Stokes' drag, intensifying as temperature decreases due to the viscous nature of the Fermi fluid. Although most data fit a model combining hydrodynamic and ballistic theories, deviations suggest an impact from the cavity acoustics, prompting further investigation.

This research underscores the need for precise experimental design, particularly in the cavity dimensions for high-frequency NEMS and MEMS, to accurately probe the quantum fluid dynamics such as thermal excitation motion or quantum turbulence.

Turbulent flow dynamics in superfluid ^{4}He using MEMS resonators

Barquist et al.[79] utilized a MEMS resonator to discern quantum turbulence in superfluid ^{4}He. Capacitive driving powers the device, and an electrical current is gauged through it by applying a DC bias on its electrodes. The MEMS is tailored in shear mode to maintain consistent velocity during measurements, facilitating the extraction of its intrinsic properties before the turbulence is generated and detected.
A tuning fork (TF) is employed to induce turbulence in the ultra-low temperature (14 mK) superfluid. This turbulent regime is demarcated by measuring the TF's force-velocity characteristics. On-resonance operation ensures that the damping force and driving force equilibrate. Initial low velocities show a linear drag dependency, i.e., $F \propto v$, signaling a laminar regime. However, velocities surpassing 140 mm witness a sudden drop, suggesting increased dissipation attributed to turbulent flow where force exhibits a non-linear velocity dependency. The critical velocity, v_c, marking the transition to turbulence, is 90 mm s^{-1}.

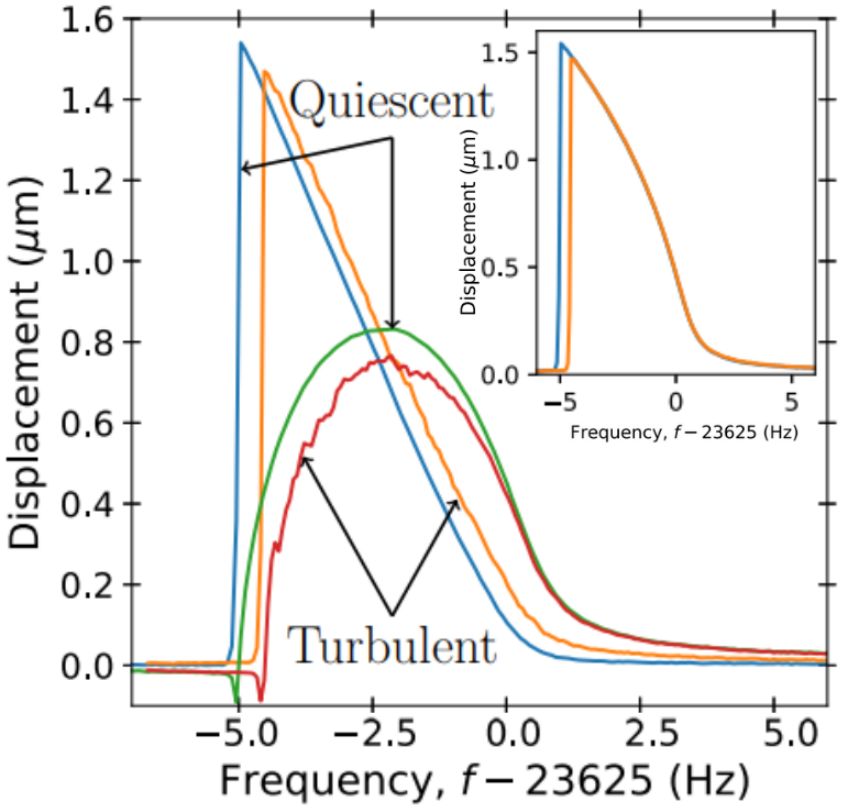

Figure 2.18: Frequency-response of MEMS with (Turbulent) and without (Quiescent) turbulence at 14 mK. The dual reverse frequency sweeps in both regimes showcase the quadrature components of the signal. The inset illustrates the signal amplitude. Turbulent flow's smaller peak underscores increased damping and the extra noise stemming from damping fluctuations. Adapted from [79].

Both frequency and time domains are utilized to observe MEMS behavior in turbulent flow. Figure 2.18 illustrates dual descending frequency sweeps with an excitation voltage of 400 mV. The 'turbulent' curve corresponds to a fork velocity of 126 mm s^{-1}. The MEMS's motion under turbulent conditions is evident from the sweep's transition to

higher frequencies and diminished amplitude compared to the 'Quiescent' sweep. The diminished peak magnitude in the turbulent setting, given identical excitation, indicates MEMS's augmented damping.

Although the sensitivity of MEMS to turbulent flow is validated across measurements, further empirical work is essential for a holistic quantitative analysis of vortex interactions with MEMS resonators.

Turbulence detection in superfluid ^{3}He-B using vibrating wires

Fisher et al.[12] were the first to observe turbulence in superfluid ^{3}He-B, deploying vibrating wires for both the generation and detection of turbulent flow. This turbulence was activated at the Landau criterion for Cooper pair breaking [84]. The real-time detection of this turbulence was elucidated by the creation of a flow barrier through entangled vortices at ultra-low temperatures. Here, the modulation in the quasi-particle dynamics due to this barrier was significant enough to map out the effects of turbulence in the fermi superfluid.

To initiate the resonator's motion, an oscillating current flowed through a wire placed in a steady magnetic field, leveraging the Lorentz force. Subsequently, the wire's induced emf was measured to determine damping from the resonance width. At low velocities in superfluid ^{3}He-B, vibrating wires manifested minimal, temperature-independent intrinsic losses. The temperature-dependent damping arising from thermal excitations is represented by $\exp(-\frac{\Delta}{KT})$. In particular, substantial thermal drag emerges as a result of Andreev scattering in the superfluid backflow around the detecting wire. This results in the quasiparticle dispersion curve tilting by an energy gap $\vec{v}.\vec{p}$ in the presence of superflow $\vec{v}$. Surpassing a critical velocity $v_c = \frac{v_L}{3}$, where $v_L = \frac{\Delta}{P_f}$ denotes the Landau critical velocity, the breakage of the cooper pair by the generating wire leads to a pronounced surge in damping due to the amplified quasiparticle flux at the detector wire [92].

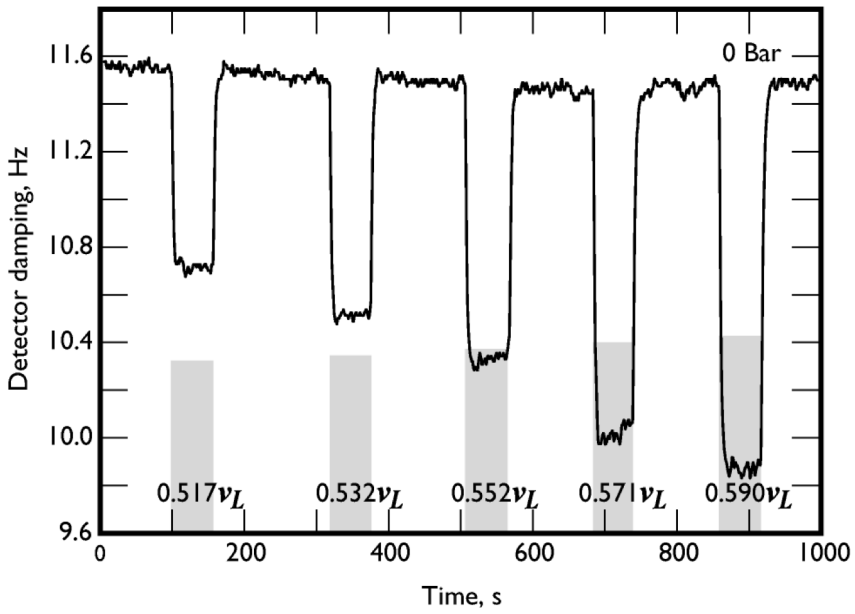

Figure 2.19: (a) Dissipation in the detector wire over time for various power levels applied to the generating wire (shaded area). For each period, the generator velocity is scaled by the Landau critical velocity. Adapted from [12].

Counterintuitively, as shown in Figure 2.19, increased thermal excitation from the generator wire leads to decreased damping in the detector wire. This implies a diminishing quasiparticle flux to the detector with rising thermal excitation density. Given the negligible quasiparticle scattering at such a low temperature, it's postulated that Andreev reflection, due to an additional flow field produced by the generator wire, shields the excitation flux from the detector wire, leading to turbulence.

Such pioneering observations of Andreev scattering due to the vortex flow field have ushered in the possibility of exploring previously unknown mechanisms in quantum fermi-liquids at ultra-low temperatures, particularly through minute vibrating structures. In conclusion, vibrating wire resonators have been instrumental in successfully demonstrating turbulence generation and detection in superfluid ^{3}He-B. Preliminary observations of Andreev scattering owing to the vortex flow field have set the stage for future investigations into the dynamic behaviors of quantum fermi-liquids, especially when studied using high-frequency NEMS and MEMS.

2.4 Superfluid ^{4}He adsorption on a nanotube resonator

Noury et al. [93] conducted an impressive study investigating the interaction of superfluid helium with carbon nanotube resonators, revealing interesting insights into quantum phase transitions and helium layering. Utilizing a suspended carbon nanotube, they probed the mechanical effects of helium adsorption on the nanotube's surface, showing, for the first time, clear discontinuities in the resonance frequency associated with first-order layering transitions. Their results underscore the unique capacity of the nanotube to detect tiny changes in mass and elasticity, making it an effective probe for superfluid helium at ultralow temperatures.

The study focuses on helium adsorption in a quasi-two-dimensional (2D) geometry, where the nanotube surface serves as a high-quality substrate for the helium layers. This 2D system is fundamentally different from bulk superfluid ^{4}He, as it allows for unique phenomena such as layering transitions and third sound excitations within the helium film. These effects, however, provide critical insights into the behavior of helium in confined geometries, serving as a precursor to understanding more complex interactions in bulk superfluid systems, which is the primary focus of this thesis.
The nanotube acts as a mechanical resonator, with its resonance frequency f_0 determined by the relationship:

$$f_0 = \frac{1}{2\pi}\sqrt{\frac{K}{M}}, \tag{2.61}$$

where K is the total spring constant, and M is the effective mass of the system. As helium atoms adsorb onto the nanotube, the total mass increases by the mass of the adsorbed helium m_{He}, leading to a shift in the resonance frequency:

$$f_0' = \frac{1}{2\pi}\sqrt{\frac{K}{M + m_{\mathrm{He}}}}. \tag{2.62}$$

This relationship allows the measurement of helium adsorption by observing the frequency shift $\Delta f = f_0 - f_0'$, which is directly proportional to the mass of the adsorbed helium.

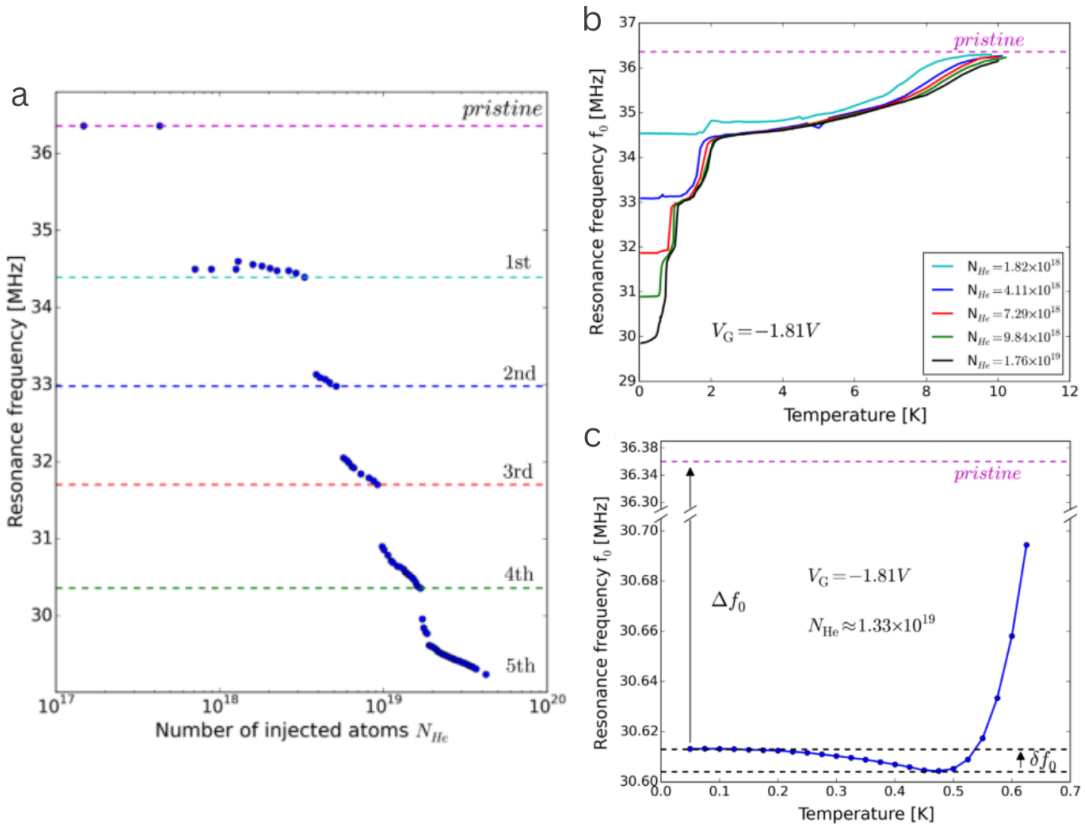

Figure 2.20: **Helium film growth and desorption on nanotube.** (a) The plot shows the resonance frequency shift as a function of helium atom adsorption. Each step corresponds to the completion of a helium layer, with the frequency decreasing progressively as successive layers form on the carbon nanotube. The stepwise nature of the frequency shift highlights the first-order layering transitions. (b) As the temperature increases, the helium layers desorb from the nanotube surface, leading to a progressive increase in resonance frequency. (c) This plot captures the spring constant effect near 0.5 K, where a slight minimum in the frequency shift is observed due to changes in surface tension and the interaction between the nanotube's elasticity and the helium film.

The study revealed the formation of discrete helium layers, with resonance frequency measurements demonstrating that each layer formed in a stepwise manner. Fig. 2.20(a) from the study illustrates the layer-by-layer growth of the helium film on the nanotube, where each step corresponds to the completion of a helium layer, causing a measurable decrease in the resonance frequency. The stepwise decrease in frequency marks the completion of successive helium layers as helium atoms condense on the nanotube surface, clearly delineating the first-order nature of the layering transitions [93].
Fig. 2.20(b) shows the desorption of helium layers with increasing temperature, where the resonance frequency rises as helium evaporates, directly correlating with the nanotube's mass change. Fig. 2.20(c) reveals a subtle spring constant effect, with a slight frequency shift minimum near 0.5 K due to changes in helium surface tension. This interaction between the nanotube's elasticity and the helium surface tension becomes more prominent as helium desorbs (supplementary of [93]).

To quantify the effects of helium adsorption, we examine the shift in the total spring constant, K_{total}, which is given by:

$$K_{\text{total}} = K_{\text{NT}} + K_{\text{He}}, \tag{2.63}$$

where K_{NT} is the intrinsic spring constant of the pristine nanotube and K_{He} is the contribution from the helium film. The helium spring constant, K_{He}, is associated with the surface tension γ of the helium film, which varies with temperature due to thermally excited third sound modes. The relation for K_{He} is:

$$K_{\mathrm{He}} = \gamma \pi^3 r_{\mathrm{He}} / L, \tag{2.64}$$

where r_{He} is the radius of the helium film on the nanotube, and L is the length of the nanotube. The resonance frequency shift δf_0 due to changes in surface tension is given by:

$$\delta f_0 = -0.074 \frac{1}{M_{\mathrm{NT}} f_0} \frac{r_{\mathrm{He}}}{L} \left(\frac{k_B T}{\hbar c} \right)^3, \tag{2.65}$$

where k_B is the Boltzmann constant, $\hbar$ is the reduced Planck constant, and c is the speed of third sound within the helium film. This cubic temperature dependence is evident in the experimental results and provides a direct link between the helium film's dynamics and the nanotube's resonance behavior.

Fig. 2.21 illustrates the temperature-dependent dynamics of third sound in the helium film adsorbed on the nanotube. The resonance frequency shift follows the cubic law, indicating the excitation of third sound modes. This temperature dependence, shown in Fig. 2.21 (a) and (b), reflects the nanotube's mechanical response to thermally excited superfluid waves. The resonance shift reveals the sound velocity in the helium layer, with a significant jump from $\sim$ 30 m/s to $\sim$ 170 m/s between the third and fourth layers, consistent with the sharp discontinuity expected in a first-order phase transition [93].

These experimental results showcase the exceptional sensitivity of nanotube resonators in detecting small mass changes and elasticity shifts. While this study focuses on helium in a 2D configuration on the nanotube surface, differing from bulk superfluid helium, it provides a valuable framework for understanding interactions in confined geometries. These findings serve as a precursor to probing more complex dynamics in bulk ^{4}He, a key aim of this thesis.

The ability of CNT resonators to detect both mass loading and elasticity changes from helium adsorption highlights their potential as powerful probes for studying bulk superfluid ^{4}He. Their minimal mass and nanoscale dimensions allow them to resolve subtle interactions with the surrounding superfluid, making them highly effective for investigating quantum turbulence, vortex interactions, and phase changes. With their unmatched sensitivity and high-frequency operation, CNTs are poised to play a pivotal role in advancing low-temperature physics, particularly in exploring quantum phenomena in bulk helium systems.

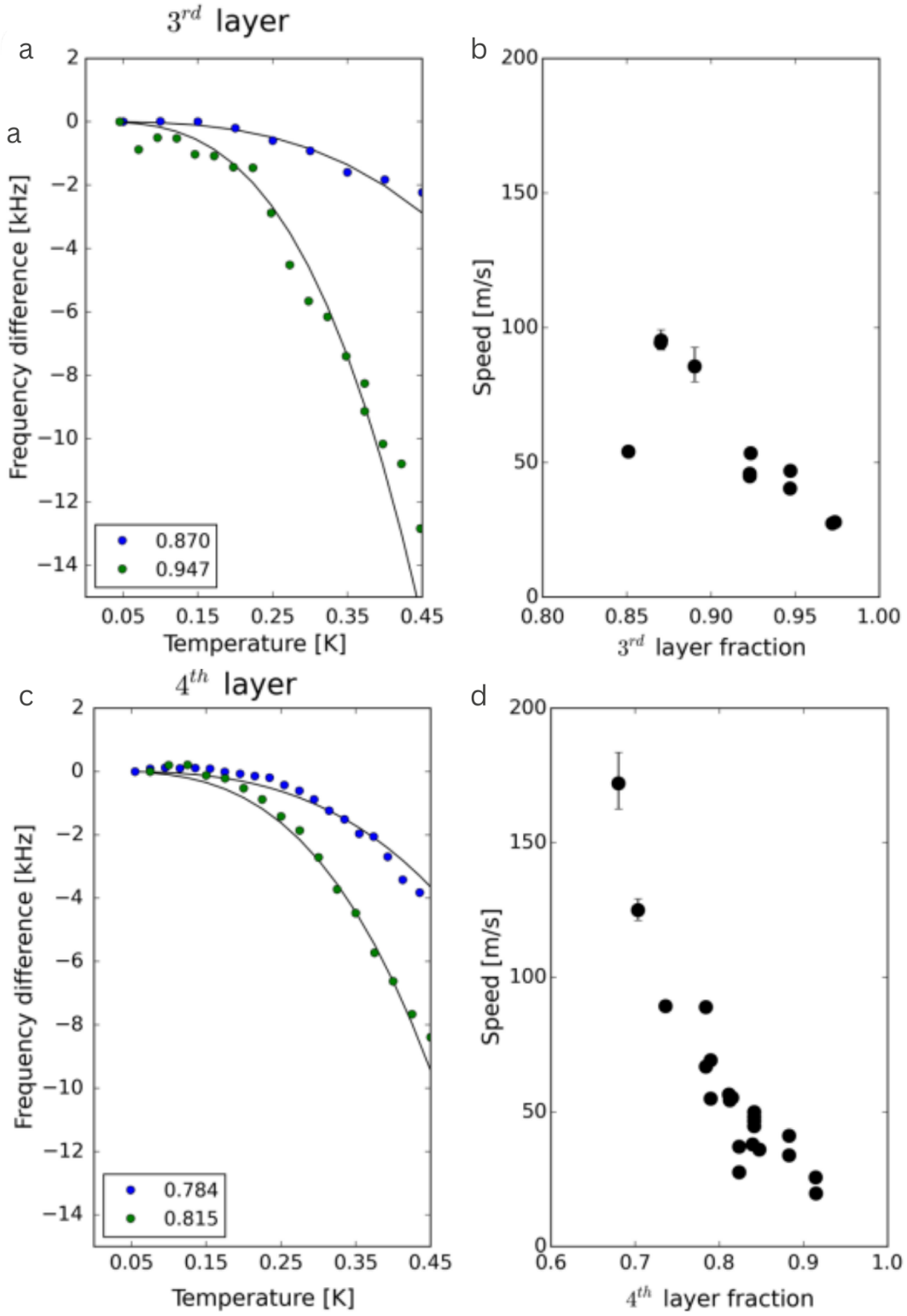

Figure 2.21: **Third sound dynamics and resonance shift.** The temperature dependence of the resonance frequency shift follows a cubic law, indicating the excitation of third sound modes within the helium film. The plot shows the significant jump in sound velocity between the third and fourth helium layers, with the velocity increasing from ∼30 m/s to ∼170 m/s, corresponding to a first-order phase transition.

2.4.1 Summary

Liquid helium, in its isotopic forms ^{3}He and ^{4}He, has been an invaluable asset in low-temperature research, enabling the exploration of intricate quantum behaviors of macroscopic systems close to absolute zero. The pivotal role of mechanical resonators, particularly MEMS, NEMS, and recently carbon nanotube resonators, in this exploration cannot be understated. Carbon nanotube resonators, in particular, have demonstrated an impressive capacity to detect helium adsorption, layering transitions, and the excitation of third sound modes in helium films. These studies in quasi-2D geometries provide critical insights into helium-fluid dynamics and are a precursor to understanding more complex behaviors in bulk superfluid helium systems, which is the focus of this review.

It is evident from past research that lighter resonators with high resonant frequencies in the megahertz range exhibit greater sensitivity to helium interactions. The study of bulk superfluid helium through mechanical resonators promises to unlock further understanding of quantum turbulence, vortex dynamics, and topological excitations in helium fluids. The miniaturization of nanomechanical oscillators, such as nanotube-based systems, offers enhanced sensitivity for detecting these phenomena, enriching our understanding of condensed matter physics and opening new possibilities for cooling technologies and quantum devices. The interplay between mechanical resonators and helium fluids remains crucial for advancements in fields ranging from low-temperature physics to cosmology, where the unique properties of helium fluids continue to offer profound insights.

Chapter 3: Modeling of nanotube vibrations in liquid ^{4}He

This chapter simulates the dynamics of vibrating CNTs submerged in superfluid ^{4}He, focusing on the damping mechanisms in NEMS and MEMS oscillators within liquid ^{4}He. Initially, we examine the temperature-dependent hydrodynamic interactions, revealing a significant frequency sensitivity of nanotubes to the viscous behavior of liquid helium near the superfluid transition. In addition, we analyze ballistic and acoustic damping mechanisms, illustrating the superior damping behavior of nanotubes compared to those of nanobeam resonators. Furthermore, we discuss the phenomenon of transverse oscillations within the normal component of superfluid helium confined in CNTs. The findings emphasize the potential of CNT resonators as potent probes for studying quantum and hydrodynamic phenomena in low-temperature physics, particularly in probing the dynamics of topological excitations and various sound waves in different-dimensional superfluid systems.

3.1 Damping mechanisms in NEMS and MEMS oscillators in ^{4}He

Mechanical oscillators immersed in liquid ^{4}He experience additional damping mechanisms beyond intrinsic losses. This section explores the dissipation mechanisms affecting resonators in helium at extremely low temperatures, evaluating their sensitivity as detectors.

Two key temperature-dependent damping regimes are the hydrodynamic and ballistic regimes. In the hydrodynamic regime, the mean free path of quasiparticles, l_{mfp}, is much shorter than the characteristic oscillator size, $l_{\mathrm{mfp}} \ll d$. In contrast, in the ballistic regime, l_{mfp} exceeds the oscillator dimensions, $l_{\mathrm{mfp}} \gg d$. For a nanotube in helium, the hydrodynamic regime occurs above approximately 1 K, while the ballistic regime dominates below this temperature.

In the hydrodynamic regime, quasiparticles frequently collide, and dissipation arises mainly from the viscous behavior of normal liquid helium, following macroscopic dynamics. However, as the temperature falls to $T \leqslant 1\,\mathrm{K}$, collisions decrease, and thermal excitations behave like a rarified gas. In the ballistic regime, damping is governed by the microscopic dynamics of the superfluid.

At the lowest temperatures, acoustic losses from the oscillating body itself become significant, limiting the probe's ability to study quantum vacuum properties. The following sections will further detail these regimes and their impact on the motion of mechanical oscillators in helium.

3.1.1 Hydrodynamic regime

From the two-fluid model (section 2.1.2), we understand that liquid ^{4}He contains both a normal and a superfluid component even below the λ transition. In this section, we elaborate on the effect of the viscous fluid surrounding a mechanical oscillator, where dissipation primarily stems from Stokes' drag. As an oscillator moves through the liquid ^{4}He, it displaces a liquid mass of $\rho_{\mathrm{H}}V$, where ρ_{H} and V denote the fluid density and the resonator volume respectively. This fluid backflow around the oscillator seemingly augments the mass of the oscillating body. Moreover, the normal fluid in close proximity to the oscillating surface exhibits rotational movement, with the penetration depth of this rotational flow expressed as:

$$\delta = \sqrt{\frac{\eta}{\pi f_0 \rho_{\mathrm{nf}}}}, \tag{3.1}$$

where ρ_{nf} and η represent the normal fluid density and viscosity [87], respectively. This small portion of normal fluid viscously adheres to the moving surface, contributing an additional mass term $\rho_{\mathrm{nf}} S\delta$, with S representing the area of the oscillating body. Consequently, a resonator oscillates with an enhanced effective mass, depicted as:

$$m_{\mathrm{H}} = m_0 + \beta\rho_{\mathrm{H}}V + B\rho_{\mathrm{nf}}S\delta, \tag{3.2}$$

Here, β and B are geometric parameters approximately equal to unity. This leads to a diminished resonant frequency, expressed as:

$$f_{\mathrm{H}} = \sqrt{\frac{k}{m_{\mathrm{H}}}}, \tag{3.3}$$

Employing Eq. (3.2) and Eq. (3.3), the normal fluid-fraction dependence of the resonance frequency alteration can be derived as:

$$\left(\frac{f_0}{f_{\mathrm{H}}}\right)^2 = 1 + \beta\frac{\rho_{\mathrm{H}}V}{m_{\mathrm{e}}} + B\frac{S}{m_{\mathrm{e}}}\sqrt{\frac{\eta\rho_{\mathrm{nf}}}{\pi f_0}}, \tag{3.4}$$

Here, m_{e} denotes the effective mass of the system, accounting for both the beam and the surrounding fluid. This theory holds validity provided the viscous penetration depth is significantly less than the nanotube dimensions. When $\delta > l$, the behavior of the displaced liquid hinges on the clamped fluid, especially when $\rho_{\mathrm{nf}} = \rho_{\mathrm{H}}$ above T_λ. In such scenarios, a comprehensive Stokes' theory is needed for precise frequency shift (or hydrodynamic losses) measurement.

Considering a large cylinder in the high-frequency limit, we model the hydrodynamic damping resulting from the frequency shift observed in Eq. (3.4). This damping is attributed to the viscous forces exerted by the surrounding fluid on the oscillating body. In this regime, we apply the principles from classical fluid dynamics as developed by Landau and Lifshitz [91]. The Stokes' force, which describes the resistive force experienced by an object moving through a viscous fluid, can be expressed as:

$$F = CS\sqrt{\pi\eta\rho_{\mathrm{nf}}f_{\mathrm{H}}}v \tag{3.5}$$

Here, F represents the drag force experienced by the oscillating object, C is a geometrical constant that depends on the shape and boundary conditions of the resonator, S is the cross-sectional area, η is the dynamic viscosity of the fluid, ρ_{nf} is the normal fluid density,

f_H is the hydrodynamic resonance frequency of the system, and v denotes the oscillation velocity.

This formulation of the Stokes' force assumes that the system operates in the high-frequency limit, where the viscous effects are primarily confined to a thin boundary layer near the surface of the resonator. The term $\sqrt{\pi\eta\rho_{nf}f_H}$ captures the dependence of the drag force on both the fluid's viscosity and density, as well as the frequency of oscillation. The model simplifies the complex interactions between the fluid and the oscillator by overlooking edge effects such as zero velocity at the oscillator boundaries, which can complicate the analysis [94].

To quantify the energy dissipation due to this hydrodynamic damping, we use the concept of the inverse quality factor, Q^{-1}. The quality factor describes the ratio of the stored energy in the system to the energy lost per oscillation cycle. The inverse quality factor for the hydrodynamic damping can be derived using the definition:

$$Q^{-1} = \frac{1}{2\pi m f_0}\frac{dF}{dv} \tag{3.6}$$

This expression relates the damping force F to the oscillation velocity v, where m is the effective mass of the system and f_0 is the natural frequency of the resonator in vacuum. Substituting the expression for the Stokes' force from Eq. (3.5), we obtain the following expression for the inverse quality factor due to hydrodynamic damping:

$$Q^{-1}_{hyd} = C\frac{S}{2m_e}\sqrt{\frac{\rho_{nf}\eta f_0}{\pi}}\left(\frac{f_0}{f_H}\right)^2, \tag{3.7}$$

This equation shows that the inverse quality factor Q^{-1}_{hyd} depends on the cross-sectional area S, the effective mass m_e of the resonator, the density ρ_{nf} and viscosity η of the normal fluid, as well as the ratio of the natural frequency f_0 to the hydrodynamic resonance frequency f_H.

At sub-kelvin temperatures, the normal fluid density ρ_{nf} approaches zero as the superfluid fraction dominates. This leads to a significant reduction in hydrodynamic damping, resulting in negligible frequency shifts and a shift in the resonator dynamics towards the ballistic regime, where the motion is no longer dominated by fluid interactions but by ballistic transport processes. In this regime, the oscillatory motion is governed by the intrinsic properties of the resonator rather than viscous drag, providing insights into the quantum mechanical behavior of the system in such low-temperature environments.

3.1.2 Ballistic regime

As the temperature decreases, the mean free path of thermal excitations such as phonons and rotons extends, becoming comparable to or exceeding the dimensions of the oscillating body. Consequently, these thermal excitations are considered as a rarified gas rather than a component of the normal fluid [95], becoming the primary source of dissipation for the oscillator within this temperature range.

We adopt a theoretical framework from Ref. [89] to ascertain the individual damping contributions from the scattering of phonons and rotons off the oscillating surface of the nanotube resonator. This framework is particularly useful for describing the interaction of excitations with surfaces in the quantum regime of superfluid ^{4}He, where both phonons and rotons are the main excitations contributing to the damping of the oscillator. The validity of this model is contingent on temperatures being low enough (typically below

1 K), such that the system resides in the ballistic regime where the interaction between the resonator and quasiparticles can be described by kinetic theory. In this regime, the damping is largely driven by scattering processes rather than classical viscous drag.
The total drag force experienced by the resonator, which moves with velocity v over a given time interval, is given by the following equation:

$$F = -\frac{1}{2}\mathcal{A}np_0vdL, \tag{3.8}$$

In this equation, $\mathcal{A} = 2.67$ is a constant for cylindrical geometry that accounts for the geometry of the resonator, while d and L represent the diameter and length of the nanotube resonator, respectively. The term p_0 represents the momentum of an individual excitation (either phonon or roton), and n is the total number density of the excitations in the superfluid helium.
The parameter n plays a crucial role in determining the total damping experienced by the resonator. It represents the number density of quasiparticles (phonons and rotons) within the superfluid helium. The significance of n is tied to its temperature dependence. For phonons, the number density increases as T^3, while for rotons, n follows an exponential dependence on temperature, $\exp(-\Delta/k_\mathrm{B}T)$, where Δ is the roton energy gap. Therefore, the damping contribution from each type of excitation can be expressed as a function of n, leading to distinct temperature-dependent behaviors for phonon and roton damping.
For phonons, we rewrite Eq. (3.8) in terms of the phonon mass-density $\rho_\mathrm{ph} = n\frac{p_0}{c_\mathrm{ph}}$ and utilize the relevant parameters from Ref. [89]. The resulting expression for the inverse quality factor due to phonon scattering is:

$$Q_\mathrm{ph}^{-1} = \mathcal{A}\frac{k_\mathrm{B}^4}{45\hbar^3 df_0(\rho+\rho_\mathrm{s})c_\mathrm{ph}^4}T^4, \tag{3.9}$$

In this equation, c_ph represents the velocity of phonons, ρ is the oscillator density, and ρ_s represents the superfluid density. The T^4 dependence indicates that phonon damping becomes more pronounced as the temperature increases, particularly at higher temperatures within the low-temperature regime (typically around 0.1 K to 1 K).
Similarly, the damping contribution from roton scattering is given by:

$$Q_\mathrm{rot}^{-1} = \frac{\mathcal{A}p_0}{\pi^2 df_0\rho}\left(\frac{m^*k_\mathrm{B}T}{2\pi\hbar^2}\right)^{3/2}\exp\left(-\frac{\Delta}{k_\mathrm{B}T}\right), \tag{3.10}$$

Here, p_0, m^*, and Δ are the Landau parameters for rotons, with p_0 representing the roton momentum, m^* the roton effective mass, and Δ the roton energy gap. The exponential dependence on temperature highlights that roton damping becomes negligible at low temperatures but grows exponentially as the temperature rises above a certain threshold (typically above 0.3 K). This behavior contrasts with the T^4 dependence for phonons, resulting in different temperature ranges where phonon and roton damping dominate.
These equations, Eq. (3.9) for phonon damping and Eq. (3.10) for roton damping, encapsulate the microscopic phenomena occurring within superfluid ^{4}He, making them applicable for describing quasiparticle dynamics at millikelvin temperatures. However, it is important to note that, while phonon and roton damping provide a significant contribution at low temperatures, real experimental measurements of high-frequency oscillators are often limited by temperature-independent damping mechanisms, such as acoustic emission [10].

3.1.3 Sound emission from acoustic dipoles

Small amplitude oscillators oscillating in a compressible fluid, such as superfluid helium, are known to emit sound waves. Each end of a doubly clamped nanotube or nanobeam behaves as an acoustic monopole, which radiates sound waves isotropically in all directions [91]. In these nanoscale resonators, the two ends form an acoustic dipole, where the oscillation of the structure generates sound waves from both ends. This dipole configuration is relevant when the separation between the two ends is smaller than the wavelength of the first sound, which is the normal sound propagation speed in the fluid. Additionally, this effect is significant at sufficiently low temperatures where second sound, a unique wave of entropy in superfluid helium, becomes observable.

In this scenario, the power radiated as sound by an infinitely long cylinder with radius R is given by the far-field approximation. According to this model, the power of sound emitted is expressed as:

$$P = \frac{\pi^2}{4c_{\mathrm{ph}}^2}\rho_{\mathrm{H}}\omega^3 R^4 L v^2, \tag{3.11}$$

where P represents the emitted sound power, c_{ph} is the velocity of the first sound, ρ_{H} is the density of superfluid helium, ω is the angular frequency of oscillation, R is the radius of the nanotube or nanobeam, L is its length, and v is the oscillation velocity.

The energy loss associated with the radiated sound per oscillation cycle can be described by the inverse quality factor Q^{-1}. The expression for the acoustic losses is given by:

$$Q_{\mathrm{ac}}^{-1} = \frac{P}{2\pi m v^2}\frac{1}{\omega}, \tag{3.12}$$

where m is the effective mass of the resonator. The mass m of the nanotube can be expressed in terms of its density ρ as:

$$\rho = \frac{m}{\pi R^2 L}. \tag{3.13}$$

Substituting this into Eq. (3.12) and using the relation $\omega = 2\pi f_0$, where f_0 is the resonant frequency, we obtain the final form of the acoustic damping:

$$Q_{\mathrm{ac}}^{-1} = \frac{\pi^3}{2}\frac{\rho_{\mathrm{H}}}{\rho}\left(\frac{df_0}{2c_{\mathrm{ph}}}\right)^2, \tag{3.14}$$

where $d = 2R$ is the diameter of the nanotube.
This equation shows that the acoustic damping increases with both the square of the diameter d and the resonant frequency f_0. At very low temperatures, acoustic losses become dominant because other forms of dissipation, such as those due to ballistic scattering, scale as T^4 and diminish as the temperature decreases. Hence, the dissipation due to acoustic emission becomes the primary limitation on the performance of the resonator.

To minimize acoustic losses, it is necessary to use resonators with smaller diameters and lower resonant frequencies. This design choice reduces the power radiated as sound, thereby enhancing the sensitivity of the mechanical probe to interactions with superfluid helium. In the millikelvin temperature range, where this sensitivity is crucial for studying the damping mechanisms, it is essential to mitigate acoustic losses for accurate measurements.

3.2 CNT resonator in liquid ^{4}He

A vibrating CNT is a promising nanomechanical probe for exploring collective quantum phenomena in superfluid ^{3}He/^{4}He, owing to its high crystallinity, impressive quality factor, and mass sensitivity reaching atomic resolution, alongside an optimal surface potential conducive for helium adsorption. Beyond the damping caused by phonons and rotons, the interaction of nanotubes with superfluids could unveil the dynamics of topological excitations, for instance, vortex-vortex interaction in cylindrical geometry, quantization of a single vortex, and quantum turbulence across the vortex core.

3.2.1 Dissipation modeling in hydrodynamic and ballistic regimes

Intrinsic damping in carbon nanotubes tends to be negligible relative to NEMS such as nanobeam resonators due to their large length-to-diameter ratio. This implies that the dissipation mechanisms mainly originate from thermal and topological excitations in superfluids. For a quantitative insight into the damping behavior of vibrating nanotubes, we consider a nanotube device [96] with a resonance frequency of 55.6 MHz and an intrinsic quality factor of approximately 5×10^6, submerged in superfluid ^{4}He.

3.2.1.1 Hydrodynamic losses

The behavior of a nanotube resonator in liquid helium close to its transition temperature serves as a robust medium for investigating the fluid's viscous properties. When operated in a viscous medium, a nanotube resonator experiences damping due to Stokes' drag, which apparently augments its mass. This apparent mass enhancement arises from two primary contributions: the clamping of the normal fluid onto the nanotube's surface and the fluid's backflow across the resonator. As a result, the resonant frequency of the nanotube when submerged in the viscous fluid descends from its vacuum value. The fractional change in frequency can be derived from Eq. (3.4), simplifying to -

$$\left(\frac{f_0}{f_{\mathrm{H}}}\right)^2 - 1 = \frac{1}{\rho_{\mathrm{NT}}}\left(\beta\rho_{\mathrm{H}} + \frac{4B}{d}\sqrt{\frac{\eta\rho_{\mathrm{nf}}}{\pi f_0}}\right). \tag{3.15}$$

Here, ρ_{NT} and d represent the density and diameter of the nanotube respectively. Eq. (3.15) implies that owing to its extremely low density and nano-scale dimensions, the nanotube may exhibit higher frequency sensitivity when compared to commercially available, denser, and larger oscillators. Figure 3.1(a) delineates the squared fractional change in resonance frequency as a function of temperature for a nanotube resonator within liquid helium. Above the transition point, the resonance frequency in helium immediately halves from its vacuum value, i.e., $f_{\mathrm{H}} \approx \frac{1}{2}f_0$, maintaining this characteristic down to the λ point. However, this fractional value surges almost linearly with the temperature below the superfluid transition, indicative of the reduction in clamped normal fluid fraction to the nanotube. Analyzing the fractional frequency response reveals a linear decrease in ρ_{nf} with a temperature drop from 1.06 K to 2.18 K since the fluid backflow term has a feeble temperature dependence. For the quantitative description, Figure 3.1(b) illustrates the normal fluid fraction dependence of the fractional frequency change within the temperature span of 1.06 K to 2.18 K, showing a substantial frequency alteration with the $\rho_{\mathrm{nf}}/\rho_{\mathrm{H}}$ over this temperature range, indicating the nanotube's superior sensitivity in exploring

the viscous behavior of helium fluid compared to NEMS, vibrating wire, and tuning fork resonators [13].

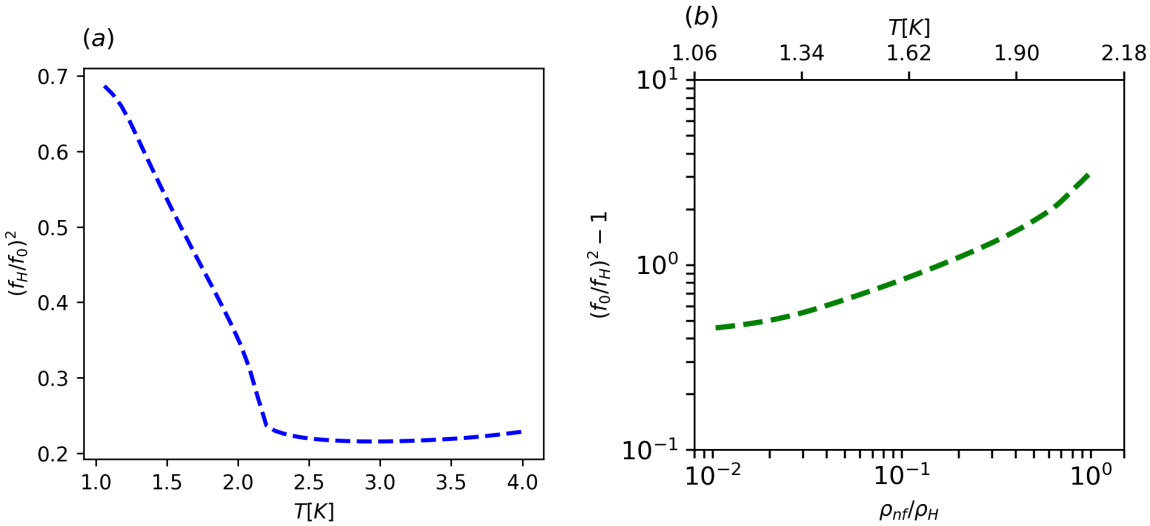

Figure 3.1: (a) The change in fractional frequency of the resonator as a function of temperature shows a linear trend in resonance frequency below the superfluid transition. This trend is attributed to the unclamping of normal fluid from the resonator surface. (b) Relationship between the fractional frequency change in the resonator and the normal fluid fraction for the nanotube using Eq. (3.15).

Moreover, the hydrodynamic drag forces exerted on the nanotube contribute to damping, especially when the oscillator size surpasses the viscous penetration depth δ as defined in Eq. (3.1). The resonance frequency width can thus be computed from Eq. (3.7) as:

$$\Delta f^{\mathrm{hyd}} = C\frac{S}{2m_0}\sqrt{\frac{\rho_{\mathrm{nf}}\eta f_0}{\pi}}\left(\frac{f_{\mathrm{H}}}{f_0}\right)^2, \tag{3.16}$$

where C is a geometrical constant, S and m_0 are the area and mass of the nanotube, respectively.

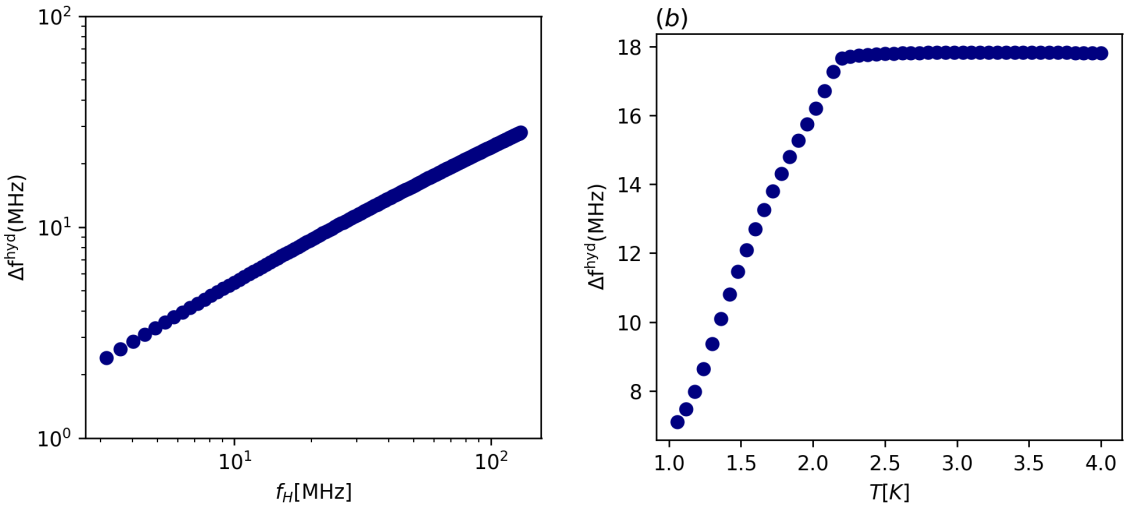

Figure 3.2: (a) Stokes' damping experienced by the resonator, plotted against its frequency at a temperature of 1.5 K under saturated vapor pressure using Eq. (3.16). (b) Resonance width as a function of temperature within a hydrodynamic framework.

The hydrodynamic damping contribution for a nanotube resonator immersed in superfluid ^{4}He at 1.5 K is illustrated in Fig. 3.2(a), utilizing the relevant liquid ^{4}He parameters from Donnelly and Barenghi [97]. The graph manifests the resonance width dependency on the nanotube's resonant frequency as per Eq. (3.16). Remarkably, the dissipations span a wide frequency range and alter nearly by an order of magnitude, authenticating the profound frequency sensitivity of our nanotube resonators in the viscous damping regime of the two-fluid system in the vicinity of transition temperature. Subsequently, Fig. 3.2(b) demonstrates the temperature dependence of hydrodynamic damping for a nanotube resonator with a resonance frequency of 55.6 MHz. Above the superfluid transition, the dissipations, which are substantial (on the order of 8 MHz) for the nanotube due to its high resonance frequency and lightweight, maintain a constant level above the lambda point. Yet, the resonance width exhibits a sharp linear decline below the transition temperature, attributed to the reduction in the effective mass of the resonator due to unclamping of normal fluid fraction. This pronounced drop in hydrodynamic losses by 61.1%, within the temperature span of 1.06 K to 2.18 K, substantiates the reliability of our carbon nanotube oscillator in describing hydrodynamic behavior.

3.2.1.2 Ballistic and acoustic losses

The mean free path of phonons and rotons [89] is illustrated in Fig. 3.3(a), and compared against both nanotube and nanobeam dimensions to discern the ballistic regime for each oscillator. It is apparent that the quasiparticles' mean free path surpasses the nanotube diameter (5 nm) around 1 K, and outstrips the nanobeam diameter (150 nm) below 0.7 K, signifying a relatively higher temperature threshold for the nanotube to enter the ballistic regime.

Therefore, a nanotube can undergo damping due to thermal excitations, as described by Eq. (3.9) and Eq. (3.10), for temperature $T \leq 1$ K, depicted by blue dashed lines in Fig. 3.3(b) for the temperature range of 0.4 K to 0.7 K. A parallel simulation for a nanobeam [14] is presented in Fig. 3.3(c), wherein a nanobeam displays a considerably narrower ballistic regime of $\approx$ 0.5 K to 0.7 K compared to that of a nanotube $\approx$ 0.4 K

to 1 K. This marked extension in the ballistic regime for the nanotube, with thermal excitation dynamics dominant down to ≈ 0.4 K, underscores its sensitivity in studying quantum fluids over an extended temperature range. Moreover, despite a notably higher resonance frequency compared to a nanobeam (1.6 MHz), our nanotube oscillator incurs substantial losses ($\approx 10^{-1}$ to 10^{-5}) from quasiparticle scattering, attributable to its low effective mass.
However, it is well-known that the high frequency cylindrical resonators act as dipole emitters at millikelvin temperatures, as described in Eq. (3.14). This implies potential acoustic losses for the nanotube; it indeed sets a bound on the sensitivity of oscillators. The red lines in Fig. 3.3(b) and Fig. 3.3(c) aggregate the damping contribution from all sources present in the superfluidic system: acoustic emissions from a nanotube are predominant at temperature $T \leqslant 0.4$ K; while for a nanobeam, first sound emission emerges as the dominant loss mechanism at $T \leqslant 0.5$ K. Therefore, it is deduced that a nanotube, with a much higher resonance frequency compared to a nanobeam, exhibits minimal acoustic losses of 2×10^{-6}, ascribed to the two order of magnitude smaller diameter of the nanotube relative to the nanobeam.

Fig. 3.3(d) illustrates the aggregate dissipation in superfluid ^{4}He for several nanotube oscillators with varied resonant frequencies and intrinsic losses. These nanotube devices, taken from Refs. [93, 98, 99, 23, 96], exhibit resonance frequencies of 30 MHz, 40 kHz, 350 MHz, 180 MHz, 55.6 MHz, respectively. For the device with the lowest resonant frequency, acoustic losses are negligible ($\approx 10^{-12}$) as indicated by the green line, where ballistic damping predominates across the entire temperature range until intrinsic losses prevail. Conversely, thermal excitation dynamics for devices with higher resonance frequencies and significant internal losses (blue and cyan lines) are suppressed by acoustic and internal losses, almost throughout the entire temperature range. However, nanotube resonators with high-quality factors ($\approx 10^5/10^6$) and few megahertz oscillation frequencies (30-60 MHz) demonstrate optimal sensitivity (red and black lines) in probing both excitation-dynamics in superfluid ^{4}He and acoustic emission from the oscillators. Hence, a 1-micron-long vibrating nanotube with an exceptionally high-quality factor stands as a potent probe for investigating distinct damping mechanisms observed in liquid helium.

Frequency	Q Factor	Length	Diameter	Publication
30 MHz	2×10^5	1.1 µm	3 nm	Noury et al., 2019
40 kHz	2245	5 µm	3 nm	Tavernarakis et al., 2018
350 MHz	1×10^5	0.8 µm	1.5 nm	Huttel et al., 2009
180 MHz	6000	0.8 µm	5 nm	Wen et al., 2018
55.6 MHz	5×10^6	1.5 µm	2 nm	Moser et al., 2014

Table 3.1: Parameters for different CNT resonators

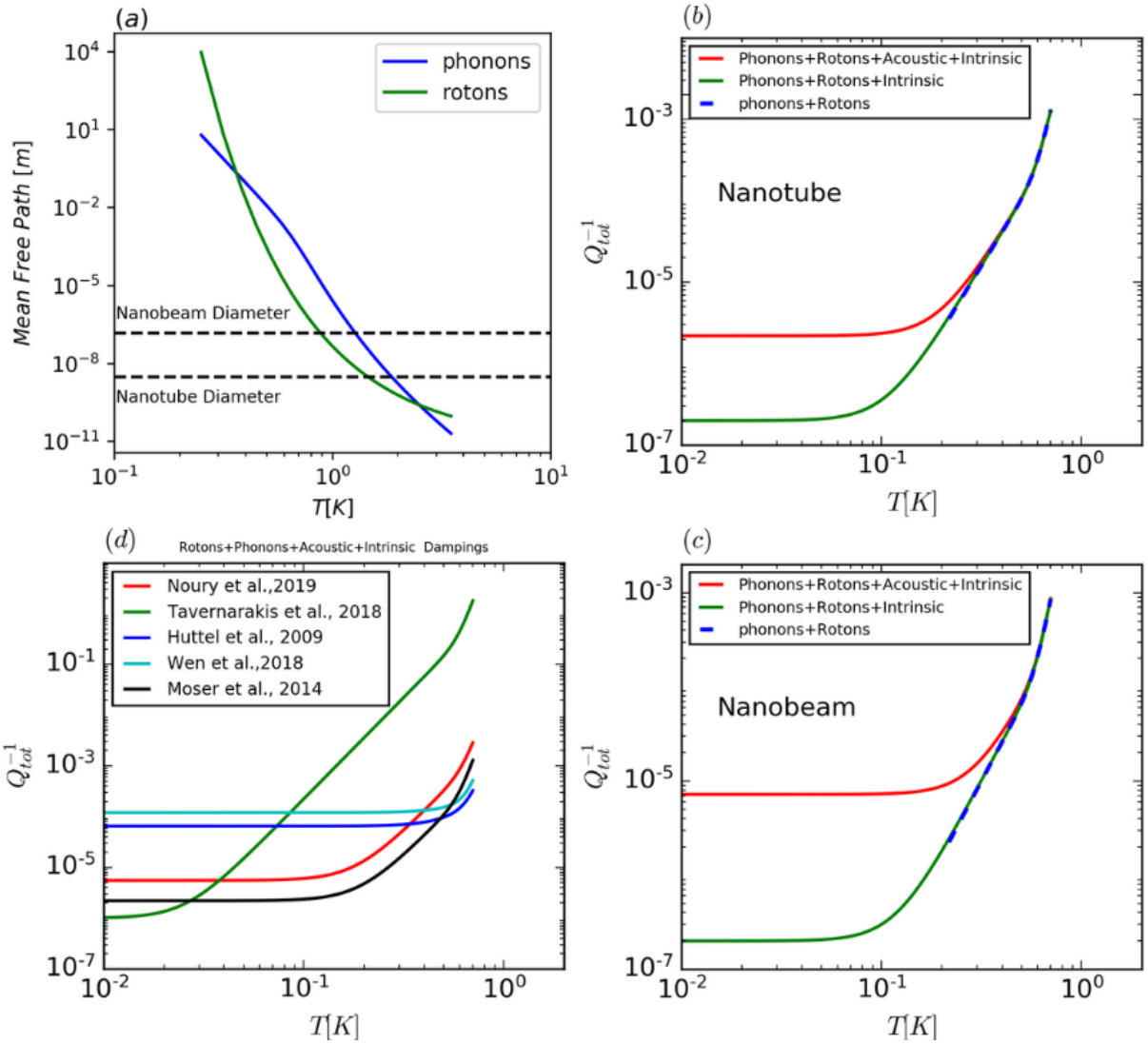

Figure 3.3: A comprehensive depiction of damping mechanisms impacting a nanotube resonator submerged in superfluid ^{4}He: (a) The temperature-dependent mean free path of phonons and rotons in ^{4}He [89], within the temperature range of 250 mK to 3.5 K. The black dashed line indicates the temperature (1 K) at which the mean free path of the quasiparticles exceeds the dimensions of the nanotubes, marking the onset of the ballistic regime. (b) Simulates the different damping mechanisms that affect a 1 µm-long nanotube resonator using Eq. (3.9), Eq. (3.10), and Eq. (3.14), indicating that the intrinsic losses are around the order of $\approx 10^{-7}$. (c) Mirrors the analysis in (b), but for a nanobeam resonator, providing a comparative insight into the damping behavior between nanotube and nanobeam resonators. (d) The overall dissipations for nanotube resonators with different resonant frequencies and internal losses (see the Table 3.1 for parameters) offer a broader perspective on how the resonant frequency and internal losses influence the damping mechanics within the superfluid environment.

3.2.2 CNT resonators: studying multidimensional sound waves in superfluid ^{4}He

CNTs loaded with superfluid helium can function as quasi-one-dimensional capillary tubes, enabling the detection of fourth sound. However, fourth sound is not exclusive

to 1D systems; it has also been observed in 2D and 3D systems when the superfluid component moves independently of the clamped normal component, particularly in confined geometries. This phenomenon is detected in 2D nanofluidic channels and 3D Helmholtz resonators when the normal component is sufficiently suppressed and the superfluid component is free to move [100, 101].

Additionally, due to the substrate potential of nanotubes, superfluid thin films can form on their surface, enabling the measurement of 3rd and 5th sound in these two-dimensional superfluid ^{4}He films [93]. Immersing nanotube resonators in a helium bath can also facilitate the probing of 2nd sound, a bulk superfluid phenomenon in 3D systems.

Beyond these longitudinal acoustic waves, a transverse sound wave can exist within the normal component of superfluid helium, driven by the geometric characteristics of the quantum fluid. A theoretical study by Tkachenko [102] suggests that superfluid helium confined in a carbon nanotube is a promising system for detecting these transverse oscillations in the normal component of ^{4}He, governed by the equation:

$$V_{\mathrm{n}} = \frac{V_{\mathrm{s}}}{\partial_r \ln\left(\frac{\rho_{\mathrm{nf}}}{S\rho_{\mathrm{H}}}\right)}\left(1 - e^{\partial_r\left(\frac{\rho_{\mathrm{nf}}(R-r)}{S\rho_{\mathrm{H}}}\right)}\right), \tag{3.17}$$

where V_{n} and V_{s} represent the velocities of the normal and superfluid components, respectively, and S and R denote the nanotube surface area and radius.
In superfluid helium, the transverse sound waves arise from the differential motion between the normal and superfluid components, as described by Landau's two-fluid model[91]. This model presents two distinct velocities: $\vec{V}_{\mathrm{s}}$ for the superfluid component and $\vec{V}_{\mathrm{n}}$ for the normal component. Unlike conventional hydrodynamics, where only longitudinal sound waves exist, in superfluid helium, the interaction between these two fluids gives rise to transverse sound waves, where the normal component oscillates perpendicularly to the direction of wave propagation.
The transverse sound propagation in superfluid helium confined within carbon nanotubes introduces a fascinating intersection of quantum fluid dynamics and nanoscale geometry. The cylindrical geometry and boundary conditions of the nanotube significantly influence the transverse wave propagation. Furthermore, the confinement of helium within such nanoscale systems alters the behavior of the normal and superfluid components, leading to the emergence of unique sound modes.
Theoretical studies, such as those by Adamenko and colleagues [103], have demonstrated that transverse sound can be observed in highly anisotropic systems like superfluid helium confined in carbon nanotubes. Their work suggests that differential motion between the normal and superfluid components creates the necessary conditions for transverse wave propagation, further validating the potential for observing these oscillations in nanoscale systems. This framework opens the possibility of experimental exploration of transverse oscillations in superfluid helium, offering new avenues for understanding the quantum fluid dynamics at the nanoscale.

Therefore, nanotube resonators present a novel avenue for investigating discrete damping mechanisms in superfluid ^{4}He stemming from various sound waves. In conclusion, a single vibrating nanotube could serve as a potent tool for detecting excitation dynamics across one-, two-, and three-dimensional superfluid systems, marking a significant advancement beyond the capabilities of current state-of-the-art nanomechanical probes.

3.3 Summary

We simulate the behavior of nanotube resonators inside superfluid helium ^{4}He, and realize their potential as nanomechanical probes for investigating quantum phenomena. The advantages of CNTs are highlighted, such as their high aspect ratio, impressive quality factor, and atomic resolution mass sensitivity. This chapter provides an analysis of hydrodynamic losses when a CNT resonator is submerged in liquid helium, pointing to the apparent mass enhancement and resonant frequency decrease due to Stokes' drag, along with a wide range of hydrodynamic damping over various frequencies and temperatures. We then examined vibration damping, mainly attributed to thermal and topological excitations within the superfluid ^{4}He, revealing the wider ballistic damping temperature range of CNTs compared to nanobeam resonators. Additionally, it sheds light on significant quasiparticle scattering losses in CNTs because of their low effective mass. Furthermore, the discussion extends to potential acoustic losses in CNT resonators, with minimal losses because of their smaller diameter. Dissipation mechanisms in various nanotube oscillators are presented, which indicates the optimal sensitivity in specific frequency ranges for nanotube resonator to study superfluids. Furthermore, we discuss the possibility to observe the transverse oscillation of superfluid inside CNTs, revealing their potential as one-dimensional capillary tubes for detecting sound waves characteristic of superfluid systems and discussing the unique behavior of superfluid helium under nanoscale confinement. Through detailed theoretical models, the chapter elucidates the interactions between CNT oscillators and the surrounding superfluid, which are crucial for understanding and interpreting the experimental observations.

Chapter 4: Nanotube growth and device characterization at room temperature

This chapter explains how we fabricate and characterize the CNT devices, particularly those with side gates in a transistor geometry and finger-gated pristine carbon nanotube devices. Starting with the basic steps of substrate preparation to fabricate electrical contacts, side-gates, and back-gate trenches, we navigate through the nanotube growth. We also describe the procedure of locating nanotubes using the scanning electron microscope (SEM) and discuss the challenges in developing metal stacks resilient to high-temperature CNT growth. Furthermore, we emphasize the significance of room temperature probing, offering insights into the potential performance of CNT devices in low-temperature environments.

4.1 Nanotube growth

Nanotube synthesis was initially done at Edward's previous lab in Oxford, specifically for the side-gated devices, which we will discuss in the next section. However, we did not continue using those devices for low-temperature measurements in both vacuum and superfluid environments. For our main measurements, we utilized finger-gated pristine nanotube devices grown in the Lancaster furnace.

Here is the Oxford furnace recipe:

- To grow nanotubes, start by flushing with Ar (2000 sccm), H_2 (1000 sccm), and CH_4 (1000 sccm).
- Heat the chemical vapour deposition (CVD) [104] furnace from room temperature to 950 °C using Ar at 200 sccm.
- Proceed with a 10-minute reduction using Ar (145 sccm) and H_2 (25 sccm).
- The growth phase lasts 30 minutes, utilizing H_2 (800 sccm) and CH_4 at rates of 220 sccm for the first chip and 240 sccm for the second—the latter producing more CNTs.
- After growth, conduct another 10-minute reduction with Ar (145 sccm) and H_2 (25 sccm).
- Finally, cool down from 950 °C to room temperature using Ar at 200 sccm.

4.1.1 Optimized nanotube recipe for Lancaster furnace

Our Lancaster CVD oven, capable of reaching 1200 °C, is equipped with a 26 mm diameter quartz tube. To enhance the control and reproducibility of the nanotube growth process, we integrated digital mass flow controllers to precisely regulate gas flow rates. Additionally, a gas handling system has been added to ensure both safety and stability throughout the growth process.

In this setup, we place a chip containing predefined W/Pt electrodes (details in the next section) inside the quartz tube. Here is the growth recipe for our on-chip ultra-clean nanotube devices:

- Start by flushing with Ar (1000 sccm), H_2 (1000 sccm), and CH_4 (1000 sccm).
- Heat the CVD furnace from room temperature to 830 °C in Ar at 1000 sccm.
- The nanotubes are grown for 10 minutes at 830 °C in 520 sccm CH_4 and 700 sccm H_2. Note: Initially, we conducted the growth at 900 °C. Subsequently, in each growth run, we gradually reduced the temperature of the CVD furnace to achieve a significant device yield without melting the electrodes.
- Cool down the furnace from 830 °C to 600 °C in Ar at 1000 sccm.
- Set the Ar flow rate to zero and open the furnace lid to speed up the cooling process. This is crucial when the growth is being done at predefined metal electrodes to prevent melting.

Through the optimization of various growth parameters, including catalyst composition, temperature, and gas flow rates, we have achieved a significant yield. Specifically, we observe a yield greater than 70% of single-wall CNTs with on-chip growth method. This CVD growth process is versatile, capable of producing CNTs on both flat SiO_2 substrates and predefined metal contacts and trenches.

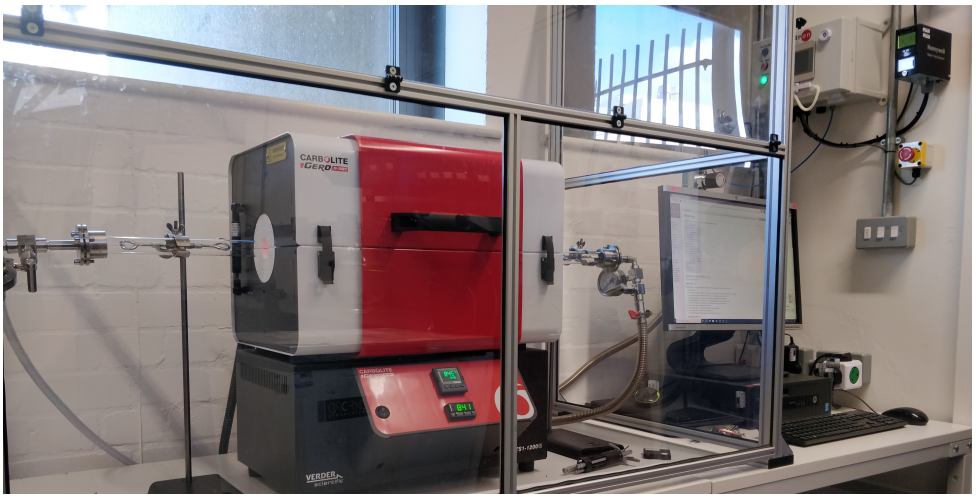

Figure 4.1: Our new furnace installed at Lancaster in December 2021.

4.2 Device fabrication

This section describes two fabrication methods. The first method involves side-gated nanotube devices, where nanotube growth is done in the initial steps and contact electrodes, trenches, and side gates are fabricated in subsequent steps. The second method provides finger-gated pristine devices, where nanotube growth occurs in the final fabrication step, and contact electrodes, trenches, finger, and global gates are fabricated initially.

The main advantage of the first fabrication method is the flexibility it offers in choosing metals for contact electrodes and gates. Since nanotube growth occurs early, there is no risk of electrode melting in the CVD furnace. However, this approach is time-consuming as it requires locating each nanotube in SEM (which may degrade nanotube quality) and aligning each SEM image in AutoCAD, as described in the next sections.

Conversely, our on-chip fabrication method restricts metal choice to high melting point metals to withstand the high temperatures during CVD growth. Nevertheless, this method yields pristine quality nanotube devices with significantly less effort.

4.2.1 Side-gated carbon nanotube devices

Here we describe the steps involved in the fabrication of nanotube resonators with side gates in the transistor geometry. This recipe is adapted from [105, 106] with some modifications.

Substrate preparation

Clean a Si/SiO_2 wafer using acetone, isopropyl alcohol, and deionized water. Dry with a nitrogen blower.

Alignment markers

Use electron beam lithography (EBL) to pattern markers on the substrate. Deposit a Cr/Au (5 nm/25 nm) layer using thermal evaporation as a reference for EBL and photolithography (PL) alignment.

Catalyst pads and deposition

Then spin coat a double-layer of e-beam resist (MMA-EL6 and PMMA-A2) onto the substrate. The recipe is as follows:

- Spin MMA at 2000 rpm for 60 seconds.
- Bake for 3 minutes at 200 °C.
- Spin PMMA at 7000 rpm for 60 seconds.
- Bake for 3 minutes at 200 °C.

After that, pattern $2 \times 2\,\mu m^2$ squares using EBL for catalyst pads. Prepare a catalyst mixture of 25 mg $Fe(NO_3)_3 \cdot 9\,H_2O$, 5.65 mg $MoO_2(acac)_2$, and 18.75 mg alumina nanoparticles in 50 mL methanol. Apply using a PMMA mask and bake for 10 minutes at 150 °C.

To ensure precise catalyst placement and minimize unintended spread on SiO_2 surfaces, a two-step lift-off process is essential. First, quickly immerse the sample in warm acetone

with a sonicator. Then, move the wet sample to another acetone beaker and leave it for 5 minutes. After that, nanotube growth is done as described in Sec. 4.1.

4.2.1.1 Locating nanotubes via SEM

We employ the SEM for identifying nanotube positions. However, prolonged exposure to SEM can degrade the quality of nanotubes. The high-energy secondary electrons produced during SEM scans can displace or knock out electrons from the carbon atoms in the nanotube lattice, leading to defects. These defects can result in poor electrical conductivity or, in severe cases, a complete loss of conductance in the nanotubes.

Secondary electron interactions may also trigger chemical reactions, particularly in the presence of residual gases such as water vapor or oxygen in the SEM chamber. These reactions can etch the nanotube structure, especially the outer shells, as shown by Mølhave et al. [107]. This damage can alter the carbon-carbon bonds, leading to disordered structures that scatter charge carriers, significantly impacting the nanotube's electronic properties.

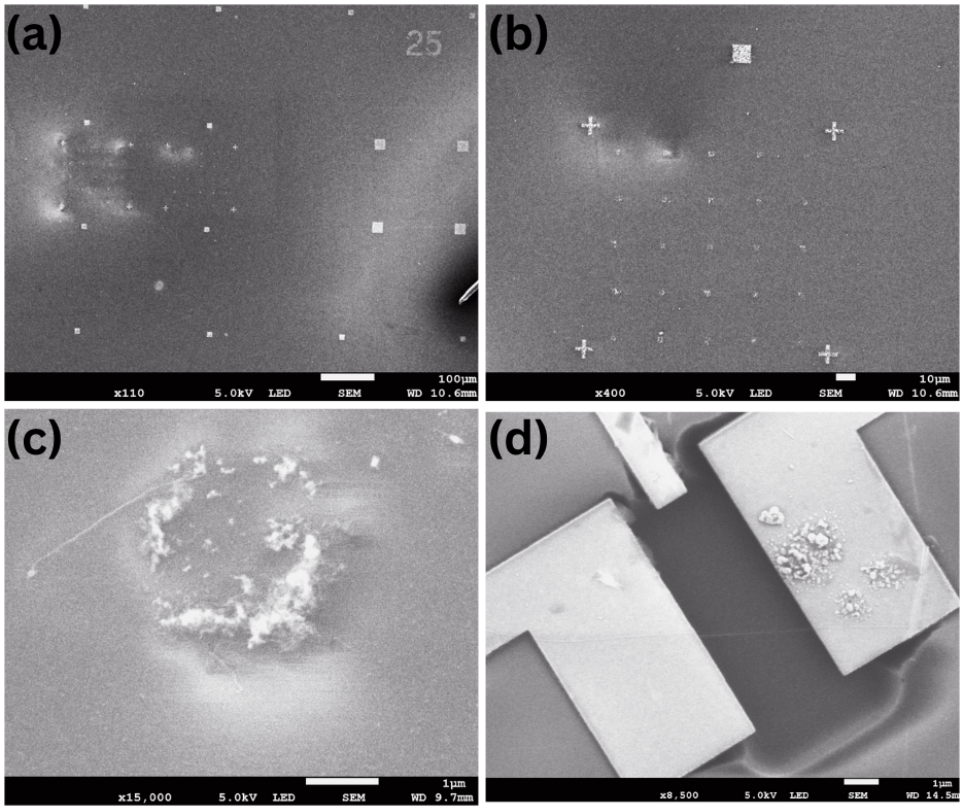

Figure 4.2: (a)-(c) Imaging CNTs in SEM to align and write the contact electrodes. (d) Final side-gated suspended CNT device after CPD drying.

To minimize these effects during SEM imaging:

- Use the In-Lens detector with a voltage between 3 kV to 5 kV, as lower voltage reduces the likelihood of damaging the nanotubes.
- Keep the working distance at approximately 10 mm to maintain a good resolution without excessive electron bombardment.

- Minimize time spent at high magnification directly on the nanotubes. Instead, first focus and adjust on an alignment mark in the device area, then capture an image covering all corner alignment marks.

Image at a resolution of 100 µm and use frame averaging to check for stage drift. Post-imaging, import the image into AutoCAD and align the software pattern with the image. This method reliably yielded an alignment precision of about 100 nm within our 100 µm scans, enabling accurate targeting of nanotubes while minimizing exposure to damaging electron beams.

For device integration, we prefer straight, elongated nanotubes, prioritizing straightness to ensure optimal device performance.

Contact electrodes and side gates with EBL

Clean the nanotube chip using standard solvents, avoiding sonication to preserve nanotubes on the substrate. Prepare PMMA (A2) and bake for 3 minutes. For nanofabrication with the Raith EBPB5200, use a beam current of 100 pA, wafer size of 2 inch, dot count of 100×10^6, and a dwell time of 10 ns for small features.

Develop by immersing the sample in a 1:3 MIBK to IPA solution for 60 seconds. Rinse with IPA and dry with nitrogen. This enhances contrast between exposed and unexposed areas. After that, deposit 5 nm/25 nm of Cr/Au using thermal evaporation.

Bondpads with PL

Spin-coat double-layer photoresist on the substrate. The recipe is as follows:

- Spin LOR-3A at 4000 rpm for 60 seconds.
- Bake for 5 minutes at 180 °C.
- Spin S1813 at 4000 rpm for 60 seconds.
- Bake for 2 minutes at 115 °C.

Then, pattern using photolithography with 2.6 seconds soft contact. Deposit a Cr/Au (10 nm/80 nm) layer using thermal evaporation.

4.2.1.2 Nanotube trenches with HF etching and CPD

To create suspended carbon nanotube devices, the substrate between the electrodes is etched, ensuring the nanotube remains free from liquid-gas interfaces through critical point drying (CPD). E-beam resist layers EL6 and PMMA are applied, and $2 \times 5\,\mu m^2$ rectangles are patterned using EBL between the electrodes to define etching areas. For Si/SiO_2 substrates, a diluted (10:1) buffered hydrofluoric acid (BHF) is the etchant of choice, with etching guided by an EBL-patterned resist mask. We left the sample for 21 minutes to etch away 1.2 µm thick oxide layer. After BHF etching, the hydrophobic sample is kept submerged during transition from BHF to water rinse and methanol CPD to prevent water bead damage.

To ensure continuous immersion of the samples in a liquid medium until reaching the critical point during flushing, it is essential to maintain a consistent level of CO_2 in the CPD chamber. Additionally, for effective prevention of dust or impurities adhering to the sample during the drying process, it is recommended to position the chip upside down.

4.2.2 Finger-gated pristine carbon nanotube devices

This method outlines the process for fabricating back-gate and local finger-gate devices. In this approach, the nanotube growth is performed as the final step, resulting in 'as-grown' pristine nanotube devices.

4.2.2.1 Metal stacks for high temperature CNT growth

To fabricate suspended devices that incorporate on-chip CNT growth in the final step, we developed a method for creating metal stacks that can withstand the high temperatures of CVD used for nanotube synthesis. Achieving this compatibility is crucial, given the inherent challenges. Many metal combinations tend to form eutectic alloys, which results in the entire stack having a melting point lower than that of its individual components[108]. Moreover, certain metals might inadvertently promote nanotube growth during the CVD process. We illustrate these phenomena with four distinct cases in Figure 4.3.

Specifically, when we introduced a thin layer of titanium (Ti) of 5 nm into the stack, it caused platinum (Pt) to melt and agglomerate, as shown in Figure 4.3(a). Incorporating a significant 20 nm layer of chromium (Cr) caused the material to permeate through both the chromium and platinum layers, as depicted in Figure 4.3(b). Interestingly, a thicker layer of tungsten (W) at 60 nm gave rise to an unusual nanowire formation, as presented in Figure 4.3(c). However, a combination of 40 nm of W and 160 nm of Pt proved to be more effective than the other stacks. A minor issue of melting was observed at 900 °C (Figure 4.3(d)), which was subsequently addressed by moderating the growth temperature.

The following fabrication steps are involved in preparing the ultra-clean nanotube devices:

Substrate cleaning

Prepare a Si/SiO_2 wafer using acetone, isopropyl alcohol, and deionized water. Dry with a nitrogen blower.

Alignment markers

Once the wafer is clean, E-beam lithography (EBL) is used to pattern the markers on the substrate. Then, a layer of W/Pt (5 nm/25 nm) is deposited onto the substrate using E-beam evaporation as a reference for EBL and PL alignment layers.

Back-gate with PL and HF etching

A double-layer of photoresist is spin-coated onto the substrate and $2 \times 5\,\mu m^2$ rectangles are patterned using the PL to create the back-gate contacts. Employ wet etching with HF to etch back-gate contacts into the substrate. Again, the etchant is a diluted (10:1) solution of BHF. Once the oxide layer is etched away, deposit another W/Pt layer (40 nm/160 nm) to wire-bond the back-gate from the upside of the substrate.

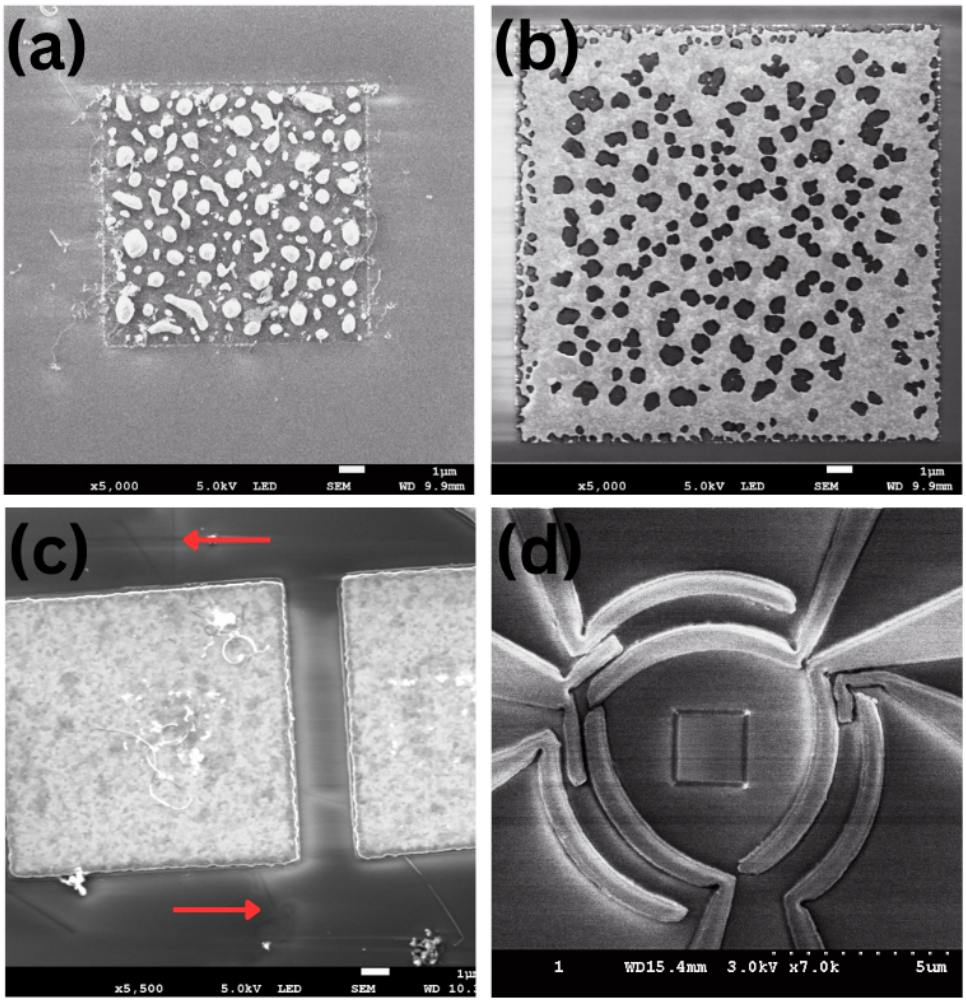

Figure 4.3: Illustration of various metal stacks' behavior under high-temperature CVD. (a) 5 nm/25 nm Ti/Pt: 5 nm Ti causing Pt agglomeration, (b) 20 nm/150 nm Cr/Pt: 20 nm Cr permeating through Cr and Pt layers, (c) 60 nm/160 nm W/Pt: 60 nm W leading to nanowire formation, and (d) 40 nm/160 nm W/Pt: This shows a slight melting at 900 °C.

Finger gates with EBL

Apply PMMA electron-beam resist to the wafer and then expose the resist to an electron beam to pattern desired structures. Develop the resist to reveal the patterns. Finally, deposit a W/Pt layer (5 nm/20 nm) through sputtering.

Contact Electrodes with EBL

To fabricate the contact electrodes, first spin-coat the EBL resist and pattern the electrodes using a beam current of 100 pA. After developing the resist, deposit the contact metals for the CNTs.

It is standard practice to use tungsten (W) and platinum (Pt) as contact metals for as-grown carbon nanotubes, due to their favorable properties in such applications [109, 106]. The goal here is to avoid the need for substrate etching, which can be achieved by depositing thicker layers of W and Pt. However, this approach has a notable drawback: thicker metal layers are less durable when exposed to high temperatures during nanotube growth.

A practical solution is to reduce the operating temperature in the furnace from 900 °C to 830 °C. This reduction allows the use of thinner metal layers, which in turn promotes smoother nanotube growth while maintaining the desired trench aspect ratio. Additionally, operating at a lower temperature mitigates the issue of excessive multi-walled nanotube growth, which can occur with thicker W layers. Such growth, when the nanotubes exceed the spacing between contacts, often leads to electrical shorts.

Through extensive testing, a W layer thickness of 40 nm was found to be optimal. This thickness stabilizes the Pt layer without significantly increasing the occurrence of unwanted multi-walled nanotubes.

Bond pads with PL

In order to write the bond pads for wire-bonding the devices, spin-coat double-layer photoresist on the substrate as per the previously mentioned recipe. After patterning the design, a fourth layer of W/Pt (40 nm/160 nm) is then deposited onto the substrate using sputtering.

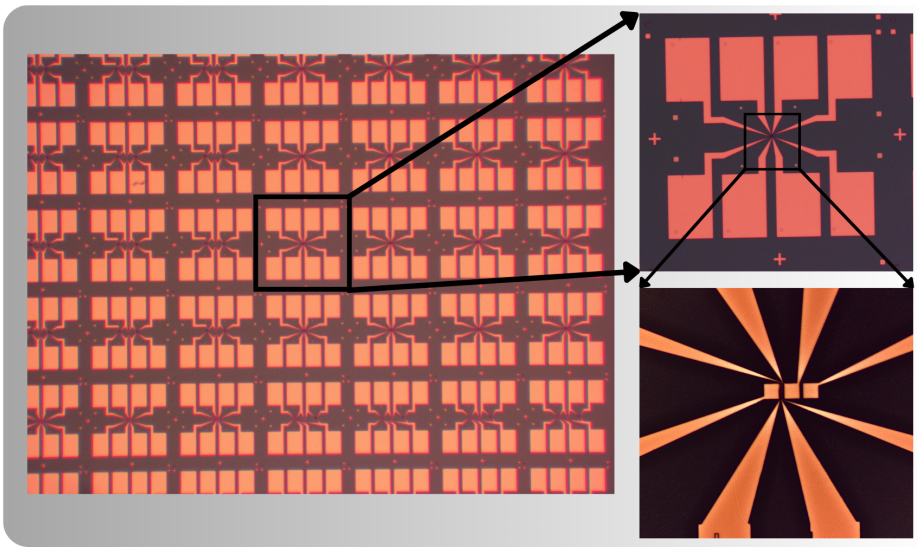

Figure 4.4: An optical image of the silicon chip with bond pads and nanotube contact electrodes.

Catalyst pads with EBL

Another layer of PMMA resist is spin-coated onto the substrate and $4 \times 4\,\mu m^2$ squares are patterned using EBL on top of the W/Pt source and drain electrodes.

Catalyst deposition and nanotube growth

We have slightly modified the recipe for the nanotube catalyst, which is adapted from Ref. [104].

Catalyst compositions:

- 20.2 mg of $Fe(NO_3)_3 \cdot 9\,H_2O$
- 4.89 mg of $MoO_2(acac)_2$

- 15 mg of Al_2O_3 nanoparticles
- 15 mL of H_2O, as suggested in [106]

Procedure:

- Stir the mixture for more than 3 hours.
- Sonicate for 1 hour. The resulting mixture should be deep orange or red in color.
- Develop the desired pattern.
- Apply the catalyst to the pattern.
- Blow off the excess using N_2.
- Spray the chip with an acetone bottle. Ensure not to spray into this bottle.
- Immerse in acetone for 20 minutes.
- Rinse with IPA.
- Nanotube growth can be done either immediately or later using the recipe described in subsection 4.1.1.

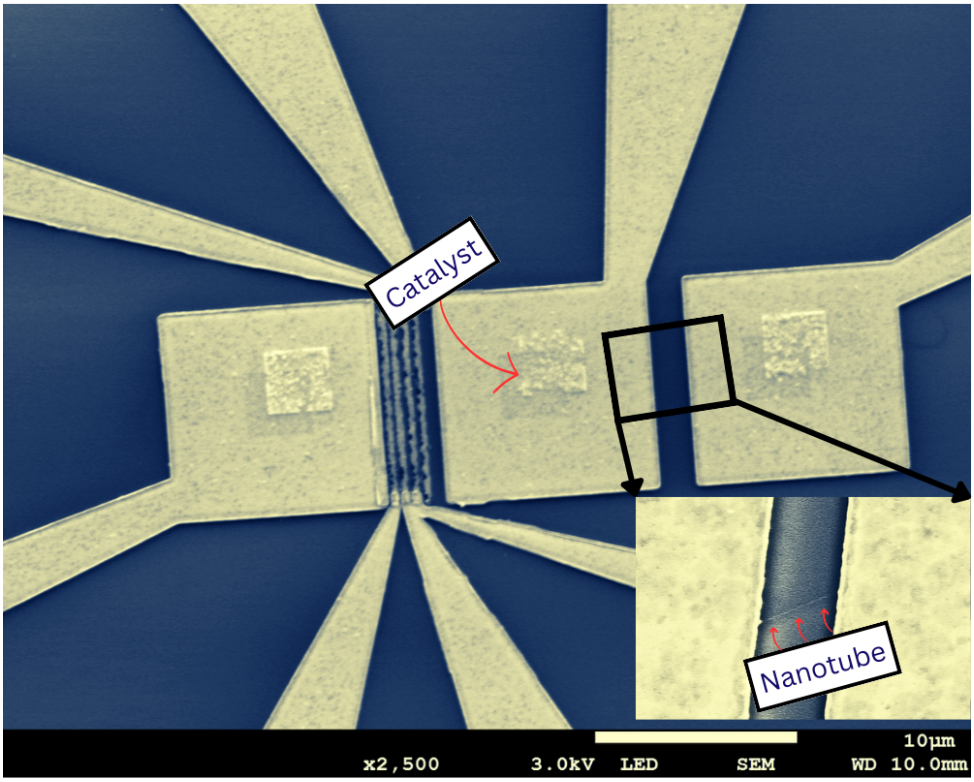

Figure 4.5: An SEM image of a CNT device with on-chip and a nanotube in the inset. This image illustrates a carbon nanotube suspended across three W/Pt contacts, with Pt positioned on top. This configuration serves the purpose of creating one back-gated and the other with local multiple quantum dot devices, either utilizing the same nanotube or different ones depending on the natural growth. The central square area is composed of Fe/Mo catalyst particles on top of the contact electrodes.

4.3 Room temperature probing

Not all types of CNT devices are suitable for low-temperature measurements. After the growth, CNTs are evaluated at room temperature using our probestation[110]. This initial assessment is crucial for several reasons:

- It aids in estimating the band gap and the contact resistance of the nanotubes.
- A preliminary understanding of whether a CNT behaves like a metal with a tiny electrical gap or a semiconductor can be established.
- The connectivity quality between the CNT and the metal contacts can be discerned.
- And also important: most devices do not have a nanotube between the electrodes at all.

The behavior of a CNT device at room temperature can provide insights into its performance at very low temperatures, although making precise predictions based on these initial tests can be challenging. Devices displaying smooth transistor-like characteristics, efficient electrical flow, and specific measurement near zero gate voltage during these tests are often indicative of their good performance at very low temperatures.

It is noteworthy that nanotubes with smaller band gaps are preferred for few-electron quantum dots, showing conductance $8\,\mu A\,V^{-1}$ at room temperature. In contrast, nanotubes with larger band gaps require a conductance level greater than this to ensure a measurable current near the band gap.

For a visual understanding, refer to Figure 4.6 for typical bias and back-gate sweeps. In particular, Figure 4.6(b) highlights the behavior of a nanotube with a small band gap.

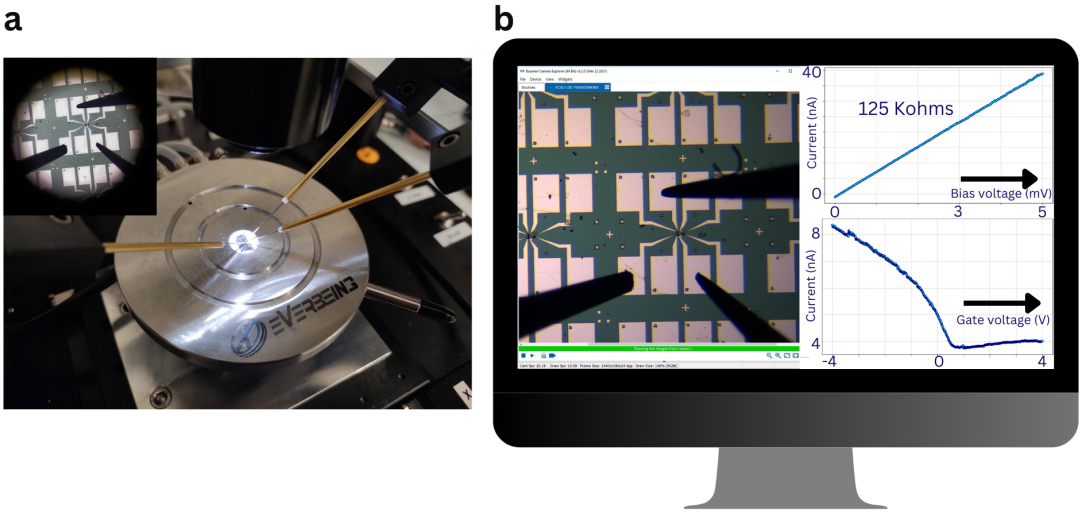

Figure 4.6: (a) Our automatic probestation picture while scanning a CNT chip. (b) Room temperature measurement post nanotube growth, aiding in the selection of ideal devices for low temperature evaluations.

4.4 Summary

This chapter discusses the fabrication, characterization, and initial evaluation of our CNT devices with a focus on side-gated and finger-gated configurations.

Device Fabrication:

Fabrication methods discussed include side-gated and finger-gated devices. The former offers flexibility in metal choice but requires time-consuming SEM alignment. The latter restricts metal choice due to CVD growth temperatures but yields pristine devices with less effort.

Nanotube Growth:

We initially experimented with nanotube synthesis at Edward's previous lab in Oxford, utilizing side-gated devices. However, for our main measurements, we switched to finger-gated pristine nanotube devices grown in the Lancaster furnace. We detail the growth recipes for both the Oxford and Lancaster setups, optimizing parameters such as gas flow rates and temperatures to achieve significant yield (with up to 70% of the time a nanotube is found between the contact electrodes) and high-quality nanotubes.

Room Temperature Probing:

Room temperature probing is conducted post-growth to evaluate device characteristics such as band gap, contact resistance, and electrical flow. Devices displaying transistor-like behavior and efficient electrical flow are preferred for subsequent low-temperature measurements.

Chapter 5: ^{4}He cell design and measurement setup

This chapter discusses the design and construction of a specialized ^{4}He cell, specifically made for submerging nanotubes in superfluid ^{4}He. We also made a ^{4}He gas handling system to integrate with the Triton dilution refrigerator. We further elucidate the measurement techniques used, including the capacitive driving approach for actuating the nanotube motion and the frequency modulation method for resonance detection. Overall, this chapter aims to provide readers with a thorough understanding of the experimental setup, underlining its design logic and operational aspects.

5.1 ^{4}He cell design

The design of a specialized experimental cell ensures the immersion of carbon nanotubes in superfluid ^{4}He. This cell is designed to be superleak-tight and customized to the unique requirements of this experiment. The cell comprises a bottom flange integrated with feedthroughs, a top flange housing capillaries and a cooling sinter, and a clamp that securely joins the two flanges.

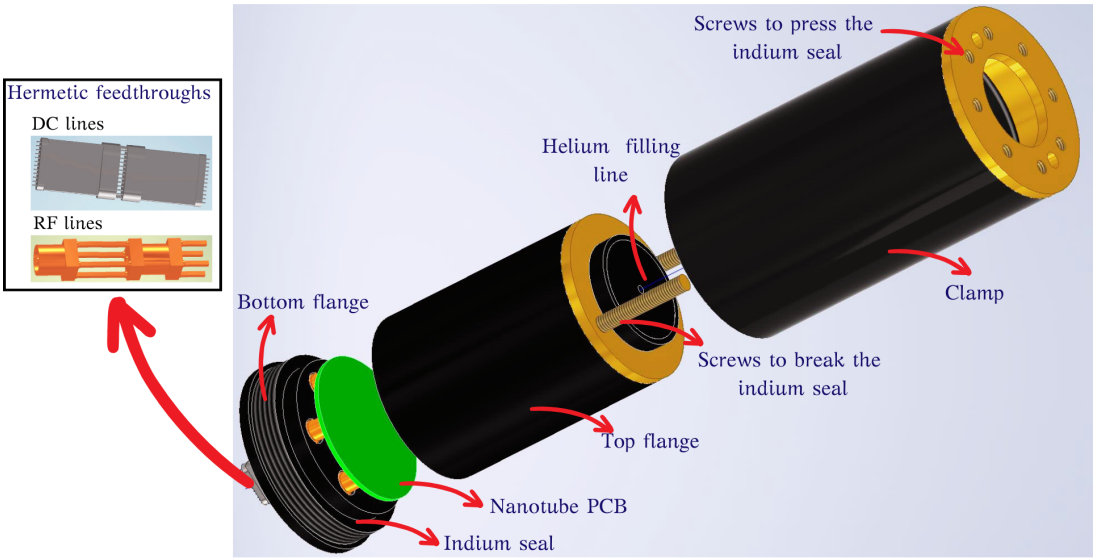

Figure 5.1: The ^{4}He cell assembly illustrating hermetic DC and RF electrical feedthroughs.

5.1.1 Bottom flange

The bottom flange, with a diameter of 27 mm, serves as the foundation of the helium cell. It houses the electrical feedthroughs, provides a mount for the PCB, and incorporates a space for an indium seal to ensure leak-proof integrity.

5.1.1.1 RF feedthroughs

The bottom flange contains six custom-made RF feedthroughs arranged in a circular pattern. The creation of these feedthroughs involves soldering two MMCX connectors back-to-back. The void between the connectors is then sealed using a two-step Clear Stycast process, ensuring a hermetic connection [111]. This construction is robust, and their fabrication is relatively quick compared to other components.
The feedthroughs are specified by the manufacturer to perform up to 6 GHz. In our experimental setup, we have used them to successfully transmit signals in the 500 MHz range. Furthermore, the feedthroughs have undergone thermal cycling three times without any observable leaks or degradation in performance. This indicates their reliability in cryogenic conditions and their suitability for repeated use.

5.1.1.2 DC feedthroughs

The central feature of the bottom flange is a DC feedthrough that offers 24 DC connections. Given the cell's compact design, utilizing a D-sub connector was not feasible. Meanwhile, Nano-D connectors, although suitable, are quite expensive and have extended lead times. Consequently, we opted for USB-C connectors due to their accessibility, smaller size, and cost-effectiveness relative to Nano-D connectors.
Constructing feedthroughs using USB-C connectors was challenging due to the precision required in soldering. The small connector pins necessitated the use of a microscope for accuracy. However, with experience and improved techniques, the soldering became more efficient and simpler to execute.

After several attempts, we successfully soldered several USB-C pairs. To ensure their hermetic nature, we again employed a two-step Stycast process. Subsequent testing within a glass cryostat at 1.5 K in superfluid ^{4}He validated their superleak-tight properties, marking their use as hermetic connectors.

5.1.1.3 Hermetic sealing

Hermetic sealing with Stycast involves a careful process to ensure a reliable seal. Initially, clear Stycast 1266 is prepared by mixing 2 g of epoxy resin with 21 drops of catalyst. The mixture is then degassed to eliminate air bubbles, typically achieved by vacuum pumping.

Once properly prepared, the Stycast is carefully applied to cover the pins of back-to-back soldered USB-C and MMCX connectors (see Fig. 5.2(a) and (b)) to create electrical hermetic feedthroughs. After curing the Stycast on these feedthroughs, they are mounted onto the bottom flange and again glued with Stycast, as shown in Fig. 5.2(e).

5.1.1.4 PCB integration and indium seal

The inner (helium) side of the bottom flange accommodates a PCB for the CNT chip, ensuring effective interfacing with the feedthroughs on the bottom flange (see Fig. 5.2(c)).

Additionally, a ring structure is incorporated along the edge of this bottom flange to place a thin indium wire (0.5 mm), taking advantage of indium's excellent sealing properties at cryogenic temperatures [112].

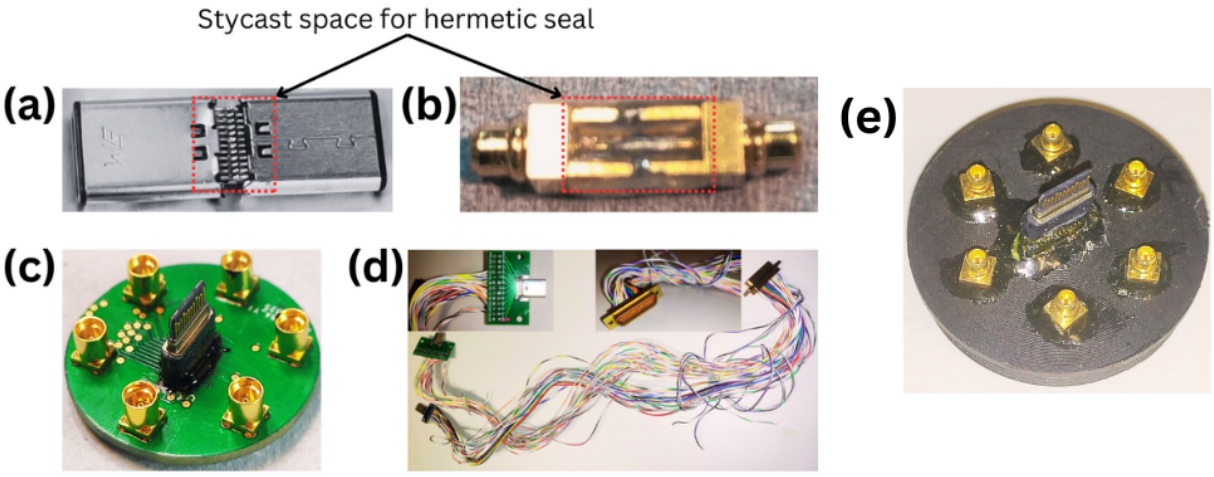

Figure 5.2: (a) DC feedthrough created with 24 lines by soldering the pins of two USB-Cs. (b) RF feedthrough made by joining two MMCX connectors. (c) The nanotube PCB with 6 MMCX connectors and a central USB-C for interfacing with the bottom flange. This allows the electrical drive and measurement of CNT motion in a superfluid bath. (d) An adaptor designed to link a 51-way D-sub connector inside the Triton fridge to the USB-C connector on the bottom flange exterior. (e) Bottom flange with RF and DC feedthroughs glued with Stycast.

5.1.2 Top flange

The top flange encapsulates the cell and is fitted with capillaries for helium introduction and a sinter for gas cooling.

5.1.2.1 Sinter

The top flange incorporates a sinter, a key component for cooling the helium gas within the cell. This sinter is connected to two silver wires emerging from the upper section of the top flange and is thermally anchored to the mixing chamber plate for effective cooling.

To fabricate this sinter:

1. Two silver wires were spot-welded onto a thin, circular silver plate, as shown in Fig. 5.3(a).
2. The assembly was annealed at 1000 °C in a controlled air environment for 10 hours. This process purifies the assembly and minimizes Kapitza resistance [113].
3. 3 g of silver powder was evenly distributed on both sides of the silver plate to achieve a 50% packing fraction.
4. The assembly underwent a compression force of approximately 2 tons.
5. To solidify the structure while ensuring it remained porous enough for superfluid passage, the sinter was heated on a hot plate at 70 °C in a nitrogen atmosphere for 20 minutes.

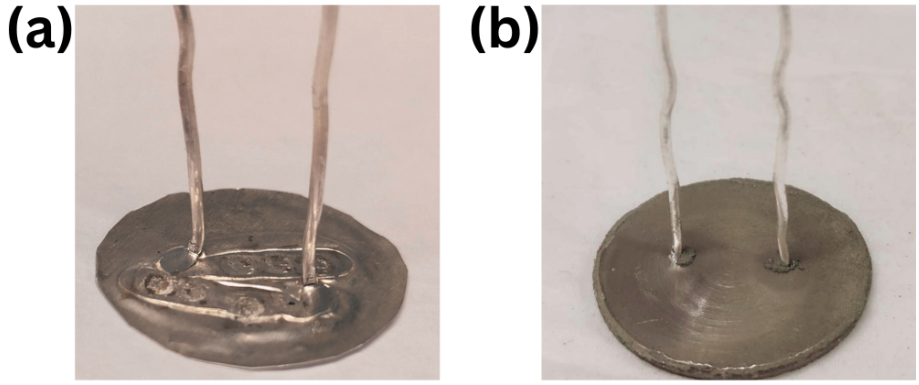

Figure 5.3: (a) A thin circular silver plate with two point-welded silver wires. (b) The completed sinter, after silver powder application and heat treatment in a nitrogen atmosphere.

5.1.2.2 Capillaries and a clamp

Two capillaries on the top flange connect to the refrigerator's fill lines, which are made of thick-walled Cu−Ni tubes, allowing ^{4}He injection into the cell.
The cell's integrity is maintained by a clamp that joins the top and bottom flanges. This clamp applies pressure on the indium through eight screws on its top, ensuring a superleak-tight seal between the top and bottom flanges.

5.2 PCB design and electronics for nanotube mechanics

The printed circuit board (PCB) designed for CNT mechanics is optimized for compactness and efficiency. It allows the measurement of up to five devices simultaneously using the DC detection technique and three devices when employing the RF measurement scheme.

This PCB incorporates two 24-pin USB-C connectors. One serves the purpose of providing the DC signal to the nanotube, while the other ensures grounding of the CNT during the wirebonding process. Additionally, the board contains six MMCX connectors, designated for supplying the RF signal to actuate the CNT motion. Notably, half of these RF connections are integrated with bias-tees on the PCB. This allows for the simultaneous application of both DC and RF gate signals to a single nanotube electrode, each being applied from a separate source.
Furthermore, the PCB is equipped with three impedance matching tank circuits, aimed at mitigating parasitic capacitances and enhancing the sensitivity of the nanotube signals. For an in-depth understanding of these circuits, refer to [114]. However, the results presented in this thesis only employ the DC detection technique, bypassing the use of the tank circuit. Hence, these circuits are not elaborated upon in this context.

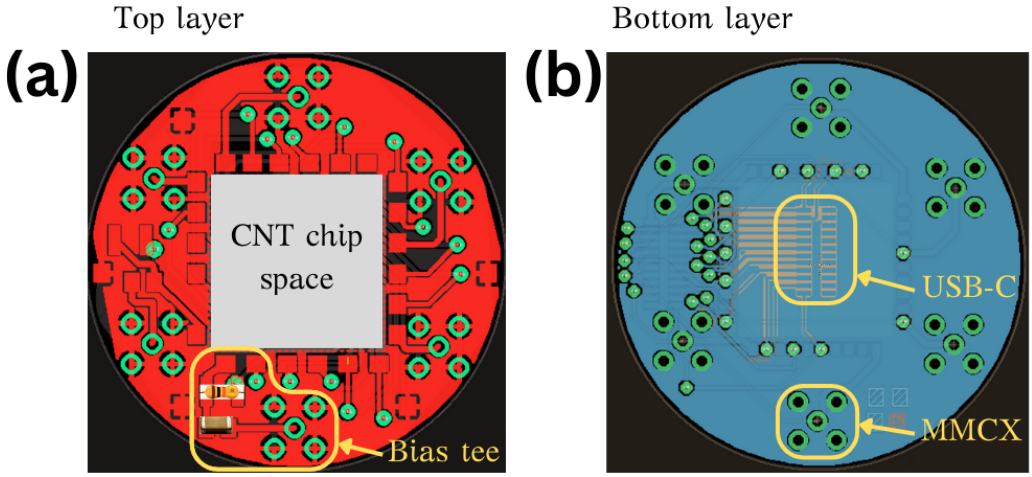

Figure 5.4: (a) The top layer of the CNT PCB, highlighting the integrated bias-tees footprint alongside the chip space with bonding pads. (b) The bottom layer of the CNT PCB, showing the 24-pin USB-C connector and RF MMCX connector footprints.

5.2.1 Grounding and wirebonding of CNT resonators

Suspended CNT devices present unique challenges during handling and wirebonding due to their mechanical and electrical fragility. It is essential to ensure that both the CNT resonator and the handler are continuously grounded to prevent potential damage.

During the wirebonding process, multiple devices can be bonded onto a single PCB. However, if the PCB pad connections or the wirebonder stage lack proper grounding, the majority of these devices may fail post-bonding. To address this, we developed a USB-C adapter in which all 24 pins are interconnected using a single copper wire, as depicted in Fig. 5.5(b). This adapter plugs into a female USB-C port on the bottom side of the PCB. The copper wire then establishes a connection to the primary ground via the wirebonder stage. This arrangement, shown in Fig. 5.5(a), is concealed between the PCB and its holder, making it invisible to the observer. To further ensure the efficiency of the wirebonding process, we minimized the placement of electrical components on the PCB's top layer, leaving only the nanotube chip. This prevents the bonder tip from becoming trapped, which could complicate the wirebonding process.

Despite adequate electrical grounding, some devices may not exhibit any current post-bonding, especially if more than two bonding attempts are made on the same CNT. This suggests that mechanical vibrations, possibly from the ultrasonic waves used during wirebonding, can degrade the contact between the CNT and the Pt electrodes. This degradation can increase the electrical resistance to the point where it becomes challenging to measure any current. Therefore, successful wirebonding of CNT devices hinges on both a robust grounding setup and sufficient hands-on practice prior to working on the main chip.

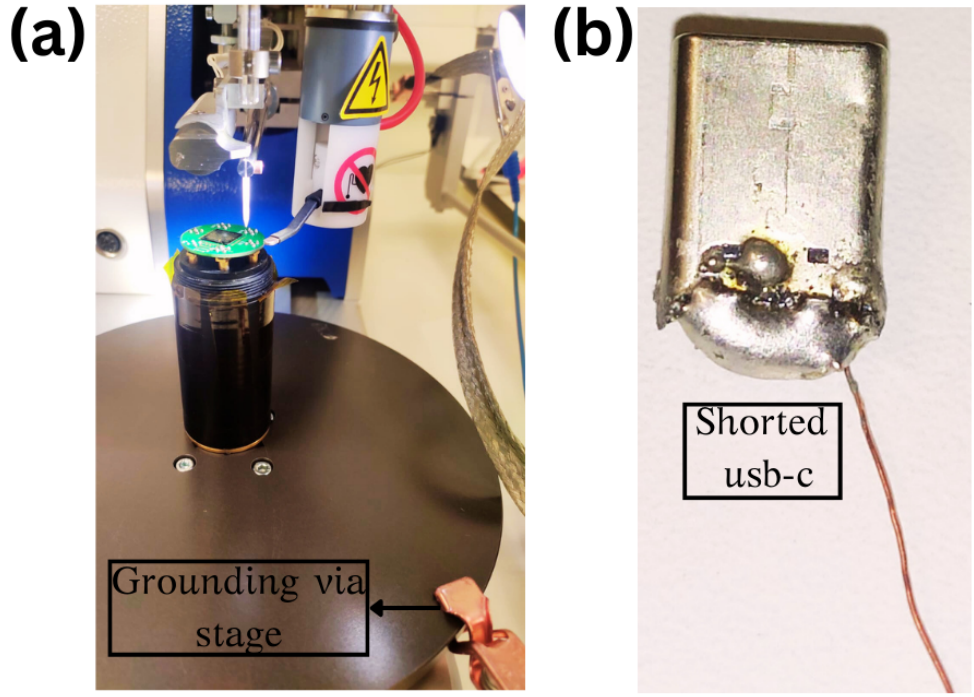

Figure 5.5: (a) Representation of the CNT chip and PCB placed on a holder during the wirebonding process, highlighting the grounding set-up. (b) The USB-C connector, shorted to ensure consistent grounding of all the bonding pads on the PCB, aiding in the protection and efficiency of the wirebonding procedure for delicate CNT devices.

5.3 Fill lines and ^{4}He gas handling panel integration in Triton dilution refrigerator

Efficient management of ^{4}He gas is critical for sustaining a superfluid environment within the experimental cell [115]. In this section, we detail the design and function of the fill lines and the ^{4}He gas handling system, both incorporated into our Triton dilution refrigerator.

The fill lines are essential as they introduce ^{4}He gas into the cell, while also providing precise control over its pressure and volume. Additionally, the ^{4}He gas handling system is designed to ensure the purity and stability of the gas environment.

5.3.1 Cu−Ni tubes for ^{4}He gas filling

For effective ^{4}He gas filling, we integrated two thick-walled capillary lines, each 1 mm in outer diameter and 0.65 mm inner diameter, extending from the dilution refrigerator's top plate (see the inset of Fig. 5.8) at room temperature down to the mixing chamber plate at 7 mK. The following details the steps involved in this process:

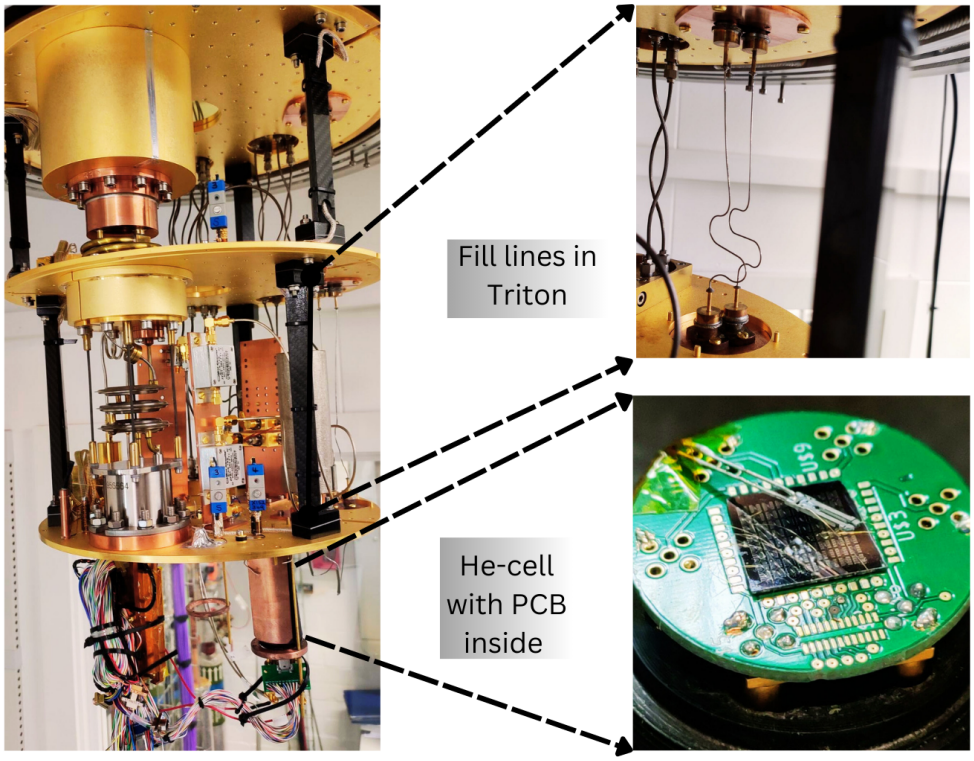

Figure 5.6: Helium cell mounted below the MC plate inside the Triton fridge and connected to the filling lines through a tee-junction.

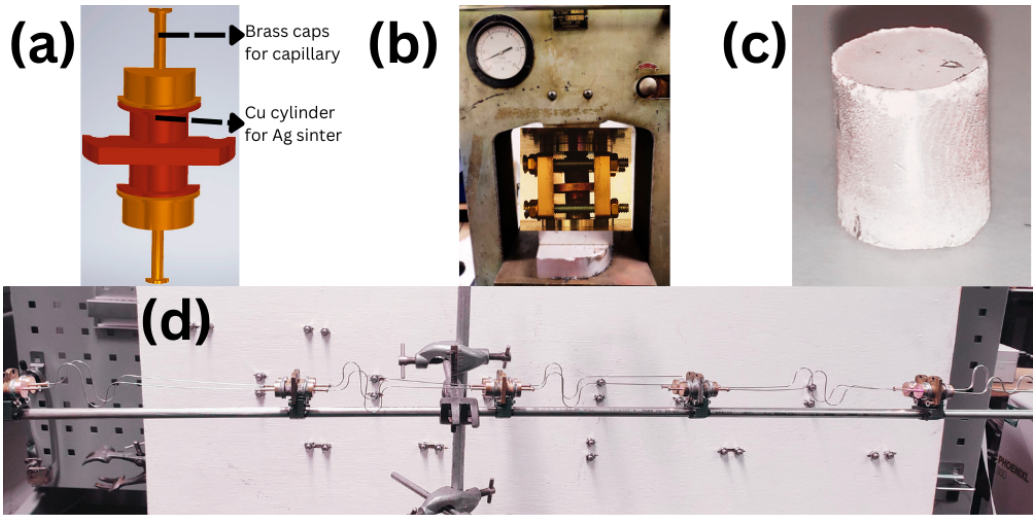

Figure 5.7: (a) This illustrates an individual sinter assembly designed to thermalize each temperature stage of the fridge. (b) The sinter process involves pressing silver powder under two tons of pressure inside the sinter assembly, forming a semi-solid heat exchanger with micropores. (c) Here is a damaged sinter, detached from the copper cylinder walls due to excessive heating during soldering. (d) This depicts the final leak-tight insert, ready for fridge installation, after soldering the Cu−Ni tubes to the sinter assembly for the five different temperature stages of the cryostat.

- The initial step involves creating an efficient sinter design as depicted in Fig. 5.7(a). The central portion of the sinter, filled with semi-solid silver powder, is constructed

from copper to optimize thermal transfer between the hot helium gas and the dilution refrigerator's cold plates. The end caps, made of brass, allow for easier soldering to the Cu–Ni tubes, ensuring the silver sinter remains intact.

- For the creation of the silver sinters, we begin by calculating the required silver powder quantity for a 50% packing fraction (taken from the current recipe in our lab) within the copper cylinder. The mass m of the silver powder needed is determined by $m = \rho \times V$, where $\rho = 10.47\,\mathrm{g/cm^3}$ represents silver's density and V is the cylinder's volume. Given a cylinder height $h = 9\,\mathrm{mm}$ and base diameter $d = 8\,\mathrm{mm}$. The mass of the required silver is then:

$$m = \rho \times \pi \left(\frac{d}{2}\right)^2 \times h \times \text{packing fraction} = 2.37\,\mathrm{g} \tag{5.1}$$

- With 2.37 g of silver powder loaded into the copper cylinder which is then placed in a pressing machine, as depicted in Fig. 5.7(b), and subjected to approximately 2 tons of pressure. We optimize the recipe to ensure the silver remains semi-solid without disintegrating back into the powder.

- Subsequently, the assembled sinter is heated on a hot plate at 70 °C in a nitrogen atmosphere for 20 minutes. Upon cooling, the sinter should adhere to the copper cylinder's inner walls without any powder residue.

- The next step is to flame-solder the brass caps to both ends of the copper cylinder. Care is taken to prevent overheating of the copper, as this could compromise the sinter's integrity. We produce multiple sinters to account for potential damage during the soldering process. Leak tests are performed after soldering each joint to ensure leak-tightness before installation into the cryostat. For the leak testing of individual sinters, we use an adapter to connect the sinter assembly directly to the leak detector.

- Finally, Cu–Ni tubes are soldered atop the brass caps. After each soldering step, leak tests are performed to guarantee the integrity of each joint. The completed two fill lines, suitable for all five temperature stages of the refrigerator, are shown in Fig. 5.7(d) and ready for mounting inside the fridge.

5.3.2 Gas handling system

The ^{4}He gas handling system, depicted in Fig. 5.8, comprises five inlets: a helium gas injection line, two inlets associated with liquid nitrogen traps, a pumping line, and an inlet for a pressure bomb. The system utilizes Swagelok connectors with the exception of the stainless steel valves, bought from Parker. A quarter-inch diameter tube has been implemented both on the panel and outside the fridge, allowing faster pumping speeds. After tightening each Swagelok joint, leak tests are conducted to check for potential leaks.

Two channels extend from the panel to the fridge's top, connecting to the Cu-Ni tube lines within the fridge via feedthroughs on its top plate (inset in Fig. 5.8). Both lines on the panel are equipped with a separate pressure gauge to monitor the pressure. A bypass valve is placed between the traps, enabling system operation without engaging the nitrogen traps, especially when utilizing purified helium directly from the dewar.

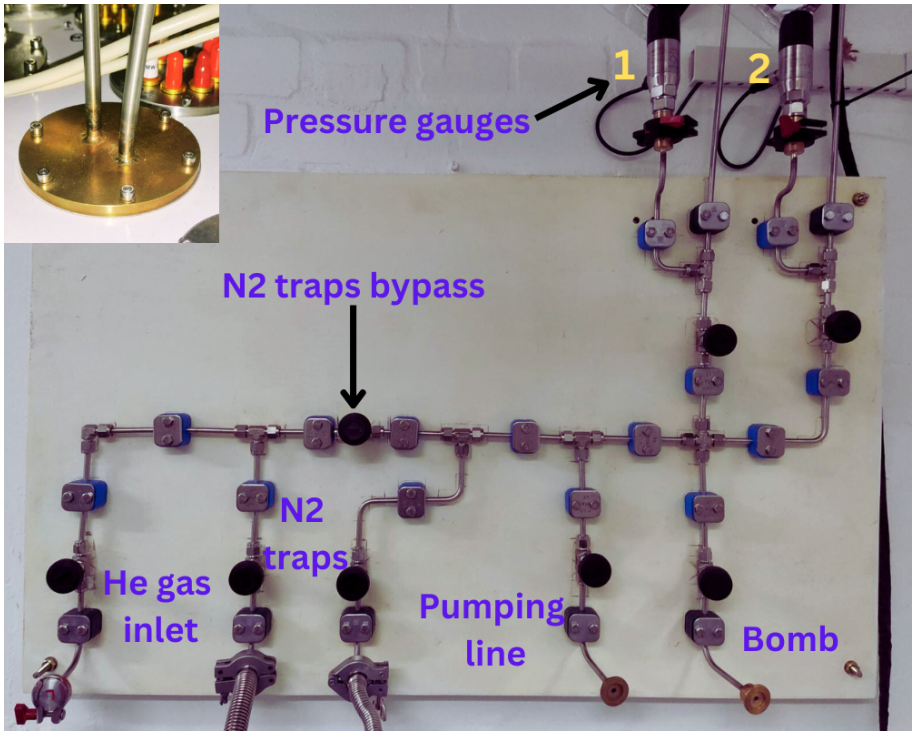

Figure 5.8: ^{4}He gas handling panel connected to the fridge's top plate through two quarter-inch tubes, as shown in inset. The inset shows the feedthrough on the fridge's room temperature top plate connects the gas handling system lines to the Cu–Ni gas lines within the fridge.

To slowly fill the ^{4}He gas into the experimental cell, starting from the ^{4}He inlet line on the panel at room temperature and down to the mixing chamber plate at 7 mK, we use the first capillary while keeping the second capillary closed. These capillaries are connected at a tee-junction below the mixing chamber and lead to the cell, which contains a nanotube chip. Typically, we introduce ^{4}He through the N_2 traps by closing the bypass to reduce the risk of any impurities that helium might contain. However, although we have a bomb for filling helium at high pressures, we are not pressurizing the helium in the measurements presented in this thesis. Thus, we fill the cell at atmospheric pressure and do not utilize the bomb at this time.
While filling the cell through the first filling line, we monitor the pressure gauge of the second filling line. We ensure the cell is full when the pressure in the second pressure gauge matches the atmospheric pressure indicated on the first gauge.

5.4 Measurement schemes

This section describes how we actuate and detect the tiny vibrations of a nanotube resonator in the millikelvin regime.

5.4.1 Actuating the mechanical motion

To initiate the motion of the nanotube, we utilize a capacitive driving scheme. In this approach, a voltage given by

$$V_\mathrm{g} = V_\mathrm{g}^\mathrm{DC} + \tilde{V}_\mathrm{g}\cos(\omega t)$$

is applied to one of the gates located beneath the nanotube, as shown in Fig. 5.9. As a result, an additional charge, $q = V_g C_g$, is induced on the nanotube, which is equal in magnitude (in an ideal case when there are no parasitic capacitances) and opposite in sign to the charge on the gate. The attraction between these charges exerts an electrostatic force on the nanotube. This force is represented by:

$$F_{el} = \frac{1}{2}\frac{dC_g}{dx}V_g^2 \tag{5.2}$$

$$= \frac{1}{2}\frac{dC_g}{dx}\left(V_g^{DC} + \tilde{V}_g\cos(\omega t)\right)^2 \tag{5.3}$$

$$= \frac{1}{2}\frac{dC_g}{dx}\left(\left(V_g^{DC}\right)^2 + 2V_g^{DC}\tilde{V}_g\cos(\omega t) + \tilde{V_g}^2\cos^2(\omega t)\right) \tag{5.4}$$

For small values of $\tilde{V}_g$ (the AC component), the term $\tilde{V_g}^2$ becomes very small and can be ignored. Therefore, the electrostatic force simplifies to:

$$F_{el} \approx \frac{1}{2}\frac{dC_g}{dx}\left(\left(V_g^{DC}\right)^2 + 2V_g^{DC}\tilde{V}_g\cos(\omega t)\right)$$

This results in two terms:

- A DC term, $\left(V_g^{DC}\right)^2$, which modulates the tension in the nanotube.
- An AC term, $2V_g^{DC}\tilde{V}_g\cos(\omega t)$, which drives the nanotube's oscillation.

Here, C_g represents the gate capacitance, and x is the distance between the nanotube and the gate electrode.

The conductance of the nanotube, G, depends on the induced charge q, which means any change in the charge $\tilde{q}$ leads to a modulation in the nanotube conductance:

$$G = \frac{dG}{dq}\tilde{q}$$

The variation in induced charge $\tilde{q}$ is given by:

$$\tilde{q} = \tilde{C}_g(\omega)V_g^{DC} + C_g\tilde{V}_g$$

Therefore, any variation in the gate voltage V_g or the capacitance C_g changes the conductance G. At the resonance frequency, this conductance undergoes changes due to the nanotube's displacement, which modulates the gate capacitance C_g. On the other hand, the gate voltage V_g can also modulate G at any driving frequency.

5.4.2 Detecting the mechanical motion

To detect vibrations of the nanotube through conductance modulation, we use a frequency modulation (FM) technique, as outlined in Ref. [116, 117]. This method involves operating a nanotube resonator as a single-electron transistor (SET). By applying a radio-frequency (RF) voltage to the gate, we control electron tunneling at the source and drain electrodes. The SET configuration allows us to closely monitor the conductance, which is directly linked to the nanotube's displacement. This displacement, and thus any conductance

changes, are detected by measuring the DC or AC current flowing through the nanotube while applying a constant DC bias across the source and drain contacts.

The schematic in Fig. 5.9 illustrates the simplified yet comprehensive FM setup we employ in our measurement to determine the resonance frequencies of a CNT resonator. In this setup, the frequency f is modulated at 79 Hz with an amplitude of about 10 kHz. Fluctuations in current are monitored through a synchronized lock-in amplifier. A prominent peak in the lock-in response, which is proportional to the derivative of the time-averaged current through the nanotube, indicates that the system has reached resonance.

When a nanotube's motion is activated by applying a radio frequency signal with angular frequency ω and amplitude δV_{g} to the back gate, the resonances are detected in direct current due to a mixing effect. When the gate voltage oscillates as

$$\delta V_{\mathrm{g}}(t) = \delta V_{\mathrm{g}} \cos(\omega t),$$

it induces vibrations in the nanotube. These vibrations are described by:

$$\delta u(t) = \delta u_0 \cos(\omega t + \phi_{\mathrm{M}}),$$

where $u(t)$ is the displacement of the nanotube, δu_0 is the vibrational amplitude, t is time, and ϕ_{M} is the phase change between the applied force and the resulting motion.

Accompanying these vibrations, an oscillation occurs in the source-drain voltage $V_{\mathrm{sd}}(t)$ due to capacitive coupling between the leads and the nanotube. This oscillation is expressed as:

$$\delta V_{\mathrm{sd}}(t) = \delta V_{\mathrm{sd}} \cos(\omega t + \phi_{\mathrm{C}}),$$

where δV_{sd} is the amplitude, and ϕ_{C} is the phase induced by capacitive coupling. These terms reflect synchronized changes in the electrostatic environment with the frequency of the applied gate voltage.

The conductance of the nanotube, $G(V_{\mathrm{g}}, u)$, depends on both the source-drain and gate voltages, as well as the displacement of the nanotube. For small variations in the driving voltages, we approximate the conductance using a linear expansion as follows:

$$G(V_{\mathrm{g}}(t), u(t)) \approx G_0 + \left(\frac{\partial G}{\partial V_{\mathrm{g}}}\right) \delta V_{\mathrm{g}}(t) + \left(\frac{\partial G}{\partial u}\right) \delta u(t)$$

Here, G_0 represents the conductance in the absence of variation, while the terms $\frac{\partial G}{\partial V_{\mathrm{g}}}$ and $\frac{\partial G}{\partial u}$ capture the rate of change of conductance with respect to the gate voltage and displacement, respectively.

The time-averaged current through the device is then expressed as:

$$I = \langle G(t) V_{\mathrm{sd}}(t) \rangle$$

Substituting the expression for $G(t)$ into this equation, we obtain:

$$I = \langle \left(G_0 + \frac{\partial G}{\partial V_{\mathrm{g}}} \delta V_{\mathrm{g}}(t) + \frac{\partial G}{\partial u} \delta u(t) \right) V_{\mathrm{sd}}(t) \rangle$$

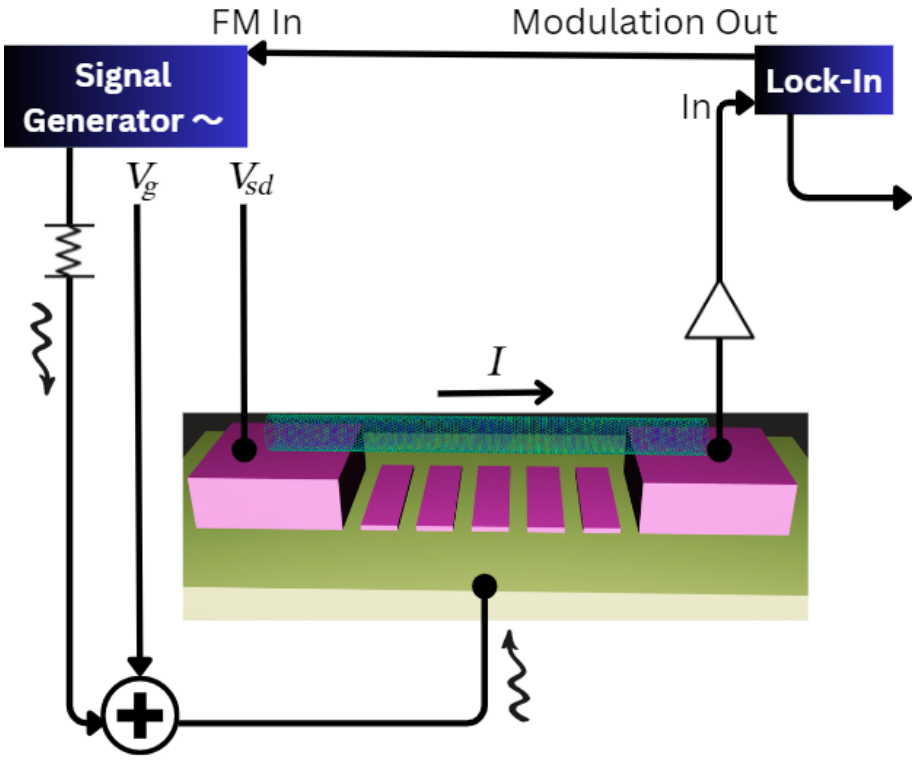

Figure 5.9: Schematic of the frequency modulation technique employed to actuate and detect the motion of a suspended CNT.

Breaking this down:

- The first term gives $G_0 V_{\text{sd}}^{\text{DC}}$, representing the DC current.
- The second term gives the contribution due to gate voltage variation, expressed as:

$$\frac{\delta V_{\text{sd}}}{2} \frac{\partial G}{\partial V_{\text{g}}} \delta V_{\text{g}} \cos(\phi_{\text{C}})$$

- The third term represents the contribution from the nanotube's displacement:

$$\frac{\delta V_{\text{sd}}}{2} \frac{\partial G}{\partial u} \delta u_0 \cos(\phi_{\text{C}} - \phi_{\text{M}})$$

Thus, the resulting average current through the device is given by:

$$I = G_0 V_{\text{sd}}^{\text{DC}} + \frac{\delta V_{\text{sd}}}{2} \left(\frac{\partial G}{\partial V_{\text{g}}} \delta V_{\text{g}} \cos(\phi_{\text{C}}) + \frac{\partial G}{\partial u} \delta u_0 \cos(\phi_{\text{C}} - \phi_{\text{M}}) \right) \tag{5.5}$$

5.4.2.1 Resonance signal and quality factor Q

To extract the quality factor Q, we analyze the derivative of the current, $\frac{dI}{df}$, with respect to frequency. Resonant peaks in $\frac{dI}{df}$ are highly sensitive to the mechanical properties of the nanotube, and the sharpness of these peaks is directly related to the quality factor Q.

The current $I(f)$ depends on both the displacement δu_0 of the nanotube and the frequency f. We assume the frequency dependence of I primarily enters through δu_0 and the phase ϕ_{M}. Differentiating the current with respect to frequency gives:

$$\frac{dI}{df} = \frac{\delta V_{\mathrm{sd}}}{2}\frac{\partial G}{\partial u}\frac{d}{df}\left[\delta u_0 \cos(\phi_{\mathrm{C}} - \phi_{\mathrm{M}})\right] \tag{5.6}$$

Since the nanotube exhibits simple harmonic motion, we describe the instantaneous displacement as:

$$\delta u(t) = \mathrm{Re}\left\{\delta u_0 e^{i2\pi f t}\right\}$$

where $\delta u_0 = \delta u_0 e^{i\phi_{\mathrm{M}}}$ is the complex amplitude of motion. Substituting this into the derivative of the current, we get:

$$\frac{dI}{df} = \frac{\delta V_{\mathrm{sd}}}{2}\frac{\partial G}{\partial u}\frac{d}{df}\left[\mathrm{Re}\left\{\delta u_0 e^{-i\phi_{\mathrm{M}}}\right\}\right] \tag{5.7}$$

For a driven harmonic oscillator, the displacement amplitude δu_0 near resonance is given by the standard Lorentzian formula:

$$\delta u_0 \propto \frac{1}{f_{\mathrm{res}}^2 - f^2 + i\frac{f_{\mathrm{res}} f}{Q}} \tag{5.8}$$

where f_{res} is the resonance frequency, and Q is the quality factor. Near resonance, the displacement δu_0 changes rapidly as a function of frequency, leading to a corresponding peak in $\frac{dI}{df}$.

Taking the absolute value of the displacement and substituting into the expression for $\frac{dI}{df}$, we obtain:

$$\frac{dI}{df} = A\left|\frac{d}{df}\left(\mathrm{Re}\left\{\frac{e^{-i\phi_{\mathrm{C}}}}{f_{\mathrm{res}}^2 - f^2 + i\frac{f_{\mathrm{res}} f}{Q}}\right\}\right)\right| + B \tag{5.9}$$

where A is a scaling factor related to the source-drain voltage δV_{sd} and B accounts for the background signal. This equation is used to fit the experimental data, and by determining the full width at half maximum (FWHM) of the resonance curve, we can extract the quality factor Q using the relation:

$$Q = \frac{f_{\mathrm{res}}}{\Delta f} \tag{5.10}$$

where Δf is the full width of the resonance peak at half maximum. Higher values of Q correspond to sharper resonance peaks and indicate lower energy dissipation in the system.

The mechanical resonances detected using this frequency modulation method can be clearly seen in the lock-in amplifier response. These sharp peaks in $\frac{dI}{df}$, which we extract by fitting the data to Eq. 5.9, are proportional to the quality factor Q and allow for accurate determination of both f_{res} and Q.

The mechanical nature of these resonances is further confirmed by their dependence on the DC gate voltage, as we discuss in Chapter 6.

Chapter 6: Characterisation of a nanotube resonator in vacuum

In this chapter, we characterize a CNT resonator in vacuum. Initially, we measure the electronic transport at 7 mK and realize a single-electron transistor (SET) within the resonator. Following this, we detect the mechanical motion of the nanotube and demonstrate how these vibrations can be tuned using a DC gate voltage. Subsequently, we determine the Q factor and investigate the influence of RF driving power on both the resonance frequency and the Q factor. After that, we study the impact of the SET on the mechanical motion of the nanotube. The chapter concludes by measuring the Duffing response in the nanotube, where we observe significant hysteresis and bistability during forward and reverse frequency sweeps.

6.1 Characterisation of a SET in the nanotube

We first perform transport measurements on a suspended CNT device. The nanotube is supported on source and drain electrodes (Fig. 4.5), and the substrate is used as a back gate to tune the nanotube's potential. Fig. 6.1 presents the differential conductance as a function of both bias voltage V_{sd} and gate voltage V_{g}. We measure the source-drain current I_{sd} by varying V_{sd} from $-8\,\mathrm{mV}$ to $10\,\mathrm{mV}$. Simultaneously, we modulate V_{g} from $-150\,\mathrm{mV}$ to $250\,\mathrm{mV}$.
Coulomb blockade in Fig. 6.1 (left panel) is evident in low-temperature transport measurements, depicting diamond-shaped areas of suppressed current known as Coulomb diamonds. This quantum phenomenon results from electrons preventing each other from tunneling onto a tiny conducting region on the nanotube due to Coulomb repulsion when thermal energy is insufficient to counteract this repulsion. The height of the diamonds corresponds to the charging energy of the quantum dot, which in our study ranges from 7 meV to 12 meV (discussed in Sec. 2.2.1.2 and Sec. 2.2.1.4). The asymmetry in the height of the Coulomb diamonds, where more energy is required to add electrons on the positive gate side compared to adding holes on the negative gate side, can be explained by the band bending effects in the nanotube. As shown in the right panel of Fig. 6.1, holes can move through the valence band, represented by the red band, with relative ease. This is due to a smaller Schottky barrier, allowing efficient tunneling of holes into and out of the valence band. In contrast, the green band represents the conduction band, where electron transport is hindered by a larger Schottky barrier. This barrier requires more energy for electrons to tunnel, resulting in reduced conductance on the positive gate side.

We determined the overall average capacitance to be approximately 20 aF, with the capacitance for the source/drain electrodes being $\approx 15\,\mathrm{aF}$, and for the gate $\approx 3\,\mathrm{aF}$. The uniformity of the diamond shapes across the entire gate range in the graph is indicative

of the high quality of our CNT.
An intriguing aspect of this measurement, as shown in Fig. 6.1 (left panel), is the noticeable abrupt jumps in the differential conductance, as indicated by the yellow arrows. These jumps can be attributed to self-oscillations in the suspended nanotube, which have been studied extensively in the literature [22, 81, 118]. Self-oscillations arise due to the interplay between the electronic and mechanical properties of the nanotube. Specifically, when an electron tunnels into the nanotube, the resulting change in electrostatic force causes a displacement in the nanotube, which affects the tunneling rate, leading to oscillatory behavior. These oscillations are particularly prominent within the $-2.5\,\mathrm{mV}$ to $2.5\,\mathrm{mV}$ bias voltage range and across the measured gate voltage, where resonant feedback between electronic transport and mechanical motion amplifies the effect.
Although these self-oscillations were not definitively confirmed in my measurements, similar phenomena were clearly demonstrated in the 2020 study by Wen et al. [81]. In these studies, self-oscillations were confirmed by observing sharp peaks in the mechanical resonance of the nanotube in response to specific bias voltages, which coincide with coherent oscillations of the nanotube's position. The phenomenon has also been confirmed by measuring the phase coherence between the mechanical motion and the tunneling current, directly correlating the oscillations with electronic transport.
These established methods—spectral analysis of mechanical resonances and phase coherence measurements—have been used to confirm self-oscillations in suspended nanotube systems, as demonstrated in previous studies.

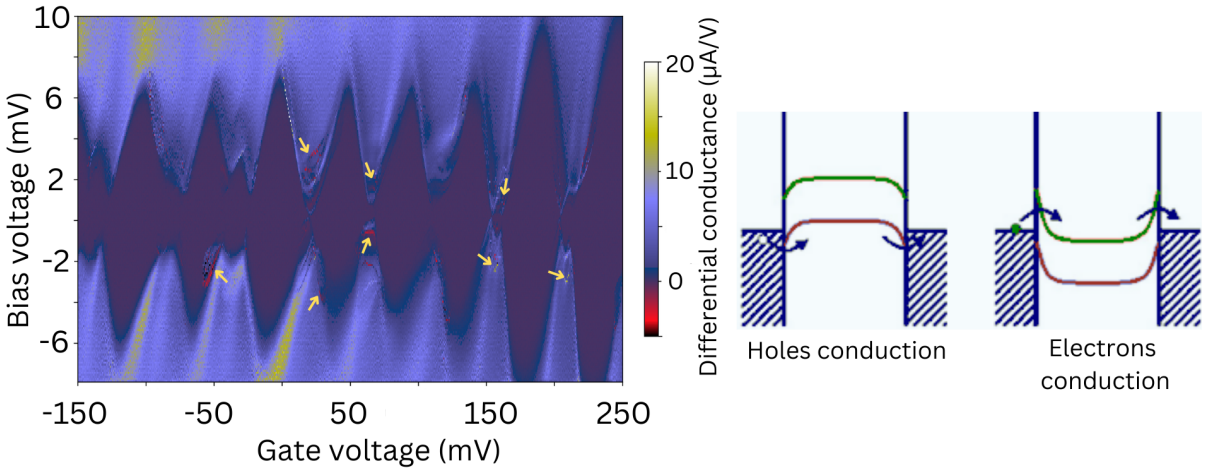

Figure 6.1: Left Panel- Stability diagram of the nanotube resonator observed at 7 mK under vacuum conditions. A comprehensive explanation of single-electron tunneling (SET) mechanism is provided in subsection 2.2.1.3. Right Panel – Illustration of the band bending effect, showing efficient hole transport through the valence band due to a smaller Schottky barrier, and hindered electron transport in the conduction band from a larger barrier. This explains the higher energy needed for electron transport at large positive gate voltages compared to hole transport at negative gate voltages in the Coulomb blockade behavior. (Redraw from [119]).

6.1.1 Tunneling rate

The tunneling rate Γ of a quantum dot is the rate at which electrons traverse the quantum dot. Therefore, Γ can be inferred from the current I through the quantum dot. This is because the current is directly proportional to the number of electrons passing through the quantum dot per unit time, i.e., $I = e \cdot \Gamma$.
The calculated tunneling rate for the given $I = 2.5\,\mathrm{nA}$ is $\Gamma \approx 15.6\,\mathrm{GHz}$. However, the conductance spikes (indicated by arrows in the left panel of Fig. 6.1) can disappear when decreasing the current, which leads to the tunneling rate falling below the mechanical resonance frequency [22].

6.2 Measurement of mechanical vibrations

6.2.1 Detection and tuning of mechanical vibrations

The measurement bandwidth of the system can be calculated by modeling the nanotube as a ballistic conductor in series with contact resistances and capacitances. In this configuration, the CNT experiences a low-pass filtering effect, and the frequency, $f_{\mathrm{bandwidth}}$, of this filter determines the measurement bandwidth [105].

We begin by calculating the total capacitance of the system, which includes the source capacitance C_{s} and the drain capacitance C_{d}. For our system, the drain capacitance is calculated using the parallel plate capacitor model:

$$C_{\mathrm{d}} = \frac{\epsilon_0 \epsilon_r A}{d}$$

where $\epsilon_0 = 8.854 \times 10^{-12}\,\mathrm{F/m}$ is the vacuum permittivity, $\epsilon_r = 3.9$ is the relative permittivity of SiO_2, $A = 10\,\mu\mathrm{m} \times 10\,\mu\mathrm{m} = 100 \times 10^{-12}\,\mathrm{m}^2$ is the area of the contact pad, and $d = 175\,\mathrm{nm} = 175 \times 10^{-9}\,\mathrm{m}$ is the thickness of the dielectric layer.

Substituting these values gives the drain capacitance:

$$C_{\mathrm{d}} \approx 1.97\,\mathrm{pF}.$$

Since the resistance of the nanotube is $R_{\mathrm{nanotube}} = 182 \times 10^3\,\Omega$, the measurement bandwidth $f_{\mathrm{bandwidth}}$ is given by the standard formula for a low-pass RC filter:

$$f_{\mathrm{bandwidth}} = \frac{1}{2\pi R_{\mathrm{nanotube}} C_{\mathrm{d}}}.$$

Substituting the values of R_{nanotube} and C_{d}, we calculate:

$$f_{\mathrm{bandwidth}} \approx \frac{1}{2\pi \times 182 \times 10^3 \times 1.97 \times 10^{-12}} \approx 443.6\,\mathrm{kHz}.$$

Thus, the calculated measurement bandwidth of the system is approximately 443.6 kHz. This bandwidth limits the system's ability to directly measure the high-frequency oscillations of the mechanical resonator, which typically operate in the MHz range. Consequently, the mechanical resonances are detected as a time-averaged signal using a lock-in amplifier, operating within the system's bandwidth constraints.
In Fig. 6.2 (top panel), the resonant frequencies of a CNT resonator are observed in the lock-in signal when the driving frequency is plotted against the gate voltage. For all datasets, frequencies are swept from lower to higher values unless explicitly stated

otherwise. The color plot represents the intensity of the lock-in signal, which indicates the resonance strength of the different vibration modes of the nanotube for the entire gate voltage range. We observed four dotted patterns (shown by green arrows), each representing a particular vibrational mode of the nanotube. The first pattern indicates the fundamental vibration mode (labeled as f_0), while the subsequent three patterns, moving upward, are associated with the 1st (f_1), 2nd (f_2), and 3rd (f_3) harmonics, respectively. As the gate voltage is reduced, the resonance frequency for the 3rd harmonic f_3 increases nearly two and half-fold, shifting from f_3 =36.8 MHz at $V_g = 1.5\,V$ to $f_3 = 94.7\,MHz$ at $V_g = -1.5\,V$.

The applied gate voltage generates an electrostatic force on the nanotube, adjusting its tension and thereby altering its natural oscillation frequency [75]. We calculated the residual tension at $V_g = 0\,V$, and the tuned tension for each mode in the respective strong and weak bending regimes at $V_g = -670\,mV$, as detailed in Appendix Sec. A.4.

This behavior is analogous to tuning a guitar string by adjusting its tension. As the gate voltage increases, both the tension and oscillation frequency of the nanotube rise, with the extent of change depending on the mode's shape and direction. The goal is to determine whether the lock-in signal's peaks or dips shift with changes in the DC gate voltage. If the signal varies with gate voltage, it is mechanical in origin; otherwise, it would indicate an electrical resonance from the measurement setup, which requires no further analysis.

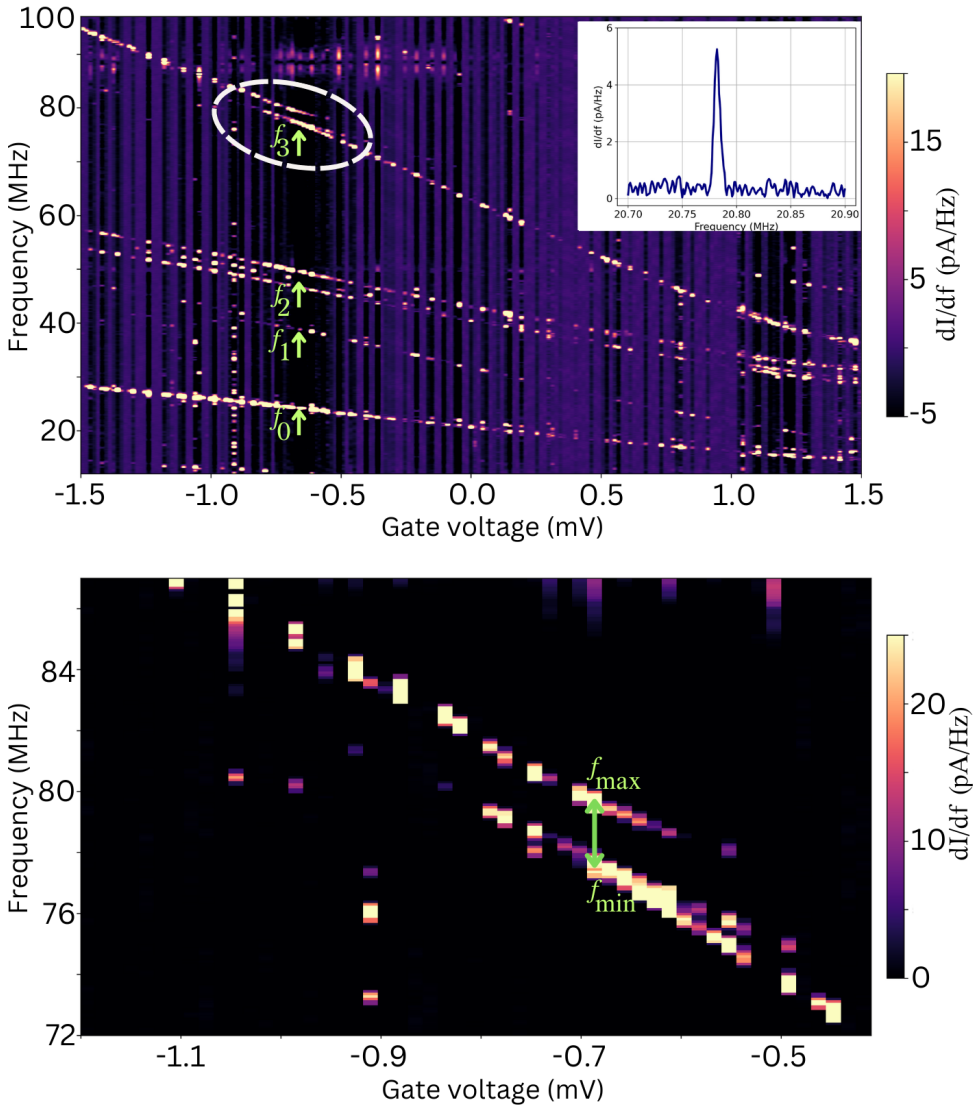

Figure 6.2: Top panel: The graph shows the driving frequency versus gate voltage, where the color intensity indicates the strength of the lock-in signal. The measurement is taken at a driving power of $-40\,\mathrm{dBm}$ and at $V_{\mathrm{sd}} = -2\,\mathrm{mV}$. The effect on resonance frequencies is observed by measuring the mixing current I_{mix} via a lock-in amplifier. Four distinct high-intensity patterns emerge as the gate voltage sweeps from positive to negative, indicated by green arrows. These patterns are attributed to the four different resonance modes of a nanotube, demonstrating that the DC gate voltage can modulate the resonance frequencies of a CNT. This data is of low resolution, with each dot representing a resonance peak or dip in the lock-in signal. (The inset illustrates a cut along $V_{\mathrm{g}} = -103.9\,\mathrm{mV}$, showing a peak in the resonance signal upon frequency sweep.). Bottom Panel: This depicts the phenomenon of avoided crossing in a higher mode, revealing how tension-induced coupling between modes allows for an energy exchange among them, achieved by the DC gate voltage adjustment.

6.2.2 Strongly-coupled mechanical modes

In our detailed analysis of the CNT resonator, we observed significant interactions between mechanical modes, particularly evident in mode anti-crossing as illustrated in the bottom

panel of Fig. 6.2. This coupling stems mainly from motion-induced tension. When a specific mode oscillates within the CNT resonator, it generates tension that affects the dynamics of another interconnected mode. A key finding is that the resonance frequency of one mode becomes commensurable with that of another, resulting in anti-crossing. This effect was notably observed when the third harmonic $f_3 = 78.8\,\mathrm{MHz}$ precisely doubled the first harmonic $f_1 = 39.4\,\mathrm{MHz}$ at $V_\mathrm{g} = -670\,\mathrm{mV}$, as indicated by the green arrows in the upper section of Fig. 6.2. This phenomenon is consistent with the theoretical model outlined in [120] and was experimentally validated in [121]. The modes f_1 and f_3 demonstrate significant tunability with gate voltage, mirroring the behavior of a bending beam, whereas modes f_0 and f_2 show lesser tunability with V_g, resembling a catenary shape as described in [105]. Interestingly, mode f_2 appears to split into two submodes, with an average frequency at the same $V_\mathrm{g} = -670\,\mathrm{mV}$ being $f_2 = 48.37\,\mathrm{MHz}$, nearly twice that of the fundamental mode $f_0 = 24.25\,\mathrm{MHz}$. Hence, when the second harmonic f_2 becomes twice the fundamental mode f_0, it results in the splitting of f_2, as observed in the upper section of Fig. 6.2 across the entire range of gate voltages measured.

Furthermore, the flexural (bending) mode coupling in CNT resonators, akin to the Duffing nonlinearity, involves the interaction between different mode harmonics driven by tension and single-electron forces. This coupling manifests when the frequencies of two modes are commensurate, especially when tension from a lower mode triggers parametric excitation in a higher mode. Such interactions lead to an avoided crossing in the resonance frequency curve. Additionally, single-electron forces also play a role by modulating the average charge through one mode's motion, affecting the spring constant of another. This modulation may either soften or stiffen the mode, depending on the measurement point along the Coulomb peak.
Therefore, this observation underscores the efficient energy transfer between modes with integer frequency ratios, attributed to nonlinear forces. This transfer is particularly pronounced at mode anti-crossing points, leading to mixed eigenfunctions and unusual spectra. Strong coupling between modes results in a frequency split, diverging from the resonators' original frequencies, with the degree of splitting indicating the strength of the coupling. By adjusting the gate voltage V_g, we confirmed the tension-induced nature of this coupling. Thus, the vibration of one mode not only generates mechanical stress within the resonator but also mutually influences the behavior of other modes.

6.2.2.1 Thermal occupation at anti-crossing points and coupling strength

A resonator enters the quantum ground state regime when its thermal energy is significantly less than the spacing between its quantum energy levels, i.e., $k_\mathrm{B}T \ll \hbar\omega$. In practical terms, at extremely low temperatures, typically in the millikelvin range, the available thermal energy $k_\mathrm{B}T$ falls short of the resonator's energy ω, implying that there is insufficient thermal energy to excite the flexural motion of the CNTs, i.e., $\omega \gg k_\mathrm{B}T$.

To understand the population of quantum states at a given temperature, we derived the thermal occupation using the relation [86]:

$$n = \frac{1}{2} + \left[\exp\left(\frac{h\omega}{k_\mathrm{B}T}\right) - 1\right]^{-1} \tag{6.1}$$

Here, we assume $T \approx T_\mathrm{MC}$, the temperature of the mixing chamber, 7 mK.
Then, we extracted n to be approximately

- For $f_\mathrm{min} = 77.73\,\mathrm{MHz}$: $n \approx 0.54$

- For $f_{\max} = 79.71\,\text{MHz}$: $n \approx 0.53$

In quantum mechanics, when n is close to $\frac{1}{2}$, the system is predominantly in its ground state. Remarkably, n being comparable to $\frac{1}{2}$ suggests that the nanotube vibrational modes are approaching the quantum ground state. The only assumption we make here is that the temperature of the CNT is equivalent to the mixing chamber temperature of our cryostat.

The coupling strength between mechanical modes, denoted as Δ, is indicative of their mutual interaction. At the point of mode anti-crossing, this strength can be quantified as half the frequency difference between the two modes: $\Delta = \frac{f_{\max} - f_{\min}}{2}$. For the given frequencies, $f_{\min} = 77.73\,\text{MHz}$ and $f_{\max} = 79.71\,\text{MHz}$, the computed coupling strength is $\Delta \approx 1\,\text{MHz}$. This value emphasizes the strong coupling, with the modes avoiding a direct crossing due to their interaction, leading to a frequency split. This split, and consequently Δ, offers insights into the magnitude of their mutual influence.
The phenomenon of anti-crossing observed in our study illustrates the complex interactions in nanomechanical systems, governed by classical mechanics principles. The nonlinear dynamics of the CNT resonator, notably influenced by motion-induced tension from the oscillatory behavior of the nanotube, play a pivotal role in the interaction between coupled modes. Such findings reveal the complexity of mechanics within CNT resonators and emphasize their value in furthering our understanding of classical mechanics principles at the nanoscale.

6.2.3 Extracting the Q factor

Before performing the nanotube measurements in superfluid ^{4}He, we aim to extract the intrinsic Q factor by driving the nanotube into the linear regime. The nanotube's Q factor is influenced by several parameters, including bias voltage, gate voltage, and driving power, which are discussed in later sections. The Q factor is measured using a frequency modulation scheme as illustrated in Fig. 5.9.
A constant DC bias of $V_{\text{sd}} = -2\,\text{mV}$ and a gate voltage of $V_{\text{g}} = -103.9\,\text{mV}$ are applied to the CNT resonator. An oscillating voltage, generated by the signal generator at $-88\,\text{dBm}$ and modulated at a low frequency of 79 Hz, is introduced onto the gate. The resulting DC current through the nanotube is amplified at room temperature and measured using a lock-in amplifier. By sweeping the driving frequency from 20.7 MHz to 20.9 MHz, a resonance peak is observed around 20.78 MHz, as shown in Fig. 6.3.
We calculate the Q value using a frequency modulation method as discussed in subsection 5.4.2, where the frequency f is modulated at 79 Hz with a frequency deviation of 10 kHz. The derivative of the measured current (derived in Eq. 5.4.2) with respect to frequency, $\left|\frac{dI}{df}\right|$, peaks at resonance. This peak is used to derive Q and f_{res} through the following equation [117]:

$$\frac{\mathrm{d}I(f)}{\mathrm{d}f} = A\left|\frac{\mathrm{d}}{\mathrm{d}f}\mathrm{Re}\left(\frac{e^{-i\phi_{\text{C}}}}{f_{\text{res}}^2 - f^2 + i\frac{f f_{\text{res}}}{Q}}\right)\right| + B \tag{6.2}$$

Here, A and B are scaling and offset parameters for the peak, respectively, obtained through fitting the experimental data. The resonant frequency f_{res} and the quality factor Q are also determined from the fit. This model presumes the nanotube behaves as a simple

harmonic oscillator and the frequency mainly depends on the instantaneous displacement and the mechanical phase of the resonator.

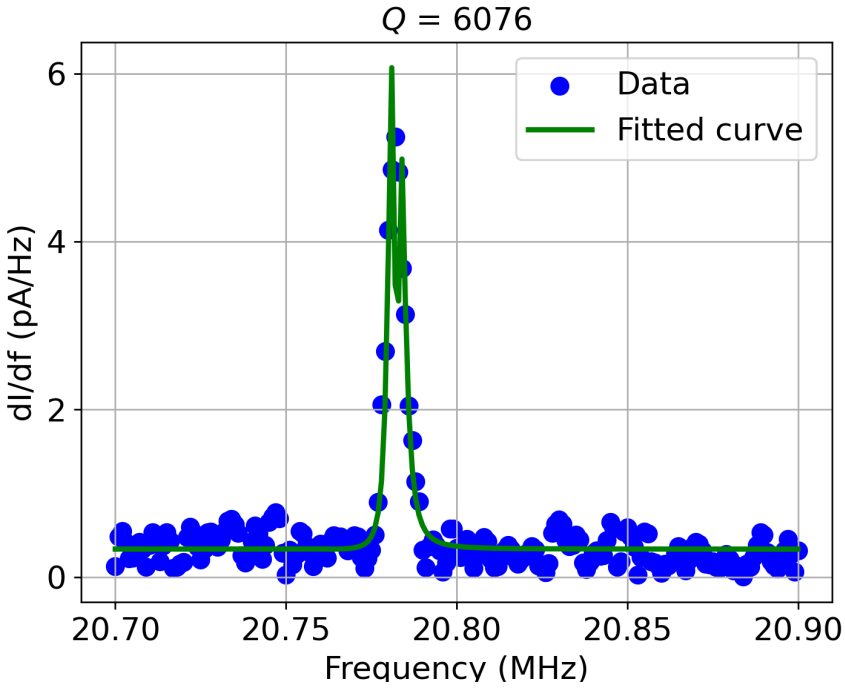

Figure 6.3: The Q factor of the nanotube in vacuum is determined to be 6076 by fitting with Eq. 6.2. The free fit parameters, A and B, are found to be 1228 and 3×10^{-13}, respectively. Here, a DC bias of $V_{\mathrm{sd}} = -2\,\mathrm{mV}$ and a gate voltage of $V_{\mathrm{g}} = -103.9\,\mathrm{mV}$ are applied, with a driving power of $-88\,\mathrm{dBm}$.

6.2.4 Power dependence of Q factor and resonance frequency

In our measurements, the inverse relationship between the RF driving power and the Q factor observed in Fig. 6.4 arises from nonlinear damping in nanotube resonators. As the driving power increases, the amplitude of the oscillations grows, causing the resonator to enter a nonlinear regime, reducing the Q factor. In this regime, the restoring force follows a cubic Duffing-type non-linearity instead of a linear dependence on displacement.

This nonlinear behavior is a direct consequence of the high aspect ratio of CNTs, which makes them susceptible to geometrical and electrostatic nonlinearities. As the amplitude of oscillation increases, additional tension is induced in the CNT due to its stretching, which modifies the resonance frequency (spring-hardening effect). This effect is observed as an upward shift in the resonance frequency with increasing drive power (Fig. 6.4, bottom panel).

At the same time, nonlinear damping arises because of energy dissipation processes that become more efficient at large oscillation amplitudes. In nanotube resonators, this dissipation is often associated with phonon-phonon interactions, electron-phonon coupling, and friction at the boundaries. The observed decrease in the Q factor at higher drive powers can be attributed to these enhanced energy loss mechanisms[75].

Previous studies have extensively characterized these nonlinear damping effects in CNT resonators. For instance, it has been demonstrated that at low driving powers, the

damping remains dominated by intrinsic material properties and external friction, maintaining a relatively high Q factor. However, as the power is increased, the resonator enters the nonlinear regime, and the Q factor decreases sharply due to the onset of nonlinear damping, as seen in other studies on high-Q nanotube resonators [75].

Thus, the observed power dependence of the Q factor and the resonance frequency in our measurements aligns well with the expected nonlinear damping behavior in CNT resonators.

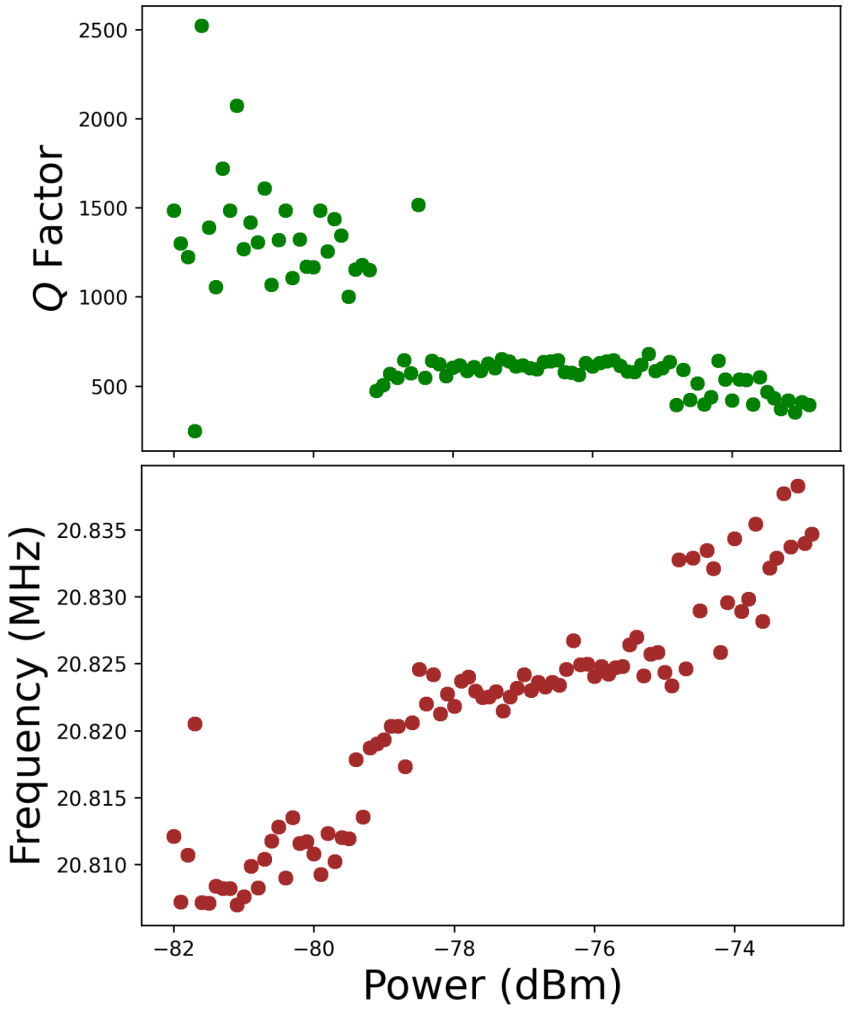

Figure 6.4: Top Panel: This illustrates the inverse relationship between the RF driving power and the Q factor of the CNT resonator, depicting a decrease in the Q factor from approximately 1500 at $-81\,\mathrm{dBm}$ to 400 at $-73\,\mathrm{dBm}$. This decline is attributed to nonlinear damping within the CNT resonator. Bottom Panel: This demonstrates the increase in resonance frequency with the amplification of driving power, highlighting enhancements in both the resonance frequency and its width due to the driving force. This behavior is attributed to the spring hardening effect, which is characteristic of tensioned oscillators. As a result, the frequency experiences a net increase of $\approx 40\,\mathrm{kHz}$ across the observed range of driving power.

6.3 The effect of the SET on the mechanical resonator

6.3.1 Resonance response across a Coulomb peak

In the previous section, we measured and tuned the CNT vibrations via DC gate voltage dependence at a constant RF drive. Now, we turn our focus onto the shift in resonance frequency due to single-electron tunneling. Fig. 6.5 (bottom-left panel) illustrates the current when the gate voltage sweeps through a single Coulomb peak (dip in this as we sit at $-2\,\mathrm{mV}$ bias). When the current is zero, it's the Coulomb blockade region and the number of electrons on the CNT is fixed. When there's a spike in the current magnitude (Coulomb dip), it indicates an electron has tunneled onto or off the CNT.

The tunneling rate, Γ, for $I = 1.75\,\mathrm{nA}$ is approximately $10.9\,\mathrm{GHz}$, which corresponds to roughly 525 times the mechanical frequency ($20.185\,\mathrm{MHz}$). This suggests many single-electron tunneling events occur for each mechanical oscillation. Therefore, single-electron tunneling applies a force that changes over time to the mechanical vibrating resonator in addition to the electrostatic force due to the DC gate as well as the driving force of the RF signal on the gate. Interestingly, these electron movements don't just make the transition from one static point to another smoothly. Instead, they change the resonance frequency at the Coulomb peak — even more than what's caused by simple tuning shifts due to modulation in the nanotube tension. Studies have shown that this changing force impacts the nanotube's inherent spring constant, softening its mechanical vibrations [122, 22, 123]. This behavior is observed in Fig. 6.5 (top-left panel), where the resonance frequency of the CNT changes with the gate voltage over a span of a single Coulomb dip.

The essential point to grasp here is how the voltage and charge on the CNT change with the gate voltage. When the CNT is at the Coulomb peak (where electrons can tunnel onto or off the nanotube), the CNT tries to balance out the voltage from the gate. This process is called 'overscreening'. When this happens, the tension in the resonator changes. The main takeaway here is that when single-electron tunneling occurs, it can cause a significant dip in the CNT's resonance frequency. This change in frequency due to tunneling is much larger than changes due to other effects, like mechanical tension.

For a detailed analysis, we consider the 1D cuts at $V_\mathrm{g} = -109.4\,\mathrm{mV}$ and $V_\mathrm{g} = -103.8\,\mathrm{mV}$ from Fig. 6.5 (top-left panel), which are illustrated in Fig. 6.5 (right panels). Along with a dip in the resonance frequency, we observed significant damping which results in a reduced Q factor at the Coulomb peak. Specifically, Fig. 6.5 (top-right panel) displays a resonance peak at $20.8\,\mathrm{MHz}$ in the lock-in signal as a function of the driving frequency. Since this is taken at a gate voltage ($V_\mathrm{g} = -109.4\,\mathrm{mV}$) away from the Coulomb peak position, the peak shape remains symmetric and has a Q factor of 2971. In contrast, moving closer to the Coulomb peak as depicted in Fig. 6.5 (bottom-right panel), the resonance peak, which occurs at approximately $20.725\,\mathrm{MHz}$, becomes asymmetric and exhibits a non-linear response with the Q factor dropping to 592.

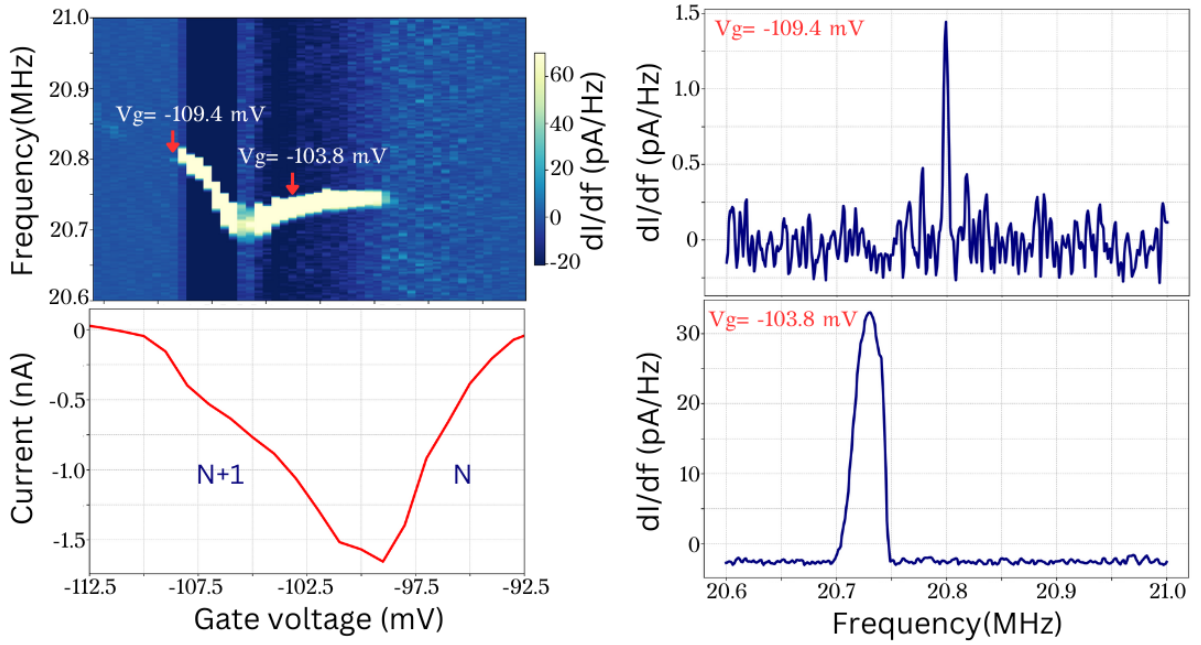

Figure 6.5: Bottom-left Panel: This illustrates the variation in current across a single Coulomb peak, with gate voltage ranging from $-92.5\,\text{mV}$ to $-112.5\,\text{mV}$ at a $-2\,\text{mV}$ bias. A zero current indicates a stable electron count on the CNT. Top-left Panel: Here, we observe a dip in the CNT's resonance frequency at or near the Coulomb peak during single-electron tunneling events, demonstrating the non-linear behavior in the nanotube's resonance signal as the gate voltage sweeps through a single Coulomb peak. Top-right Panel: Away from the Coulomb peak, the resonance signal exhibits a linear response with a Q factor of ≈ 2971. Bottom-right Panel: Close to the Coulomb peak, the resonance signal gives a non-linear response, characterized by a Q factor of ≈ 592.

The damping in mechanical motion arises from two key contributors: intrinsic damping and damping due to the stochastic backaction force associated with electron tunneling (for details refer to [75]). This stochastic force varies with electron numbers N and $N+1$ and is influenced by the CNT's charge and its proximity to the gate, both of which oscillate with the CNT. The aggregate damping is captured by the total Q factor, inclusive of electron tunneling effects. Notably, a shift from N to $N+1$ electrons reduces the Q factor, emphasizing the role of individual electron tunneling events. Damping is most pronounced when CNT oscillation leads to significant charge shifts. Additionally, the damping varies with gate voltage, affecting the Q factor as we change gate voltage.

6.3.1.1 Optimizing DC gate setpoint for intrinsic Q factor: nonlinear and linear regimes

The primary goal of this measurement is to optimize the intrinsic Q factor of the CNT resonator by carefully selecting the gate voltage setpoint, which influences the coupling between the mechanical motion of the nanotube and single-electron tunneling (SET) [75]. The resonance behavior and the Q factor are highly sensitive to the proximity of the Coulomb peak, where SET effects are strongest. As we move away from the Coulomb peak, the coupling between electron tunneling and the mechanical vibrations weakens, pushing the system into a more linear regime. In this linear regime, the signal-to-noise ratio (SNR) is lower due to weaker SET-induced coupling, which leads to a narrower

resonance peak and a higher Q factor, as demonstrated by the sharp peak with a Q factor of 2971 (Fig. 6.5, top-right panel). However, this weak coupling also limits the resonator's excitation, producing a weaker overall signal.

Conversely, at the Coulomb peak, where SET effects are strongest, the interaction between electron tunneling and mechanical vibrations is significantly enhanced, improving the SNR. This stronger coupling introduces additional damping due to stochastic back-action forces [75, 23], broadening the resonance peak and reducing the Q factor to 592 (Fig. 6.5, bottom-right panel). Even at this relatively low drive power, the resonator is pushed into a nonlinear regime, where the increased amplitude further broadens the resonance signal. This nonlinearity manifests as a softening of the mechanical spring constant due to SET effects, causing significant dips in the resonance frequency.

To optimize the Q factor, the gate voltage must be precisely tuned near, but not directly at, the Coulomb peak. By adjusting the drive power to avoid excessive damping from SET coupling while still benefiting from enhanced interaction at the Coulomb peak, we can maximize the resonator's performance. This careful balance of gate voltage and drive power is crucial for achieving optimal performance in the CNT resonator, emphasizing the interplay between electron tunneling and mechanical motion.

After selecting the optimal gate voltage setpoints, we then proceed to study the resonance response as a function of bias voltage.

6.3.2 Resonance response with bias voltage

We examine how bias voltage affects the Q factor and resonance frequency of the CNT resonator. By employing the FM technique, we determine the resonance frequency in relation to the bias voltage V_{sd} through measuring the mixing current via lock-in detection against frequency f. We maintain a constant DC gate voltage $V_{\mathrm{g}} = -104.3\,\mathrm{mV}$ and a driving power of $-78\,\mathrm{dBm}$. The resulting lock-in signal is presented as a color map in the top-left panel of Fig. 6.6.

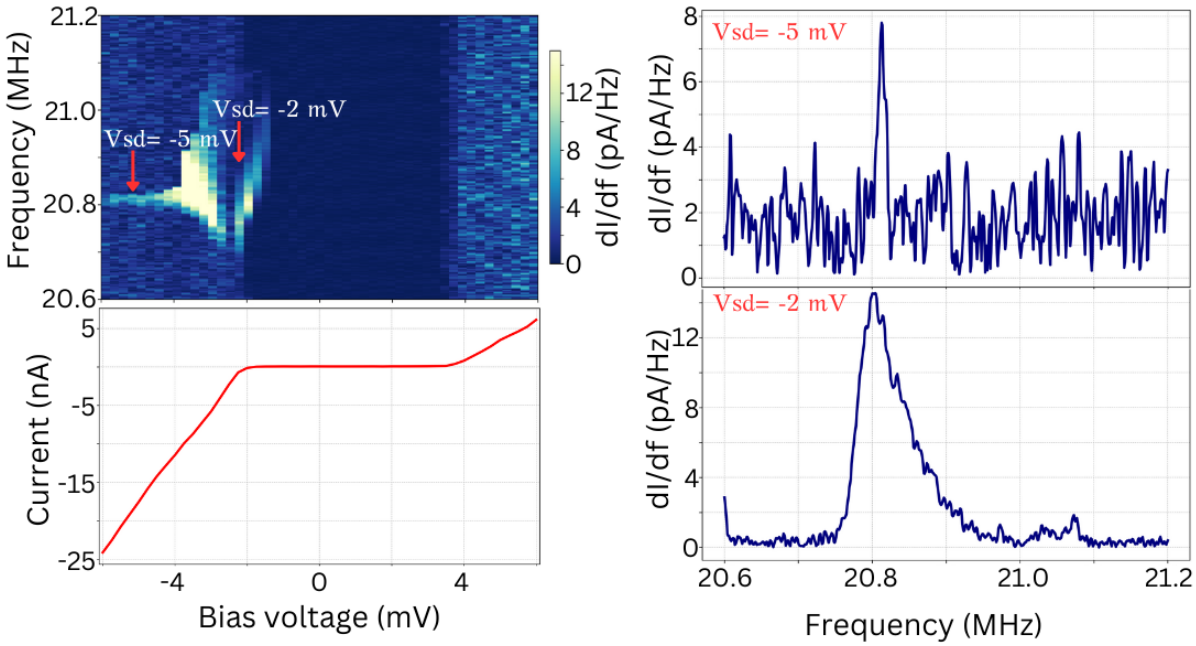

Figure 6.6: Top-left Panel: Demonstrates the response of the nanotube's resonance signal as a function of bias voltage. Bottom-left Panel: Shows the IV characteristics of the CNT resonator across the entire bias voltage range, with resonance responses measured at a driving power of $-78\,\mathrm{dBm}$ and a gate voltage $V_\mathrm{g} = -104.3\,\mathrm{mV}$. Top-right Panel: Presents a 1D cut of the resonance signal at a bias voltage $V_\mathrm{sd} = -5\,\mathrm{mV}$, where the resonance peak is nearly linear with a Q factor of 550. Bottom-right Panel: Depicts resonance at $V_\mathrm{sd} = -2\,\mathrm{mV}$, highlighting a reduced Q factor of 110 and a fin-shaped peak indicative of spring-softening Duffing oscillators.

Throughout the entire range of positive bias voltage, no resonance signal is detected unless the drive power is increased (details not shown here). In contrast, applying a negative bias voltage results in a significant change in the Q factor and a noticeable shift in the resonance frequency. However, these changes do not follow a monotonic relationship with the bias voltage. This data is reproducible; confirmation comes from measuring the same plot up to three times, each time observing the same behavior.

To further illustrate, 1D cuts taken at two different bias voltages, $V_\mathrm{sd} = -5\,\mathrm{mV}$ and $V_\mathrm{sd} = -2\,\mathrm{mV}$, from the top-left panel of Fig. 6.6, show variations in the Q factor. Specifically, at $V_\mathrm{sd} = -5\,\mathrm{mV}$, the Q factor is 550, which reduces to 110 at $V_\mathrm{sd} = -2\,\mathrm{mV}$. The latter condition also displays a fin-shaped resonance peak, similar to the behavior observed in Duffing oscillators. Overall, these findings highlight the CNT resonator's asymmetric response to bias voltage, providing insights on its potential as a SET and revealing the complexities of nanoscale mechanics.

The distinction between positive and negative biases is notable. The lack of resonance signal under positive bias may be due to electrostatic interactions at the CNT-electrode interface or from SET operations. Such interactions might suppress mechanical vibrations, particularly due to the "back-action" effect from single-electron tunneling that synchronizes with the CNT resonator's frequency, thereby influencing the Q factor.

On the other hand, the irregularities observed under negative bias could be attributed to electro-mechanical dynamics that affect localized charge distributions in the CNT due to SET operations. This could lead to periodic changes in mechanical stiffness, resulting in variations in the Q factor and resonance frequency. The fin-shaped resonance peak

observed at $-2\,\mathrm{mV}$ bias (illustrated in the bottom-right panel of Fig. 6.6) suggests the involvement of nonlinear mechanical dynamics. Such nonlinearity could originate from three primary sources: electrostatic nonlinearity, nonlinearity due to single-electron tunneling, and geometric nonlinearity resulting from mechanical tension. Although the sensitivity to bias is not yet fully understood, it encourages further investigation, which could uncover intriguing aspects of physics.

6.4 Duffing response with RF driving power

To identify the linear driving regime, we plot the resonance frequency response of the CNT against various driving powers. The **dynamic range** of the mechanical oscillator, a key parameter in our applications, represents the range of drive powers where the resonance exhibits a linear response. This spans from the lowest drive power, where the signal just surpasses noise, to the highest, where nonlinear behavior begins.

In Fig. 6.7, the top-left panel shows the upward frequency sweep, while the bottom-left panel presents the downward sweep. During the upward sweep, increasing drive power causes an upward shift in the resonance frequency, marking the onset of nonlinearity. This nonlinear behavior is further confirmed by the hysteresis loop seen between the upward and downward sweeps, which indicates the presence of multiple stable resonance frequencies at high RF excitation levels.

At a drive power of $-88\,\mathrm{dBm}$, the CNT oscillates with such a small amplitude that its motion is nearly indistinguishable from noise. As the drive power increases to $-83\,\mathrm{dBm}$, a Lorentzian resonance lineshape becomes evident in the lock-in amplifier and digital multimeter (DMM) readings, indicating that the system is in the linear regime, where the restoring force is proportional to displacement (Hooke's law). However, at $-73\,\mathrm{dBm}$, the response transitions to a nonlinear regime, forming a characteristic "sharkfin" lineshape typical of Duffing systems. Further increasing the drive power to $-72\,\mathrm{dBm}$ results in bistability and hysteresis, as seen in Fig. 6.7 (bottom-right panel). This bistability allows the CNT resonator to oscillate in either a high- or low-amplitude state at the same frequency. The presence of hysteresis depends on the direction of the frequency sweep, confirming the Duffing stiffening effect.

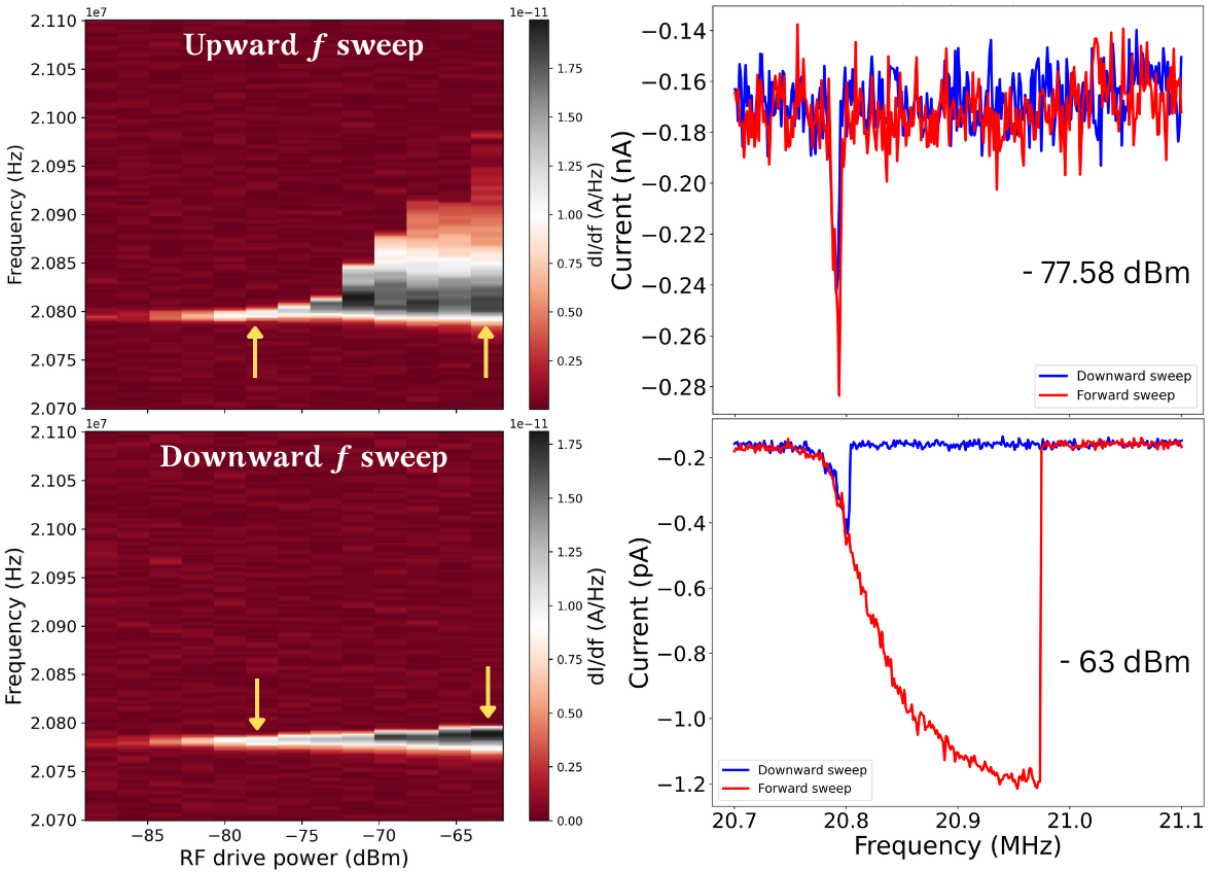

Figure 6.7: Top-left: Resonance frequency vs. power for upward sweep. Bottom-left: Resonance frequency vs. power for downward sweep, showing bistability and hysteresis due to Duffing nonlinearity. Right: 1D cuts at $-77.58\,\mathrm{dBm}$ (linear lineshape without hysteresis) and $-63\,\mathrm{dBm}$ (hysteresis with bistability) for both sweeps. The electrostatic driving force is controlled by the oscillating gate voltage $V_{\mathrm{g}}^{\mathrm{AC}}$, with gate and bias voltage setpoints of $V_{\mathrm{g}} = -103.9\,\mathrm{mV}$ and $V_{\mathrm{sd}} = -2\,\mathrm{mV}$.

The 1D cuts at $-77.58\,\mathrm{dBm}$ (right panels of Fig. 6.7) reveal a clean Lorentzian lineshape without hysteresis, indicating linear behavior. By contrast, the cuts at $-63\,\mathrm{dBm}$ show clear bistability and hysteresis, confirming nonlinear behavior at higher driving powers. This phenomenon is observed using the one-source mixing technique, which allows us to monitor mechanical resonance across different driving forces by analyzing the mixing current I_{mix} as a function of driving frequency f. The electrostatic driving force is modulated by the oscillating gate voltage $V_{\mathrm{g}}^{\mathrm{AC}}$.

The size and shape of the hysteresis loop provide insight into the nonlinear dynamics of the system. Critical power and frequency values define the thresholds between linear and nonlinear behavior. Moreover, the intricate amplitude response at large drive powers reveals the interplay between the resonator's material properties, its geometry, and the applied electrostatic force.

6.4.1 Displacement and velocity of nanotube mechanical motion dependence on electrostatic force in vacuum

The displacement and velocity data shown in Fig. 6.8 were extracted from the resonance response to RF power sweeps in vacuum (see Fig. 6.7). The detailed derivation and

calculations for displacement and velocity as functions of force are provided in Appendix Sec. A.3. This data reveals the transition from linear to nonlinear dynamics of the CNT resonator as a function of electrostatic force in a Duffing-type system.

In the upward frequency sweep (Fig. 6.8(a)), the displacement amplitude of the nanotube initially increases linearly with the applied electrostatic force, rising rapidly to a maximum of approximately 4 pm at around 0.5 pN. Beyond this force threshold, the displacement begins to change nonlinearly, no longer following a linear relationship with the force. This nonlinear behavior is characteristic of the Duffing response, where the mechanical properties of the system, such as stiffness, change with amplitude, leading to a deviation from the linear Hooke's law behavior.

Similarly, the velocity data (Fig. 6.8(c)) initially shows a linear increase with electrostatic force, reaching a peak of approximately 0.5 mm s^{-1} at around 0.5 pN. This velocity corresponds to the critical velocity V_{C1} in vacuum, at which the nanotube enters the nonlinear regime. Beyond this point, the velocity exhibits nonlinear behavior, reflecting the same Duffing dynamics observed in the displacement data. The critical velocity V_{C1} represents the threshold beyond which the nanotube's motion is no longer governed by linear dynamics, and nonlinear forces dominate its mechanical response.

In contrast, the results from the downward frequency sweep (Fig. 6.8(b) and (d)) display hysteresis, as confirmed by the power sweep data shown in Fig. 6.7. During the downward sweep (Fig. 6.8(d)), the critical velocity V_{C2} is observed at a lower electrostatic force compared to V_{C1}, indicating a delayed transition into the nonlinear regime. The forward sweep retains higher amplitude and velocity. This is due to the stiffening of the nanotube, which shifts the frequency toward higher values. This frequency shift results in the observed hysteresis loop. In the downward sweep, the system enters a lower-amplitude state sooner, leading to the bistability characteristic of Duffing systems.

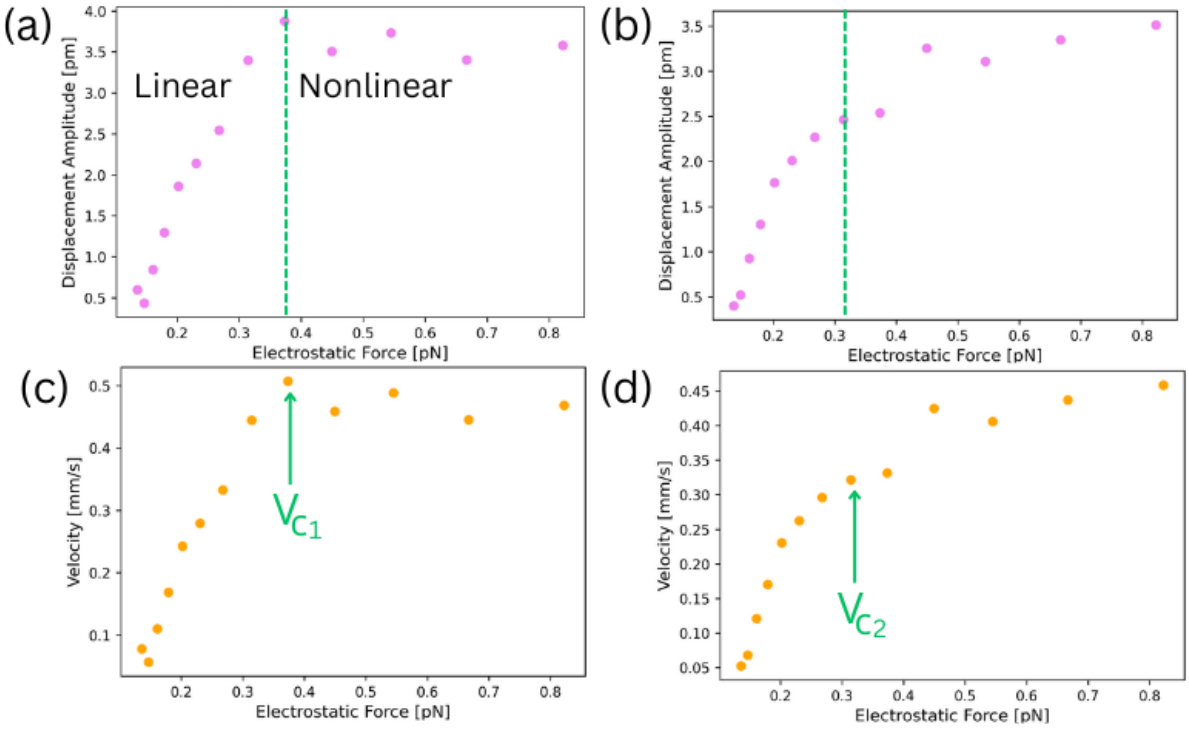

Figure 6.8: (a) Displacement amplitude versus electrostatic force during the upward frequency sweep: The displacement amplitude initially increases linearly with electrostatic force, reaching a maximum of 4 pm at 0.5 pN before transitioning to a nonlinear regime. (b) Displacement amplitude during the downward sweep shows hysteresis, with a delay in the transition to the nonlinear regime compared to the upward sweep. (c) Velocity versus electrostatic force during the upward sweep: The velocity shows a linear increase up to $0.5\,\mathrm{mm\,s^{-1}}$ at 0.5 pN, marking the critical velocity V_{C1} at which the nanotube enters the nonlinear regime, after which it changes nonlinearly. (d) Velocity during the downward sweep exhibits hysteresis, with a slightly lower critical velocity V_{C2}, and lower velocity retained at larger forces compared to the upward sweep due to the stiffening of the nanotube in the forward sweep.

6.5 Summary

This chapter presents an in-depth characterization of a nanotube resonator in vacuum, focusing on its electronic transport properties, mechanical vibrations, and nonlinear dynamics. Key findings include:

1. **Single-electron tunneling and coulomb blockade**: Transport measurements at 7 mK revealed Coulomb blockade phenomena, characterized by diamond-shaped regions of suppressed current. The charging energy of the quantum dot within the CNT ranged from 7 meV to 12 meV. Self-oscillations in the suspended CNT, attributed to the interplay between electronic and mechanical properties, were also observed. The SET tunneling rate, calculated from the current, was approximately 15.6 GHz.

2. **Mechanical vibrations and resonance tuning**: The mechanical vibrations of the CNT were detected, and the resonance frequency was tunable via the DC gate

voltage. The gate voltage adjusted the electrostatic force on the CNT, altering its tension and consequently its natural oscillation frequency, akin to tuning a guitar string. The fundamental mode and higher harmonics were observed, with the third harmonic f_3 showing significant frequency tunability, increasing from 36.8 MHz to 94.7 MHz as the gate voltage was varied from 1.5 V to −1.5 V.

3. **Coupling between mechanical modes and anti-crossing**: Strong coupling between mechanical modes was observed, particularly in the form of mode anti-crossing, where resonance frequencies of different modes interact. This coupling, driven by motion-induced tension, was most notable when the third harmonic f_3 doubled the first harmonic f_1, resulting in energy transfer and avoided crossing in the frequency spectrum. The thermal occupation number $n \approx 0.53$ suggests that the CNT resonator approaches the quantum ground state at millikelvin temperatures.

4. **Influence of single-electron tunneling on resonance**: The resonance frequency was significantly modulated by SET events. At the Coulomb peak, the resonance frequency dipped due to changes in the CNT's spring constant, a result of the electrostatic force from tunneling electrons. The Q factor was lower near the Coulomb peak due to additional damping from electron tunneling, with a reduction from 2971 (away from the peak) to 592 (at the peak).

5. **Bias voltage effects**: The resonance frequency and Q factor were found to depend asymmetrically on the applied bias voltage. Under negative bias, the CNT exhibited clear nonlinear responses, with the Q factor decreasing from 550 at −5 mV bias to 110 at −2 mV, accompanied by a fin-shaped resonance peak characteristic of spring-softening Duffing oscillators.

6. **Nonlinearity and Duffing response**: The CNT resonator exhibited Duffing nonlinearity at higher RF driving powers, transitioning from linear resonance behavior at low powers to a nonlinear regime at higher powers. At −73 dBm, a characteristic "sharkfin" lineshape appeared, and at −72 dBm, bistability and hysteresis emerged, indicating multiple stable resonance frequencies. The critical electrostatic force for this transition was approximately 0.5 pN, corresponding to a displacement of 4 pm and a critical velocity of 0.5 mm s^{-1} during upward frequency sweeps.

In conclusion, this chapter demonstrates the significant interplay between single-electron tunneling and mechanical vibrations in the CNT resonator. The system's behavior is highly tunable through gate voltage, bias voltage, and RF driving power, exhibiting complex nonlinear dynamics such as mode coupling, Duffing nonlinearity, and resonance hysteresis. These findings are crucial for understanding the fundamental quantum and mechanical properties of nanoscale resonators.

Chapter 7: Measurements of a CNT resonator in superfluid ^{4}He

This chapter presents a detailed investigation of the dynamics of a nanotube resonator operating in superfluid ^{4}He at millikelvin temperatures. The aim is to investigate the interactions between the nanotube and the superfluid, with a focus on how helium adsorption, hydrodynamic forces, and quantum vortices affect the resonator's mechanical properties.Additionally, the response of the nanotube to varying radio frequency (RF) drive powers is explored, particularly to understand the nonlinear mechanical effects and the critical velocity at which the nanotube enters the turbulent regime. The study also investigates vortex pinning to the nanotube surface, explored through the generation of Kelvin waves. Finally, the chapter examines how temperature changes near the superfluid transition affect the resonator's behavior.

Note: Although many nanotube resonators have been fabricated and characterized, this thesis presents all the experimental data from the same device in Chapters 6 and 7, including Appendix Fig. A.1.

Cooldowns	**Figures**
1st	Fig. A.1
2nd	Fig. 7.1, Fig. 7.3, Fig. 7.4 and Fig. 7.6
3rd	Fig. 7.9 and Fig. 7.10

Table 7.1: Different cooldowns and the corresponding data.

7.1 Operating CNT resonator in superfluid ^{4}He

To investigate the dynamics of thermal excitation in superfluid ^{4}He, we first cooled a CNT resonator to the base temperature in vacuum, confirming the stability of the resonance frequency at this stage, as shown in Fig. 7.1 (top-left panel). We then gradually introduced ^{4}He gas into the experimental cell through the second capillary (Fig. 5.8) at 1 bar, while keeping the first capillary closed at 5×10^{-6} mbar. These capillaries connect at a tee-junction leading to the cell, which contains the CNT chip. The helium was introduced from the top plate of the fridge (at room temperature) to the mixing chamber plate (at 7 mK). It took about an hour to fill the cell, during which time the pressure equalized between the two capillaries. Throughout this period, the resonance frequency remained stable. However, the temperature of the mixing chamber rose to 1.5 K during the helium injection (Fig. 7.1, bottom-left panel).

After stopping the helium injection, the temperature began to decrease, eventually stabilizing at 135 mK. During this cooling process, we observed an increase in noise and a

gradual decrease in the Q factor of the resonator. Specifically, the Q factor values dropped from 425 to 347 and then to 188 over time, as shown in the 1D resonance cuts in Fig. 7.1 (right panels). Over the next 6–7 hours, the resonance signal completely disappeared, although the background noise remained constant. We initially expected the resonance to shift as the nanotube became covered in helium gas and disappear upon immersion in superfluid helium. However, this delayed disappearance, occurring only several hours later, was unexpected. The discrepancy can be attributed to the experimental setup, particularly the presence of a solid silver plate sinter (see Sec. 5.1.2.1) placed above the nanotube chip, which cooled the helium gas before it interacted with the nanotube.

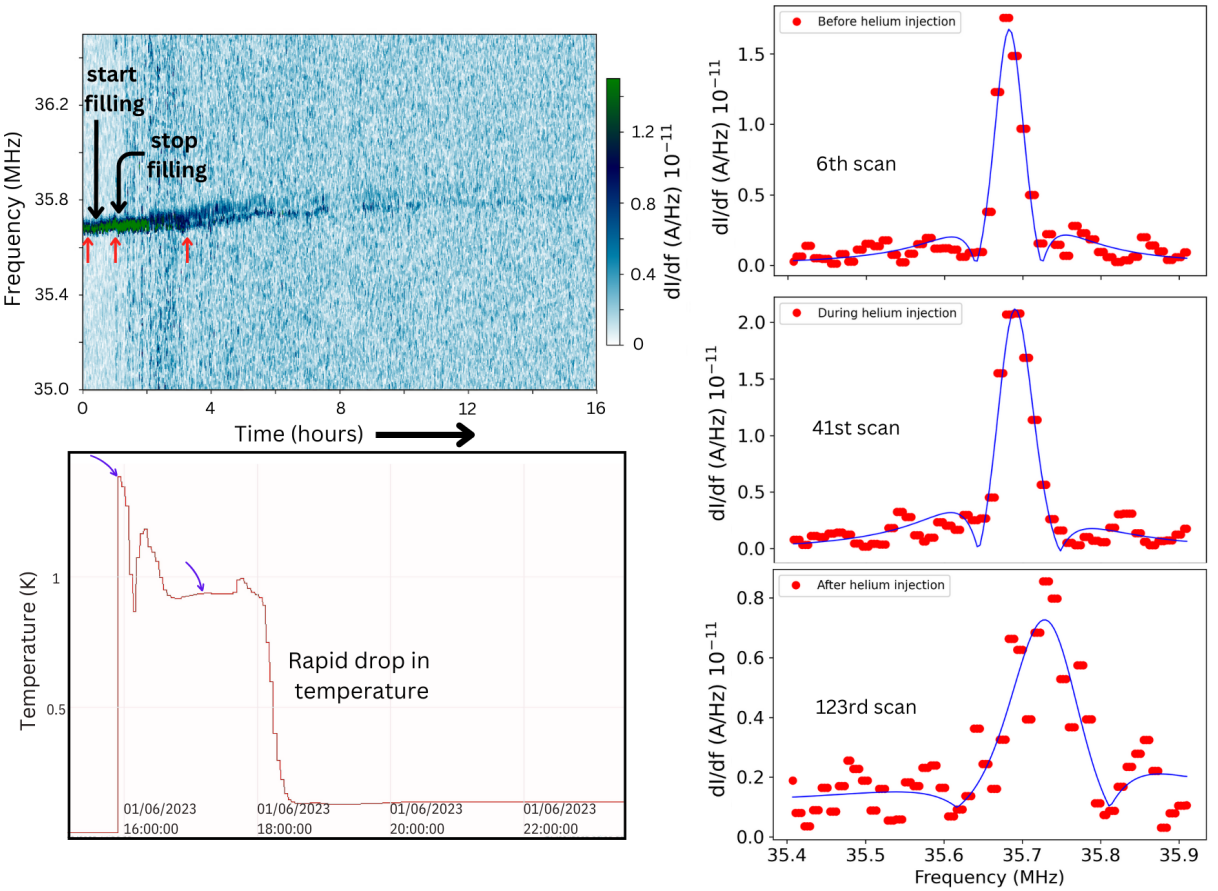

Figure 7.1: Top-left Panel: This panel shows the variation in resonance frequency of the first harmonic of the nanotube resonator before and after the introduction of superfluid ^{4}He at a gate voltage of $V_g = -825\,\text{mV}$. Initially, the frequency remains stable at the base temperature in vacuum. After ^{4}He gas is introduced, the frequency remains stable for a while, but noise increases and the Q factor gradually decreases. The resonance frequency disappears completely within $6 - 7$ hours, likely due to damping induced by remnant vortices generated during the rapid cooling of helium via the Kibble-Zurek mechanism. Bottom-left Panel: The temperature profile of the mixing chamber shows a rise to 1.5 K during the filling of ^{4}He (indicated by blue arrows), followed by a rapid decrease and stabilization at 135 mK after stopping the helium injection. Right Panels: These panels display 1D resonance cuts (marked by red arrows in the top-left panel) before, during, and after helium injection, with Q factors of 425, 347, and 188, respectively, highlighting the gradual noise enhancement and resonance degradation over time after the ^{4}He filling.

7.1.1 Slow response of nanotube resonance upon helium injection

The helium cell setup is illustrated in Fig. 7.2 (left panel). A large silver sinter plate, suspended by two silver wires thermally anchored to the mixing chamber plate, was positioned above the CNT chip. These silver wires ensured efficient cooling of the helium gas as it entered the cell. When the helium gas was introduced through the capillary fill line, it first condensed onto the sinter plate due to its porous structure, acting as a cryopump. This delayed the interaction of helium with the CNT chip, as the sinter absorbed most of the helium gas before it could reach the nanotube.

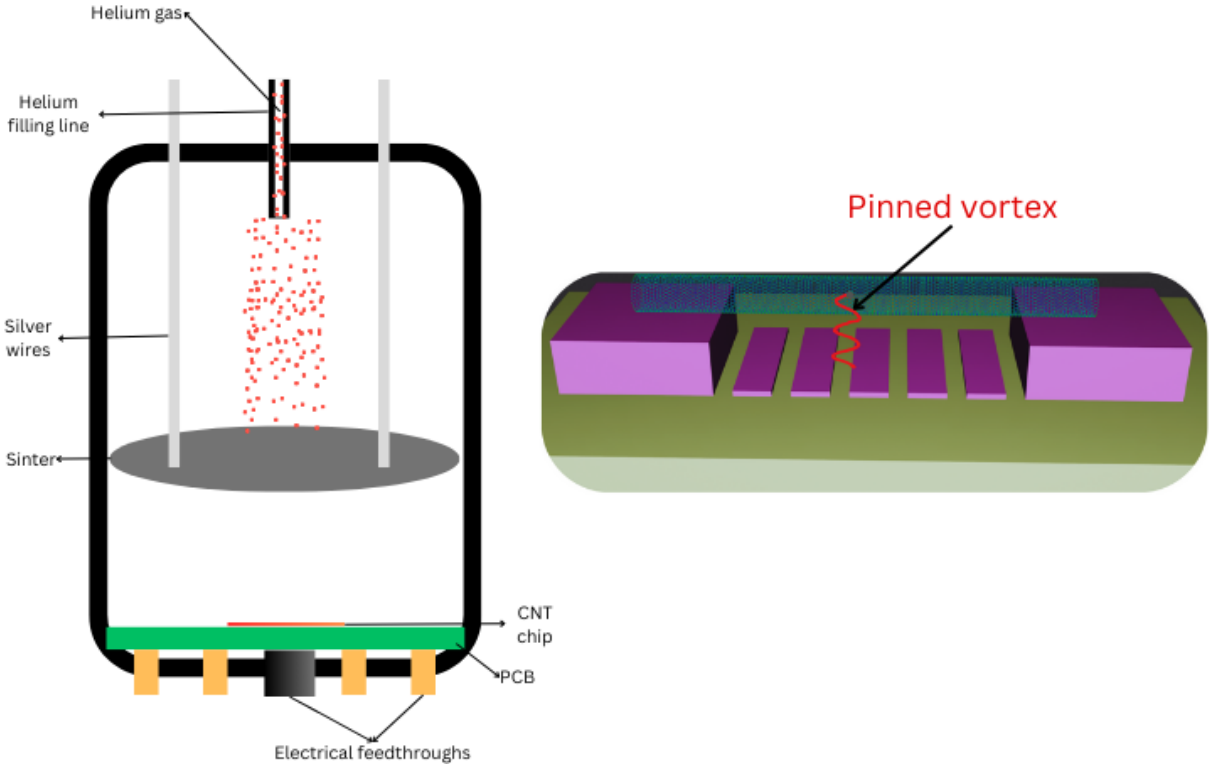

Figure 7.2: Left panel: Schematic of the helium cell showing the sinter plate positioned above the CNT chip. Helium gas (red dots) enters via the helium fill line, first condensing on the sinter plate before interacting with the CNT chip. Right panel: A schematic illustrating the scenario where vortices, generated via the Kibble-Zurek mechanism during rapid cooling, become pinned between the suspended nanotube and the gate electrode beneath it. This vortex pinning is believed to cause the significant noise increase observed in the resonance signal after helium injection, consistent with the phase noise observed by Barkist et al. in MEMS resonators inside superfluid ^{4}He [124].

Initially, no changes were observed in the nanotube resonance as the helium condensed onto the sinter plate. However, after about an hour, the sinter plate reached saturation, and helium began interacting with the nanotube, leading to resonance damping and additional noise. During a previous cooldown (Appendix, Fig. A.1), we observed a slight downward shift, the signal eventually disappeared after helium injection after an extended period. During this cooldown, the faster filling of helium led to an earlier interaction with the nanotube and a more pronounced damping.

Once the nanotube became fully immersed in superfluid helium at millikelvin temperatures, the resonance disappeared, as expected under such conditions. Typically, the resonance reappears as helium condenses at 135 mK when the system transitions into the superfluid phase, but at a lower frequency due to helium adsorption onto the nanotube.

7.1.2 Role of the Kibble-Zurek mechanism

In this experiment, the resonance did not reappear after cooling to 135 mK, despite the expectation that it would reemerge at the same drive power used in vacuum. Instead, the resonance only reappeared after significantly increasing the drive power, suggesting that remnant vortices formed during the rapid cooling from 1.5 K to 135 mK, inhibiting normal resonance behavior in the superfluid. This behavior can likely be explained by the Kibble-Zurek mechanism (KZM), which describes the formation of topological defects, such as quantized vortices, during rapid phase transitions [125, 9]. In this case, the transition was from a normal fluid state at 1.5 K to superfluid helium at 135 mK. As helium was injected at a high flow rate and cooled rapidly from room temperature to millikelvin temperatures, the system's fluctuations froze before reaching equilibrium, resulting in the formation of these remnant vortices [126].

These vortices dampened the nanotube's motion, preventing the resonance from reappearing at normal power levels. This behavior was also observed during the first cooldown, where the rapid filling of helium caused the system to heat up to 1.5 K. Although this temperature is below the superfluid transition threshold, the helium retained a significant normal component, which affected the system's behavior. After the helium injection was stopped, the system cooled to 135 mK, fully immersing the nanotube in superfluid helium. However, a superfluid ^{4}He film in the capillaries likely prevented further cooling of the mixing chamber by maintaining a thermal connection between the still plate and the mixing chamber of the cryostat. To disconnect these two stages and achieve the cryostat's base temperature, a ^{4}He film burner is needed.

Therefore, behavior suggests that the damping observed in the nanotube's motion, even at very low temperatures, was due to the quantized vortices generated by the Kibble-Zurek mechanism during the rapid cooling phase, rather than by thermal excitations from the normal helium component.

7.1.3 Noise observations after helium injection

Following the discussion of the Kibble-Zurek mechanism, we also observed a significant increase in background noise immediately after the helium injection (Fig. 7.1 (top-left panel)), particularly as the helium interacted with the nanotube. This noise was not present during the vacuum measurements, where the background was normal, but became prominent once helium was introduced, even at the lowest temperatures. We attribute this noise to vortex pinning between the nanotube and the gate electrodes beneath it, as illustrated in Fig. 7.2 (right panel). Defects on the nanotube, as well as impurities or melting in the gate electrodes, can facilitate vortex pinning. The vortices generated through the Kibble-Zurek mechanism likely became pinned in the system. The minimum energy required for a vortex to attach to a surface is explained in detail in Sec. 7.4.3. A similar phenomenon was observed by Barquist et al. [124], they detected noise in a MEMS response in superfluid ^{4}He, linked to vortex pinning between the resonator and the substrate. The recurring observation of this noise at lowest temperatures upon

helium interaction across multiple cooldowns (Fig. 7.9 and the Appendix, Fig. A.1) further supports that vortex dynamics are responsible for the observed increase in noise.

7.2 Downward frequency shift after ^{4}He injection

After injecting ^{4}He into the system, a broad frequency sweep was conducted for a range of gate voltages, similar to the measurement performed in vacuum (Fig. 6.2). Initially, no resonances were detected within the helium environment under the same measurement parameters used in vacuum (Fig. 7.3, top panel).
Upon increasing the driving power from $-48\,\mathrm{dBm}$ to $-28\,\mathrm{dBm}$, multiple resonances reappeared, as shown in Fig. 7.3 (bottom panel). The lock-in signal intensity, representing the resonance strength of the nanotube, revealed distinct vibrational modes of the nanotube in superfluid ^{4}He, denoted as f_0, f_1, f_2, and f_3. These modes display a downward frequency shift compared to their counterparts in vacuum, as shown in Fig. 6.2. The observed downward shift in resonance frequency can be attributed to the adsorption of helium atoms onto the surface of the nanotube, forming solid layers of ^{4}He and consequently increasing the effective mass of the nanotube. This increase in mass results in the reduced vibration frequencies.
Notably, the higher harmonic modes exhibit a more pronounced frequency shift than the fundamental mode. This behavior can be explained by differences in the distribution of helium atoms along the nanotube in various vibrational modes, which more strongly affect the higher harmonics. The fundamental frequency of a CNT resonator, f_0, depends on the mass, length, and tension of the nanotube and is given by

$$f_0 = \frac{1}{2L}\sqrt{\frac{T}{m}},$$

where m is the linear mass density. Higher harmonic frequencies are integer multiples of f_0, represented by

$$f_n = n \cdot f_0$$

for the n-th harmonic. Helium adsorption increases the nanotube's mass, leading to a modified linear mass density $m + \Delta m$. Thus, the resonance frequencies adjust to

$$f_0' = \frac{1}{2L}\sqrt{\frac{T}{m + \Delta m}}$$

for the fundamental mode and

$$f_n' = n \cdot f_0'$$

for the n-th harmonic. The corresponding frequency shifts,

$$\Delta f_0 = f_0 - f_0'$$

and

$$\Delta f_n = f_n - f_n',$$

gives that

$$\Delta f_n = n \cdot \Delta f_0,$$

indicating that higher harmonic modes exhibit a shift that is n times that of the fundamental mode. This conclusion aligns with experimental data, where higher harmonics are more significantly affected by the increased mass due to helium adsorption.
The adhesion of helium atoms on the surface of the nanotube likely forms solid layers of ^{4}He, increasing the mass and decreasing the resonance frequency. This behavior is consistent with the expected influence of helium atom distribution on different vibrational modes, especially the higher harmonics.

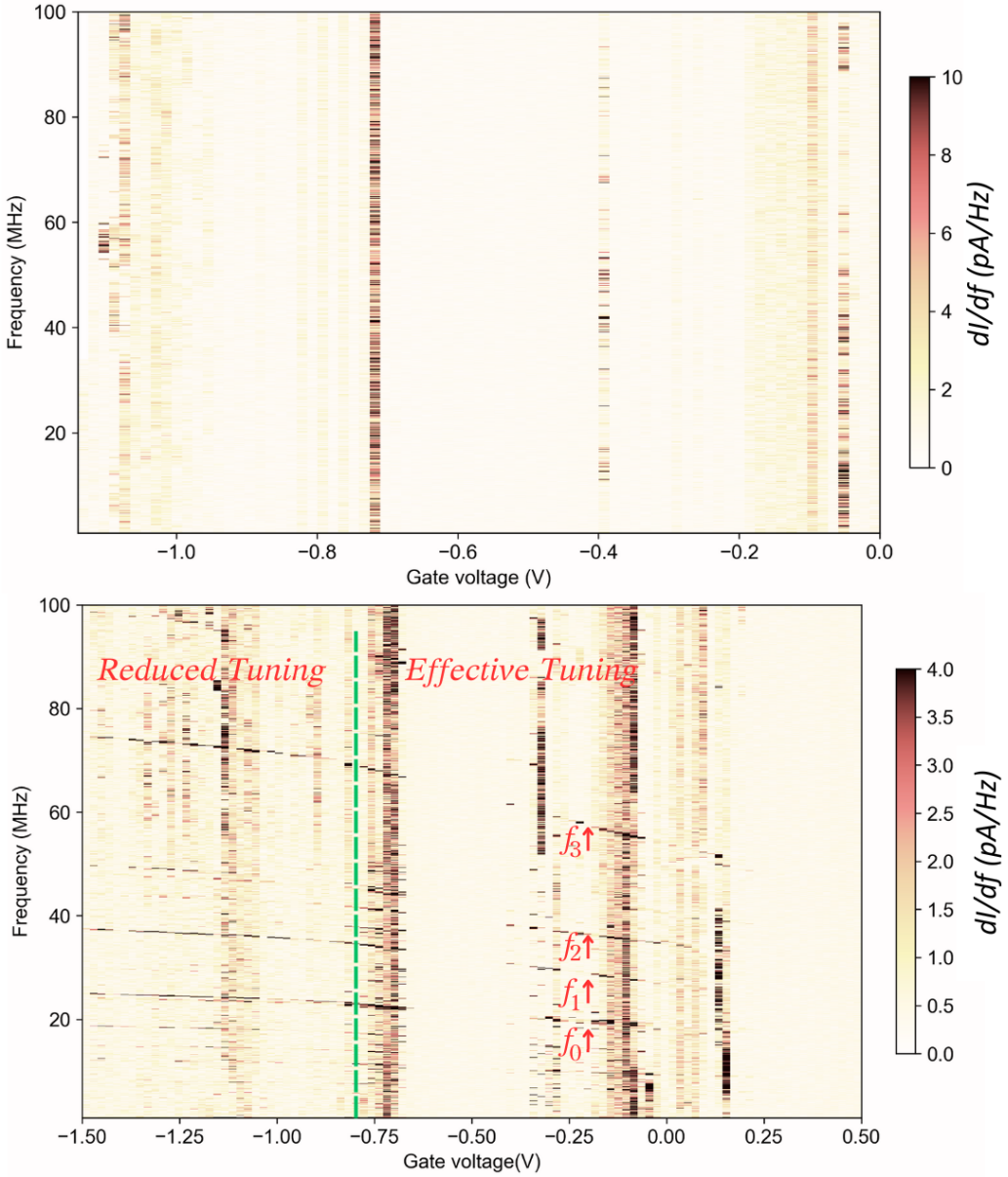

Figure 7.3: Top panel: No resonances detected in superfluid helium at a driving power of −48 dBm. Bottom panel: Resonances reappear at −28 dBm, demonstrating the effect of helium adsorption on the nanotube. The downward shift in vibrational modes compared to vacuum is attributed to helium mass loading. The green dashed line separates two regions of gate voltage tunability: (1) a region with effective frequency tuning up to −0.8 V, and (2) a region with reduced tunability from −0.8 V to −1.5 V, due to surface tension effects and increasing electrostatic screening.

7.2.1 Frequency shift due to helium adsorption and hydrodynamic drag

The downward frequency shift observed in the CNT immersed in superfluid helium is primarily caused by two factors: (i) the hydrodynamic contribution from the surrounding helium fluid, and (ii) mass loading from helium adsorption onto the nanotube surface. In the following, we calculate both contributions and estimate the number of helium layers adsorbed onto the nanotube by comparing the frequencies in vacuum (Fig. 6.2) with those measured in superfluid helium (Fig. 7.3) at $V_g = 0$ V.

Observed frequency shift

The CNT's resonance frequency in vacuum for the third harmonic is $f_{\text{vac}} = 63.2\,\text{MHz}$, which decreases to $f_{\text{He}} = 54\,\text{MHz}$ when immersed in superfluid ^{4}He. The total observed frequency shift is:

$$\Delta f_{\text{exp}} = f_{\text{vac}} - f_{\text{He}} = 63.2\,\text{MHz} - 54\,\text{MHz} = 9.2\,\text{MHz}.$$

Hydrodynamic contribution

The frequency shift due to hydrodynamic drag is caused by the interaction between the oscillating nanotube and the surrounding helium fluid. Using the model from Eq.3.4, the hydrodynamic shift caused by the fluid back-flow around the nanotube is:

$$\left(\frac{f_0}{f_H}\right)^2 - 1 = \beta \frac{\rho_{\text{H}} V}{m_{\text{e}_{\text{NT}}}},$$

where β is the geometric factor, ρ_{H} is the helium density, V is the nanotube volume, and $m_{\text{e}_{\text{NT}}}$ is the effective mass of the nanotube. This result reflects the contribution of helium's hydrodynamic drag to the total frequency shift. This gives:

$$\Delta f_{\text{hydro}} = 1.57\,\text{MHz} \quad \text{(for the third harmonic)}.$$

Helium adsorption contribution

The remaining frequency shift is attributed to mass loading from helium adsorption onto the nanotube surface. The shift due to helium adsorption is:

$$\Delta f_{\text{ads}} = \Delta f_{\text{exp}} - \Delta f_{\text{hydro}} = 9.2\,\text{MHz} - 1.57\,\text{MHz} = 7.63\,\text{MHz}.$$

To estimate the number of helium layers adsorbed, we use the areal density of helium atoms per layer, approximately 11 atoms/nm^2 [93]. The mass of one helium layer can be computed as:

$$m_{\text{layer}} = \text{areal density} \times A \times m_{\text{He atom}} = 6.89 \times 10^{-22}\,\text{kg}.$$

The total mass of adsorbed helium is given by:

$$m_{\text{He}} = 3.83 \times 10^{-21}\,\text{kg},$$

corresponding to approximately 5.56 helium layers:

$$N = \frac{m_{\text{He}}}{m_{\text{layer}}} = \frac{3.83 \times 10^{-21}}{6.89 \times 10^{-22}} \approx 5.56\,\text{layers}.$$

Results for different harmonic modes

Following similar calculations for different harmonic modes at $V_g = 0$ V, we obtain the following results:

- For the **fundamental mode** ($f_{vac} = 21\,\text{MHz}, f_{He} = 18\,\text{MHz}$), the hydrodynamic shift is 0.52 MHz, and the adsorption shift is 2.48 MHz, corresponding to 5.43 helium layers.
- For the **first harmonic** ($f_{vac} = 32\,\text{MHz}, f_{He} = 27\,\text{MHz}$), the hydrodynamic shift is 0.80 MHz, and the adsorption shift is 4.20 MHz, corresponding to 6.09 helium layers.
- For the **second harmonic** ($f_{vac} = 42.25\,\text{MHz}, f_{He} = 34.5\,\text{MHz}$), the hydrodynamic shift is 1.05 MHz, and the adsorption shift is 6.70 MHz, corresponding to 7.52 helium layers.
- For the **third harmonic** ($f_{vac} = 63.2\,\text{MHz}, f_{He} = 54\,\text{MHz}$), the hydrodynamic shift is 1.57 MHz, and the adsorption shift is 7.63 MHz, corresponding to 5.56 helium layers.

These results show that higher harmonics experience more pronounced frequency shifts due to increased sensitivity to the adsorbed helium mass, in line with previous estimate.

7.2.2 Tuning behavior of nanotube frequencies in superfluid helium

In addition to the downward shift of resonance frequencies, we observed a significant change in the tunability of the nanotube resonance frequencies as a function of gate voltage in superfluid helium compared to vacuum. In vacuum, the frequencies are highly tunable with gate voltage, especially at larger negative voltages, where the tuning effect is most pronounced. However, in superfluid helium, two distinct regions of tuning behavior emerged, as shown in the bottom panel of Fig. 7.3 (dashed green line).

From 0.25 V to −0.8 V, the frequencies exhibit some degree of tunability, though less pronounced than in vacuum. Beyond −0.8 V, the tuning becomes even more suppressed as the gate voltage decreases to −1.5 V. This reduction in tunability reflects the combined influence of mass loading through surface tension and electrostatic screening, which are unique to the superfluid helium environment [93, 127].

7.2.2.1 Effect of surface tension and electrostatic screening

The reduced tunability of resonance frequencies in superfluid helium is primarily due to two factors: surface tension, and electrostatic screening by the adsorbed helium layers.

- **Surface tension**: The adsorbed helium layers introduce surface tension that affects the nanotube's spring constant. As more helium accumulates, the spring constant increases, effectively stiffening the nanotube and reducing its mechanical flexibility. This stiffening limits the nanotube's ability to respond to gate voltage changes, leading to a diminished tunability of the resonance frequency [128].

- **Electrostatic screening**: We attribute electrostatic screening as the most critical factor influencing the reduced tunability, caused by the adsorbed helium layers. In superfluid helium, the helium layers act as a dielectric barrier, weakening the electrostatic coupling between the gate and the nanotube. As the gate voltage increases, these helium layers partially screen the electric field, reducing the effect of the gate voltage on the nanotube. This screening becomes more pronounced at larger negative gate voltages, affecting the tunability of the resonance frequency.

At large negative gate voltages, the enhanced electrostatic screening by the helium layers significantly reduces the ability of the gate voltage to induce strain in the nanotube, thus limiting frequency tuning. The dielectric nature of the helium atoms increasingly shields the electric field, preventing it from fully reaching the nanotube. This behavior contrasts with vacuum conditions, where the absence of a dielectric allows for stronger electrostatic interaction and greater tunability of the resonance frequency.

7.2.2.2 Effect of helium layer surface tension on nanotube spring constant

The surface tension of the helium layers significantly affects the spring constant of the nanotube, which, in turn, influences its mechanical response and tunability. As helium atoms adsorb onto the nanotube surface, they increase the effective radius of the nanotube and introduce additional surface tension, which modifies the nanotube's spring constant. This effect is particularly pronounced in superfluid helium, where the helium layers are uniform and exert a quantifiable influence on the nanotube's mechanical properties.

The spring constant contribution from the helium layers, k_{He}, can be expressed as [93]:

$$k_{\mathrm{He}} = \gamma \frac{\pi^3 r_{\mathrm{He}}}{L}, \tag{7.1}$$

where r_{He} is the radius of the helium layer, L is the length of the nanotube, and γ is the surface tension of the helium layer. The surface tension γ influences k_{He}, and as helium layers form, both the surface tension and the mass increase, contributing to reduced tunability of the nanotube's resonance frequency in response to gate voltage.

We can rearrange Eq. 7.1 to solve for the surface tension γ:

$$\gamma = \frac{k_{\mathrm{He}} L}{\pi^3 r_{\mathrm{He}}}. \tag{7.2}$$

The spring constant k_{He} can be derived from the observed shift in resonance frequency between the pristine nanotube and the helium-coated nanotube. The resonance frequency of a helium-coated nanotube is given by:

$$f_1 = \frac{1}{2\pi} \sqrt{\frac{k_{\mathrm{NT}} + k_{\mathrm{He}}}{m_{\mathrm{NT}} + m_{\mathrm{He}}}}, \tag{7.3}$$

where f_1 is the resonance frequency, k_{NT} is the nanotube's intrinsic spring constant, m_{NT} is the nanotube mass, and m_{He} is the adsorbed helium mass.

Assuming the mass change is relatively small, the frequency shift Δf_{ads} due to helium adsorption can be approximated as:

$$\frac{f_1}{f_0} \approx 1 - \frac{k_{\mathrm{He}}}{2k_{\mathrm{NT}}}, \tag{7.4}$$

where $f_0 = 63.2\,\text{MHz}$ is the resonance frequency in vacuum, and $\Delta f_{\text{ads}} = 7.63\,\text{MHz}$ represents the frequency shift caused by helium adsorption. Thus, the relationship between the frequency shift and k_{He} becomes:

$$\frac{\Delta f_{\text{ads}}}{f_0} = \frac{k_{\text{He}}}{2k_{\text{NT}}}. \tag{7.5}$$

Solving for k_{He}, we get:

$$k_{\text{He}} = 2k_{\text{NT}}\frac{\Delta f_{\text{ads}}}{f_0}. \tag{7.6}$$

By substituting $k_{\text{NT}} = 1.18 \times 10^{-7}\,\text{N/m}$, $\Delta f_{\text{ads}} = 7.63\,\text{MHz}$, and $f_0 = 63.2\,\text{MHz}$, we find:

$$k_{\text{He}} = 2 \times 1.18 \times 10^{-7} \times \frac{7.63}{63.2} = 2.85 \times 10^{-8}\,\text{N/m}. \tag{7.7}$$

This result shows that, although k_{He} is an order of magnitude smaller than k_{NT}, it still makes a significant contribution to the overall spring constant and mechanical stiffness of the nanotube.

Finally, using $L = 1.5 \times 10^{-6}\,\text{m}$ and $r_{\text{He}} \approx 1.77 \times 10^{-9}\,\text{m}$, we can calculate the surface tension from Eq. 7.2 as:

$$\gamma = \approx 7.77 \times 10^{-7}\,\text{N/m}. \tag{7.8}$$

This calculated surface tension γ is approximately $7.77 \times 10^{-7}\,\text{N/m}$, which aligns with expectations for helium films. The surface tension of helium layers depends on various factors, including chemical potential, film thickness, surface coverage, and temperature, all of which play a role in mechanical response [127].

The quantitative impact of surface tension and spring constant changes underscores how helium adsorption alters the resonance behavior of the nanotube and limits its tunability with gate voltage.

Connecting observations to our data

The reduction in tunability beyond $-0.8\,\text{V}$ in our data arises from the combined effects of mass loading, surface tension, and partial electrostatic screening by the adsorbed helium layers. As helium accumulates, the nanotube becomes heavier, and the increasing surface tension stiffens the spring constant, reducing its responsiveness to gate voltage.

At low negative gate voltages, the resonance frequency is effectively tuned, but as the voltage becomes more negative, these combined effects become more pronounced, leading to a marked decrease in tunability. This behavior is consistent with our data and underscores the distinct influence of superfluid helium compared to vacuum.

Despite this reduction in tunability, the resonance frequencies of the nanotube remain adjustable in superfluid helium, which is a key advantage of CNT resonators. This allows for the exploration of various frequency-dependent phenomena, such as acoustic modes in cavities [19], phase transitions [129], and resonant Kelvin waves in quantized vortices [17, 18].

7.3 Response with RF power in ^{4}He

We now examine how RF driving power affects the resonance dynamics of the nanotube within superfluid ^{4}He. By lowering the mixing chamber temperature to 85 mK from

135 mK through controlled helium film pumping, we monitored the nanotube's response over a frequency range of 17.1 MHz to 18.1 MHz for both upward and downward frequency sweeps, starting with a drive power of −38 dBm.

Increasing the RF power initially broadens the resonance peak and strengthens the response, indicating a reduction in the quality factor. As the nanotube enters the nonlinear regime at higher powers (discussed further in Chapter 6), the resonance broadening becomes more pronounced. This behavior contrasts with the Duffing non-linearity seen in vacuum, where hysteresis typically occurs during frequency sweeps. In superfluid helium, no such hysteresis is observed. The right panels of Fig. 7.4 show 1D cuts from the forward and reverse sweeps at three power levels: −30 dBm, −25 dBm, and −18 dBm.

A drift of 19.92 kHz (detailed calculation shown in Sec. A.5) in peak positions is observed for both forward and reverse sweeps across all power levels. This drift is caused by the lock-in amplifier's time constant and has been accounted for in the 1D plots. A similar drift was observed in vacuum measurements (Fig. 6.7), but in vacuum, the 1D cuts were derived directly from the current through the nanotube, measured with a DMM. In contrast, significant damping in the superfluid environment prevents detecting the resonance through the CNT current alone. However, the lock-in signal clearly shows the absence of hysteresis, suggesting that the nonlinearity here arises from interactions between the nanotube and superfluid ^{4}He, rather than intrinsic mechanical properties.

The key difference between the superfluid helium and vacuum environments is that in helium, nonlinearity stems from interactions between the resonator and quantum vortices. These vortices absorb mechanical energy from the nanotube, causing nonlinear damping. As RF power increases, these interactions intensify, broadening the resonance peak until the resonance eventually disappears at a critical power level of approximately −21 dBm.

The disappearance can be attributed to energy transfer from the nanotube to the vortices. Once the nanotube reaches a critical velocity, it generates and transfers energy to the vortices, exciting vortex waves (Kelvin waves) along the vortex lines. This energy transfer leads to increased damping, and as the vortices accumulate energy, they detach from the nanotube, resulting in overdamping and the disappearance of resonance.

Interestingly, as the RF power increases further, the resonance reappears. This suggests that the vortices either detach from the resonator or reorganize into a more stable configuration, allowing the nanotube to resume oscillations. The absence of hysteresis and bistability in these power sweeps confirms that vortex dynamics, rather than mechanical Duffing nonlinearity, dominate the nanotube's behavior in superfluid ^{4}He.

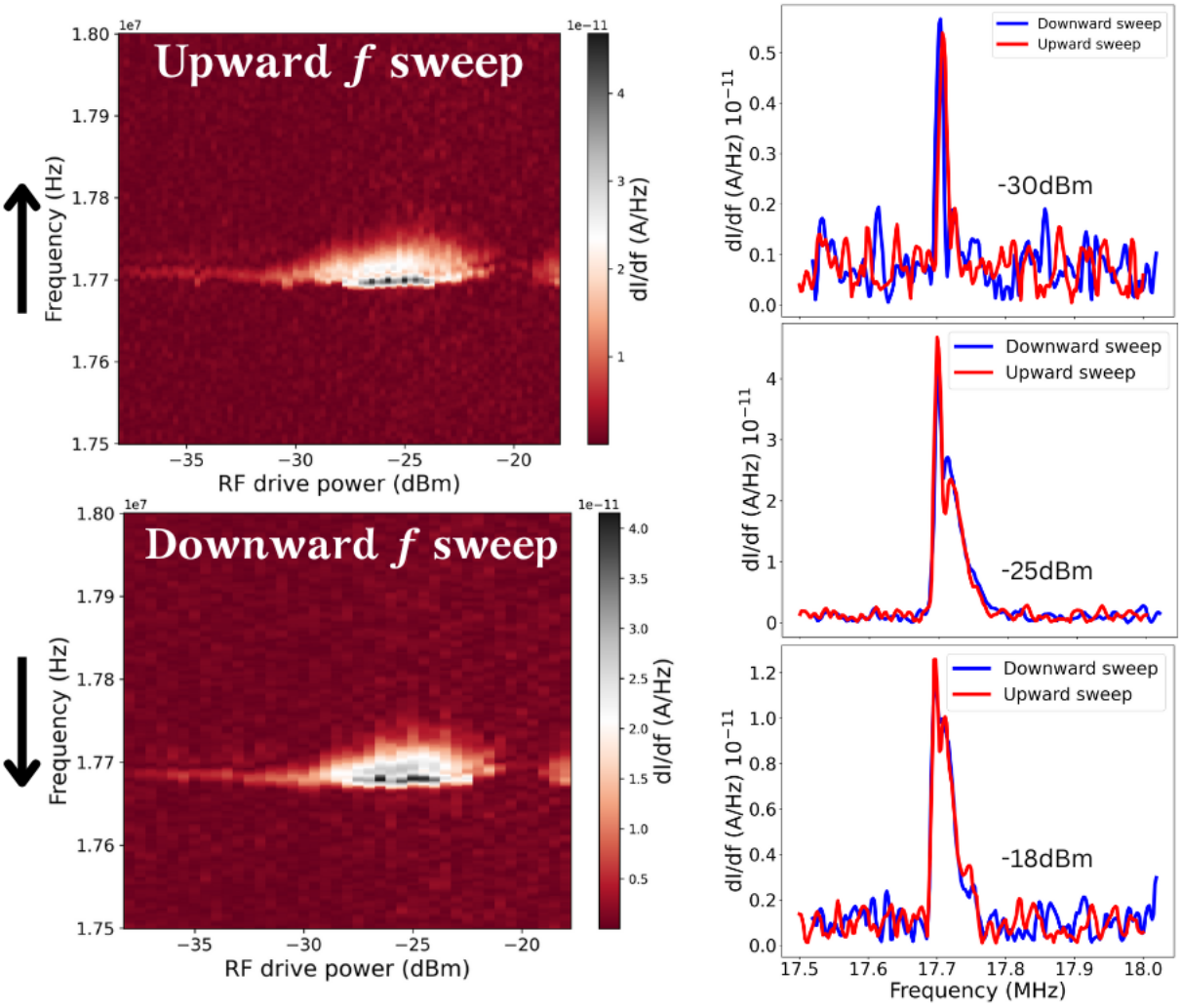

Figure 7.4: Top-left: Resonance frequency sweep upwards as a function of driving power. Bottom-left: Resonance frequency sweep downward. These graphs demonstrate changes in nanotube resonance behavior, including broadening, attenuation, and disappearance at critical power levels in superfluid ^{4}He. The measurements are conducted at a DC gate voltage of $-128.5\,\mathrm{mV}$. Right panels: 1D cuts from forward and reverse sweeps were taken at three different powers: $-30\,\mathrm{dBm}$, $-25\,\mathrm{dBm}$, and $-18\,\mathrm{dBm}$. Unlike in vacuum, the frequency sweeps in superfluid ^{4}He do not exhibit hysteresis or bistability at any power level. However, we observe a consistent drift in the peak positions of 19.92 kHz, caused by the lock-in amplifier's time constant. This drift has been accounted for in the 1D plots.

Increasing RF power reveals that quantum vortices play a crucial role in the nanotube's nonlinear dynamics in superfluid helium. These interactions cause significant damping and lead to the temporary disappearance of the resonance. As power continues to rise, the reorganization or detachment of vortices allows the resonance to reemerge, underscoring the intriguing dynamics between the resonator and the superfluid environment.

7.3.1 Displacement and velocity response of nanotube to electrostatic force in superfluid helium

Figure 7.5 presents the displacement and velocity data of the nanotube resonator, obtained from RF power sweeps conducted in superfluid helium (see Fig. 7.4). These measurements provide insights into the mechanical behavior of the nanotube under electrostatic forces and how quantum vortices in superfluid helium affect its dynamics.

Figure 7.5(a) shows the displacement as a function of electrostatic force during an upward frequency sweep. Initially, the displacement increases linearly, reaching approximately 5 pm at 0.7 pN, near the threshold for entering the nonlinear regime. Beyond this point, the displacement peaks at 9 pm around 1 pN, followed by a sharp drop. This rapid decline in displacement indicates the onset of strong damping, likely caused by interactions between the nanotube and quantized vortices in the superfluid. Quantum vortices, as described by London [130], Feynman [131], and Anderson [132], disrupt the steady-state motion of mechanical resonators through vortex shedding or pinning, which absorbs energy and causes the resonance to disappear at higher electrostatic forces. This behavior occurs after the critical velocity V_{cs} is reached in superfluid helium.

The velocity data in Fig. 7.5(c) exhibits a similar pattern to the displacement. Initially, the velocity increases linearly with electrostatic force, reaching 0.5 mm s^{-1} around 0.7 pN in superfluid helium. For comparison, in vacuum (Fig. 6.8(c)), the same velocity is achieved at a lower electrostatic force of 0.4 pN, corresponding to the critical velocity V_{c1}. The higher force required in helium suggests additional damping due to excitations in the superfluid. As the system transitions into the nonlinear regime, the velocity peaks at around 0.9 mm s^{-1} near 1 pN, followed by a sharp decline as the system enters a turbulent state. This transition marks increased damping due to vortex formation, with the resonance disappearing completely as the velocity drops to zero, consistent with the critical velocity V_{cs} for vortex generation.

After the initial resonance disappearance, the velocity rises again as the electrostatic force continues to increase. This suggests that vortices either detach from the resonator or reorganize into a more stable configuration, allowing the nanotube to resume oscillations. A similar phenomenon was observed by Barquist et al. [124] in their studies on a tuning fork, where a sharp drop in velocity marked the transition to turbulence, followed by a recovery of the resonance. In our case, the smaller size of the nanotube makes it more sensitive to vortex interactions, leading to a complete damping and temporary disappearance of resonance. This re-emergence supports the role of vortex dynamics, particularly vortex generation and detachment, in the system's nonlinear response, as seen in previous studies by Barquist et al. [79] and Guthrie et al. [133], who explored vortex-induced dissipation and vortex pinning in nanomechanical resonators.

The downward frequency sweep, shown in Figs. 7.5(b) and 7.5(d), follows similar trends to the upward sweep. Both displacement and velocity exhibit comparable behavior, with no significant hysteresis between the sweeps. This absence of hysteresis suggests that the observed damping and disappearance of resonance are primarily due to quantum vortex interactions rather than the intrinsic mechanical properties of the nanotube. The consistent behavior in both sweeps confirms that vortex dynamics dominate the nanotube's motion in superfluid helium.

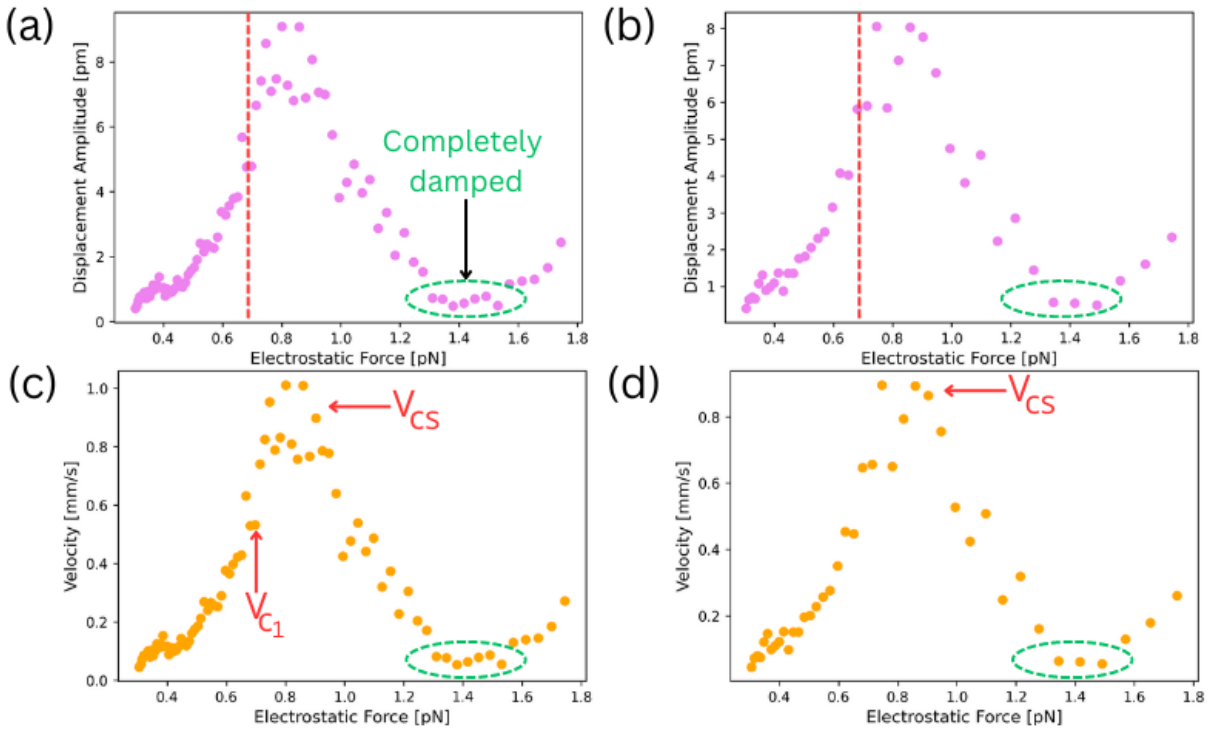

Figure 7.5: (a) Displacement as a function of electrostatic force during the upward frequency sweep: The displacement peaks at around 9 pm near 1 pN before sharply decreasing, indicating strong damping effects due to quantum vortex interactions. The red dashed line marks the transition to the nonlinear regime, while the green circle highlights the region where the resonance is completely damped. (b) Displacement during the downward sweep shows similar trends, confirming the absence of hysteresis and supporting the role of vortex dynamics. (c) Velocity as a function of electrostatic force during the upward frequency sweep: Velocity reaches V_{c1} at $0.5\,\mathrm{mm\,s^{-1}}$ near 0.7 pN in superfluid, while in vacuum (Fig. 6.8(c)) only 0.4 pN is required to achieve the same velocity. Then, the velocity reaches V_{cs} at $0.9\,\mathrm{mm\,s^{-1}}$ near 1 pN in superfluid helium before sudden decline, this sharp drop in velocity marks the transition to the turbulent regime. The velocity rises again as the electrostatic force increases, indicating vortex detachment or reorganization. (d) The velocity during the downward sweep mirrors the upward sweep, reinforcing the observation that vortex dynamics dominate the system's nonlinear behavior. The green circle in all subfigures highlights the region where the resonance is completely damped, with no measurable resonant response.

7.4 Kelvin wave-induced sidebands in a CNT resonator in superfluid helium

Building on our earlier observations, we continued to monitor the resonance behavior of a CNT resonator immersed in superfluid ^{4}He as a function of the RF drive power. To improve detection sensitivity, the dc gate voltage was maintained near the Coulomb peak, where strong coupling between single-electron tunneling and the mechanical motion of the CNT enhances the signal-to-noise ratio (SNR). However, this gate voltage tuning also modulates the frequency of the nanotube. This setup allowed us to detect subtle interactions between the CNT resonator and the surrounding superfluid.

As the RF drive power increased, a sideband appeared at 18.3 MHz, offset by 400 kHz from the CNT primary resonance at 18.7 MHz (Fig. 7.6). This sideband emerged around −41 dBm and intensified as the RF power increased. A second, weaker sideband was detected at −31 dBm, but our analysis focuses on the more prominent first sideband.

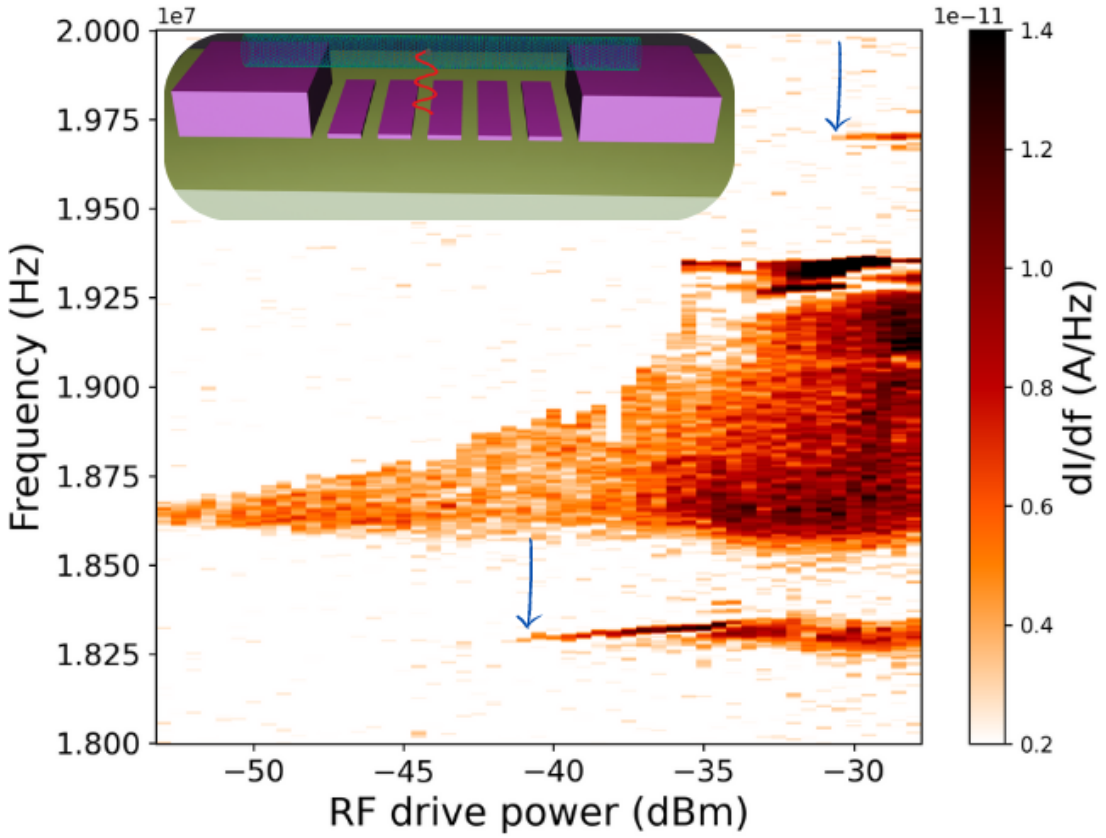

Figure 7.6: This graph shows the resonance frequency response of the CNT resonator as a function of RF drive power near the Coulomb peak ($V_g = -105\,\text{mV}$). A prominent sideband is observed 400 kHz away from the central resonance at 18.7 MHz, appearing at −41 dBm and attributed to the third harmonic of Kelvin waves propagating along a vortex pinned to the nanotube. A second, weaker sideband is detected at −31 dBm, but due to its lower intensity, it is less well-resolved and was not analyzed further. Inset: A schematic illustrating the scenario of a vortex pinned between the suspended nanotube and the gate electrode beneath it.

7.4.1 Origin of the sidebands

We initially hypothesized that the observed sidebands might result from acoustic emissions. Using the classical acoustic model $f = \frac{v}{2L}$, where $v = 238\,\text{m}\,\text{s}^{-1}$ (speed of sound in superfluid helium) and $L = 1.5\,\mu\text{m}$ (CNT length), we calculated a resonance frequency of 79.34 MHz, far above the observed sideband spacing. This discrepancy ruled out acoustic resonance as the source of the sidebands.

Instead, we considered Kelvin waves, helical oscillations propagating along quantized vortices pinned between the CNT and the gate electrode (Fig. 7.6). The Kelvin wave dispersion relation, given by [134], is:

$$\omega = vk^2 = \frac{\kappa}{4\pi}k^2 \log\left(\frac{1}{ka}\right),$$

where $\kappa = 0.0997 \times 10^{-6}\,\mathrm{m^2\,s^{-1}}$ is the quantum of circulation, $k = \frac{j2\pi}{L}$ is the wavenumber, $a = 1 \times 10^{-10}\,\mathrm{m}$ is the vortex core radius, and L is the wavelength. In our device geometry, the nanotube is positioned 175 nm from the gate, resulting in a wavelength $L = 350\,\mathrm{nm}$.

We calculated the first three harmonics of the Kelvin waves to be 2.6 MHz, 9.2 MHz, and 19.1 MHz. Notably, the third harmonic (19.1 MHz) closely matches the CNT resonance frequency of 18.7 MHz, with a 400 kHz difference corresponding to the sideband. This suggests that the sideband is produced by frequency mixing between the CNT's mechanical oscillations and the Kelvin waves, confirming that the sideband spacing matches the predicted Kelvin wave frequency.

Our observation of a 400 kHz sideband, offset from the primary resonance frequency of 18.7 MHz, is consistent with the theoretical predictions of resonant coupling between mechanical oscillations and Kelvin wave modes. Specifically, we observe that the sideband emerges when the resonance frequency of the nanotube aligns with the third harmonic of Kelvin waves. This behavior matches well with the findings of Nakagawa *et al.* [135], who numerically studied vortex dynamics in superfluid helium and demonstrated that vortex damping peaks when the oscillation frequency of the mechanical oscillator coincides with the Kelvin wave mode frequency.

The tunability of the CNT resonator is key to observing Kelvin wave-induced sidebands. By adjusting the gate voltage near the Coulomb peak, we can precisely control the nanotube's mechanical resonance frequency, improving detection sensitivity to subtle interactions with the surrounding superfluid. Matching the resonance frequency between the CNT and Kelvin waves–challenging in conventional systems–is essential for detecting these sidebands, as frequency mismatches have previously hindered similar experiments. Other researchers, including Guthrie et al. [133] and Kamppinen et al. [16], have similarly proposed to detect Kelvin waves experimentally, but these efforts have yet to achieve successful detection due to challenges with frequency alignment and sensitivity.

7.4.2 Non-linear power dependence and sideband dynamics

The intensity of Kelvin wave-induced sidebands is closely tied to the RF drive power, with the first sideband appearing around −41 dBm. We observe a power-law dependence of sideband intensity I_{sideband} on RF drive power P:

$$I_{\mathrm{sideband}} \propto P^{\alpha}$$

where α is the scaling exponent characterizing the non-linearity of the system. Similar vortex-based systems, such as those studied by Nakagawa *et al.* [135], demonstrated that Kelvin waves can scale quadratically with input power, corresponding to $\alpha \approx 2$ in highly non-linear regimes.

Our experimental results show two distinct power regimes (Fig. 7.7):

1. **First regime**: Between −41 dBm and −35 dBm, the scaling exponent $\alpha = 1.02$ suggests a near-linear response. In this regime, energy input is efficiently coupled to the CNT's mechanical oscillations, generating sidebands through frequency mixing with weak non-linearity. This behavior is consistent with weakly non-linear dynamics of Kelvin waves, as noted by Nakagawa *et al.* [135]. Additionally, this aligns with the weak

turbulence model of L'vov and Nazarenko [136, 137], where energy cascades smoothly to smaller scales without significant dissipation. In weak turbulence, Kelvin waves interact weakly, allowing energy to transfer across scales while maintaining the wave structure. This regime reflects a weakly non-linear state, as predicted by weak turbulence theory.

2. **Second regime**: Beyond $-35\,\mathrm{dBm}$, the scaling exponent shifts to $\alpha = -0.31$, indicating **non-linear damping**. At this higher power level, the system enters a more complex non-linear regime where dissipation mechanisms such as vortex reconnections and rough surface-induced dissipation (RSID) dominate. Simultaneously, a second sideband appears, likely due to the excitation of additional Kelvin wave modes or higher harmonics, redistributing energy across multiple modes. This behavior aligns with simulations by Nakagawa *et al.* [135], which predict multi-mode Kelvin wave excitation at higher power levels. Moreover, this is consistent with the strong turbulence model of Kozik and Svistunov [138, 139], where strong interactions between Kelvin waves lead to significant energy dissipation. In strong turbulence, highly non-linear interactions, such as vortex reconnections, rapidly transfer energy to smaller scales, resulting in increased dissipation through phonon emission. This is reflected in the observed energy dissipation and the emergence of additional sidebands in our experiments.

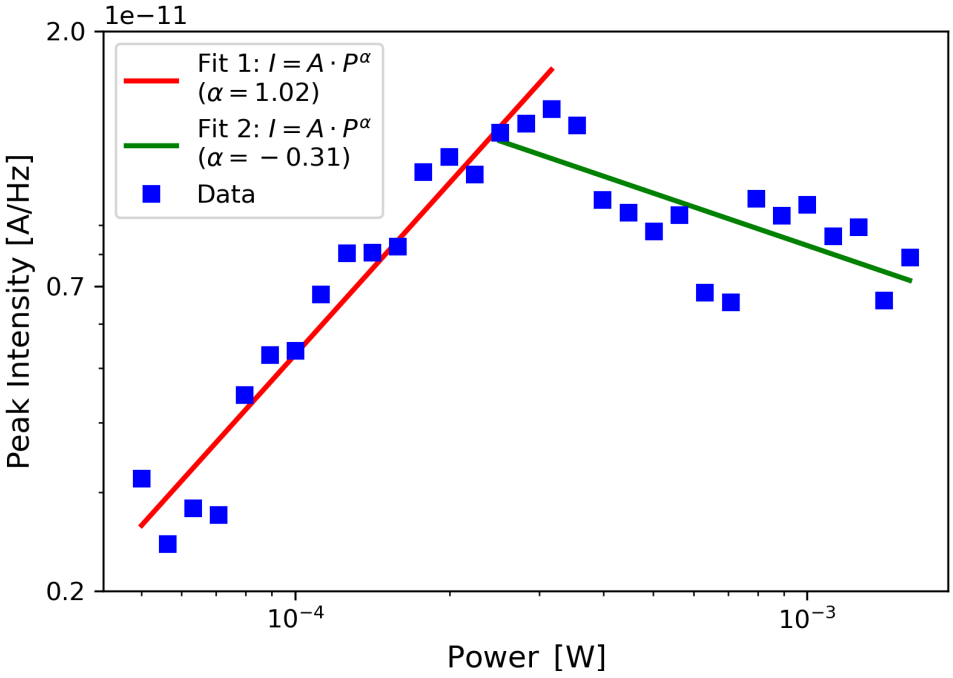

Figure 7.7: Power dependence of Kelvin wave-induced sideband intensity (log-log scale). The red line represents the first regime with a scaling exponent $\alpha = 1.02$, while the green line shows the second regime with $\alpha = -0.31$, indicating non-linear damping and the appearance of the second sideband.

7.4.3 Vortex energy density and tension in the context of pinning and sideband observation

To fully understand the dynamics of vortex pinning and its impact on the observed sidebands in the CNT resonator, two key physical quantities need to be considered: **energy

density** and **vortex tension per unit length**. The energy density describes how energy is distributed around the vortex core when pinned to the nanotube, while the tension governs the energy transfer that leads to Kelvin wave excitations and subsequent sideband formation.

7.4.3.1 Energy loss due to vortex pinning on the nanotube surface

The energy lost by a quantized vortex when pinned to the nanotube can be calculated based on vortex dynamics in superfluid helium. The energy density near the vortex core is given by:

$$\text{Energy density} = \frac{\rho_s V_\theta^2}{2} = \frac{\rho_s}{2}\left(\frac{\kappa}{2\pi r}\right)^2$$

where: - ρ_s is the superfluid density ($\rho_s \approx 145\,\mathrm{kg\,m^{-3}}$), - $V_\theta = \frac{\kappa}{2\pi r}$ is the tangential velocity at a distance r from the vortex core, - $\kappa = 0.0997 \times 10^{-6}\,\mathrm{m^2\,s^{-1}}$ is the quantum of circulation.

The total kinetic energy per unit length of a **free vortex** is calculated by integrating the energy density from the vortex core radius $a = 1 \times 10^{-10}\,\mathrm{m}$ to the nanotube length $R = 1.5\,\mu\mathrm{m}$:

$$E_{\text{free}} = \frac{\rho_s \kappa^2}{4\pi} \log\left(\frac{R}{a}\right)$$

When the vortex is pinned to the surface of the nanotube (as illustrated in Fig. 7.8), the portion of the vortex near the pinned surface experiences a significant loss of rotational energy. This results in a reduced total kinetic energy, given by:

$$E_{\text{pinned}} = \frac{\rho_s \kappa^2}{4\pi} \log\left(\frac{d/2}{a}\right)$$

where $d = 2\,\mathrm{nm}$ is the diameter of the nanotube. The energy loss due to vortex pinning can thus be expressed as:

$$\Delta E = \frac{\rho_s \kappa^2}{4\pi} \log\left(\frac{R}{d/2}\right)$$

This loss of rotational energy, as depicted in the **pinned vortex profile** in Fig. 7.8, results in an energy loss of approximately $\Delta E \approx 8.39 \times 10^{-13}\,\mathrm{J\,m^{-1}}$, consistent with energy dissipation reported in similar systems [135].

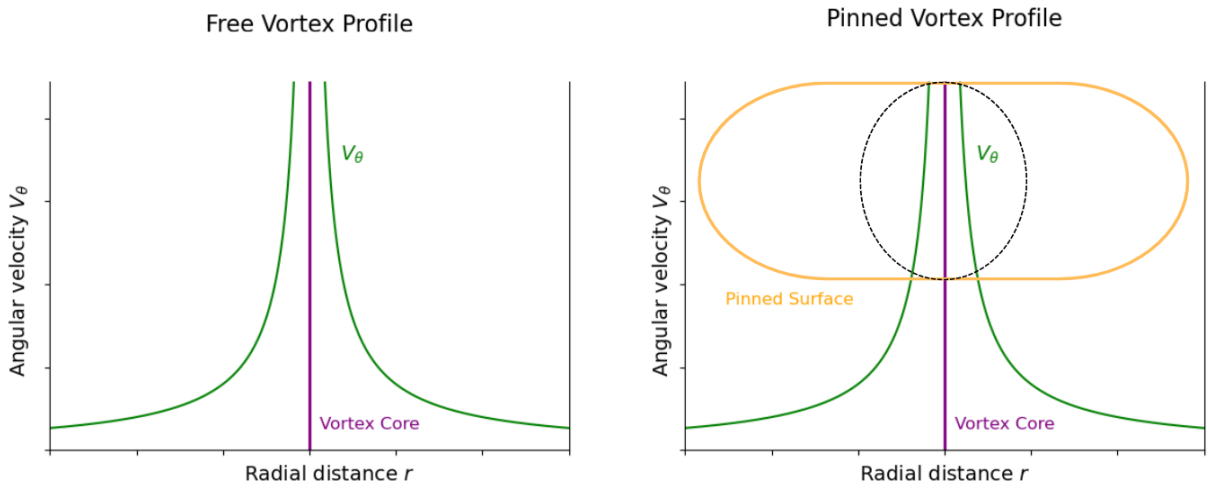

Figure 7.8: Vortex pinning on a surface. The free vortex profile (left) shows the rotational energy concentrated near the core. In the pinned vortex profile (right), energy loss near the surface (shown with dashed black circle) stabilizes the vortex, which is essential for understanding its interaction with nanostructures like CNTs.

7.4.3.2 Vortex tension and its relevance to sideband observations

Vortex tension per unit length quantifies the energy required to stretch or deform the vortex line under external forces, such as the mechanical oscillations of the CNT resonator. This tension directly influences Kelvin wave excitations, which manifest as sidebands in the frequency spectrum. The vortex tension is expressed as:

$$\epsilon = \frac{\rho_s \kappa^2}{4\pi} \ln\left(\frac{R_0}{a_0}\right)$$

where $R_0 = 175\,\text{nm}$ is the distance between the nanotube and the gate electrode. Substituting the known values into this equation yields:

$$\epsilon \approx 8.56 \times 10^{-13}\,\text{J}\,\text{m}^{-1}$$

This vortex tension modulates the interaction between the vortex and the CNT resonator, facilitating energy transfer and the excitation of Kelvin waves, which in turn leads to the formation of sidebands in the system. As shown in Fig. 7.8, the **pinned vortex profile** represents the stable configuration that results from the energy dissipation near the pinned surface.

Previous studies, including Avenel and Varoquaux [140], Donnelly [134], and Nakagawa et al. [135], have reported vortex pinning energy losses ranging from $1 \times 10^{-14}\,\text{J}\,\text{m}^{-1}$ to $1 \times 10^{-11}\,\text{J}\,\text{m}^{-1}$. Our calculated energy dissipation of $8.39 \times 10^{-13}\,\text{J}\,\text{m}^{-1}$ falls within this range. The close agreement between our calculated vortex tension and the values from Nakagawa et al. reinforces the validity of our energy loss analysis and highlights the critical role of vortex dynamics—including pinning and Kelvin wave excitations—in the formation of sidebands in our experiment.

Therefore, through the precise tunability and enhanced sensitivity of the CNT resonator, we achieve successful detection of Kelvin wave-induced sidebands, advancing the experimental study of vortex interactions in superfluid helium.

7.5 Temperature dependence of resonance in ^{4}He

In previous sections, we observed significant damping in ^{4}He, which we attributed to remnant vortices. These vortices likely interfered with the resonance behavior, making it difficult to replicate the simulation results from Chapter 3. To investigate this further, we conducted temperature-dependent measurements of the CNT resonator in ^{4}He.

Initially, we warmed the cryostat to 30 K to remove helium from the experimental cell, then cooled it back down to 1 K, allowing helium gas to gradually fill the cell. This approach helped control the helium condensation process and allowed us to explore the effect of temperature on the resonance frequency and damping.
Since the third harmonic f_3 shows a significant downward frequency shift upon helium adsorption compared to other modes (as shown in Fig. 7.3), we chose to track this mode while changing the temperature inside the ^{4}He cell. Fig. 7.9 illustrates the variation in nanotube resonance frequency with respect to the cryostat temperature inside the superfluid ^{4}He. As the temperature increased from 1.5 K to 7 K, we observed only small frequency shift of approximately 150 kHz at 7 K. However, after quickly cooling the system to 85 mK, we observed a significant increase in noise, especially in the off-resonance background, as illustrated in Fig. 7.9.

This enhanced noise at 85 mK is likely caused by remnant vortices formed during the rapid cooling process, as predicted by the Kibble-Zurek mechanism [125, 9]. These vortices likely became pinned between the nanotube and the gate electrode beneath it, disturbing the nanotube's mechanical motion. The strong coupling between the nanotube's mechanical motion and single-electron tunneling events enables us to detect these disturbances in the electrical current signal, even off-resonance. Similar vortex-induced noise has been observed in MEMS resonators, where vortex pinning between the resonator and the substrate contributes to more pronounced phase noise [124].

Despite the increase in noise at 85 mK, the quality factor ($Q = 1317.2$) was the highest observed in helium, although still lower than in vacuum measurements. This suggests that, while remnant vortices contribute to the noise, the mechanical properties of the nanotube improve at low temperatures. As the temperature was raised and helium began to evacuate, the Q factor gradually decreased due to increased damping. The lowest Q value, $Q = 246.9$, was observed near the λ-transition at 2.15 K, where helium transitions from a superfluid to a normal fluid.

At higher temperatures, such as 23 K, when helium was mostly in the gaseous phase, the resonance frequency continued to decrease, reaching 66.62 MHz. This behavior, shown in Fig. 7.10, suggests that the nanotube's spring constant may have been modulated by the interaction with helium, resulting in further frequency shifts. Additionally, the Q factor remained low at these higher temperatures, consistent with increased viscous damping from the normal liquid and gas phases of helium.

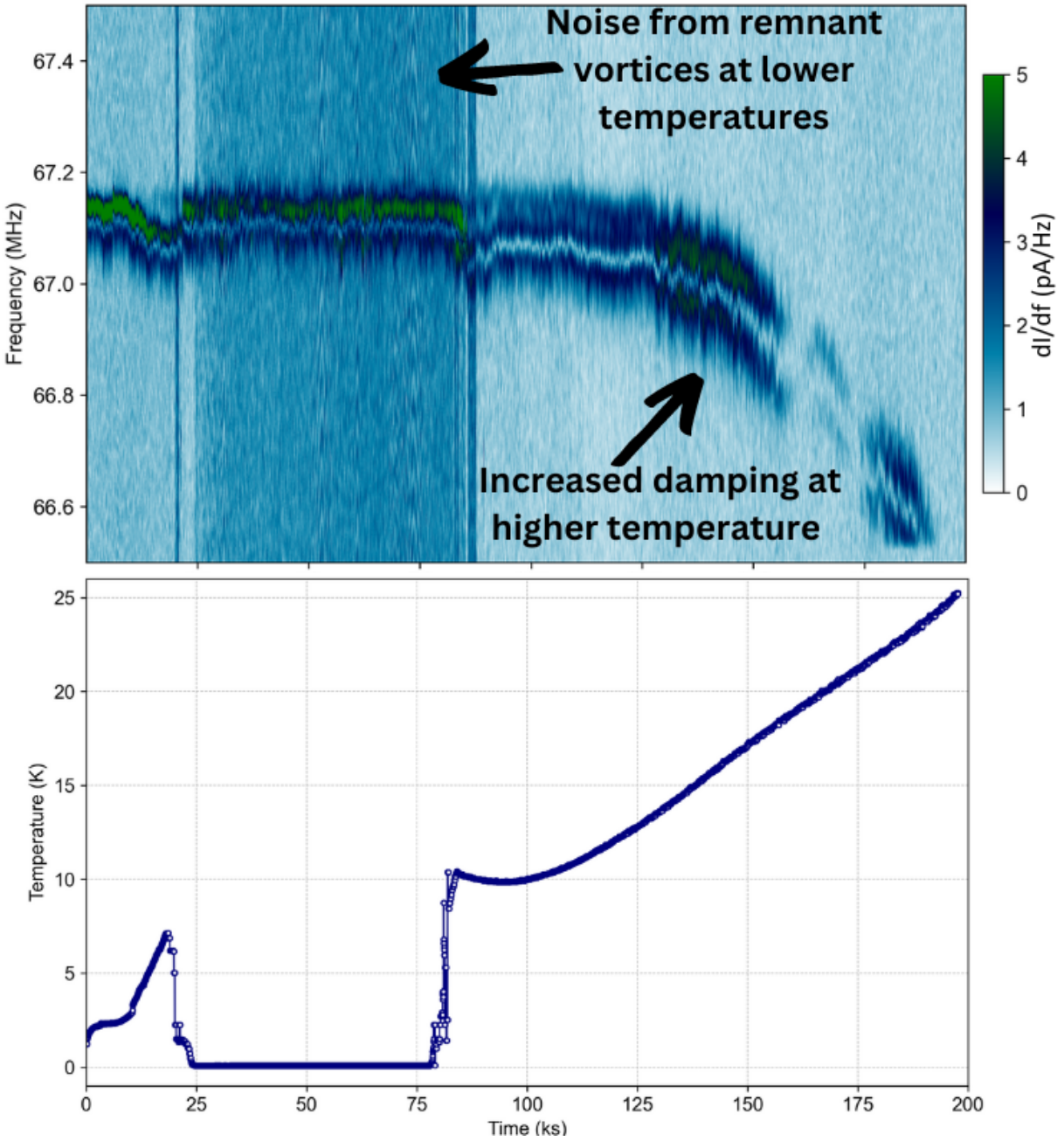

Figure 7.9: Top Panel: The resonance frequency of the third harmonic of the carbon nanotube resonator is plotted against time as the temperature in the superfluid ^{4}He bath is varied, at a gate voltage of $V_g = -758\,\text{mV}$. The resonance frequency exhibits a gradual decrease as the temperature rises from 1.5 K to approximately 7 K, followed by more significant frequency shifts and reduced Q factor at higher temperatures. The color intensity in the plot represents the amplitude of the resonance signal, with darker regions indicating stronger resonance responses. This data shows clear noise in the background (off-resonance) when cooled to the lowest temperature 85 mK, attributed to the interaction between the resonator and remnant vortices present in superfluid ^{4}He via KZM. Bottom Panel: This plot tracks the temperature of the cryostat over the same period, showing the controlled temperature changes during the experiment. The time correlation between the cryostat temperature and the resonance frequency shifts confirms the dependence of the resonator's behavior on the ^{4}He temperature and phase transitions.

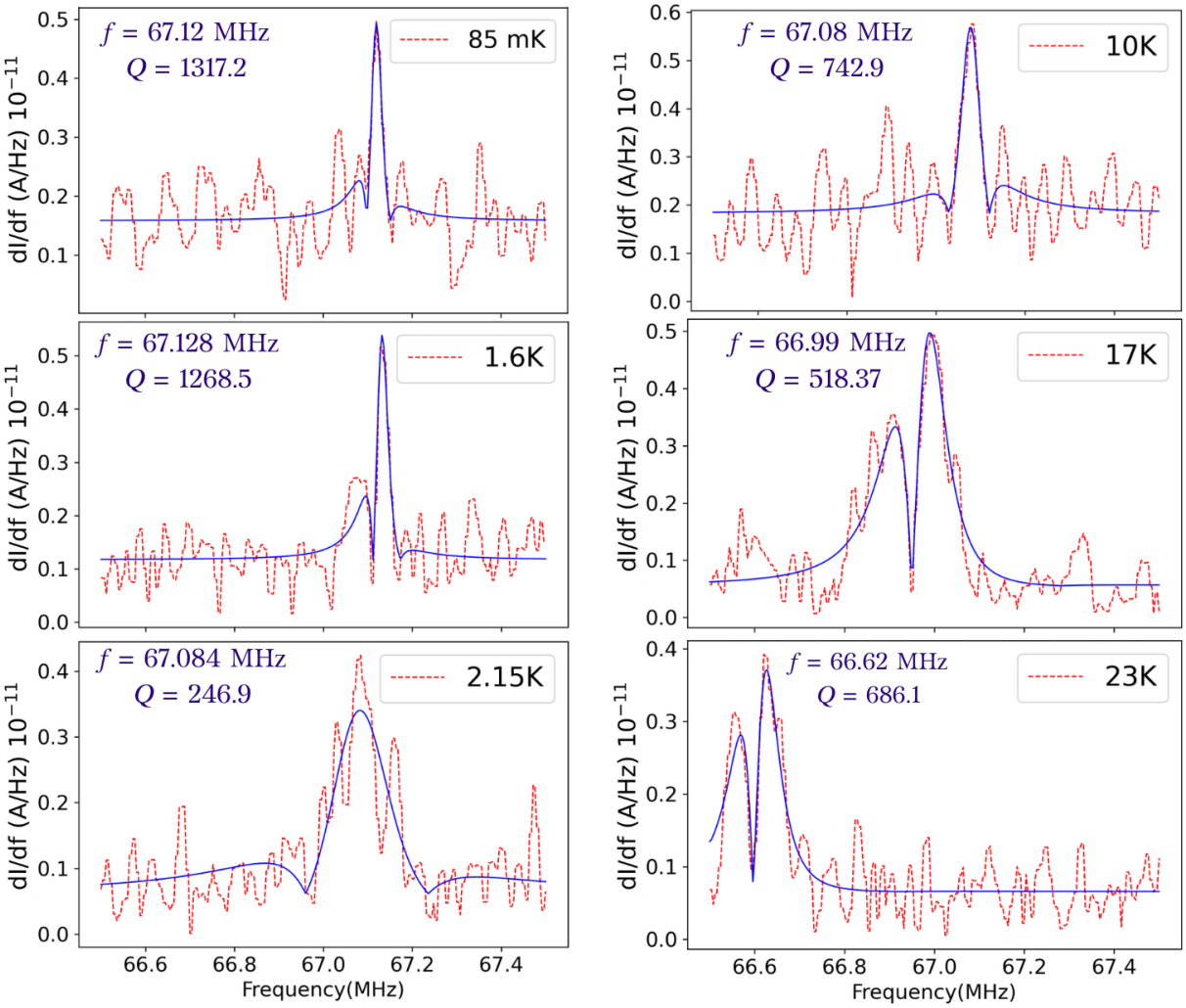

Figure 7.10: One-dimensional cut of resonances at various temperatures, derived from Fig. 7.9. The red dashed line is the data and blue solid lines are fits to the Eq. 6.2. Measurements at 85 mK and 1.6 K are conducted with the CNT immersed in ^{4}He. Notably, the background noise at 85 mK is higher than that at 1.6 K. In contrast, measurements at 2.15 K, 10 K, 17 K, and 23 K are taken as ^{4}He is being pumped out and the mixing chamber's temperature is raised above the λ transition. The frequency decreases with increasing temperature, while the Q factor shows significant fluctuations (lowest at 2.15 K) but generally decreases as the temperature rises.

Therefore, the temperature-dependent measurements provided valuable insights into the interaction between the CNT resonator and ^{4}He. The presence of remnant vortices at low temperatures introduced significant noise and damping (detailed analysis of vortex pinning and depinning events from the off-resonance noise is shown in Fig. A.6), though the quality factor improved at cryogenic temperatures compared to higher temperatures in helium. As the temperature increased, the resonance frequency shifted downward, with larger shifts occurring above the λ-transition, where viscous effects in the normal fluid phase became more prominent. These results align with existing studies on helium damping effects and confirm the influence of temperature on the resonance properties of the CNT resonator.

7.6 Summary

This chapter provides a detailed investigation of the interactions between a nanotube resonator and superfluid ^{4}He, focusing on helium adsorption, vortex dynamics, and Kelvin wave-induced sidebands.

Key findings include:

1. **Helium adsorption and frequency shifts**: The adsorption of helium atoms onto the nanotube surface results in significant downward shifts in resonance frequency, with higher harmonic modes showing more pronounced shifts. The estimated adsorption of 5 to 6 helium layers contributes to the reduced vibration frequencies, particularly affecting the third harmonic mode.

2. **Gate voltage tunability in superfluid**: The CNT's resonance frequencies remain tunable with gate voltage in superfluid ^{4}He, though this tunability is reduced at larger negative voltages (beyond $-0.8\,\mathrm{V}$). This reduction is due to the combined effects of mass loading from helium adsorption, surface tension, and electrostatic screening from the helium layers.

3. **Vortex dynamics and critical velocity**: Vortex pinning was consistently observed throughout the measurements, causing additional damping and noise at millikelvin temperatures. Quantized vortices generated via the Kibble-Zurek mechanism play a dominant role in shaping the behavior of the CNT resonator. A critical velocity of $0.9\,\mathrm{mm\,s^{-1}}$ marks the transition to turbulence, where vortex interactions lead to non-linear damping and the temporary disappearance of the resonance at large driving force.

4. **Kelvin wave-induced sidebands**: Sidebands were observed at higher RF drive powers, offset by 400 kHz from the main resonance at 18.7 MHz. These sidebands, attributed to the third harmonic of Kelvin waves along vortices pinned between the CNT and the gate electrode, provide direct evidence of vortex dynamics in superfluid ^{4}He. The sideband intensity scales non-linearly with input power, highlighting the interplay between the nanotube's mechanical oscillations and vortex excitations.

5. **Temperature dependence and vortex-induced noise**: Temperature-dependent measurements reveal that as the temperature increases from 1.5 K to 7 K, the resonance frequency shifts downward by 150 kHz, with a notable increase in noise at 85 mK due to vortex pinning, as seen in the enhanced off-resonance fluctuations. This significant noise at low temperatures suggests that remnant vortices strongly disturb the nanotube's motion. The quality factor reaches its highest value of 1317.2 at low temperatures but decreases significantly near the superfluid-to-normal fluid transition at 2.15 K, where viscous damping becomes prominent.

Chapter 8: Conclusions and outlook

This thesis has explored the interactions between carbon nanotube resonators and superfluid ^{4}He, focusing on key phenomena such as helium adsorption, hydrodynamic forces, quantum vortex dynamics, and nonlinear mechanical responses. Through comprehensive experimental studies, we have gained new insights into the mechanical properties of CNTs at millikelvin temperatures and demonstrated how single-electron tunneling (SET) and superfluid helium affect the nanotube's dynamics. These results have broad implications for understanding quantum fluids and nanomechanical resonators.

The work presented here emphasizes the successful fabrication and characterization of ultra-clean CNT resonators, both in vacuum and in superfluid ^{4}He. The close dimensional match between the CNT diameter (0.5 nm to 1.5 nm) and the coherence length of superfluid ^{4}He (0.34 nm [21]) facilitated strong interactions with quantum excitations. This allowed us to probe subtle quantum phenomena, including vortex dynamics and energy dissipation, with unprecedented sensitivity.

Before immersing the nanotube inside superfluid ^{4} He, we tested the sensitivity of these probes by simulating them in both the hydrodynamic and ballistic regimes of liquid ^{4}He. The theoretical results indicated a significant reduction in frequency and quality factor in the hydrodynamic temperature limit of liquid ^{4}He, surpassing the measurements made with previously used resonators such as vibrating wires, tuning forks, and Al NEMS. The smaller dimensions of the CNT resonators seem to extend the ballistic regime. Their significant aspect ratio and low mass also emphasized substantial damping due to excitations in superfluid ^{4}He, such as rotons and phonons, at lower temperatures. Furthermore, simulation results suggested that CNT resonators experience substantial acoustic losses in the superfluid bath due to their high frequencies, potentially limiting their sensitivity to thermal excitations in superfluid ^{4}He at sub-millikelvin temperatures. In our simulations, we presumed the nanotube was initially driven in a linear regime, so any observed losses and non-linearity in helium would originate from the excitations in superfluid ^{4}He.

8.1 CNT resonator in vacuum

The initial characterization of the CNT resonator in vacuum established a foundation for understanding its behavior in more complex environments, such as superfluid helium. Even in vacuum, the resonator exhibited several nonlinear phenomena and coupling effects, which are crucial for interpreting its performance in superfluid helium.

Key observations from vacuum measurements include:

Nonlinear dynamics and single-electron tunneling

- **SET-induced nonlinearities**: The CNT resonator in vacuum displayed strong nonlinearities due to the interaction between SET and the nanotube's mechanical motion. This coupling enabled highly sensitive vibration measurements, even with a direct current (DC) bias across the device, leading to self-oscillations.

- **Self-oscillations**: These self-oscillations were driven by the electrostatic forces generated during electron tunneling events, which caused abrupt jumps in the differential conductance. These conductance jumps highlighted the intricate coupling between electronic transport and mechanical motion.

- **Coulomb peak nonlinearities**: Nonlinear effects were most pronounced near Coulomb peaks, where variations in gate and bias voltages significantly influenced the system's behavior. This behavior provided insights into how electronic and mechanical degrees of freedom interact in nanoscale systems.

Mode coupling and quantum ground state proximity

- **Quantum regime and phonon population**: At millikelvin temperatures, the CNT resonator's phonon population approached $n \approx 0.53$, suggesting that the system was nearing the quantum ground state. This proximity to the quantum regime provides a promising platform for future quantum sensing applications. This effect, reported by Samanta et al., highlights how significant vibrations can persist even as the system nears the quantum ground state [141].

- **Mode coupling and anti-crossing**: Strong coupling between vibrational modes was observed, particularly in the form of anti-crossing. This coupling, driven by motion-induced tension, was especially clear in the third harmonic f_3, with a measured coupling strength of approximately 1 MHz.

Duffing nonlinearity and bistability

- **Duffing nonlinearity**: As the driving power increased, the system transitioned from a linear regime to Duffing-type nonlinearity. This transition was marked by hysteresis and bistability during forward and reverse frequency sweeps.

- **Relevance to quantum applications**: These nonlinear mechanical responses are particularly significant for quantum applications, where controlled nonlinearities can be used for precise tuning and sensing.

Quality factor optimization

- **Intrinsic Q factor in vacuum**: The CNT resonator's intrinsic Q-factor was measured to be 6076 in the linear regime, decreasing significantly with increased driving power due to nonlinear damping.

- **Potential for improvement**: The Q factor can be enhanced by fine-tuning the DC gate and bias voltage settings. Previous devices, such as the one shown in Fig. A.5, have achieved quality factors as high as 2×10^4 under DC current conditions in

vacuum. With further refinement of these voltage parameters, there is potential for even greater improvements, as other studies have reported Q factors reaching up to 5×10^6 for carbon nanotube resonators in vacuum [96].

These findings form the basis for understanding how CNT resonators behave in more complex environments, particularly in superfluid helium. The relationship between SET tunneling and nonlinear dynamics, as well as the observation of mode coupling, underscores the need for a deeper exploration of quantum transport in nanoscale systems.

8.2 CNT resonator in superfluid ^{4}He

The immersion of the CNT resonator in superfluid ^{4}He revealed several important phenomena, including helium adsorption, quantum vortex dynamics, and nonlinear mechanical responses. These results provide valuable insights into the interactions between nanomechanical systems and quantum fluids.

Key findings from the superfluid experiments include:

Helium adsorption and frequency shifts

- **Mass loading from helium layers**: Helium adsorption onto the nanotube surface caused a significant downward shift in resonance frequency due to increased mass loading. Approximately 5 to 6 layers of helium were adsorbed, altering the effective mass and mechanical properties of the resonator.
- **Sensitivity of higher harmonics**: Higher harmonics, particularly the third harmonic f_3, exhibited more pronounced frequency shifts due to their greater sensitivity to mass loading. Additionally, the resulting change in surface tension due to increase in mass altered the mechanical properties of the resonator, particularly influencing how the resonance frequencies are tuned with the DC gate.

Quantum vortices and nonlinear damping

- **Vortex pinning and damping**: Quantum vortices, generated through the Kibble-Zurek mechanism, introduced significant damping and noise at millikelvin temperatures. These vortices became pinned to the nanotube, affecting the overall dynamics and leading to additional dissipation.
- **Transition to turbulence**: The resonance disappeared entirely at a critical velocity of approximately $0.9\,\mathrm{mm\,s^{-1}}$, indicating the transition to turbulence driven by vortex-induced damping. This critical velocity marked the onset of quantum turbulence.

Kelvin waves and sidebands

- **Kelvin wave-induced sidebands**: Sidebands in the resonance spectrum were attributed to Kelvin waves propagating along the pinned vortices. These sidebands, detected at 18.3 MHz with a 400 kHz offset from the main resonance, provided experimental evidence of dynamic interactions between the nanotube and quantum vortices.

- **Vortex tension and energy density**: The calculated energy density of the pinned vortex and vortex tension per unit length were approximately $8.39 \times 10^{-13}\,\mathrm{J\,m^{-1}}$ and $8.56 \times 10^{-13}\,\mathrm{J\,m^{-1}}$, respectively, in line with previous experimental and theoretical studies [135].

Nonlinear dynamics in superfluid

- **Absence of Duffing hysteresis**: In contrast to vacuum measurements, no Duffing-type hysteresis was observed in superfluid helium. Instead, the nonlinearity was dominated by vortex interactions, which led to damping rather than mechanical bistability.
- **Vortex-dominated nonlinearity**: The absence of hysteresis in power sweeps confirmed that the observed nonlinearity was primarily driven by vortex dynamics, distinguishing it from the mechanical Duffing nonlinearity seen in vacuum.

Temperature dependence

- **Temperature-dependent shifts**: As the temperature increased from 1.5 K to 7 K, resonance frequency shifts were minimal. However, at 85 mK, remnant vortices introduced significant noise and damping, even though the normal component of helium was negligible at this temperature.
- Q **factor at low temperatures**: The Q-factor was highest at low temperatures but dropped significantly near the superfluid λ-transition temperature (2.15 K) due to increased damping from the normal fluid component.

Therefore, the interaction of the CNT resonator with superfluid helium revealed intricate dynamics dominated by vortex interactions, nonlinear damping, and Kelvin wave phenomena. These results provide valuable insights into the behavior of nanomechanical systems in quantum fluids and demonstrate the potential of CNT resonators as sensitive probes for studying quantum vortices and superfluid dynamics.

8.3 Outlook and future directions

While this study provides a detailed investigation of CNT-superfluid interactions, there remain several opportunities to improve and expand upon these findings:

- **Experimental cell modifications**: Using a copper or brass experimental cell could improve thermalization and allow for more precise temperature control, reducing the risk of pressure-induced cell explosions at higher temperatures.
- **Gradual helium filling**: Filling the helium cell slowly at low pressures (below 1 bar) could minimize remnant vortex formation and improve the accuracy of measurements, especially in the ballistic and hydrodynamic regimes, and can be directly compared with simulation results.

- **Integration of tuning forks**: Introducing a tuning fork near the CNT resonator would allow for real-time monitoring of pressure and temperature, enhancing the precision of experiments in both vacuum and superfluid environments as the behavior of tuning forks in both normal and superfluid helium is well understood..
- **Multiple CNT devices characterization**: Future studies should aim to characterize multiple CNT resonators during the same cooldown, ensuring consistency and reliability in the results. This would also allow for more robust conclusions about the interactions between CNTs and superfluid helium.
- **Exploration of superfluid ^{3}He**: Given the promising results in superfluid ^{4}He, extending the experiments to superfluid ^{3}He could reveal new quantum mechanical effects and provide further opportunities to study phase transitions in quantum fluids.

8.4 Summary

This work demonstrates the potential of CNT resonators as highly sensitive probes for studying quantum fluids, specifically superfluid ^{4}He. The findings provide valuable insights into phenomena such as helium adsorption, quantum vortex dynamics, and Kelvin wave interactions. These results lay a solid foundation for future research in nanomechanical resonators and quantum fluid dynamics, offering exciting prospects for further theoretical and experimental investigations using a smallest doubly-clamped CNT resonator.

Appendix A: Appendix

A.1 Measurements in helium

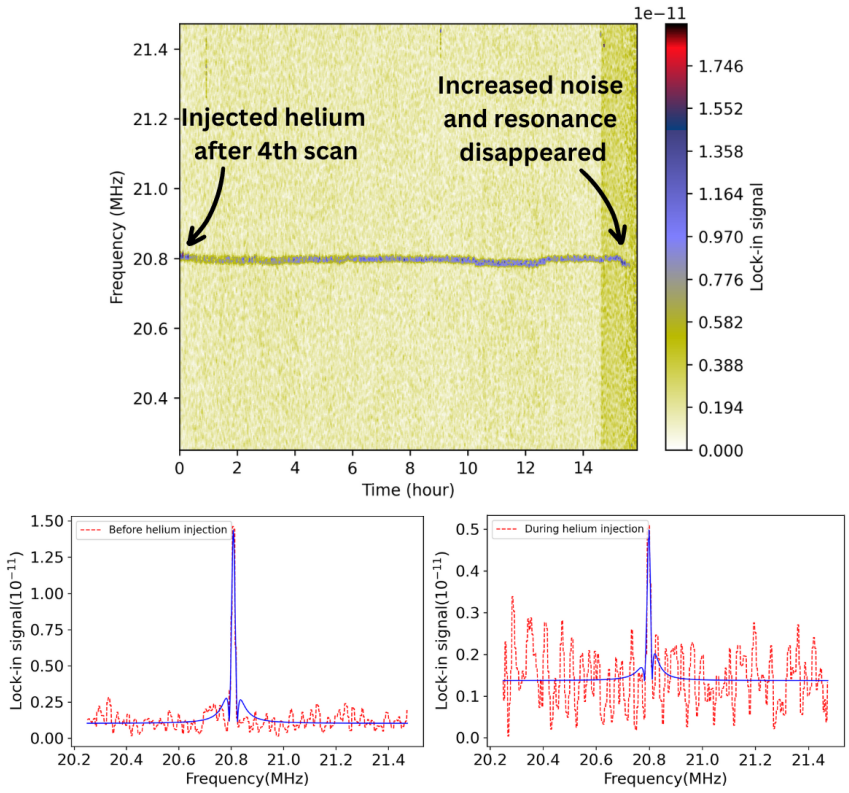

Figure A.1: Top Panel: This illustrates the behavior of the nanotube resonance over time, both before and after the injection of ^{4}He, using the same device discussed in Chapters 6 and 7. Initially, the nanotube cell was filled with ^{4}He for 30 minutes via the first fill line, while the second fill line remained closed, similar to the process explained in Fig. 7.1. Subsequently, the helium filling was stopped without equalizing pressure in the second line's pressure gauge. Initially, the frequency stabilized at the base temperature in vacuum across the first four frequency sweeps. Following the injection of helium gas, there was no significant immediate frequency shift; however, there was an observable increase in noise and a decrease in resonance amplitude. These changes are clearly visible in the bottom two 1D resonance cuts from the top panel, illustrating the conditions before and during ^{4}He injection. The effect of helium on the resonance was not evident until after 15 hours, likely due to the minimal amount of helium present in the cell, which may suggest a high impedance to filling. Additionally, only a minor increase in mixing plate temperature to 90 mK was observed, in contrast to the scenario presented in Fig. 7.1. The resonance frequency exhibited a downward shift before disappearing entirely after 15 hours. Beyond this point, no resonances, including fundamental and higher harmonics, could be detected at this driving power.

A.2 Other CNT devices measured in vacuum at 7mK

A.2.1 Resonance frequency at multiple Coulomb peaks

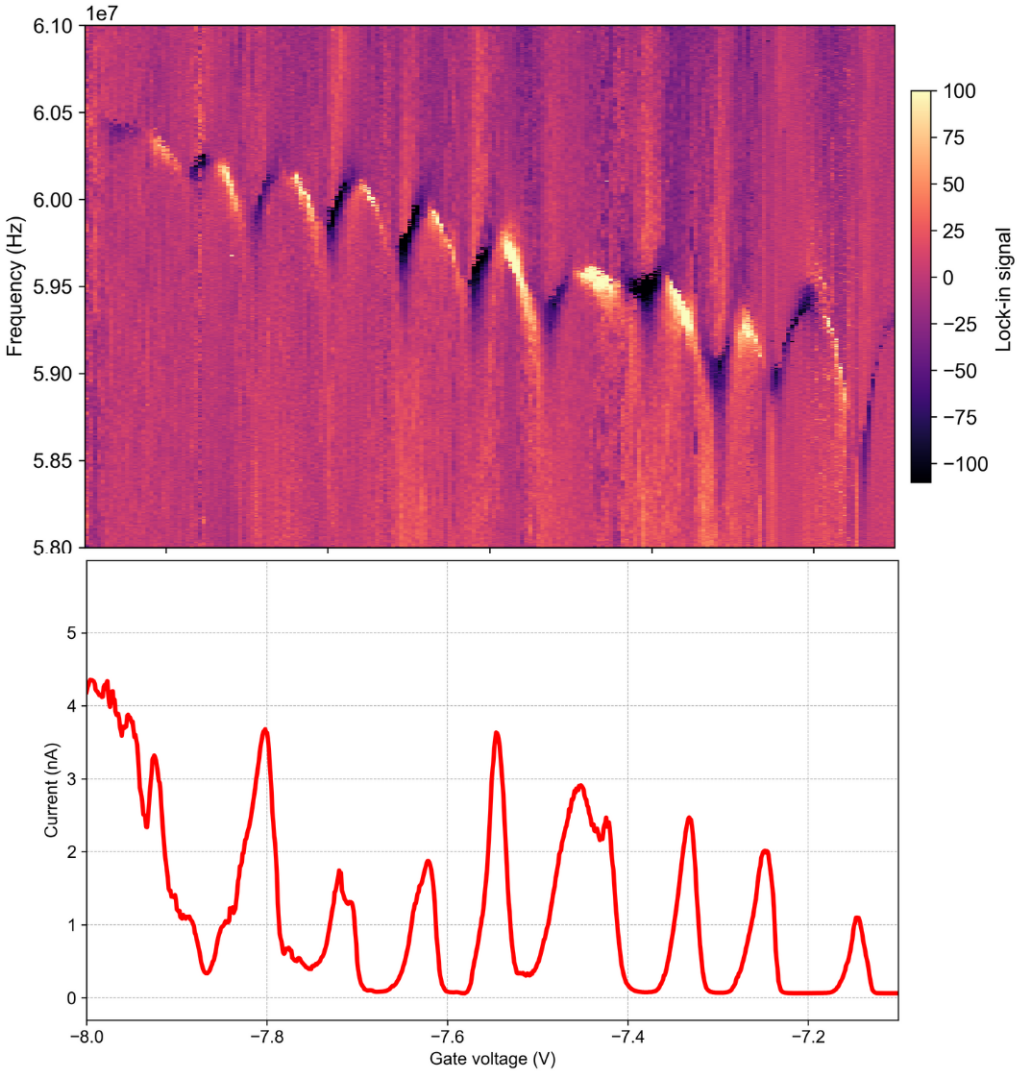

Figure A.2: Top Panel: This graph shows how the resonance frequency varies with gate voltage at Coulomb peaks, similar to Fig. 6.5. This reveals several distinct features: a slope, resulting from tension at a fixed charge; a frequency offset, indicating a difference in tension between charge states; and frequency dips, caused by single-electron tunneling events. Bottom Panel: The Coulomb oscillations in the current passing through a nanotube quantum dot. During the Coulomb blockade, the current is zero, indicating a fixed number of electrons on the CNT. Between different charge states, there are peaks in the current, signifying single-electron tunneling events.

A.2.2 Resonance behavior with bias voltage at high drives

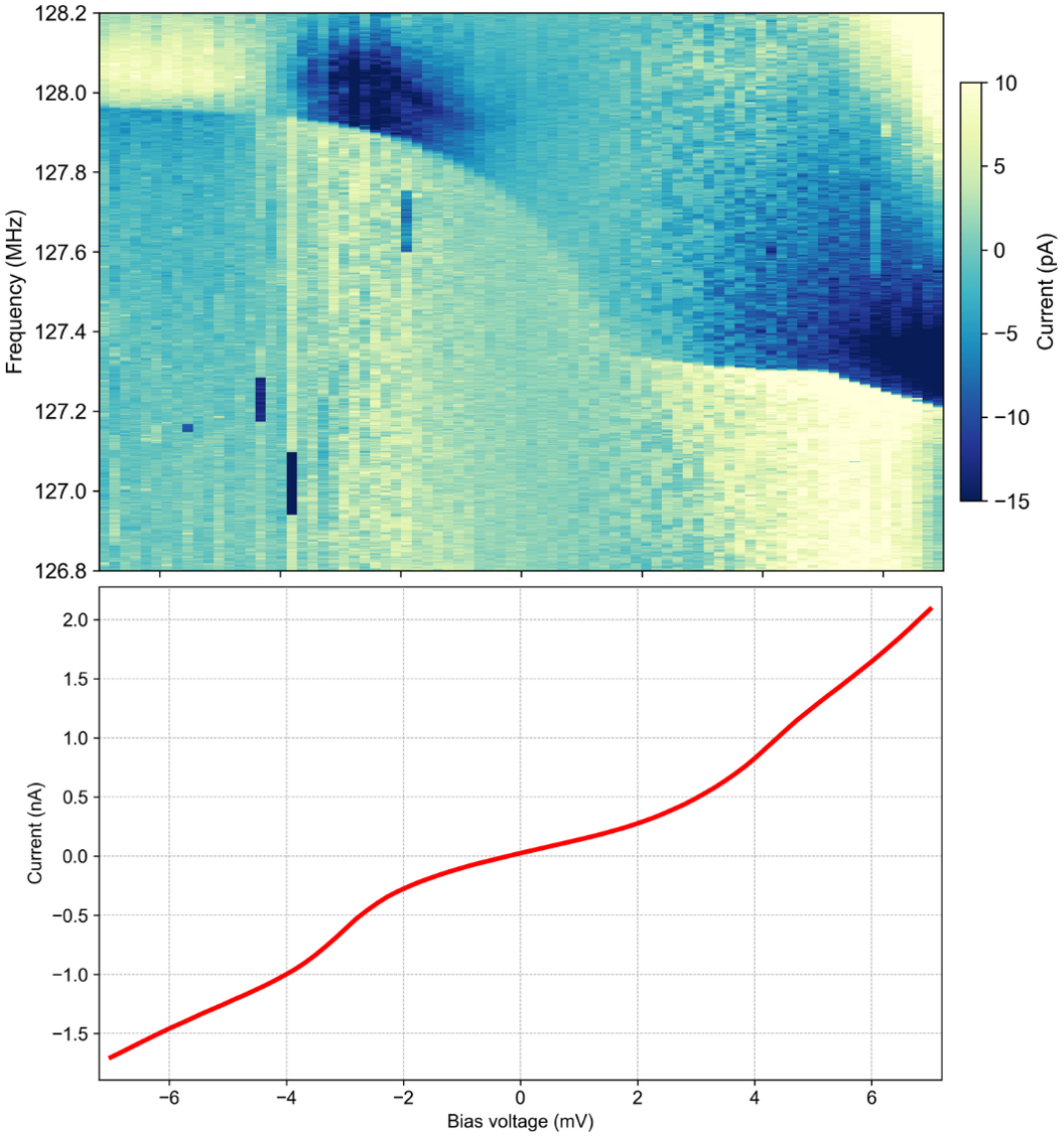

Figure A.3: Top Panel: This panel shows the resonance signal observed in the DC of a nanotube, plotted against the bias voltage. This signal is similar to what is depicted in Fig. 6.6 for another nanotube device. The measurement is conducted under high drives, where resonance becomes nonlinear and readily detectable in DC current. Bottom Panel: The corresponding IV characteristics of the nanotube resonator across the entire range of bias voltage. These characteristics are measured at a constant gate voltage and drive power.

A.2.3 Bias sweep OFF and ON resonance

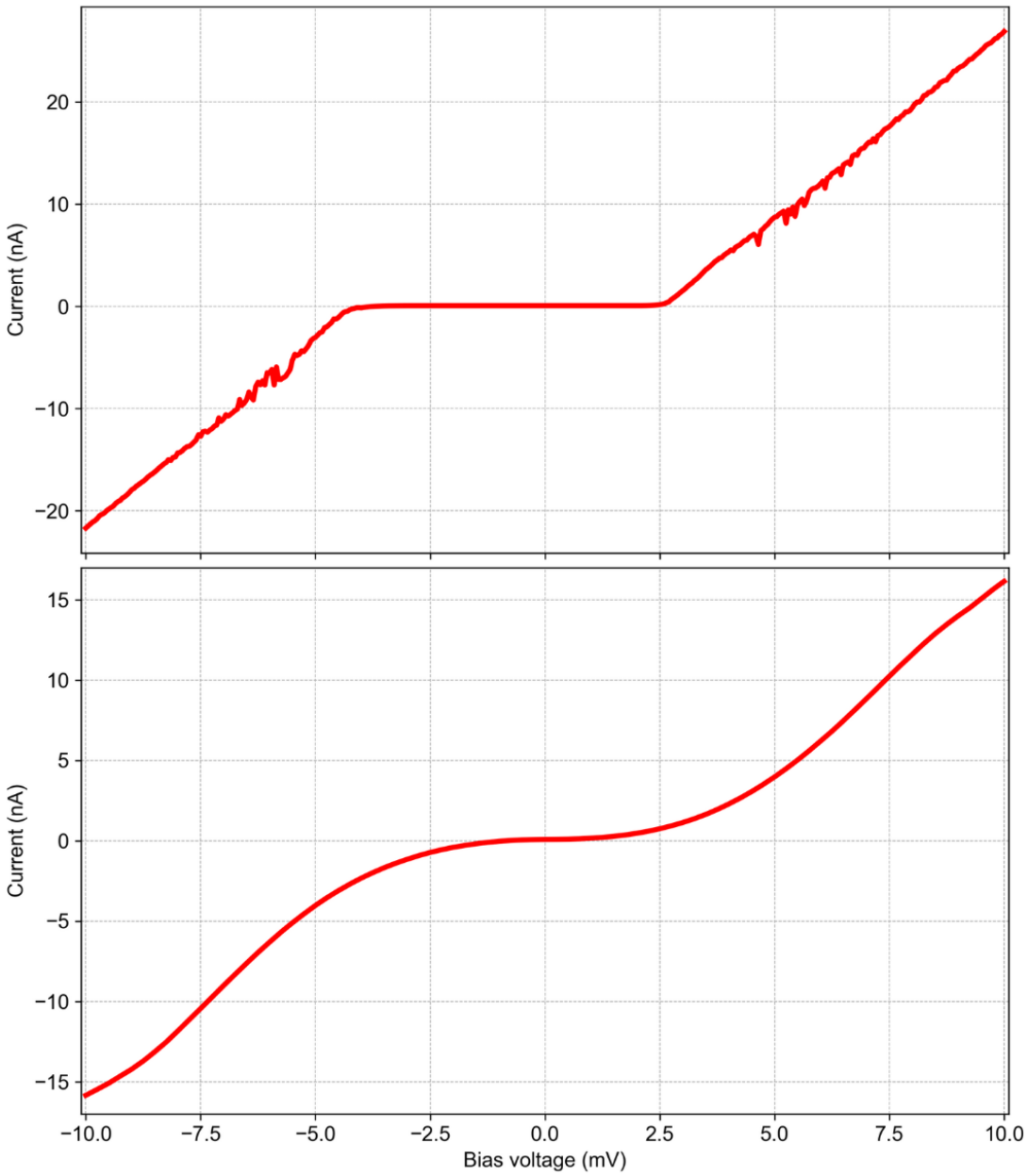

Figure A.4: Top Panel: The bias sweep of a nanotube when there is no oscillating signal applied. The Coulomb blockade region is clearly visible as the suppressed current for low bias. Bottom Panel: The bias sweep of the same device at resonance.

A.2.4 Q factor comparison and dependence on nanotube cleanliness

The Q factor of a nanotube resonator is a key parameter reflecting energy dissipation within the system. In our experiments, we observed substantial variation in the Q factors across devices, attributable to differences in nanotube cleanliness, contact quality, and the measurement technique used. Specifically, devices with ultra-clean nanotubes and well-formed electrical contacts tend to exhibit significantly higher Q factors.

One such ultra-clean device, measured using the direct current (DC) technique, displayed a Q factor of approximately 20,000, as shown in Figure A.5. This high Q factor is particularly noteworthy, as the DC measurement method typically suffers from a lower signal-to-noise ratio compared to more sensitive techniques such as frequency modulation (FM) detection. The device's pristine nature and excellent contacts are evidenced by the clean Coulomb diamonds observed in Fig. 2.7, indicative of minimal defect presence and a low Schottky barrier, which reduces energy dissipation. Similar trends have been observed in literature, where ultra-clean CNTs and minimized surface contamination lead to record-high Q factors [96].

In contrast, a device measured using the FM technique, discussed in Sec. 6.2.3, exhibited a lower Q factor of 6,076. Despite the higher sensitivity of FM detection, this device likely contained defects introduced during fabrication, which increased energy dissipation by scattering charge carriers. Such imperfections have been shown to significantly reduce Q, as even minor defects or surface contamination can induce surface friction, which limits the resonator's performance [99].

The literature corroborates these findings, where ultra-clean nanotubes at low temperatures have demonstrated Q factors exceeding 100,000, highlighting the critical role of nanotube quality in enhancing Q values. Devices cooled to millikelvin temperatures with minimal contamination and well-formed electrical contacts have been reported to achieve Q factors as high as 5 million [96, 82]. However, such high Q values require the use of ultra-sensitive detection methods and noise suppression in the electrostatic environment, factors not always feasible in standard DC measurements.

In conclusion, the significant Q factor variations observed in our experiments underscore the importance of nanotube cleanliness and contact quality. The $Q = 20,000$ device, measured with the DC technique, demonstrates that ultra-clean CNTs can exhibit high performance even under less sensitive measurement conditions, while devices with defects or suboptimal contacts exhibit lower Q factors. Future work should focus on optimizing fabrication techniques and minimizing defects to consistently achieve high Q values in CNT resonators.

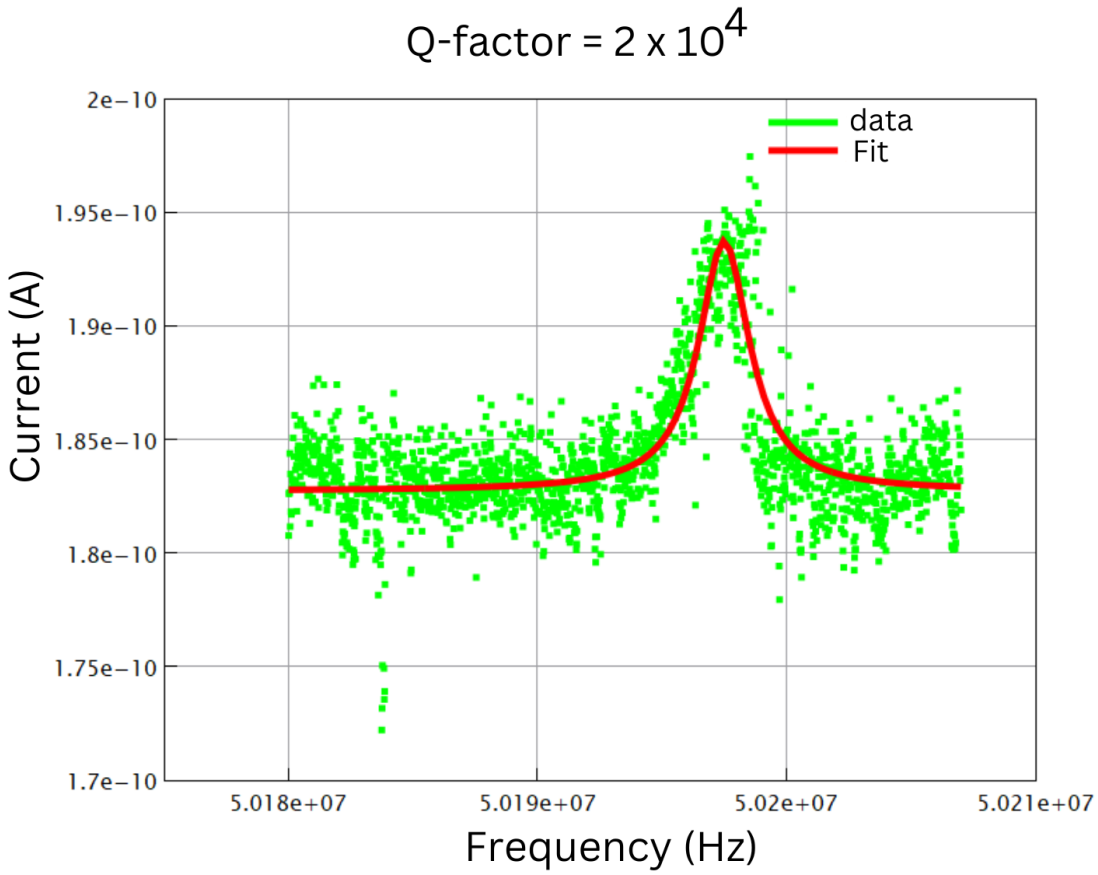

Figure A.5: The quality factor Q measured using the DC current technique for an ultra-clean carbon nanotube device, showing a Q value of approximately 20,000. This high Q factor reflects the pristine nature of the nanotube and well-formed electrical contacts, resulting in minimal energy dissipation.

A.2.5 Stability diagram of a semi-metallic nanotube

Figure A.6 presents the stability diagram of a carbon nanotube with a small band gap and very high transparency between the electrical contacts and the nanotube itself. In regions corresponding to negative gate voltages and small positive gate voltages, the observed small diamond shapes in the diagram indicate characteristics similar to Fabry–Perot oscillations, as depicted in the top panel of Fig. A.6. This phenomenon highlights the small energy required for current to flow through the nanotube. Notably, the stability diagram also shows reproducible oscillations superimposed on the Fabry–Perot patterns, which are highlighted by black arrows. Moreover, distinct Fano resonances appear at specific gate voltages, indicated by green arrows. These are likely due to the interference from electrons undergoing resonant tunneling in the nanotube quantum dot [142].
As the gate voltage shifts to more negative values (shown in the middle panel of Fig. A.6), the electrical contacts exhibit increased transparency, diminishing the Coulomb blockade effect. Conversely, at higher positive gate voltages (bottom panel of Fig. A.6), the transparency decreases, enhancing the Coulomb blockade effect and resulting in the appearance of pronounced Coulomb diamonds.
This behavior can be elucidated by examining controlled band bending. The inset of the middle panel in Fig. A.6 illustrates hole movement through the valence band, where green and red bands signify the conduction and valence bands, respectively. Here, holes

can tunnel into and out of the valence band by overcoming a relatively small Schottky barrier, thus facilitating efficient hole transport. Conversely, the inset of the bottom panel portrays electron transport through the conduction band, where electrons face a higher Schottky barrier when tunneling in and out, leading to reduced conductance. This disparity in conductance is primarily due to two mechanisms: high conductance in the valence band is achieved through Fabry–Perot interference, while low conductance in the conduction band arises from the Coulomb blockade regime.

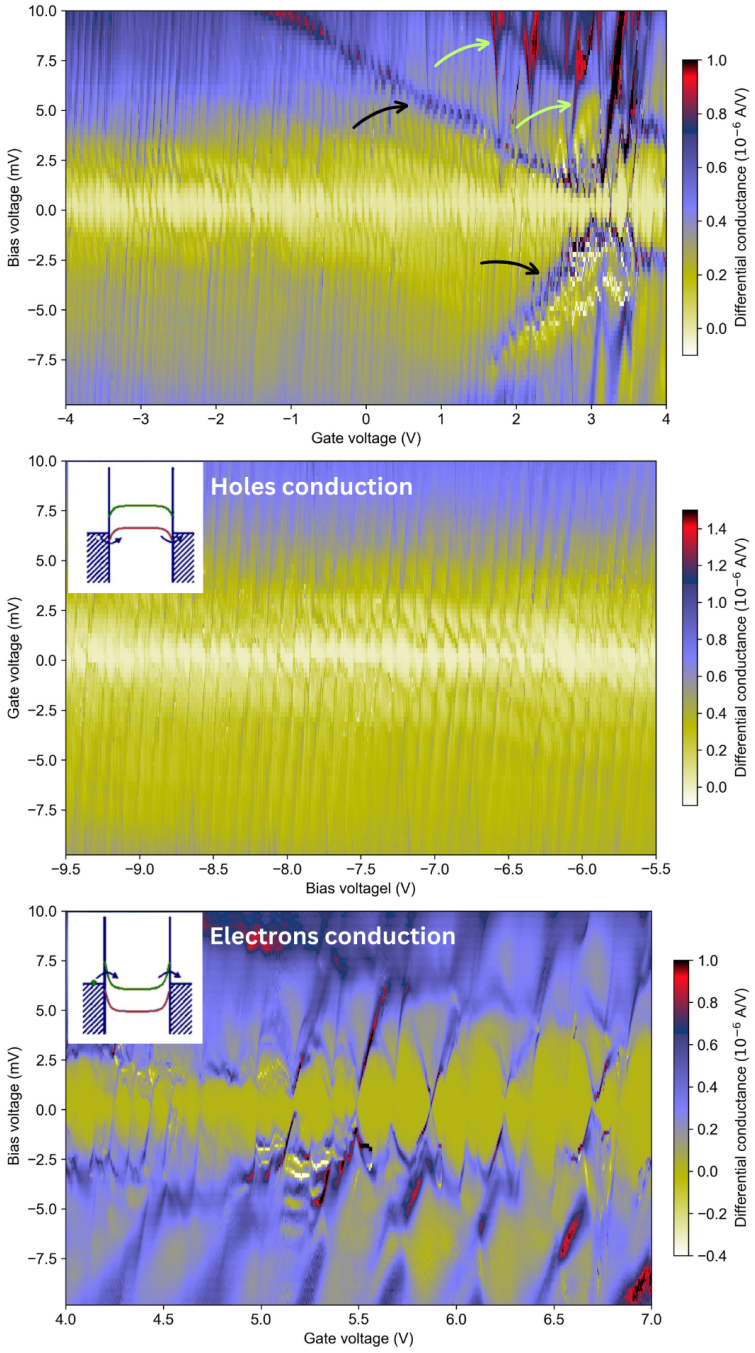

Figure A.6: Top Panel: This displays patterns that do not closely resemble diamonds but suggest the presence of Fabry–Perot oscillations and indicate the low energy required for electrical current to pass through the nanotube when gate voltages range from negative to small positive. The diagram also exhibits reproducible oscillations and pronounced Fano resonances, marked by black and green arrows, respectively. Middle Panel: Demonstrates increased transparency of electrical contacts and diminished Coulomb blockade effect at larger negative gate voltages, facilitated by controlled band bending and efficient hole transport through the valence band. Bottom Panel: Shows an enhanced Coulomb blockade effect due to reduced transparency at high positive gate voltages, with pronounced Coulomb diamonds emerging and reduced electron conductance through the conduction band. Insets detail the band bending effect: efficient hole transport through the valence band due to a small Schottky barrier (middle panel) and hindered electron transport in the conduction band due to a higher barrier (bottom panel), demonstrating the interplay between Fabry–Perot interference and Coulomb blockade in nanotube conductance.

A.2.6 Fundamental and higher harmonics at Coulomb peak

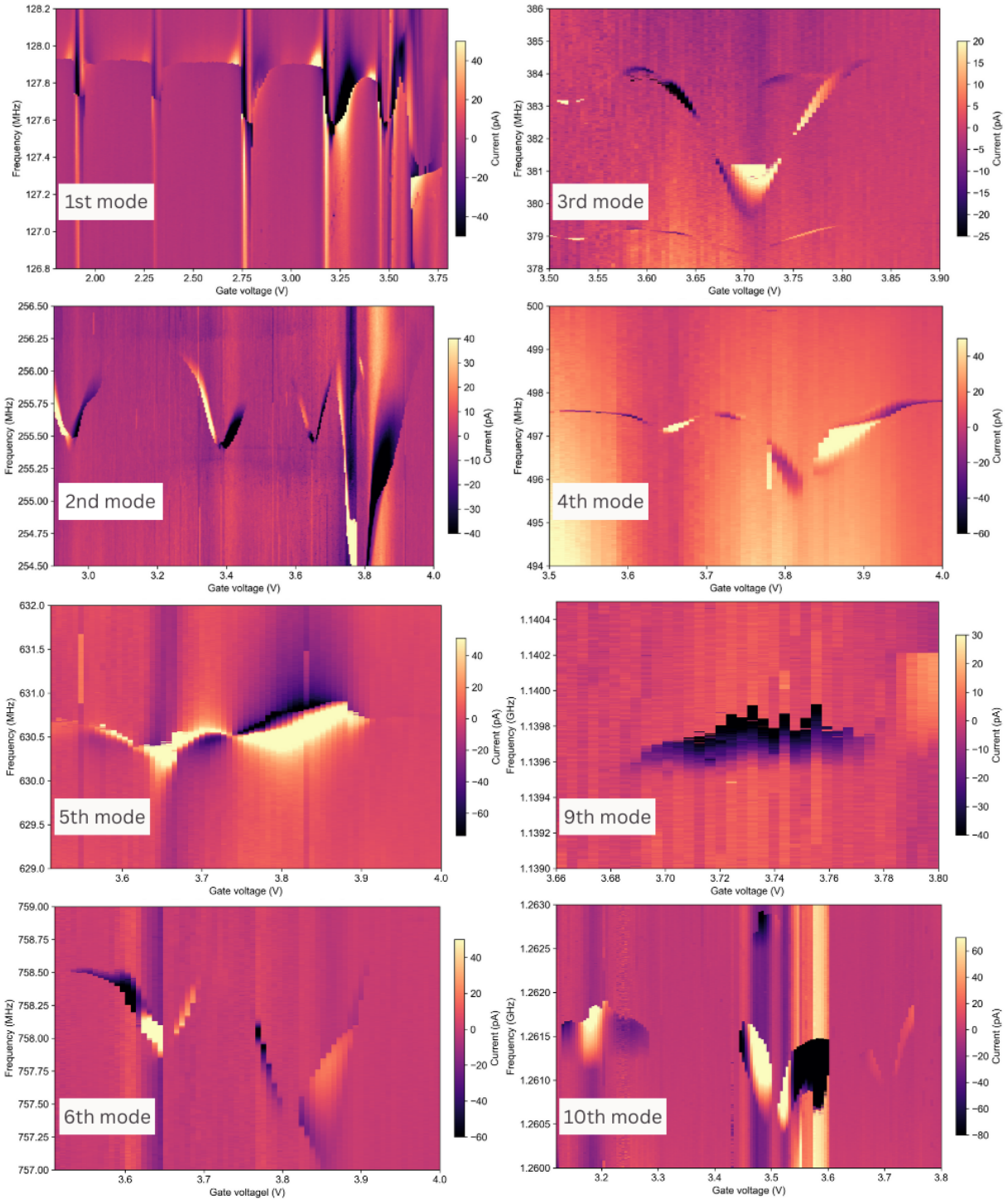

Figure A.7: The fundamental and higher harmonics are clearly visible at the Coulomb peaks in the DC current of the same nanotube, as shown in Fig. A.6. To enhance visibility, we have subtracted the average current from each column. Remarkably, gigahertz oscillations (9^{th} and 10^{th} modes) are observable in direct current due to the coupling of the CNT resonator with single-electron tunneling.

A.2.7 Stability diagram of a metallic nanotube

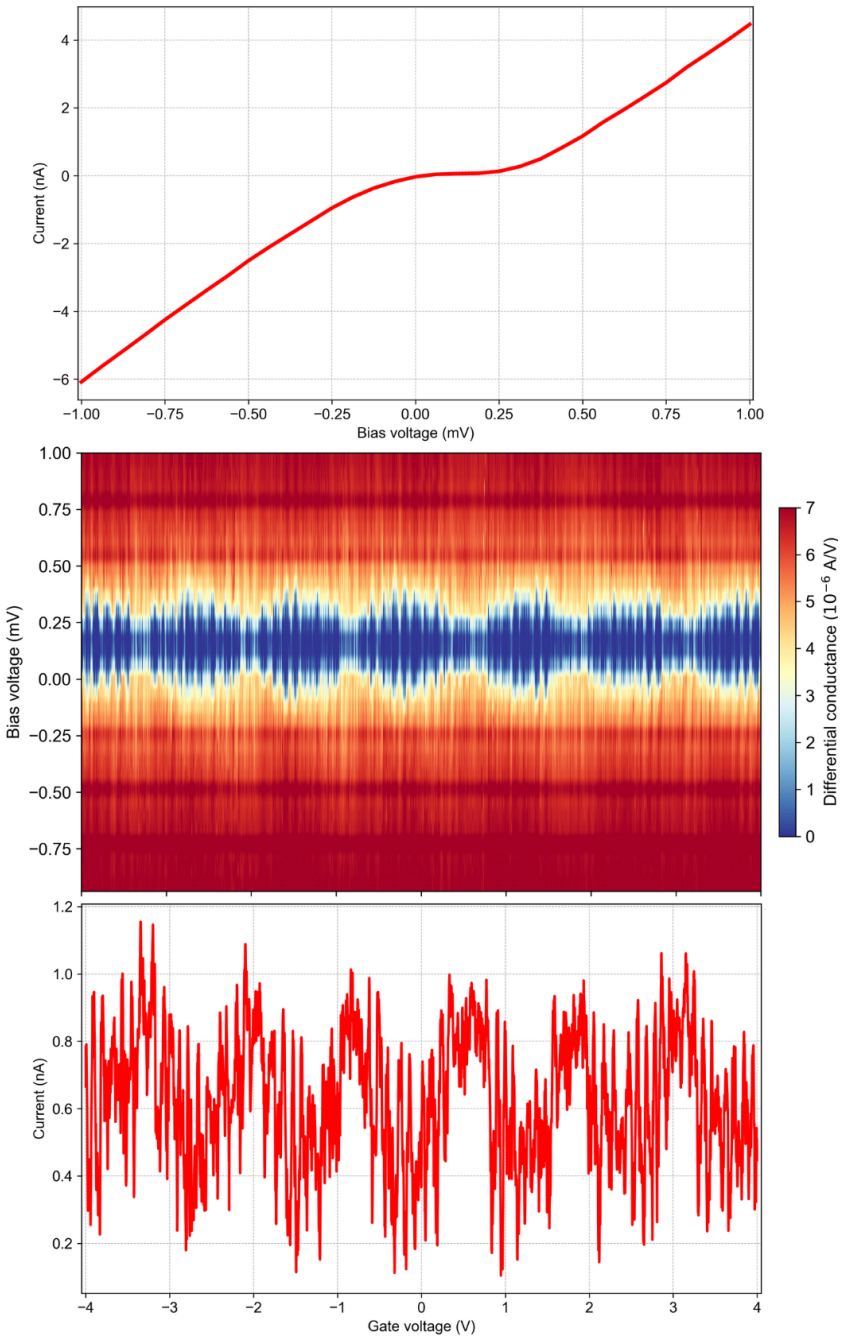

Figure A.8: Top Panel: The bias sweep of a metallic nanotube reveals little to no Coulomb blockade regime, as current becomes detectable at very low source-to-drain voltages, typically in the microvolt range. Middle Panel: The stability diagram displays a gradual modulation of conductance on the fast oscillations as a function of the gate voltage. Instead of the typical Coulomb diamonds, the conductance oscillations resemble Fabry–Perot oscillations[143]. Bottom Panel: This depicts the current in the nanotube as a function of the gate voltage, clearly showing the slow oscillations superimposed on the rapid ones. However, the mechanical resonance was not observed in this metallic nanotube, leading to a preference for small bandgap nanotube devices. In small bandgap devices, mechanical resonances are relatively easier to detect due to the Coulomb blockade effect.

A.3 Displacement and velocity versus electrostatic force calculation using FM technique

To detect the vibrations of the nanotube, we use a frequency modulation (FM) technique. The nanotube is operated as a single-electron transistor (SET) in which the mechanical vibrations modulate its conductance. The displacement of the nanotube $u(t)$ is linked to its conductance, which is measured as a current flowing through the nanotube.

The lock-in amplifier measures the derivative of the current with respect to the frequency of the driving signal, $\frac{dI}{df}$. At resonance, where the mechanical motion is maximum, the derivative of the current peaks, indicating the maximum displacement amplitude δu_0. The displacement amplitude of the nanotube near resonance is modeled using a Lorentzian response function:

$$\delta u_0 \propto \frac{1}{f_{\text{res}}^2 - f^2 + i\frac{f_{\text{res}} f}{Q}},$$

where f_{res} is the resonant frequency, f is the driving frequency, and Q is the quality factor. For our nanotube, the quality factor was determined to be 6076, with a resonant frequency around 20.78 MHz. The maximum displacement occurs at the resonance frequency.

A.3.1 Calculation of displacement amplitude

To calculate the exact displacement amplitude δu_0, a device-specific constant C_{cal} is introduced. This constant relates the current response measured by the lock-in amplifier to the mechanical displacement. The displacement amplitude is given by:

$$\delta u_0 = C_{\text{cal}} \cdot \left(\frac{dI}{df}\right)_{\text{peak}},$$

where C_{cal} is the calibration constant in units of **pA/nm/Hz**, and $\left(\frac{dI}{df}\right)_{\text{peak}}$ is the peak value of the current derivative at resonance.

The calibration constant C_{cal} can be calculated using the system's capacitance and electrical properties. In this case, the gate capacitance C_{g} is 3 aF, and the nanotube-gate separation d is 175 nm. The change in capacitance per displacement $\frac{dC_{\text{g}}}{dx}$ is:

$$\frac{dC_{\text{g}}}{dx} \approx \frac{C_{\text{g}}}{d} = \frac{3 \times 10^{-18}\,\text{F}}{175 \times 10^{-9}\,\text{m}} = 1.71 \times 10^{-11}\,\text{F/m}.$$

The current change per unit displacement is given by:

$$\frac{dI}{dx} = \frac{dI}{dC_{\text{total}}} \cdot \frac{dC_{\text{g}}}{dx},$$

where $\frac{dI}{dC_{\text{total}}} = \frac{V_{\text{sd}}}{R_{\text{nanotube}}}$ depends on the source-drain voltage V_{sd} and the nanotube resistance R_{nanotube}. For $V_{\text{sd}} = 2\,\text{mV}$ and $R_{\text{nanotube}} = 182\,\text{k}\Omega$. Here, C_{total} is the total capacitance. This gives:

$$\frac{dI}{dC_{\text{total}}} \approx 1.1 \times 10^{-8}\,\text{A/F},$$

and thus:

$$\frac{dI}{dx} = 1.1 \times 10^{-8} \times 1.71 \times 10^{-11} = 1.90 \times 10^{-19}\,\mathrm{A/m} = 1.90 \times 10^{-10}\,\mathrm{pA/nm}.$$

Thus, the calibration constant C_{cal} is $1.90 \times 10^{-10}\,\mathrm{pA/nm/Hz}$.

A.3.2 Displacement amplitude and velocity for $\frac{dI}{df}$ at nanotube resonance

If $\frac{dI}{df} = 17.5\,\mathbf{pA/MHz}$ and $f_{\mathbf{res}} = 20.78\,\mathbf{MHz}$: The displacement amplitude is calculated using the calibration constant C_{cal} is $1.90 \times 10^{-10}\,\mathrm{pA/nm/Hz}$:

$$\delta u_0 = C_{\mathrm{cal}} \cdot \left(\frac{dI}{df}\right)_{\mathrm{peak}} = 1.90 \times 10^{-10} \times 17.5 \times 10^{-3} = 3.395 \times 10^{-12}\,\mathrm{m}.$$

Thus, the displacement amplitude is approximately 3.395 pm.
The maximum velocity is given by:

$$v_{\max} = 2\pi f_{\mathrm{res}} \delta u_0 = 2\pi \times 20.78 \times 10^6 \times 3.395 \times 10^{-12}\,\mathrm{m}$$

$$v_{\max} \approx 0.441\,\mathrm{mm/s}.$$

Thus, the maximum velocity of the nanotube resonator at resonance varies as a function of the peak value of $\frac{dI}{df}$, with higher values of $\frac{dI}{df}$ leading to larger displacement amplitudes and velocities.

A.3.3 Calculation of electrostatic force

The electrostatic force F_{el} on the nanotube is derived from the capacitive interaction between the nanotube and the gate electrode. The force is expressed as:

$$F_{\mathrm{el}} = \frac{1}{2}\frac{dC_{\mathrm{g}}}{dx} V_{\mathrm{g}}^2$$

where:

- C_{g} is the gate capacitance.
- x is the distance between the nanotube and the gate.
- V_{g} is the total gate voltage: $V_{\mathrm{g}} = V_{\mathrm{g}}^{\mathrm{DC}} + \tilde{V}_{\mathrm{g}} \cos(\omega t)$.

This results in:

$$F_{\mathrm{el}} = \frac{1}{2}\frac{dC_{\mathrm{g}}}{dx}\left(\left(V_{\mathrm{g}}^{\mathrm{DC}}\right)^2 + 2V_{\mathrm{g}}^{\mathrm{DC}}\tilde{V}_{\mathrm{g}}\cos(\omega t) + \tilde{V_{\mathrm{g}}}^2 \cos^2(\omega t)\right)$$

For small values of $\tilde{V}_{\mathrm{g}}$, we can neglect the $\tilde{V_{\mathrm{g}}}^2$ term, which simplifies the force to:

$$F_{\mathrm{el}} \approx \frac{1}{2}\frac{dC_{\mathrm{g}}}{dx}\left(\left(V_{\mathrm{g}}^{\mathrm{DC}}\right)^2 + 2V_{\mathrm{g}}^{\mathrm{DC}}\tilde{V}_{\mathrm{g}}\cos(\omega t)\right)$$

DC and AC components of the force

The total electrostatic force consists of a constant DC component and an oscillatory AC component:

- The DC component is given by:

$$F_{\mathrm{DC}} = \frac{1}{2}\frac{dC_{\mathrm{g}}}{dx}\left(V_{\mathrm{g}}^{\mathrm{DC}}\right)^2$$

- The AC component is:

$$F_{\mathrm{AC}} = \frac{dC_{\mathrm{g}}}{dx} V_{\mathrm{g}}^{\mathrm{DC}} \tilde{V}_{\mathrm{g}} \cos(\omega t)$$

Numerical Calculation, for the specific case where:

- $V_{\mathrm{g}}^{\mathrm{DC}} = -128\,\mathrm{mV} = -0.128\,\mathrm{V}$
- $\tilde{V}_{\mathrm{g}} = 0.089\,\mathrm{V}$ (converted from $-18\,\mathrm{dBm}$)
- $\frac{dC_{\mathrm{g}}}{dx} = 1.71 \times 10^{-11}\,\mathrm{F/m}$

DC Component:

$$F_{\mathrm{DC}} = \frac{1}{2} \times 1.71 \times 10^{-11} \times (-0.128)^2$$

$$F_{\mathrm{DC}} \approx 1.44 \times 10^{-13}\,\mathrm{N}$$

AC Component:

$$F_{\mathrm{AC}} = 1.71 \times 10^{-11} \times (-0.128) \times 0.089 \cos(\omega t)$$

$$F_{\mathrm{AC}} \approx -2.00 \times 10^{-13} \cos(\omega t)\,\mathrm{N}$$

Total combined force

The total electrostatic force is the sum of the DC and AC components:

$$F_{\mathrm{total}}(t) = F_{\mathrm{DC}} + F_{\mathrm{AC}} \cos(\omega t)$$

Substituting the calculated values:

$$F_{\mathrm{total}}(t) = 1.44 \times 10^{-13} - 2.00 \times 10^{-13} \cos(\omega t)\,\mathrm{N}$$

- Maximum: $F_{\mathrm{max}} = 3.44 \times 10^{-13}\,\mathrm{N}$
- Minimum: $F_{\mathrm{min}} = -0.56 \times 10^{-13}\,\mathrm{N}$

So, the total force oscillates between these two values over time.

A.4 Tension calculation in nanotube resonator

The tension in a nanotube resonator can be modulated by applying a gate voltage V_g, which induces an electrostatic force between the gate and the nanotube. This force leads to a displacement of the nanotube and increases the tension within the device. The total tension T in the nanotube is the sum of the initial, built-in tension T_0 and the tension generated by the applied gate voltage. The mechanical response of the CNT resonator is governed by this total tension, which can be expressed in different bending regimes depending on the magnitude of the gate voltage.

For a tension-dominated resonator, the resonance frequency f_n for the n-th mode is given by the following equation:

$$f_n = \frac{n}{2L}\sqrt{\frac{T}{\mu}}$$

where L is the length of the CNT, T is the total tension, and μ is the linear mass density of the nanotube, given by $\mu = \frac{m_{\mathrm{NT}}}{L}$, with m_{NT} as the mass of the nanotube. The mode number n represents the harmonic mode (e.g., $n = 1$ for the fundamental mode). The dependence of the resonance frequency on tension allows for the calculation of tension across different modes of oscillation.

Given the CNT parameters: $L = 1.5 \times 10^{-6}\,\mathrm{m}$, $m_{\mathrm{NT}} = 1.62 \times 10^{-18}\,\mathrm{kg}$, the linear mass density μ is determined by the mass of the nanotube divided by its length:

$$\mu = \frac{m_{\mathrm{NT}}}{L} = \frac{1.62 \times 10^{-18}\,\mathrm{kg}}{1.5 \times 10^{-6}\,\mathrm{m}} = 1.08 \times 10^{-12}\,\mathrm{kg/m}$$

A.4.1 Residual tension for each mode

To calculate the residual tension for each mode at $V_g = 0\,\mathrm{V}$, we use the frequencies measured in vacuum in Fig. 6.2: $f_0 = 21\,\mathrm{MHz}$, $f_1 = 32\,\mathrm{MHz}$, $f_2 = 42.25\,\mathrm{MHz}$, $f_3 = 63.2\,\mathrm{MHz}$
The residual tension for each mode is calculated using the formula for tension in a tension-dominated resonator:

$$T = 4L^2 f_n^2 \mu$$

Now, we can calculate the residual tension T_0 for each mode at $V_g = 0\,\mathrm{V}$:
For $f_0 = 21\,\mathrm{MHz}$:

$$T_0 = 4(1.5 \times 10^{-6})^2(21 \times 10^6)^2(1.08 \times 10^{-12}) = 4.29\,\mathrm{nN}$$

For $f_1 = 32\,\mathrm{MHz}$:

$$T_1 = 4(1.5 \times 10^{-6})^2(32 \times 10^6)^2(1.08 \times 10^{-12}) = 9.95\,\mathrm{nN}$$

For $f_2 = 42.25\,\mathrm{MHz}$:

$$T_2 = 4(1.5 \times 10^{-6})^2(42.25 \times 10^6)^2(1.08 \times 10^{-12}) = 15.6\,\mathrm{nN}$$

For $f_3 = 63.2\,\mathrm{MHz}$:

$$T_3 = 4(1.5 \times 10^{-6})^2(63.2 \times 10^6)^2(1.08 \times 10^{-12}) = 37.5\,\mathrm{nN}$$

A.4.2 Tension modulation for each mode at $V_g = -670\,\mathrm{mV}$

The total tension in each mode for frequencies – $f_0 = 24.25\,\mathrm{MHz}$, $f_1 = 39.4\,\mathrm{MHz}$, $f_2 = 48.37\,\mathrm{MHz}$, $f_3 = 78.8\,\mathrm{MHz}$ at $V_\mathrm{g} = -670\,\mathrm{mV}$ can be calculated using different bending regimes. The modes f_1 and f_3 are calculated using the strong-bending regime due to their higher tunability, while the modes f_0 and f_2 use the weak-bending regime, as they are less tunable. The residual tension T_0 is now replaced with the mode-specific residual tension calculated above.

A.4.2.1 Strong bending regime

For the first harmonic f_1 and third harmonic f_3, we apply the strong-bending regime where the tension scales with $V_\mathrm{g}^{2/3}$. The total tension in this regime is modeled as:

$$T_\mathrm{strong} = T_n + \left(\frac{ESV_\mathrm{g}^2}{L^2}\right)^{1/3}$$

where $E = 1 \times 10^{12}\,\mathrm{Pa}$ [99] is the Young's modulus, and $S = \pi r^2 = 3.14 \times 10^{-18}\,\mathrm{m}^2$ is the cross-sectional area of the CNT, with a radius $r = 1\,\mathrm{nm}$.
First harmonic ($n = 1$, $f_1 = 39.4\,\mathrm{MHz}$):

$$T_1 = 9.95 \times 10^{-9} + \left(\frac{1 \times 10^{12} \times 3.14 \times 10^{-18} \times (-670 \times 10^{-3})^2}{(1.5 \times 10^{-6})^2}\right)^{1/3} = 7.04\,\mathrm{nN}$$

Third harmonic ($n = 3$, $f_3 = 78.8\,\mathrm{MHz}$):

$$T_3 = 37.5 \times 10^{-9} + \left(\frac{1 \times 10^{12} \times 3.14 \times 10^{-18} \times (-670 \times 10^{-3})^2}{(1.5 \times 10^{-6})^2}\right)^{1/3} = 4.73\,\mathrm{nN}$$

A.4.2.2 Weak bending regime

For the fundamental mode f_0 and second harmonic f_2, we apply the weak-bending regime where the tension increases quadratically with the gate voltage. The total tension in this regime is modeled as:

$$T_\mathrm{weak} = T_n + \frac{\epsilon_0 V_\mathrm{g}^2}{d^2}$$

where $\epsilon_0 = 8.854 \times 10^{-12}\,\mathrm{F/m}$ is the permittivity of free space, and $d = 1.2 \times 10^{-6}\,\mathrm{m}$ is the distance between the CNT and the gate.
Fundamental mode ($n = 1$, $f_0 = 24.25\,\mathrm{MHz}$):

$$T_0 = 4.29 \times 10^{-9} + \frac{8.854 \times 10^{-12} \times (-670 \times 10^{-3})^2}{(1.2 \times 10^{-6})^2} = 3.19\,\mathrm{nN}$$

Second harmonic ($n = 2$, $f_2 = 48.37\,\mathrm{MHz}$):

$$T_2 = 15.6 \times 10^{-9} + \frac{8.854 \times 10^{-12} \times (-670 \times 10^{-3})^2}{(1.2 \times 10^{-6})^2} = 4.32\,\mathrm{nN}$$

Thus, the total tensions for the different modes at $V_\mathrm{g} = -670\,\mathrm{mV}$ are:

- Fundamental mode: $T_0 = 3.19\,\mathrm{nN}$
- First harmonic: $T_1 = 7.04\,\mathrm{nN}$
- Second harmonic: $T_2 = 4.32\,\mathrm{nN}$
- Third harmonic: $T_3 = 4.73\,\mathrm{nN}$

A.5 Estimation of frequency shift due to Lock-in time constant

In Fig. 7.4 (Left panel), the frequency sweep is performed from 17.5 MHz to 18 MHz with a total of 251 frequency points. The time delay between consecutive frequency points is 10 ms, and the lock-in amplifier used for signal detection has an integration time constant of 100 ms. Due to the finite time constant of the lock-in amplifier, the system exhibits a phase lag during the frequency sweeps, leading to a measurable frequency shift between the forward and reverse sweeps.

To estimate this frequency shift, we first calculate the sweep rate. The total frequency range is 0.5 MHz (500 kHz) and the number of points is 251, yielding a frequency step of approximately 1.992 kHz between each point. With a time delay of 10 ms (0.01 s) between points, the sweep rate is given by:

$$\text{sweep rate} = \frac{\Delta f_{\text{step}}}{\text{time per step}} = \frac{1.992\,\text{kHz}}{0.01\,\text{s}} = 199.2\,\text{kHz/s}$$

Next, we calculate the frequency shift using the lock-in time constant, which is 100 ms (0.1 s). The frequency shift due to this time constant is given by the product of the sweep rate and the time constant:

$$\Delta f = \text{sweep rate} \times \text{time constant} = 199.2\,\text{kHz/s} \times 0.1\,\text{s} = 19.92\,\text{kHz}$$

Thus, the estimated frequency shift between the forward and reverse sweeps is approximately 19.92 kHz due to system's response lag caused by the lock-in amplifier's integration time.

A.6 Analysis of vortex number fluctuations from background noise

We attribute the observed off-resonance noise in the nanotube resonator response in superfluid ^{4}He to the dynamic processes of vortex pinning and depinning, influenced by interactions between the nanotube and the underlying substrate. These interactions lead to stochastic fluctuations in vortex number, which we analyze through a power spectral and autocorrelation study of the off-resonance signal. To quantify this relationship between vortex number fluctuations and background noise in the CNT resonator, we follow the methodological framework established by Barquist et al. [124], originally applied to MEMS devices, adapting it for the nanotube resonator in a superfluid helium.

The CNT resonator in our study is driven by a capacitive gate voltage, defined as:

$$V_{\text{g}}(t) = V_{\text{g}}^{\text{DC}} + \tilde{V}_{\text{g}} \cos(\omega t), \tag{A.1}$$

where V_g^{DC} is the static DC voltage component, $\tilde{V}_g$ is the AC driving voltage, and ω is the angular driving frequency. This capacitive actuation induces mechanical vibrations in the nanotube, described by the displacement function:

$$x(t) = A(t)\cos(\omega t + \phi(t)), \tag{A.2}$$

where $A(t)$ and $\phi(t)$ are the time-varying amplitude and phase, respectively, influenced by interactions between the resonator and surrounding vortices. The current $I(t)$ through the nanotube depends on this displacement $x(t)$ and is expressed as:

$$I(t) = G(V_g, x(t))V_{sd}, \tag{A.3}$$

where $G(V_g, x(t))$ is the conductance of the nanotube, modulated by $x(t)$, and V_{sd} is the source-drain voltage. Fluctuations in $x(t)$ induced by vortex pinning and depinning cause variations in G, and consequently, in $I(t)$. To monitor these fluctuations, we use a lock-in amplifier to measure the response $R = \frac{dI}{df}$, which captures frequency fluctuations in the system.

On resonance, the response $\frac{dI}{df}$ is predominantly governed by amplitude fluctuations of the CNT resonator, resulting in a stable signal phase locked to the driving force. Here, phase noise is minimal, with amplitude fluctuations dominating due to a coherent, locked phase response. Off-resonance, however, the mismatch between the driving frequency and the natural resonance frequency destabilizes the system. This instability makes the system more sensitive to phase fluctuations, amplifying the impact of vortex-induced phase noise. Consequently, the off-resonance signal becomes dominated by fluctuations in the effective resonance frequency, which are driven by stochastic vortex pinning and depinning.

A.6.1 Quantifying vortex number fluctuations

We derive the vortex number fluctuations ΔN by analyzing the fluctuations in the lock-in signal R. The relationship between vortex pinning, energy dissipation, and noise fluctuations is given by:

$$\frac{d\Gamma}{dN} = \frac{\epsilon}{8\pi^2 d m f_0}, \tag{A.4}$$

where $\epsilon = 8.56 \times 10^{-19}\,\mathrm{J}\,\mu\,\mathrm{m}^{-1}$ represents the vortex line energy density, $d = 175\,\mathrm{nm}$ is the distance between the resonator and the substrate, $m = 1.62 \times 10^{-18}\,\mathrm{kg}$ is the CNT mass, and $f_0 = 67.1\,\mathrm{MHz}$ is the resonance frequency. Using this dissipation rate $\frac{d\Gamma}{dN}$, we calculate the change in vortex number ΔN from changes in R by:

$$\Delta N = \frac{\Delta R}{\left(\frac{dR}{d\Gamma}\right)\left(\frac{d\Gamma}{dN}\right)}. \tag{A.5}$$

The lock-in response R_{res} is inversely proportional to the damping Γ, so we find:

$$\frac{dR}{d\Gamma} = -\frac{R_{res}}{\Gamma}. \tag{A.6}$$

This inverse relationship implies that as damping Γ increases due to vortex activity, the signal R decreases accordingly.

The complete expression for R, taking into account external factors such as gate voltage V_g^{DC} and resonance frequency f_0, is:

$$R \propto \frac{V_g^{DC}}{\Gamma \cdot f_0}. \tag{A.7}$$

Thus, the derivative with respect to Γ is refined as:

$$\frac{dR}{d\Gamma} = -\frac{V_{\mathrm{g}}^{\mathrm{DC}}}{\Gamma^2 f_0}. \tag{A.8}$$

A.6.2 Gaussian and Poisson noise distributions in vortex fluctuations

We select a frequency slice at 66.6 MHz from the top panel in Fig. 7.9, where substantial background noise is observed in superfluid helium at the lowest measured temperature, and plot the resulting noise distribution.

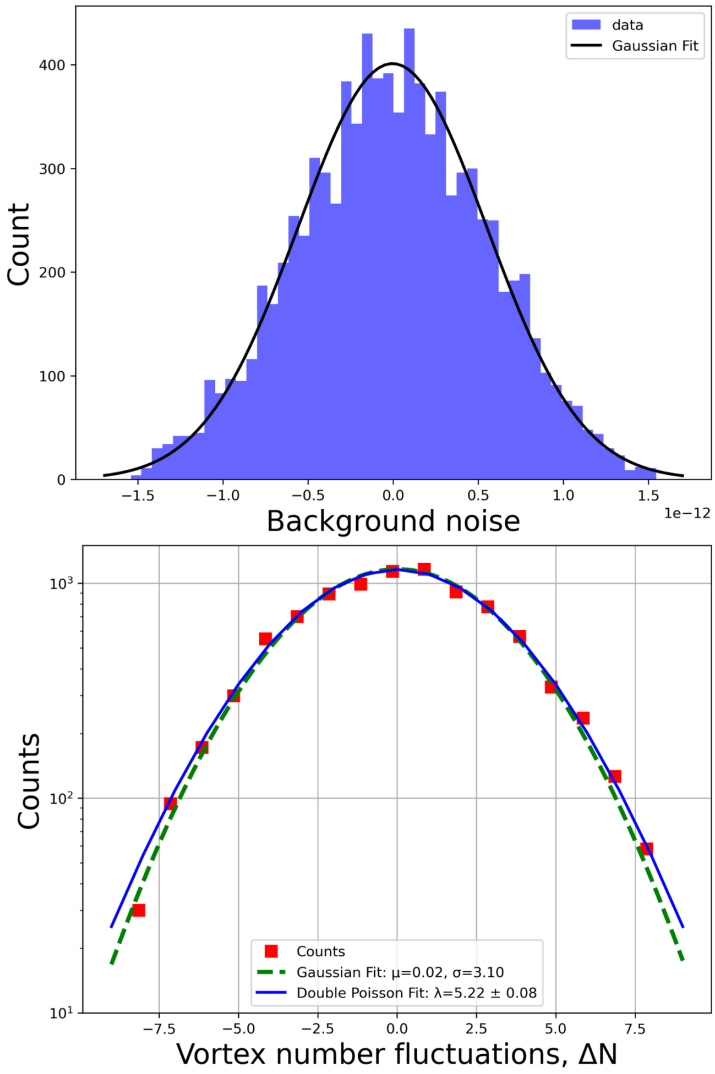

Figure A.9: Top panel: Gaussian fit of the R-channel noise. The black solid line represents the Gaussian fit with mean $\mu = -3.86 \times 10^{-15}$ and standard deviation $\sigma = 5.54 \times 10^{-13}$. Bottom panel: Distribution of ΔN, the change in pinned vortices beneath the CNT resonator. The red solid line shows a double Poisson fit with $\lambda = 4.27 \pm 0.06\,\mathrm{s}^{-1}$, while the blue dashed line shows a Gaussian fit with $\mu = 0.02$ and $\sigma = 2.90$.

In Fig. A.9, we analyze the noise distribution in the lock-in signal R, fitting it to a Gaussian distribution with a mean of $\mu = -3.86 \times 10^{-15}$ and standard deviation $\sigma =$

5.54×10^{-13}, indicating Gaussian behavior of the noise. Similarly, the distribution of vortex number fluctuations ΔN is fitted with both a double Poisson model and a Gaussian model, yielding a Poisson mean capture/removal rate $\lambda = 4.27 \pm 0.06\,\mathrm{s}^{-1}$. The Poisson fit aligns with the stochastic, discrete nature of vortex pinning and depinning, while the Gaussian fit suggests the system remains close to equilibrium.

A.6.3 Power spectral density and autocorrelation of vortex noise

In Fig. A.10 (top panel), the power spectral density (PSD) of vortex number noise $S_N(f)$ reveals a power-law decay $S_N(f) \sim f^{-0.50}$. This frequency scaling, indicative of scale-invariance, suggests a random-walk-like process in vortex dynamics, a characteristic of turbulent vortex interactions in superfluid helium. Such behavior aligns with the chaotic, uncorrelated nature of vortex capture and release events across multiple timescales, similar to findings in MEMS resonator studies.

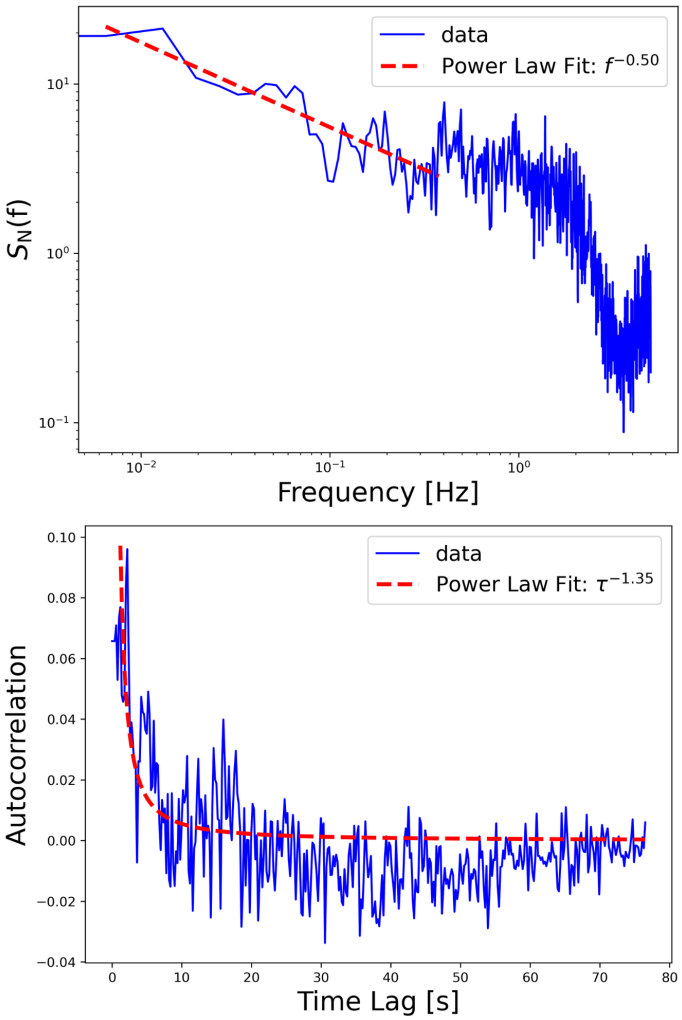

Figure A.10: Top panel: Power spectral density (PSD) of vortex number noise $S_N(f)$ derived from the amplitude noise data. The fitted power-law $S_N(f) \sim f^{-0.50}$ suggests a random walk process with significant vortex number correlations. Bottom panel: Autocorrelation function of vortex number fluctuations with the fitted power law $\langle N(t)N(t+\tau)\rangle \sim \tau^{-1.35}$. The power-law fit shows long-time correlations, deviating from the behavior of a random walk.

The autocorrelation function for vortex number fluctuations, shown in Fig. A.10 (bottom panel), decays as $\langle N(t)N(t+\tau)\rangle \sim \tau^{-1.35}$, suggesting long-time correlations in vortex dynamics. This deviation from the simple random walk model indicates that vortex interactions introduce memory effects, where past pinning events influence future dynamics, likely due to vortex-vortex interactions or clustering.

Our results imply that vortex dynamics in CNT resonators are distributed across a wide range of timescales, contributing to both amplitude and phase noise in the system. The absence of a dominant peak in the PSD further supports the notion of a broad, chaotic frequency distribution driven by random vortex events. The flattening of the autocorrelation function at large time lags may indicate a saturation point in the number of pinning vortices, suggesting that vortex interactions limit the system's ability to continually accumulate vortices. These observations are consistent with Barquist et al.'s findings on MEMS devices in quantum turbulence, reinforcing the stochastic, multi-scale nature of vortex dynamics in superfluid helium environments.

Bibliography

[1] Gregg Jaeger. "The Ehrenfest classification of phase transitions: introduction and evolution". In: *Archive for history of exact sciences* 53 (1998), pp. 51–81.

[2] Pyotr Kapitza. "Viscosity of liquid helium below the λ-point". In: *Nature* 141.3558 (1938), pp. 74–74.

[3] John F Allen and AD Misener. "Flow of liquid helium II". In: *Nature* 141.3558 (1938), pp. 75–75.

[4] DD Osheroff et al. "New magnetic phenomena in liquid he 3 below 3 mk". In: *Physical Review Letters* 29.14 (1972), p. 920.

[5] AJ Leggett. "Interpretation of recent results on He 3 below 3 mK: A new liquid phase?" In: *Physical Review Letters* 29.18 (1972), p. 1227.

[6] N David Mermin and David M Lee. "Superfluid helium 3". In: *Scientific American* 235.6 (1976), pp. 56–71.

[7] David R Tilley. Superfluidity and superconductivity. Routledge, 2019.

[8] Grigory E Volovik. The universe in a helium droplet. Vol. 117. Oxford University Press on Demand, 2003.

[9] Wojciech H Zurek. "Cosmological experiments in superfluid helium?" In: *Nature* 317.6037 (1985), pp. 505–508.

[10] DI Bradley et al. "Crossover from hydrodynamic to acoustic drag on quartz tuning forks in normal and superfluid 4 He". In: *Physical Review B* 85.1 (2012), p. 014501.

[11] AM Guénault et al. "Acoustic damping of quartz tuning forks in normal and superfluid He 3". In: *Physical Review B* 100.10 (2019), p. 104526.

[12] Shaun N Fisher et al. "Generation and Detection of Quantum Turbulence in Superfluid H 3 e- B". In: *Physical review letters* 86.2 (2001), p. 244.

[13] David Ian Bradley et al. "Operating nanobeams in a quantum fluid". In: *Scientific Reports* 7.1 (2017), pp. 1–8.

[14] AM Guénault et al. "Probing superfluid He 4 with high-frequency nanomechanical resonators down to millikelvin temperatures". In: *Physical Review B* 100.2 (2019), p. 020506.

[15] William Frank Vinen. "Mutual friction in a heat current in liquid helium II I. Experiments on steady heat currents". In: *Proceedings of the Royal Society of London. Series A. Mathematical and Physical Sciences* 240.1220 (1957), pp. 114–127.

[16] Timo Kamppinen, Jere T Mäkinen, and Vladimir B Eltsov. "Superfluid He 4 as a rigorous test bench for different damping models in nanoelectromechanical resonators". In: *Physical Review B* 107.1 (2023), p. 014502.

[17] WF Vinen, Makoto Tsubota, and Akira Mitani. "Kelvin-Wave Cascade on a Vortex in Superfluid H e 4 at a Very Low Temperature". In: *Physical review letters* 91.13 (2003), p. 135301.

[18] Vladimir B Eltsov and VS L'vov. "Amplitude of waves in the kelvin-wave cascade". In: *JETP Letters* 111 (2020), pp. 389–391.

[19] AB Shkarin et al. "Quantum optomechanics in a liquid". In: *Physical review letters* 122.15 (2019), p. 153601.

[20] NB Kopnin and MM Salomaa. "Mutual friction in superfluid he 3: Effects of bound states in the vortex core". In: *Physical Review B* 44.17 (1991), p. 9667.

[21] Pierre-François Duc et al. "Critical flow and dissipation in a quasi–one-dimensional superfluid". In: *Science Advances* 1.4 (2015), e1400222.

[22] Gary A Steele et al. "Strong coupling between single-electron tunneling and nanomechanical motion". In: *Science* 325.5944 (2009), pp. 1103–1107.

[23] Yutian Wen et al. "Measuring carbon nanotube vibrations using a single-electron transistor as a fast linear amplifier". In: *Applied Physics Letters* 113.15 (2018), p. 153101.

[24] Florian Vigneau et al. "Ultrastrong coupling between electron tunneling and mechanical motion". In: *Physical Review Research* 4.4 (2022), p. 043168.

[25] Heike Kamerlingh Onnes. "Investigations into the properties of substances at low temperatures, which have led, amongst other things, to the preparation of liquid helium". In: *Nobel lecture* 4 (1913), pp. 306–336.

[26] Fritz London. "The λ-phenomenon of liquid helium and the Bose-Einstein degeneracy". In: *Nature* 141.3571 (1938), pp. 643–644.

[27] Laszlo Tisza. "Transport phenomena in helium II". In: *Nature* 141.3577 (1938), pp. 913–913.

[28] EL Andronikashvili. "A direct observation of two kinds of motion in helium II". In: *Journal of Physics, USSR* 10.201 (1946), p. 1.

[29] Lev Landau. "Theory of the superfluidity of helium II". In: *Physical Review* 60.4 (1941), p. 356.

[30] T Ellis and Peter VE McClintock. "The breakdown of superfluidity in liquid 4He V. Measurement of the Landau critical velocity for roton creation". In: *Philosophical Transactions of the Royal Society of London. Series A, Mathematical and Physical Sciences* 315.1532 (1985), pp. 259–300.

[31] Christian Enss and Siegfried Hunklinger. Low-temperature physics. Springer Science & Business Media, 2005.

[32] D Schmoranzer et al. "Acoustic emission by quartz tuning forks and other oscillating structures in cryogenic 4 He fluids". In: *Journal of Low Temperature Physics* 163.5-6 (2011), pp. 317–344.

[33] D Schmoranzer et al. "Dynamical similarity and instabilities in high-Stokes-number oscillatory flows of superfluid helium". In: *Physical Review B* 99.5 (2019), p. 054511.

[34] L Landau. "On the theory of superfluidity". In: *Physical Review* 75.5 (1949), p. 884.

[35] Richard P Feynman. "Atomic theory of the two-fluid model of liquid helium". In: *Physical Review* 94.2 (1954), p. 262.

[36] DV Osborne. "The rotation of liquid helium II". In: *Proceedings of the Physical Society. Section A* 63.8 (1950), p. 909.

[37] WF Vinen. "Detection of single quanta of circulation in rotating helium II". In: *Nature* 181.4622 (1958), pp. 1524–1525.

[38] Mark Theodore Noble. New methods of measurements in superfluid helium. Lancaster University (United Kingdom), 2019.

[39] Andrei Nikolaevich Kolmogorov. "The local structure of turbulence in incompressible viscous fluid for very large Reynolds numbers". In: *Proceedings of the Royal Society of London. Series A: Mathematical and Physical Sciences* 434.1890 (1991), pp. 9–13.

[40] L Skrbek. "Quantum turbulence". In: *Journal of Physics: Conference Series*. Vol. 318. 1. IOP Publishing. 2011, p. 012004.

[41] Richard P Feynman. "Chapter II application of quantum mechanics to liquid helium". In: *Progress in low temperature physics*. Vol. 1. Elsevier, 1955, pp. 17–53.

[42] Richard P Feynman. "Superfluidity and superconductivity". In: *Reviews of modern physics* 29.2 (1957), p. 205.

[43] Carlo F Barenghi, Ladislav Skrbek, and Katepalli R Sreenivasan. "Introduction to quantum turbulence". In: *Proceedings of the National Academy of Sciences* 111.supplement_1 (2014), pp. 4647–4652.

[44] William Frank Vinen. "The detection of single quanta of circulation in liquid helium II". In: *Proceedings of the Royal Society of London. Series A. Mathematical and Physical Sciences* 260.1301 (1961), pp. 218–236.

[45] Tony Guenault. Basic superfluids. CRC press, 2002.

[46] Andrew John Guthrie. Nanoscale devices for studying quantum fluids and electrostatic field-effects in superconducting nanoconstrictions. Lancaster University (United Kingdom), 2020.

[47] WF Vinen. "An introduction to quantum turbulence". In: *Journal of Low Temperature Physics* 145.1-4 (2006), pp. 7–24.

[48] TWB Kibble. "Topology of cosmic domains and strings". In: *Journal of Physics A: Mathematical and General* (1976).

[49] G Krstulovic. "Kelvin-wave cascade and dissipation in low temperature superfluid vortices". In: *Physical Review E* (2012).

[50] M Tsubota and M Kobayashi. "Energy spectra of quantum turbulence". In: *Progress in Low Temperature Physics* (2009).

[51] Osborne Reynolds. "XXIX. An experimental investigation of the circumstances which determine whether the motion of water shall be direct or sinuous, and of the law of resistance in parallel channels". In: *Philosophical Transactions of the Royal society of London* 174 (1883), pp. 935–982.

[52] Kostya S Novoselov et al. “Electric field effect in atomically thin carbon films”. In: *science* 306.5696 (2004), pp. 666–669.

[53] Valentin N Popov. “Carbon nanotubes: properties and application”. In: *Materials Science and Engineering: R: Reports* 43.3 (2004), pp. 61–102.

[54] Riichiro Saito et al. “Electronic structure of graphene tubules based on C 60”. In: *Physical Review B* 46.3 (1992), p. 1804.

[55] Ronald Hanson et al. “Spins in few-electron quantum dots”. In: *Reviews of modern physics* 79.4 (2007), p. 1217.

[56] S De Franceschi et al. “Electron cotunneling in a semiconductor quantum dot”. In: *Physical review letters* 86.5 (2001), p. 878.

[57] Edward A Laird et al. “Quantum transport in carbon nanotubes”. In: *Reviews of Modern Physics* 87.3 (2015), p. 703.

[58] Mildred S Dresselhaus and Phaedon Avouris. “Introduction to carbon materials research”. In: *Carbon nanotubes: synthesis, structure, properties, and applications*. Springer, 2001, pp. 1–9.

[59] Jean-Christophe Charlier, Xavier Blase, and Stephan Roche. “Electronic and transport properties of nanotubes”. In: *Reviews of modern physics* 79.2 (2007), p. 677.

[60] Luis EF Foa Torres, Stephan Roche, and Jean-Christophe Charlier. Introduction to graphene-based nanomaterials: from electronic structure to quantum transport. Cambridge University Press, 2014.

[61] Patrick Steger. “Fabrication of a Carbon Nanotube Mechanical Resonator Using a Quartz Tuning Fork Based Transfer Method”. Master’s Thesis. Universität Regensburg, Institut II für Experimentelle und Angewandte Physik, Fakultät für Physik, Mar. 2019.

[62] Philip Richard Wallace. “The band theory of graphite”. In: *Physical review* 71.9 (1947), p. 622.

[63] Sander J Tans et al. “Individual single-wall carbon nanotubes as quantum wires”. In: *Nature* 386.6624 (1997), pp. 474–477.

[64] Stefan Frank et al. “Carbon nanotube quantum resistors”. In: *science* 280.5370 (1998), pp. 1744–1746.

[65] Marc Bockrath et al. “Single-electron transport in ropes of carbon nanotubes”. In: *Science* 275.5308 (1997), pp. 1922–1925.

[66] Michael J Biercuk et al. “Electrical transport in single-wall carbon nanotubes”. In: *Carbon Nanotubes: Advanced Topics in the Synthesis, Structure, Properties and Applications* (2008), pp. 455–493.

[67] Stefan Heinze et al. “Carbon nanotubes as Schottky barrier transistors”. In: *Physical review letters* 89.10 (2002), p. 106801.

[68] Sander J Tans, Alwin R M Verschueren, and Cees Dekker. “Room-temperature transistor based on a single carbon nanotube”. In: *Nature* 393 (1997), pp. 49–52.

[69] Marc Bockrath et al. “Single-electron transport in ropes of carbon nanotubes”. In: *Science* 275 (1997), pp. 1922–1925.

[70] Leo P Kouwenhoven and Leonid Glazman. "Coulomb blockade and the Kondo effect in single-atom transistors". In: *Physics World* 14 (2001), pp. 33–38.

[71] Pablo Jarillo-Herrero, Jeroen A van Dam, and Leo P Kouwenhoven. "Quantum superposition of charge states in double quantum dots". In: *Nature* 439 (2005), pp. 953–956.

[72] Mark A Reed et al. "Observation of discrete electronic states in a zero-dimensional semiconductor nanostructure". In: *Physical Review Letters* 60 (1991), pp. 535–537.

[73] Menno Poot and Herre SJ van der Zant. "Mechanical systems in the quantum regime". In: *Physics Reports* 511.5 (2012), pp. 273–335.

[74] Marc Dequesnes, SV Rotkin, and NR Aluru. "Calculation of pull-in voltages for carbon-nanotube-based nanoelectromechanical switches". In: *Nanotechnology* 13.1 (2002), p. 120.

[75] HB Meerwaldt, GA Steele, and HS Van Der Zant. "Carbon nanotubes: Nonlinear high-Q resonators with strong coupling to single-electron tunneling". In: *Fluctuating Nonlinear Oscillators: From Nanomechanics to Quantum Superconducting Circuits* (2012), pp. 312–340.

[76] William Weaver Jr, Stephen P Timoshenko, and Donovan Harold Young. Vibration problems in engineering. John Wiley & Sons, 1991.

[77] Yue Kuen Kwok. Applied complex variables for scientists and engineers. Cambridge University Press, 2010.

[78] S Sapmaz et al. "Carbon nanotubes as nanoelectromechanical systems". In: *Physical Review B* 67.23 (2003), p. 235414.

[79] CS Barquist et al. "Damping of a microelectromechanical oscillator in turbulent superfluid He 4: A probe of quantized vorticity in the ultralow temperature regime". In: *Physical Review B* 101.17 (2020), p. 174513.

[80] WF Vinen and JJ Niemela. "Quantum turbulence". In: *Journal of Low Temperature Physics* 128.5-6 (2002), pp. 167–231.

[81] Yutian Wen et al. "A coherent nanomechanical oscillator driven by single-electron tunnelling". In: *Nature physics* 16.1 (2020), pp. 75–82.

[82] Joel Moser et al. "Ultrasensitive force detection with a nanotube mechanical resonator". In: *Nature nanotechnology* 8.7 (2013), pp. 493–496.

[83] H Yano et al. "Observation of laminar and turbulent flow in superfluid 4 He using a vibrating wire". In: *Journal of low temperature physics* 138.3-4 (2005), pp. 561–566.

[84] CAM Castelijns et al. "Landau critical velocity for a macroscopic object moving in superfluid B 3: Evidence for gap suppression at a moving surface". In: *Physical review letters* 56.1 (1986), p. 69.

[85] RJ Zieve, CM Frei, and DL Wolfson. "Energy loss from a moving vortex in superfluid helium". In: *Physical Review B* 86.17 (2012), p. 174504.

[86] Keith C Schwab and Michael L Roukes. "Putting mechanics into quantum mechanics". In: *Physics Today* 58.7 (2005), pp. 36–42.

[87] R Blaauwgeers et al. “Quartz tuning fork: thermometer, pressure-and viscometer for helium liquids”. In: *Journal of Low Temperature Physics* 146.5-6 (2007), pp. 537–562.

[88] David Ian Bradley et al. “Nanoelectronic primary thermometry below 4 mK”. In: *Nature communications* 7.1 (2016), pp. 1–7.

[89] Masashi Morishita et al. “Mean free path effects in superfluid 4 He”. In: *Journal of low temperature physics* 76.5-6 (1989), pp. 387–415.

[90] LD Landau. EM Lifshitz Fluid Mechanics, 2nd. 1987.

[91] LD Landau and EM Lifshitz. “Fluid Mechanics Pergamon”. In: *New York* 61 (1959).

[92] Herman Z Cummins. “Experimental studies of structurally incommensurate crystal phases”. In: *Physics Reports* 185.5-6 (1990), pp. 211–409.

[93] Adrien Noury et al. “Layering transition in superfluid helium adsorbed on a carbon nanotube mechanical resonator”. In: *Physical review letters* 122.16 (2019), p. 165301.

[94] L Bruschi and M Santini. “Vibrating wire viscometer”. In: *Review of Scientific Instruments* 46.11 (1975), pp. 1560–1568.

[95] Michele Sciacca, Antonio Sellitto, and David Jou. “Transition to ballistic regime for heat transport in helium II”. In: *Physics Letters A* 378.34 (2014), pp. 2471–2477.

[96] Joel Moser et al. “Nanotube mechanical resonators with quality factors of up to 5 million”. In: *Nature nanotechnology* 9.12 (2014), pp. 1007–1011.

[97] Russell J Donnelly and Carlo F Barenghi. “The observed properties of liquid helium at the saturated vapor pressure”. In: *Journal of physical and chemical reference data* 27.6 (1998), pp. 1217–1274.

[98] A Tavernarakis et al. “Optomechanics with a hybrid carbon nanotube resonator”. In: *Nature communications* 9.1 (2018), pp. 1–8.

[99] Andreas K Huttel et al. “Carbon nanotubes as ultrahigh quality factor mechanical resonators”. In: *Nano letters* 9.7 (2009), pp. 2547–2552.

[100] Fabien Souris et al. “Ultralow-dissipation superfluid micromechanical resonator”. In: *Physical Review Applied* 7.4 (2017), p. 044008.

[101] Filip Novotnỳ et al. “Detection of Quantized Vortices Using Fourth Sound Attenuation”. In: *Journal of Low Temperature Physics* (2024), pp. 1–12.

[102] O Tkachenko and S Vilchynsky. “Transverse sound propagation in superfluid helium inside a carbon nanotube”. In: *Journal of molecular liquids* 127.1-3 (2006), pp. 158–159.

[103] IN Adamenko et al. “Transverse sound in differentially moving superfluid helium”. In: *Physical Review B—Condensed Matter and Materials Physics* 77.14 (2008), p. 144515.

[104] Jing Kong et al. “Synthesis of individual single-walled carbon nanotubes on patterned silicon wafers”. In: *Nature* 395.6705 (1998), pp. 878–881.

[105] Vera A Sazonova. A tunable carbon nanotube resonator. Cornell University, 2006.

[106] Hugh Olen Hill Churchill. "Quantum dots in gated nanowires and nanotubes". PhD thesis. Harvard University, 2012.

[107] Kristian Mølhave et al. "Electron irradiation-induced destruction of carbon nanotubes in electron microscopes". In: *Ultramicroscopy* 108.1 (2007), pp. 52–57.

[108] G Ainsley, AA Bourne, and RWE Rushforth. "Platinum investment casting alloys". In: *Platinum Metals Review* 22.3 (1978), pp. 78–87.

[109] GTJ Goetz. "Single electronics with carbon nanotubes". In: (2010).

[110] Sjors J Tans, Alwin RM Verschueren, and Cees Dekker. "Room-temperature transistor based on a single carbon nanotube". In: *Nature* 393.6680 (1998), pp. 49–52.

[111] Roger E Little and Yu Liu. "A Compact Demountable Superleak-Tight Seal for Low Temperature Experiments". In: *Review of Scientific Instruments* 44.3 (1973), pp. 346–347.

[112] Gur K White. Experimental techniques in low-temperature physics. 1997.

[113] JC Bishop and JCA Van der Sluijs. "The Kapitza conductance and its enhanced power anomaly for clean silver to helium-four interfaces at temperatures between 1 and 2 K". In: *Journal of Low Temperature Physics* 39 (1980), pp. 93–112.

[114] N Ares et al. "Sensitive radio-frequency measurements of a quantum dot by tuning to perfect impedance matching". In: *Physical Review Applied* 5.3 (2016), p. 034011.

[115] Frank Pobell. Matter and methods at low temperatures. Springer Science & Business Media, 1996.

[116] Vincent Gouttenoire et al. "Digital and FM demodulation of a doubly clamped single-walled carbon-nanotube oscillator: towards a nanotube cell phone". In: *Small* 6.9 (2010), pp. 1060–1065.

[117] Edward A Laird et al. "A high quality factor carbon nanotube mechanical resonator at 39 GHz". In: *Nano letters* 12.1 (2012), pp. 193–197.

[118] Kyle Willick and Jonathan Baugh. "Self-driven oscillation in Coulomb blockaded suspended carbon nanotubes". In: *Physical Review Research* 2.3 (2020), p. 033040.

[119] K Grove-Rasmussen, HI Jørgensen, and PE Lindelof. "Fabry–Perot interference, Kondo effect and Coulomb blockade in carbon nanotubes". In: *Physica E: Low-dimensional Systems and Nanostructures* 40.1 (2007), pp. 92–98.

[120] Ali H Nayfeh and Dean T Mook. Nonlinear oscillations. John Wiley & Sons, 2008.

[121] A Eichler et al. "Strong coupling between mechanical modes in a nanotube resonator". In: *Physical review letters* 109.2 (2012), p. 025503.

[122] Michael T Woodside and Paul L McEuen. "Scanned probe imaging of single-electron charge states in nanotube quantum dots". In: *Science* 296.5570 (2002), pp. 1098–1101.

[123] Benjamin Lassagne et al. "Coupling mechanics to charge transport in carbon nanotube mechanical resonators". In: *Science* 325.5944 (2009), pp. 1107–1110.

[124] CS Barquist et al. "Phase noise in a Duffing oscillator induced by quantum turbulence". In: *Physical Review B* 106.9 (2022), p. 094502.

[125] Thomas WB Kibble. "Topology of cosmic domains and strings". In: *Journal of Physics A: Mathematical and General* 9.8 (1976), p. 1387.

[126] Wojciech Hubert Zurek. "Cosmological experiments in condensed matter systems". In: *Physics Reports* 276.4 (1996), pp. 177–221.

[127] WM Saslow et al. "Theory of first-order layering transitions in thin helium films". In: *Physical Review B* 54.9 (1996), p. 6532.

[128] G Zimmerli, Giampaolo Mistura, and MHW Chan. "Third-sound study of a layered superfluid film". In: *Physical review letters* 68.1 (1992), p. 60.

[129] Emile Hoskinson, RE Packard, and Thomas M Haard. "Quantum whistling in superfluid helium-4". In: *Nature* 433.7024 (2005), pp. 376–376.

[130] Fritz London. Superfluids, Volume 1: Macroscopic Theory of Superfluid Helium. Dover Publications, 1954.

[131] R.P. Feynman. "Application of quantum mechanics to liquid helium". In: *Progress in Low Temperature Physics* 1 (1955), pp. 17–53.

[132] P.W. Anderson. "Considerations on the flow of superfluid helium". In: *Reviews of Modern Physics* 38.2 (1966), pp. 298–310.

[133] Andrew Guthrie et al. "Nanoscale real-time detection of quantum vortices at millikelvin temperatures". In: *Nature Communications* 12.1 (2021), p. 2645.

[134] Russell J Donnelly. Quantized vortices in helium II. Vol. 2. Cambridge University Press, 1991.

[135] Tomo Nakagawa et al. "Dynamics of pinned quantized vortices in superfluid He 4 in a microelectromechanical oscillator". In: *Physical Review B* 108.14 (2023), p. 144110.

[136] Laurent Boué et al. "Exact solution for the energy spectrum of Kelvin-wave turbulence in superfluids". In: *Physical Review B—Condensed Matter and Materials Physics* 84.6 (2011), p. 064516.

[137] Jason Laurie et al. "Interaction of Kelvin waves and nonlocality of energy transfer in superfluids". In: *Physical Review B—Condensed Matter and Materials Physics* 81.10 (2010), p. 104526.

[138] Evgeny Kozik and Boris Svistunov. "Kelvin-wave cascade and decay of superfluid turbulence". In: *Physical review letters* 92.3 (2004), p. 035301.

[139] Evgeny Kozik and Boris Svistunov. "Scale-separation scheme for simulating superfluid turbulence: Kelvin-wave cascade". In: *Physical review letters* 94.2 (2005), p. 025301.

[140] O Avenel and E Varoquaux. "Observation of Singly Quantized Dissipation Events Obeying the Josephson Frequency Relation in the Critical Flow of Superfluid He 4 through an Aperture". In: *Physical review letters* 55.24 (1985), p. 2704.

[141] C Samanta et al. "Nonlinear nanomechanical resonators approaching the quantum ground state". In: *Nature Physics* (2023), pp. 1–5.

[142] Francesco Borsoi et al. "Transmission phase read-out of a large quantum dot in a nanowire interferometer". In: *Nature communications* 11.1 (2020), p. 3666.

[143] Alois Dirnaichner et al. “Secondary electron interference from trigonal warping in clean carbon nanotubes”. In: *Physical review letters* 117.16 (2016), p. 166804.